Dissertation

A Measurement of W Boson Pair Production in pp Collisions at $\sqrt{s} = 8$ TeV with the ATLAS Experiment

Philip Sommer

Fakultät für Mathematik und Physik
Albert-Ludwigs-Universität Freiburg

A Measurement of W Boson Pair Production in pp Collisions at $\sqrt{s} = 8$ TeV with the ATLAS Experiment

Dissertation

zur Erlangung des Doktorgrades der
Fakultät für Mathematik und Physik der

Albert-Ludwigs-Universität
Freiburg im Breisgau

vorgelegt von

Philip Sommer

September 2016

Dekan:	Prof. Dr. Dietmar Kröner
Betreuer der Arbeit:	Prof. Dr. Karl Jakobs
Referent:	Prof. Dr. Karl Jakobs
Koreferent:	Prof. Dr. Horst Fischer
Prüfer:	Prof. Dr. Harald Ita
	Prof. Dr. Gregor Herten
	Prof. Dr. Karl Jakobs

Datum der mündlichen Prüfung:
22. November 2016

Contents

Introduction

The Standard Model of particle physics provides a theoretical description of the fundamental constituents of matter and their interactions via three of the four fundamental forces. It successfully describes measurements over a large kinematic range and has withstood most stringent experimental tests. Within the Standard Model, the laws of nature are derived based on symmetry principles. The underlying symmetry of the electroweak interaction $\mathrm{SU}(2)_L \otimes \mathrm{U}(1)_Y$ is particularly interesting. The spontaneous breaking of this symmetry causes three of the four mediators of the electroweak force, namely the W^+, W^- and Z bosons, to be massive while the photon γ, as the fourth mediator, remains massless. Another property of the underlying symmetry is its non-Abelian structure that causes self-interactions between the mediators of the electroweak theory. One of the key processes to study these self-interactions is the production of pairs of W bosons in particle collisions at high energy. The behaviour of the production rate at high energy is governed by gauge-cancellations between processes involving longitudinal polarisation states of the W bosons. These are tested here in high energy proton–proton collisions. The mechanisms to produce pairs of W bosons are the radiation of two W bosons off of the proton constituents and the production via the exchange of a virtual photon γ or a Z boson that couple to W bosons through the above mentioned self-interactions. The Standard Model makes precise predictions of these couplings. Both production mechanisms grow infinitely large with energy but interfere destructively such that the effects of longitudinally polarised gauge bosons cancel exactly if the coupling strengths of W bosons to quarks, the photon and the Z boson are as predicted in the Standard Model.

For the analysis of proton–proton collisions, theoretical calculations including corrections from perturbative quantum chromodynamics are indispensable in the description of the W^+W^- process and form the foundation of the tests of the Standard Model described above. Those theoretical calculations were steadily improved over the past years. Confronting these calculations with experimental data also is an important incentive to perform measurements of the W^+W^- production process. The main contributions made in the course of this thesis lie in the measurement of fiducial and total production cross sections and their comparison to theoretical calculations. Real corrections to the production cross sections from initial state radiation, i.e. the radiation of gluons off of the proton constituents participating in the W^+W^- production and the splitting of gluons to a quark and an anti-quark, play an important role for the studies presented here. The strong interaction confines the outgoing quarks and gluons to bound states that are manifested in the experimental signature of so-called hadronic jets. Previous measurements of W boson pair production at the Tevatron and the LHC were restricting the measured phase space region to final states without hadronic jets, thus introducing a high sensitivity to effects at the phase space boundaries. In the course of this thesis the phase space was, for the first time

in the ATLAS experiment, extended to also contain final states with one hadronic jet. This considerably reduces the sensitivity to uncertainties from theoretical calculations and consequently results in a more precise measurement.

The ATLAS experiment is designed for the measurement of particles produced in proton–proton collisions delivered by the Large Hadron Collider located at CERN. In this thesis, measurements of the production of two W bosons in proton–proton collisions at a centre-of-mass energy of $\sqrt{s} = 8$ TeV are presented. A dataset corresponding to an integrated luminosity of $20.3\ \text{fb}^{-1}$ recorded in the year 2012 is analysed. For the measurement, the W bosons are identified by their decay products of an electron or a muon together with their associated neutrinos. Leptons are a clear and unambiguous signature of an electroweak process at a hadron-collider experiment. Since the final state of W^+W^- events involves two neutrinos, it is impossible to fully reconstruct the W bosons. This causes the selected event sample to be largely contaminated with contributions from other processes that mimic the W^+W^- signature. The harsh experimental conditions related to the largely increased instantaneous luminosity at the Large Hadron Collider in the year 2012 aggravate the situation. The analysis is thus experimentally challenging and requires a good understanding of the detector and the background processes contributing to the selected data.

The reconstruction of leptons and the knowledge of their reconstruction efficiency plays a crucial role. A measurement of electron identification efficiencies in $Z \to ee$ decays and the statistical combination with complementary measurements was conducted in the course of this thesis. The isolation of the electrons measured in the electromagnetic calorimeter is used to estimate contributions from background processes. The measured efficiencies are combined with other measurements in $Z \to ee$ and $J/\psi \to ee$ decays in a χ^2 minimisation and benefit all analyses at the ATLAS experiment that use electron final states. In the analysis of $pp \to W^+W^-$ production, the focus lies in the measurement of fiducial and total production cross sections. Within the work presented in this thesis, criteria to select W^+W^- candidate events with a high purity are determined and contributions from W+jets and $Z/\gamma^* \to \ell\ell$ events to the selected data are estimated. The rejection of background processes and their estimation requires detailed studies of different variables that allow a discrimination of signal and background processes. Further contributions lie in the estimation of theoretical uncertainties and the calculation of cross sections. The latter is performed in a maximum profile likelihood fit. An emphasis is made on the consideration of migrations of events between final states with zero and one hadronic jet.

The theoretical framework of the Standard Model as well as the phenomenology of hadron-collider experiments is discussed in Chapter 1. The experimental setup, i.e. the Large Hadron Collider and the ATLAS detector, are presented in Chapter 2. In Chapter 3 the reconstruction of particles from the data recorded by the ATLAS detector is described. Measurements of electron identification efficiencies are summarised in Chapter 4. The results and methods presented there have already been published in Refs. [1–3]. In the following chapters, W boson pair production is discussed. Chapter 5 starts with a summary of the theoretical aspects, followed by a summary of recent theoretical developments and a review of previous measurements. Then, the measurement of W^+W^- production is presented. The selection of W^+W^- events from data is detailed in Chapter 6, the estimation of contributions from W+jets and $Z/\gamma^* \to \ell\ell$ events is presented in Chapters 7 and 8, respectively. Chapter 9 de-

scribes the measurement of cross sections and the associated theoretical uncertainties. A first set of fiducial and total cross-section measurements is performed in final states with zero hadronic jets and is summarised in Chapter 10, together with measurements of differential cross sections and limits on anomalous WWZ and $WW\gamma$ couplings. Those results have been published in Refs. [4, 5]. Finally, results for the production of two W bosons in association with one hadronic jet as well as combined results from final states with zero or one hadronic jet are reported in Chapter 11. They have been published in Ref. [6]. A summary of the results is given in the last Chapter.

1 Theoretical Overview

A description of the fundamental constituents of matter and their interactions is formulated in the Standard Model of particle physics. The Standard Model represents the theoretical framework of the experimental measurements presented in this thesis. Its basic concepts are briefly outlined in Section 1.1. The phenomenology of proton–proton collisions at high energies is introduced in Section 1.2. Further details relevant specifically in the context of W boson pair production are given in Chapter 5.

1.1 The Standard Model of Particle Physics

The Standard Model of particle physics is a quantum field theory describing the properties and interactions of all known particles. It emerged during the 1960s and 1970s from the unification of the electromagnetic and weak interactions into an electroweak theory [7–9], and the theory of the strong interaction [10–12]. The electroweak and strong interactions are described via gauge fields, representing spin-1 particles. The gauge fields follow from the postulation of local gauge invariance under local $\mathrm{SU}(3) \otimes \mathrm{SU}(2) \otimes \mathrm{U}(1)$ symmetry transformations. Interactions between fundamental particles are mediated by quanta of these fields which are summarised in Table 1.1. The strong interaction is mediated by eight gluons. The electroweak interaction is mediated by one massless photon and three massive gauge bosons, W^+, W^- and Z, that follow as linear combinations of the quanta of the underlying $\mathrm{SU}(2)_L \otimes \mathrm{U}(1)_Y$ symmetry group. Mass terms for the $W^\pm$ and Z bosons are incorporated in the Standard Model by breaking the electroweak symmetry [13–15].

The Standard Model has withstood most stringent experimental tests and at the same time has proven to be very predictive. The most notable experimental confirmations are the observations of the massive gauge bosons in the year 1983 [16–19] and the observation of a scalar boson that is predicted by electroweak symmetry breaking in the year 2012 [20, 21].

Interaction	Mediator				underlying
	Name	Symbol	Charge	Mass	symmetry group
Electromagnetic	Photon	γ	0	0	$\mathrm{SU}(2)_L \otimes \mathrm{U}(1)_Y$
Weak	W^+ boson	W^+	+1	~ 80.4 GeV	$\mathrm{SU}(2)_L \otimes \mathrm{U}(1)_Y$
Weak	W^- boson	W^-	−1	~ 80.4 GeV	$\mathrm{SU}(2)_L \otimes \mathrm{U}(1)_Y$
Weak	Z boson	Z	0	~ 91.2 GeV	$\mathrm{SU}(2)_L \otimes \mathrm{U}(1)_Y$
Strong	8 Gluons	g	0	0	$\mathrm{SU}(3)_C$

Table 1.1: The mediators of the fundamental interactions with their electrical charge and mass. The photon, the $W^\pm$ and Z bosons represent linear combinations of the gauge fields of the $\mathrm{SU}(2)_L \otimes \mathrm{U}(1)_Y$ symmetry.

Family	1^{st}	2^{nd}	3^{rd}	I_3	Y	Q
Leptons	$\begin{pmatrix} \nu_e \\ e \end{pmatrix}_L$	$\begin{pmatrix} \nu_\mu \\ \mu \end{pmatrix}_L$	$\begin{pmatrix} \nu_\tau \\ \tau \end{pmatrix}_L$	$1/2$	-1	0
				$-1/2$	-1	-1
	e_R	μ_R	τ_R	0	-2	-1
Quarks	$\begin{pmatrix} u \\ d' \end{pmatrix}_L$	$\begin{pmatrix} c \\ s' \end{pmatrix}_L$	$\begin{pmatrix} t \\ b' \end{pmatrix}_L$	$1/2$	$1/3$	$2/3$
				$-1/2$	$1/3$	$-1/3$
	u_R	c_R	t_R	0	$4/3$	$2/3$
	d_R	s_R	b_R	0	$-2/3$	$-1/3$

Table 1.2: The fundamental matter particles grouped into quarks and leptons with their electroweak quantum numbers. They are arranged in three generations of left-handed doublets and right-handed singlets of spin-½ fields. The down-type quarks d', s', b' are linear combinations of d, s, b.

1.1.1 Particle Content

The symmetry principles postulated in the Standard Model imply the existence of associated quantum numbers that are conserved in the interactions it describes. The quantum number associated to the $\mathrm{SU}(3)_C$ symmetry is called colour. The quantum numbers associated to the $\mathrm{SU}(2)_L$ and $\mathrm{U}(1)_Y$ gauge groups are called weak isospin I and weak hypercharge Y, respectively. Their relation to the electrical charge is given by $Q = I_3 + \frac{Y}{2}$, where I_3 is the third component of the weak isospin. All matter is described by fermionic fields of spin-½ particles that are classified according to their electroweak quantum numbers and whether or not they participate in the strong interaction. Triplets of red, green or blue, and colour neutral singlets of the $\mathrm{SU}(3)_C$ group are called quarks and leptons, respectively. The $\mathrm{SU}(2)_L$ group represents a chiral symmetry and the associated gauge bosons couple to left-handed fermion fields only. Hence, the fermion fields are further arranged into left-handed doublets, carrying a weak isospin $I = 1/2$, and right-handed singlets carrying $I = 0$. Each fermion comes in a threefold family replication. Fermions of different families have identical quantum numbers and only differ in their mass. Overall, there are six quarks and six leptons. The three families of leptons contain the electron e, the muon μ and the τ-lepton. They have an electrical charge of -1. Each of their left-handed representatives forms a doublet with an associated neutrino, ν_e, ν_μ or ν_τ, that carries no electrical charge. The third component of the weak isospin of the charged leptons and the neutrinos takes the values $-1/2$ and $+1/2$, respectively. Left-handed quark doublets are classified into up-type and down-type with a value of the third component of the weak isospin of $\pm 1/2$. The up-type quarks have an electrical charge of $+2/3$ and are named up u, charm c and top t. Down-type quarks have an electrical charge of $-1/3$ and are named down d, strange s and bottom b. The right-handed counterparts of the leptons and quarks carry the same electrical charge but no weak isospin. Since neutrinos carry neither electrical charge nor colour, only left-handed neutrinos participate in the interactions described by the Standard Model. A summary of the fermionic matter and their quantum numbers is given in Table 1.2. For each of the matter particles there exists an anti-particle which has the same additive quantum numbers but with op-

posite sign and its chirality is flipped, e.g. the anti-particle of the left-handed electron is right-handed and has electrical charge +1.

1.1.2 Fields and Gauge Interactions

The Standard Model describes particles as quantum fields. Their propagation and interactions are described in the Lagrange formalism. A detailed explanation of this formalism can be found e.g. in Refs. [22, 23] on which the discussion in the following sections is based on. The equations of motion for a freely propagating fermion ψ with mass m follow from the Euler-Lagrange equation applied to a Lagrangian density:

$$\mathcal{L} = \overline{\psi}\left(i\gamma^\mu\partial_\mu - m\right)\psi. \tag{1.1}$$

The Lagrangian density is invariant under so-called global gauge transformations of the fermion field $\psi \to e^{i\alpha}\psi$, where the phase factor α is a real constant. The symmetry principles of the Standard Model require the invariance under *local* gauge transformations, i.e. the phase factor α is allowed to depend on space-time coordinates x:

$$\psi \to e^{i\alpha(x)}\psi. \tag{1.2}$$

The Lagrangian in Eq. 1.1 is not invariant under a local gauge transformation, since the derivative introduces a term $\partial_\mu\alpha(x)$. Local gauge invariance is established by modifying the derivative such that the term $\partial_\mu\alpha(x)$ is canceled. This is achieved by introducing a vector field A_μ with the desired transformation properties, $A_\mu \to A_\mu + \frac{1}{e}\partial_\mu\alpha$. The modified derivative becomes:

$$\partial_\mu \to \partial_\mu - ieA_\mu. \tag{1.3}$$

The vector field A_μ is also called a gauge field. It couples to the fermion field ψ with strength e. The invariance under the transformation in Eq. 1.2 corresponds to a symmetry under a $\mathrm{U}(1)$ gauge transformation and A_μ can be identified with the photon field. With the modified derivative the Lagrangian density in Eq. 1.1 becomes:

$$\mathcal{L}_{\mathrm{QED}} = \underbrace{i\overline{\psi}\gamma^\mu\partial_\mu\psi}_{\text{kinetic term of }\psi} - \underbrace{m\overline{\psi}\psi}_{\text{mass term of }\psi} + \underbrace{e\overline{\psi}\gamma^\mu A_\mu\psi}_{\text{interaction term}} - \underbrace{\frac{1}{4}F_{\mu\nu}F^{\mu\nu}}_{\text{kinetic term of }A_\mu}, \tag{1.4}$$

and contains kinetic terms for the fermion field ψ and the photon field A_μ, a mass term for ψ and a term for the interaction between the fermion and photon fields with a strength given by the coupling constant e. The kinetic term of the photon field uses the expression $F_{\mu\nu} = \partial_\mu A_\nu - \partial_\nu A_\mu$. The Lagrangian density in Eq. 1.4 can be identified with the Lagrangian density of quantum electrodynamics (QED). Similar to the above prescription, the Lagrangian density of quantum chromodynamics is obtained by requiring symmetry under local $\mathrm{SU}(3)_C$ gauge transformations, which is described in Section 1.1.3. The symmetry requirement under local $\mathrm{SU}(2)_L \otimes \mathrm{U}(1)_Y$ gauge transformations yields the Lagrangian density of the electroweak theory and is described in Section 1.1.4.

1.1.3 Quantum Chromodynamics

The theory of strong interactions is quantum chromodynamics (QCD) and it is derived by requiring gauge invariance under local $\mathrm{SU}(3)_C$ transformations on quark colour fields q. The Lagrangian density of free colour fields is:

$$\mathcal{L} = \overline{q}_j \left(i\gamma^\mu \partial_\mu - m \right) q_j, \tag{1.5}$$

where q_j represents three quark fields with colour charge j = red, green, blue. The requirement of local gauge invariance corresponds to the transformation:

$$q_j \rightarrow e^{i\alpha_a(x)\frac{\lambda_a}{2}} q_j \tag{1.6}$$

where the generators of the group λ_a, $a = 1, \ldots, 8$, are a set of eight linearly independent, trace-less 3×3 matrices. The matrices λ_a do not commute with each other, $\left[\frac{\lambda_a}{2}, \frac{\lambda_b}{2}\right] = i f_{abc} \frac{\lambda_c}{2}$. The variables f_{abc} are the structure constants of SU(3). Symmetry groups with non commuting generators are called non-Abelian. Local gauge invariance of Eq. 1.5 is retained analogously to Section 1.1.2 by introducing vector fields with transformation properties such that the terms in $\partial_\mu \alpha_a$ cancel:

$$\partial_\mu \rightarrow \partial_\mu + i g_\mathrm{s} \frac{\lambda_a}{2} G^a_\mu \tag{1.7}$$

$$G^a_\mu \rightarrow G^a_\mu - \frac{1}{g_\mathrm{s}} \partial_\mu \alpha_a - f_{abc} \alpha_b G^c_\mu, \tag{1.8}$$

with eight gluon fields G^a_μ that couple with strength g_s. The gluon fields have more complicated transformation properties than the vector field A_μ introduced in Section 1.1.2. This leads to the Lagrangian density of quantum chromodynamics:

$$\mathcal{L}_\mathrm{QCD} = i\overline{q}_j \gamma^\mu \partial_\mu q_j - m\overline{q}_j q_j - g_\mathrm{s} \left(\overline{q}_j \gamma^\mu \frac{\lambda_a}{2} q_j \right) G^a_\mu - \frac{1}{4} G^a_{\mu\nu} G^{\mu\nu}_a. \tag{1.9}$$

The field strength tensor $G^a_{\mu\nu}$ is defined as $G^a_{\mu\nu} = \partial_\mu G^a_\nu - \partial_\nu G^a_\mu - g_\mathrm{s} f_{abc} G^b_\mu G^c_\nu$. There are eight vector gluon fields G^a_μ in order to compensate the phase variation of three quark colour fields. Compared to $F_{\mu\nu}$ additional terms describing self interactions between gluon fields are present in $G_{\mu\nu}$. This is a consequence of the non-vanishing structure constants of the $\mathrm{SU}(3)_C$ symmetry group, i.e. its non-Abelian structure.

1.1.4 Electroweak Theory

The electromagnetic and weak interactions are described in a unified electroweak theory with an $\mathrm{SU}(2)_L \otimes \mathrm{U}(1)_Y$ gauge symmetry. The Lagrangian density of the electroweak theory is slightly more complex than the examples shown before. It is introduced in the following as the sum of four terms $\mathcal{L}_\mathrm{EW} = \mathcal{L}_1 + \mathcal{L}_2 + \mathcal{L}_3 + \mathcal{L}_4$. Experimental observations suggest that the weak interaction affects left-handed fermion fields only (and right-handed anti-fermion fields). The fermion fields are represented by the left-handed doublets χ_L and the right-handed singlets ψ_R introduced in Table 1.2. For leptons and quarks of the first family

they take the form:

$$\chi_L = \begin{pmatrix} \nu_e \\ e \end{pmatrix}_L \qquad \text{and} \qquad \chi_L = \begin{pmatrix} u \\ d \end{pmatrix}_L, \tag{1.10}$$

$$\psi_R = e_R \qquad \text{and} \qquad \psi_R = u_R \text{ and } d_R, \tag{1.11}$$

where the corresponding fermions of the second and third family follow accordingly. The Lagrangian density for these fermion fields is required to be invariant under local gauge transformations corresponding to both the $\mathrm{SU}(2)_L$ and $\mathrm{U}(1)_Y$ symmetry groups following the approaches already used in Sections 1.1.2 and 1.1.3:

$$\chi_L \rightarrow e^{i\beta(x)Y + i\alpha_a(x)\tau_a}\chi_L \tag{1.12}$$

$$\psi_R \rightarrow e^{i\beta(x)Y}\psi_R, \tag{1.13}$$

where $\alpha(x)$ and $\beta(x)$ are the phase transformation factors of the $\mathrm{SU}(2)_L$ and $\mathrm{U}(1)_Y$ symmetry groups. The Pauli matrices τ_a, $a = 1, 2, 3$, and the weak hypercharge operator Y are the generators of the groups. For the left- and right-handed lepton fields, Y takes the values -1 and -2, respectively. As for the case of QCD, the Lagrangian density is obtained by modifying the derivative ∂_μ in the Lagrangian of a free field with the vector fields of the $\mathrm{SU}(2)_L$ symmetry group, W^a_μ, the vector field of the $\mathrm{U}(1)_Y$ symmetry group, B_μ, and the field strength tensors $W^a_{\mu\nu}$ and $B_{\mu\nu}$:

$$\begin{aligned} \mathcal{L}_1 &= \bar{\chi}_L \gamma^\mu \left[i\partial_\mu - g\frac{\tau_a}{2} W^a_\mu + \frac{g'}{2} B_\mu \right] \chi_L \\ &\quad + \bar{\psi}_R \gamma^\mu \left[i\partial_\mu + g' B_\mu \right] \psi_R - \frac{1}{4} W^a_{\mu\nu} W^{\mu\nu}_a - \frac{1}{4} B_{\mu\nu} B^{\mu\nu}. \end{aligned} \tag{1.14}$$

where the coupling strength is given by the constants g for the fields W^a_μ and g' for the field B_μ. The kinetic terms of the vector fields of the electroweak theory $W^a_{\mu\nu}$ contain terms describing self interactions between the vector fields W^a_μ, $a = 0, 1, 2$, due to the non-vanishing structure constants of SU(2). The term $\mathcal{L}_1$ describes an interaction between massless fermion fields and massless gauge fields. This is in contradiction to experimental observation of massive fermions and the massive $W^\pm$ and Z bosons listed in Table 1.1.

In general, adding mass terms of vector fields of the form $\frac{1}{2} m W^a_\mu W^\mu_a$ renders Eq. 1.14 to violate gauge invariance. Massive gauge fields can be accommodated, however, by breaking the $\mathrm{SU}(2)_L \otimes \mathrm{U}(1)_Y$ symmetry. The mass terms are generated by introducing an $\mathrm{SU}(2)_L$ doublet of complex scalar fields ϕ for which gauge invariance is required:

$$\mathcal{L}_{\text{Higgs}} = (\partial_\mu \phi)^* (\partial^\mu \phi) \underbrace{-\mu^2 \phi^* \phi + \lambda (\phi^* \phi)^2}_{=-V(\phi)}, \tag{1.15}$$

The symmetry can be spontaneously broken by choosing the potential $V(\phi)$ such that the field ϕ does not vanish at the minimum of the potential, i.e. $\mu^2 < 0$ and $\lambda > 0$ in Eq. 1.15. The value of the field in the minimum of the potential is $|\phi_0| = \sqrt{-\mu^2/2\lambda}$ and known as the vacuum expectation value. The $\mathrm{SU}(2)_L \otimes \mathrm{U}(1)$ gauge invariant expression for Eq. 1.15 is

obtained using the modified derivative ∂_μ:

$$\mathcal{L}_2 = -\left|\left(i\partial_\mu - g\frac{\tau_a}{2}W_\mu^a - i\frac{g'}{2}B_\mu\right)\phi\right|^2 - V(\phi) \tag{1.16}$$

and added to $\mathcal{L}_{\text{EW}}$. In a chosen minimum of $\phi_0 = \frac{1}{\sqrt{2}}\begin{pmatrix} 0 \\ v \end{pmatrix}$ the gauge fields of Eq. 1.16 acquire mass terms:

$$\left|\left(-ig\frac{\tau_a}{2}W_\mu^a - i\frac{g'}{2}B_\mu\right)\phi_0\right|^2 = \left(\frac{1}{2}vg\right)^2 W_\mu^+ W^{-\mu} + \frac{1}{8}v^2\left(g^2+g'^2\right)Z_\mu Z^\mu + 0\left(g^2+g'^2\right)A_\mu A^\mu, \tag{1.17}$$

where the gauge fields are expressed as linear combinations of the $\text{SU}(2)_L$ and $\text{U}(1)_Y$ fields with the weak mixing angle θ_W:

$$W_\mu^\pm = \frac{1}{\sqrt{2}}\left(W_\mu^1 \mp iW_\mu^2\right) \tag{1.18}$$

$$Z_\mu = \cos\theta_W W_\mu^3 - \sin\theta_W B_\mu \tag{1.19}$$

$$A_\mu = \sin\theta_W W_\mu^3 + \cos\theta_W B_\mu. \tag{1.20}$$

The fields $W_\mu^\pm$, Z_μ and A_μ can be identified with the $W^\pm$ bosons of mass $m_W = \frac{1}{2}vg$, the Z boson of mass $m_Z = m_W/\cos\theta_W$ and the massless photon field, where the weak mixing angle is defined with $\tan\theta_W = g'/g$. The electromagnetic coupling constant e introduced in Eq. 1.3 can be expressed as $e = g\sin\theta_W = g'\cos\theta_W$. The self couplings in Eq. 1.14 are explicitly expressed in terms of the vector fields $W_\mu^\pm$, Z_μ and A_μ in Section 5.1 where the theory of W boson pair production is discussed.

Introducing the scalar fields in Eq. 1.15 is a convenient way to generate gauge boson masses. The potential $V(\phi)$, however, introduces further terms in the Lagrangian density in Eq. 1.16 which are shown here for a parametrisation of the field ϕ around the ground state:

$$\mathcal{L} = \frac{1}{2}\left(\partial_\mu h\right)^2 + \left[m_W^2 W_\mu^+ W^{-\mu} + m_Z^2 Z_\mu Z^\mu\right]\left(1+\frac{h}{v}\right)^2 \tag{1.21}$$

$$-\lambda v^2 h^2 - \lambda v h^3 - \frac{1}{4}\lambda h^4, \text{ using } \phi = \frac{1}{\sqrt{2}}\begin{pmatrix} 0 \\ v+h(x) \end{pmatrix}. \tag{1.22}$$

The Lagrangian density contains a mass term for the field $h(x)$ with $m_h = \sqrt{2\lambda v^2}$ which describes a scalar particle referred to as the Higgs boson. In addition, the Lagrangian density contains coupling terms, most notably couplings of the field $h(x)$ and the heavy gauge bosons $W^\pm$ and Z, and the mass terms of the heavy gauge bosons already derived in Eq. 1.17.

Another $\text{SU}(2)_L \times \text{U}(1)_Y$ gauge invariant term is introduced to account for mass terms for the fermion fields, here shown for lepton fields χ_L and ψ_R:

$$\mathcal{L}_3 = -G_\ell\left[\overline{\chi}_L\phi\psi_R + \overline{\psi}_R\phi^*\chi_L\right]. \tag{1.23}$$

with arbitrary parameters G_ℓ, $\ell = e, \mu, \tau$. Using the same parametrisation of ϕ as in Eq. 1.22

the term becomes:

$$\mathcal{L} = \frac{G_\ell v}{\sqrt{2}}\left(\bar{\ell}_L \ell_R + \bar{\ell}_R \ell_L\right) - \frac{G_\ell}{\sqrt{2}}\left(\bar{\ell}_L \ell_R + \bar{\ell}_R \ell_L\right) h \tag{1.24}$$

and represents mass terms for the fermions $m_\ell = G_\ell v/\sqrt{2}$ and the interaction of electrons with the scalar field. Unless right-handed neutrinos are introduced, the same mechanism requires their left-handed counterparts to be massless. The mass terms of the quark fields follow in a similar way. Since there are also right-handed down-type quarks, the parameters corresponding to G_ℓ in Eq. 1.23 are matrices, G_q^{ij}, for the quark families i, j and up- and down-type quarks q:

$$\mathcal{L}_4 = -G_d^{ij}\left(\bar{u}_i, \bar{d}_i\right)_L \phi\, d_{jR} - G_u^{ij}\left(\bar{u}_i, \bar{d}_i\right)_L \phi\, u_{jR} + \text{ h.c.} \tag{1.25}$$

The matrices G_q^{ij} are diagonal if the left-handed quark fields are rotated with respect to the solutions of Eq. 1.9 by a unitary transformation, $u_L^i \to u_L^{i\prime} = U_u^{ij} u_L^j$ and $d_L^i \to d_L^{i\prime} = U_d^{ij} d_L^j$, as was already indicated in Table 1.2. The matrix $V = U_u^\dagger U_d$ is called the CKM matrix.

1.2 Phenomenology of Proton-Proton Collisions

The Lagrangian formalism discussed so far does not provide the tools necessary to derive theoretical predictions of observables that can be experimentally verified in proton–proton collisions. The main results of the measurements presented in this thesis are cross sections. The relevant steps to perform the theoretical calculations are briefly outlined in the following. The discussion is based on Refs. [24–26].

Theoretical cross sections are calculated from scattering amplitudes $\mathcal{M}$ that follow from the Lagrangian density of the Standard Model using a perturbative expansion. The scattering amplitude represents the transition rate from the initial to the final state and contains all the dynamical information of the process under investigation. The differential scattering cross section $\mathrm{d}\sigma$ of two particles is given by:

$$\mathrm{d}\sigma = \frac{|\mathcal{M}|^2}{F}\mathrm{d}Q, \tag{1.26}$$

where the factors F and $\mathrm{d}Q$ represent the incident flux and a Lorentz invariant phase space factor, respectively [22].

1.2.1 Factorisation and Parton Distribution Functions

The proton is a composite of quarks and gluons which constitute its partons. The internal structure of the proton cannot be described in a perturbative approach. The processes studied in this thesis, on the other hand, happen at very high energies and therefore can very well be calculated in perturbative QCD. The low energy, non-perturbative effects in the proton and the hard scattering at high energy can be factorised [27]. The cross sections of a process with two initial-state protons p_1 and p_2 that produces the final state X, $\sigma_{p_1 p_2 \to X}$,

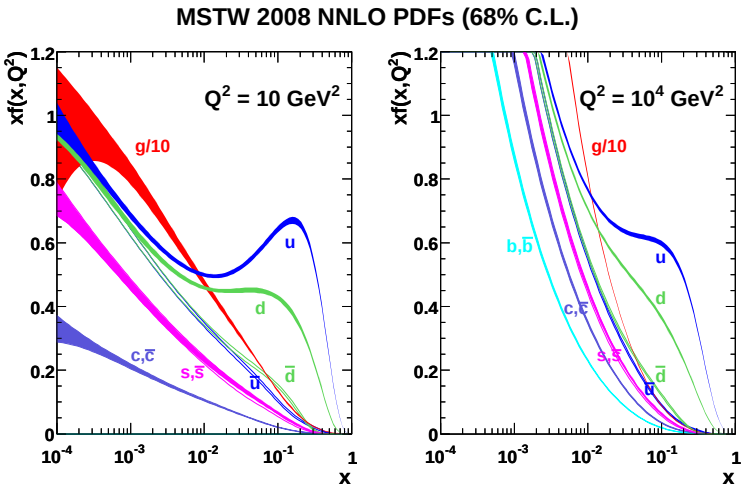

Figure 1.1: Parton distribution functions $xf_q(x, Q^2)$ for momentum transfers of $Q^2 = 10\,\text{GeV}^2$ (left) and $Q^2 = 10^4\,\text{GeV}^2$ (right) by the PDF fitting group MSTW. The dependence on the momentum faction x carried by a parton is extracted in global PDF fits from experimental data. Taken from Ref. [28].

is given by the sum of partonic cross sections $\sigma_{q_1 q_2 \to X}$:

$$\mathrm{d}\sigma_{p_1 p_2 \to X} = \int \mathrm{d}x_1 \mathrm{d}x_2 \sum_{q_1, q_2} f_{q_1}(x_1, \mu_\mathrm{F}) f_{q_2}(x_2, \mu_\mathrm{F}) \cdot \mathrm{d}\sigma_{q_1 q_2 \to X}(x_1 x_2 s, \mu_\mathrm{R}, \mu_\mathrm{F}), \tag{1.27}$$

where q_1 and q_2 are the partons of the proton. The functions $f_q(x, \mu_\mathrm{F})$ are the parton distribution functions (PDFs) and represent the density of the partons q inside a proton that carry the longitudinal momentum fraction x.

The parton distribution functions are determined experimentally using data from e.g. deep inelastic scattering in electron–proton collisions. The experimental data allow to parametrise the PDFs as a function of the longitudinal momentum fraction x for a reference value of the momentum Q_0^2 transferred in the hard interaction. The evolution of the parametrisation to different values Q^2 is driven by modifications of the momenta of the partons from the emission of gluons off of quarks and the splitting of gluons to $q\bar{q}$ pairs. These modifications can be explicitly computed using perturbative QCD. The PDF at any value Q^2 can be calculated from the PDF at the reference scale Q_0^2 using the DGLAP evolution equations [29–31]. An example of a PDF is shown in Fig. 1.1 for two different values of the momentum transfer Q^2. The valence quarks of the proton, two u- and one d-quark, are visible as an enhancement of the probability for larger values of x.

The distinction whether perturbative corrections modify the PDF or are included in the partonic cross section $\sigma_{q_1 q_2 \to X}$ is done at a threshold μ_F, known as the factorisation scale. The factorisation introduces a μ_F-dependence in both the PDF and the partonic cross section which would vanish if both quantities were calculated including all perturbative orders.

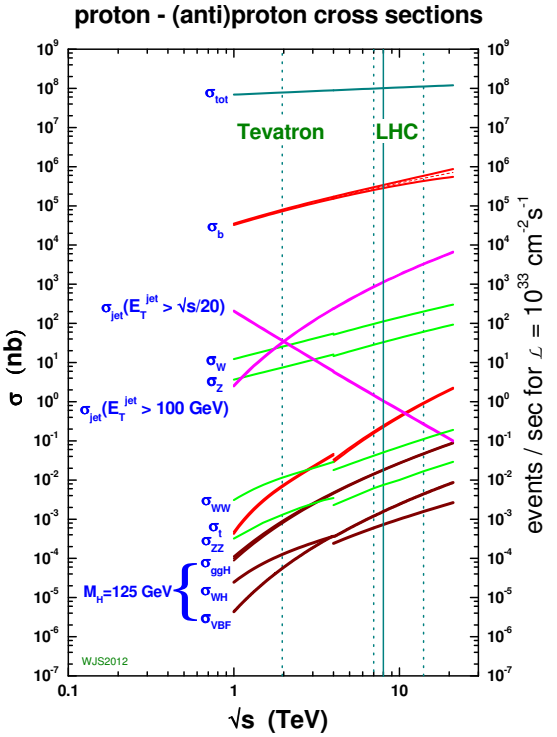

Figure 1.2: Cross sections for various processes as a function of the centre-of-mass energy $\sqrt{s}$ as calculated using perturbative QCD. The cross sections in $p\bar{p}$ collisions and pp collisions are shown for $\sqrt{s} < 4$ GeV and $\sqrt{s} > 4$ GeV, respectively. Also shown are the production rates in Hz for a luminosity of 10^{33} cm^{-2}s^{-1}. Taken from Ref. [32].

1.2.2 Partonic Cross Sections

The partonic cross section $\sigma_{q_1 q_2 \to Y}$ is calculated as a perturbative series, which schematically can be expressed as an expansion in terms of the strong coupling constant α_s, defined as $\alpha_s = g_s^2/4\pi$:

$$\sigma_{q_1 q_2 \to Y} = \alpha_s^k \sum_{m=0}^{n} c_m \alpha_s^m . \tag{1.28}$$

The coefficients c_m are functions of the kinematic variables x_1, x_2 and the centre-of-mass energy s. Each increment of the series contains additional virtual loop contributions and the real emission of quarks and gluons. Theoretical calculations typically only contain a finite number of coefficients c_m. They are classified by the number of terms included as leading-order ($n = 0$), next-to-leading order ($n = 1$), next-to-next-to-leading order ($n = 2$), etc. The leading power k may differ depending on the process under investigation. The processes studied in this thesis start contributing at $k = 0$ with certain sub-processes starting to contribute at $k = 2$.

The presence of virtual loop corrections introduces singularities in the calculation of scattering amplitudes that are associated with the high and low energy behaviour of the particles participating in the loops. These singularities can be absorbed by reparametrising the coupling and mass parameters of the theory in a procedure known as renormalisation. The procedure introduces an energy-scale dependence in the strong coupling constant α_s and the coefficients c_m. The scale dependence reduces when including higher order terms in the perturbative series. A cross section calculated according to Eq. 1.27 would be invariant

under changes of the renormalisation and factorisation scales, μ_R and μ_F, if all perturbative orders were included. The scale dependence of theoretical calculations is therefore frequently used to estimate uncertainties due to missing higher order contributions.

Cross sections of various processes occurring in pp collisions and calculated using perturbative QCD are shown in Fig. 1.2. The W^+W^- production cross section is many orders of magnitude smaller than the total inelastic pp cross section.

1.2.3 Event Simulation

The theoretical calculations are described in Eq. 1.27 as two distinct problems, i.e. the parametrisation of the proton structure into PDFs and the calculation of the partonic cross sections. For an accurate simulation of a pp collision, the fact that final state gluons and quarks fragment and transform into colour neutral hadrons also needs to be considered. The stochastic nature of the fragmentation and the probabilistic connection of the individual regimes usually rely on computer simulations using Monte Carlo techniques. These are implemented in so-called event generators which also perform a numerical integration of the phase space in Eq. 1.26. An overview of event generators is given e.g. in Ref. [33]. Based on this overview, the simulation of the fragmentation is briefly outlined below. Event generators provide information of the four momenta of the final state particles produced in the proton–proton interactions which are subsequently passed through a simulation of the experimental setup [34].

Additional final state radiation of quarks and gluons and the hadronisation of final state quarks and gluons are modelled by so-called parton-shower programs. The parton shower can be viewed as an approximate perturbative treatment of higher order QCD corrections. It is usually implemented as an iterative, random generation of gluon emissions and gluon splittings. Each quark or gluon generated can undergo further splitting such that a cascade of partons develops. The evolution to lower energies makes use of the DGLAP splitting functions and depends on the momenta of the previous iteration. The iterative procedure is truncated at an energy scale typically chosen to be 1 GeV.

The hadronisation of the particles generated in the parton shower to colour neutral hadrons is using phenomenological, non-perturbative models. Two alternative models are commonly used, string models [35] and cluster models. String models are based on the assumption that the potential energy between two quarks increases linearly as their spacial separation increases. Gluons are described as kinks in the potential. Pairs of $q\bar{q}$ are created from the vacuum if the potential energy exceeds the threshold of quark pair creation until the quarks lost their kinetic energy. The resulting quarks are used to form hadrons. In cluster models all quarks are grouped into colour neutral clusters where gluons are split into $q\bar{q}$ pairs first. The clusters are subsequently fragmented into hadrons based on fragmentation functions measured in experiments.

Additional activity accompanying the hard interaction is collectively referred to as the underlying event. This includes additional interactions, and the fragmentation of the proton remnants. These processes are simulated using phenomenological models as well.

2 The ATLAS Detector at the LHC

The experimental setup used for the measurements presented in this thesis is located at the European Organization for Nuclear Research (CERN) in Geneva, Switzerland. Protons are accelerated in a collider with 26.7 km circumference, called the Large Hadron Collider (LHC). Along the ring, experimental caverns are excavated, one of which hosts the ATLAS experiment, a multipurpose detector designed to record the particles produced in proton–proton collisions. The accelerator complex and detector structure are outlined in Sections 2.1 and 2.2, respectively.

2.1 The Large Hadron Collider

The LHC is a hadron-hadron accelerator and collider installed in an underground tunnel of eight arcs and eight straight sections that previously hosted the LEP [36] accelerator. It is capable of accelerating protons as well as heavy ions with unprecedented energies and instantaneous luminosities. The luminosity represents the flux of colliding particles and has the dimension of particles per area per time. The design parameters for proton–proton collisions are a centre-of-mass energy of the colliding protons of $\sqrt{s} = 14$ TeV with instantaneous luminosities of $L = 10^{34}\,\mathrm{cm}^{-2}\mathrm{s}^{-1}$ [37, 38]. The operation of two counter-rotating beams of equally charged particles necessitates two opposite magnetic dipole fields to bend the particles on a circular path. At four points around the ring the beams are brought to collision. A total of 1232 super conducting niobium-titanium (NbTi) magnets are installed in the tunnel producing a magnetic dipole field of 8.33 T. For the LHC, a design of twin-bore magnets was realised, where both beams run in two adjacent pipes. The magnets are cooled below the critical temperature with superfluid helium. In addition, a set of 392 multipole magnets are installed to focus the proton beams, most importantly close to the interaction points, where the proton bunches are brought to collision. The protons are injected into the LHC ring with an energy of 450 GeV after passing through a number of successive pre-accelerators. The ring is intercepted by a set of eight 400 MHz superconducting cavity systems for each proton beam to accelerate them to a design energy of 7 TeV. The setup allows to operate 2808 bunches of protons, corresponding to a separation of 25 ns, with $1.15 \cdot 10^{11}$ protons each.

For two bunches containing N_1 and N_2 particles colliding with frequency f, the luminosity is given by:

$$\mathcal{L} = f \frac{N_1 N_2}{4\pi\sigma_x\sigma_y}, \tag{2.1}$$

with horizontal and vertical Gaussian beam dimensions of width σ_x and σ_y. Between April 2012 and December 2012 the LHC was operating at a centre-of-mass energy of $\sqrt{s} = 8$ TeV with typically 1368 bunches of up to $1.7 \cdot 10^{11}$ protons that were separated by 50 ns. The

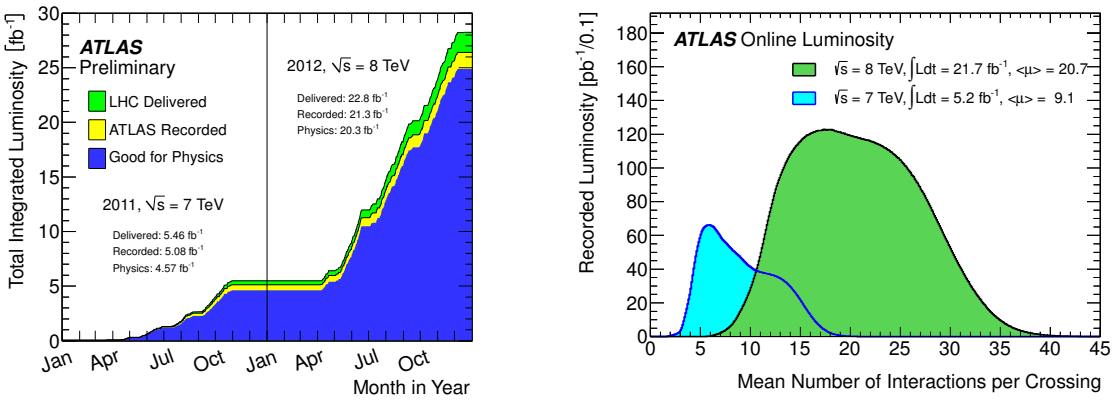

Figure 2.1: The integrated luminosity of pp collisions delivered to and recorded by the ATLAS experiment in the year 2011 at a centre-of-mass energy of $\sqrt{s} = 7$ TeV and in the year 2012 at $\sqrt{s} = 8$ TeV (left). The average number of pp interactions per bunch crossing in the years 2011 and 2012 (right). Taken from Ref. [42].

peak luminosity delivered to the ATLAS experiment was $7.7 \cdot 10^{33}$ s^{-1}cm^{-1} amounting to an integrated luminosity of 22.7 fb^{-1} which was determined with a precision of ±1.9% [39] in van-der-Meer scans [40] following the methodology described in Ref. [41]. The ATLAS experiment recorded 20.3 ± 0.4 fb^{-1} of proton–proton collisions with all detector components operating under nominal conditions. The high instantaneous luminosity causes several pp collisions in the same bunch-crossing. During the run at $\sqrt{s} = 8$ TeV an average of 21 and a maximum of 41 pp collisions per bunch-crossing were present. The evolution of the integrated luminosity delivered by the LHC and recorded by the ATLAS detector as well as the distribution of the number of pp interactions per bunch crossing are shown in Fig. 2.1.

2.2 The ATLAS Detector

The ATLAS experiment is designed to record and reconstruct the proton–proton interactions produced by the LHC. The different detector systems are described in the following based on Ref. [43]. A graphical representation of the detector is given in Fig. 2.2. It consists of an inner detector (ID) for the reconstruction of the trajectories of charged particles that is embedded in a superconducting solenoid producing a magnetic field of $B = 2$ T. This allows a measurement of the transverse momentum of charged particles from the curvature of the tracks. Around the solenoid, electromagnetic and hadronic calorimeters are assembled, designed according to their purpose of providing a measurement of the energy in electromagnetic showers with high resolution and a measurement of hadronic showers with adequate resolution. The detector is completed by the muon spectrometer. It consists of a system of air-core toroid magnets, one large barrel toroid and two smaller endcap toroids, that produce a field of approximately $B = 0.5$ T and $B = 1$ T, respectively. The bending plane of charged particle tracks in the the muon spectrometer is perpendicular to that in the inner detector. Different detectors for the space coordinate measurements of muons are assembled inside and around the toroid magnets. A three-level trigger system is used

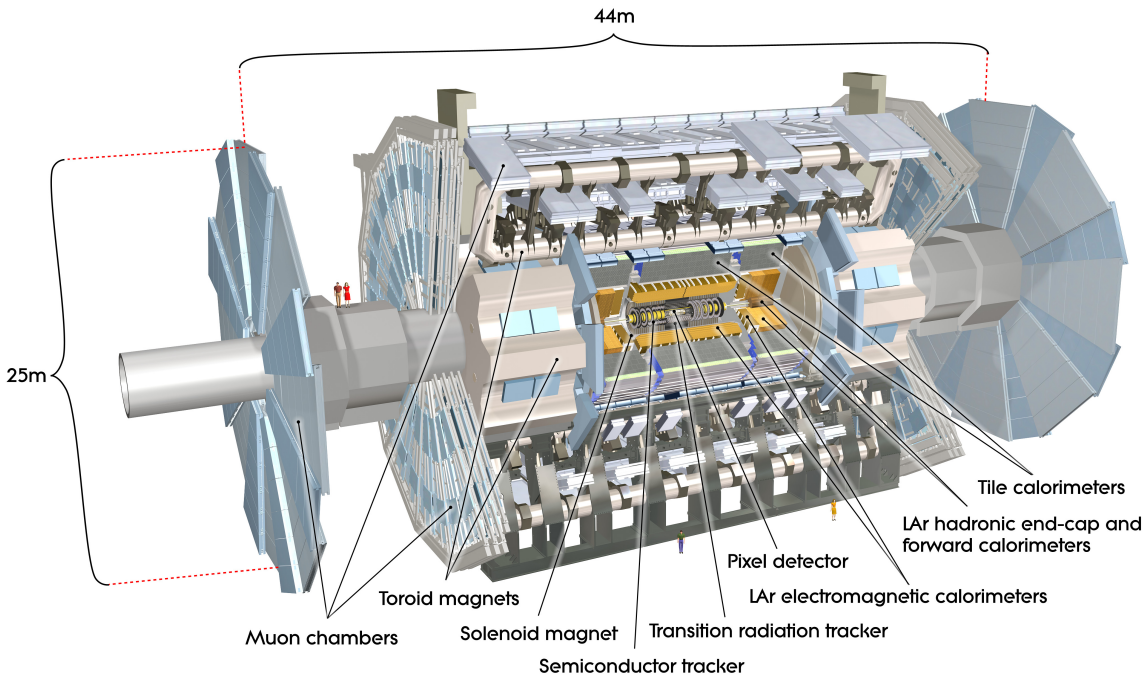

Figure 2.2: Cut-away view of the ATLAS detector. It is assembled in several layers around the interaction point and symmetric in the forward and backward directions. Taken from Ref. [43].

to select events for readout.

In the ATLAS experiment, coordinates are measured from the nominal pp interaction point. The z-axis is defined in the beam direction, the x-axis points towards the centre of the LHC ring and the y-axis points upwards. The azimuthal and polar angles ϕ and θ are measured from the x-axis counter-clockwise in the x-y-plane and from the z-axis, respectively. The polar angle is used to define the pseudorapidity $\eta = -\ln\tan(\theta/2)$ and the transverse energy $E_{\mathrm{T}} = E \cdot \sin\theta$. Distances are measured in the pseudorapidity azimuthal-angle space as $\Delta R = \sqrt{(\Delta\eta)^2 + (\Delta\phi)^2}$.

2.2.1 The Inner Detector

The inner detector is designed for the measurement of the trajectories of charged particles with a high spatial resolution within $|\eta| < 2.5$. It consists of three independent sub-systems, a pixel and a silicon microstrip detector, and straw tubes interleaved with fibres or foils that cause charged particles to produce transition radiation when traversing. The layout of the inner detector is shown in Fig. 2.3. The three subsystems are embedded in the cylindrical envelope of the solenoid magnet and arranged in concentric cylinders around the beam axis in the central region of the detector and discs in the forward regions. The central and forward regions are denoted barrel and endcap regions, respectively.

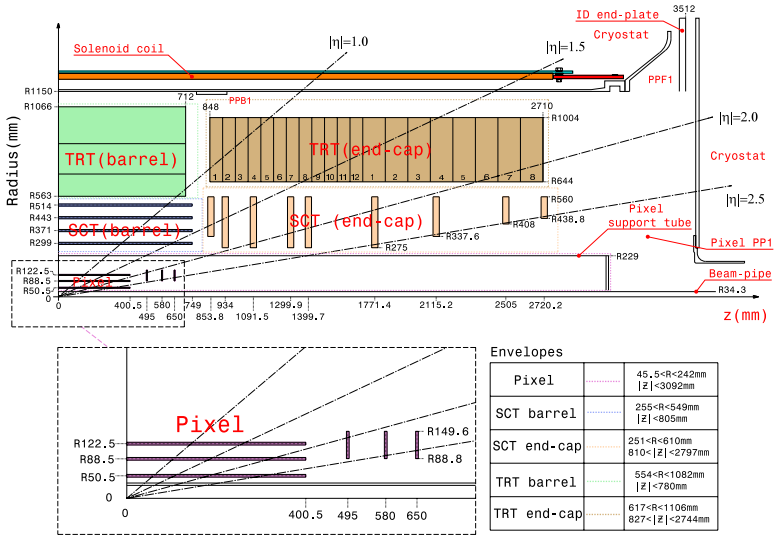

Figure 2.3: Plan of a quarter-section of the inner detector. The inner detector consists of the Pixel system, the Semiconductor Tracker (SCT) and the Transition Radiation Tracker (TRT) sub-detectors. Taken from Ref. [43].

Pixel detector

The Pixel detector [44] represents the innermost layers of the ATLAS detector. It is designed to provide a measurement of three space coordinates of charged particles over the full pseudorapidity range of $|\eta| < 2.5$. It consists of three layers of silicon pixel sensors in the barrel and three discs in each endcap with a pixel size of $50 \times 400\,\mu\text{m}^2$. In total, the detector has 80 million pixels covering an area of $1.7\ \text{m}^2$. The innermost barrel layer is installed at a radius of 5 cm. The high granularity of the pixel detector and its proximity to the interaction point is crucial for the reconstruction of primary and secondary vertices with a high resolution. Each layer provides a measurement of space points with an intrinsic resolution of $10\,\mu$m in azimuthal direction and $115\,\mu$m in axial (radial) direction of the barrel layer (disc layers).

Semiconductor Tracker (SCT)

The Semiconductor Tracker (SCT) [45] is made of four layers in the barrel with two silicon micro-strip sensors each. The pitch-size of the sensors is $80\,\mu$m. In each endcap nine disc layers with radial strips of roughly the same pitch-size are installed to cover the full pseudorapidity up to $|\eta| < 2.5$. The two sensors of a layer in both the barrel and the endcaps are rotated by 40 mrad to one another, which allows a measurement of the z-coordinate of charged particles in the barrel layers and the radial coordinate in the disc layers. Each layer provides measurements with an intrinsic resolution of $17\,\mu\text{m} \times 580\,\mu\text{m}$.

Transition Radiation Tracker (TRT)

The silicon sensors of the Pixel and SCT detectors are complemented by the Transition Radiation Tracker (TRT) [46]. It is made of 298,304 straw tube proportional counters with up to

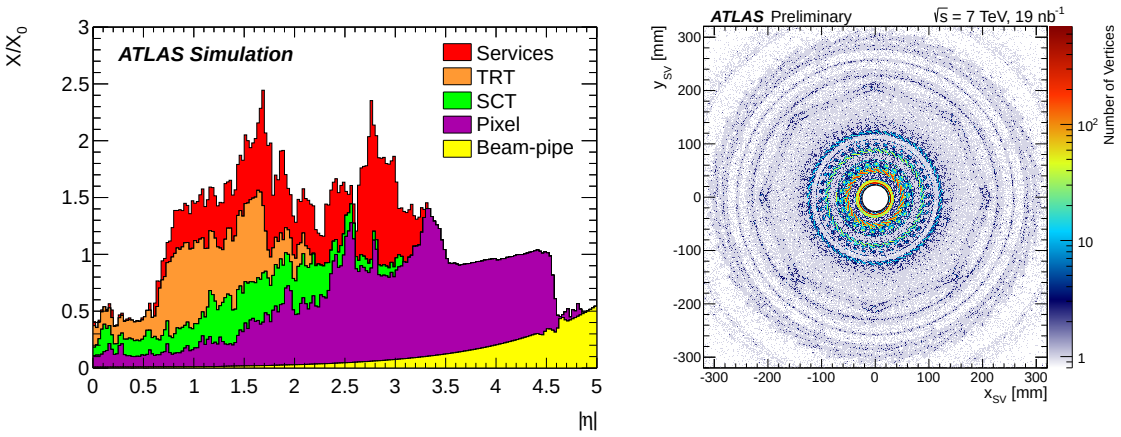

(a) (b)

Figure 2.4: (a) Amount of material in units of the radiation length, X_0, that is traversed by a particle when passing through the inner detector as a function of pseudorapidity, η. Taken from Ref. [47]. (b) Number of secondary vertices reconstructed from hadronic interactions of particles with the detector material in data as a function of the transverse positions (x, y). Taken from Ref. [48].

73 and 160 layers in the barrel and the endcaps, respectively. The straw tubes have a diameter of 4 mm and are interleaved with polypropylene. The use of straw tubes with transition radiation elements combines the measurement of tracks of charged particles and the identification of particles with a high Lorentz factor γ. For an efficient absorption of transition radiation the straw tubes are filled with a Xenon-based gas mixture, causing the signal from photons from transition radiation to yield higher signal amplitudes than the signal of hits from minimum-ionizing particles. The TRT modules extend up to $|\eta| = 2.0$. The barrel modules are divided in the middle at $|\eta| = 0$ to host the front-end electronics. By using the drift time for the determination of the drift circles an intrinsic azimuthal resolution of the TRT of 130 μm is achieved. The low resolution relative to the Pixel and SCT detectors is compensated by a large number of typically 36 hits per track and by extending the lever arm of the measurement of the trajectories of charged particles significantly.

Material Distribution in the Inner Detector

The amount of material in the inner detector has consequences for the event reconstruction. In particular electrons and photons have a high probability to interact with the detector material and either undergo bremsstrahlung (electrons) or convert to an electron-positron pair (photons). This can highly affect the probability of their identification and the reconstruction of their four momenta. The knowledge of the material distribution is therefore crucial. It is shown in Fig. 2.4a in units of the radiation length X_0.

The material distribution can be indirectly measured by reconstructing the vertices of the interactions of particles with the detector material. Both converted photons [49] and hadronic interactions [50] are used. The space coordinates of reconstructed secondary vertices of hadronic interactions is shown in Fig. 2.4b. These measurements are complemented

by a material estimation based on comparisons of the shower development of electrons and unconverted photons in the electromagnetic calorimeter [47].

2.2.2 Calorimetry

The calorimeter system is designed to provide a measurement of the energy of electrons, photons and hadrons by fully absorbing them. It covers a range $|\eta| < 4.9$ and is depicted in Fig. 2.5. The calorimeter system is made of several sampling detectors. The electromagnetic calorimeters have a thickness of $X_0 > 22$, several layers and a high granularity to allow a high spatial resolution. Hadronic calorimeters are placed directly outside the electromagnetic calorimeter using different materials in the central region of $|\eta| < 1.7$ and the endcaps with $1.5 < |\eta| < 3.2$. Together with the electromagnetic calorimeter the total thickness including support structures in units of interaction lengths is $\lambda_0 = 11$ at $\eta = 0$. This thickness contains hadronic showers in the detector. Two additional calorimeters are installed in the forward region of $3.1 < |\eta| < 4.9$

Electromagnetic Calorimeter

The electromagnetic calorimeter [51] is a liquid-argon sampling calorimeter with lead absorber plates that are interleaved with readout electrodes. The layers are arranged in an accordion shape to provide a symmetry in ϕ without azimuthal cracks. The electromagnetic calorimeter consists of a barrel component with $|\eta| < 1.475$ and two endcap components with $1.375 < |\eta| < 3.2$. A presampler layer is placed directly in front of the barrel component with $|\eta| < 1.8$. It is used to correct for energy loss upstream the electromagnetic calorimeter. The electromagnetic calorimeter is segmented into up to three longitudinal layers. It has a high granularity over the full acceptance of the inner detector of $|\eta| < 2.5$ with a reduced granularity only in the transition region between the barrel and endcap components. The front layer has a very fine lateral segmentation in η with cells of typically $\Delta\eta \times \Delta\phi = 0.025/8 \times 0.1$. It covers a range of $|\eta| < 1.4$ and $1.5 < |\eta| < 2.4$. Beyond that range only two layers are realised. The typical cell size in the middle layer of $\Delta\eta \times \Delta\phi = 0.025 \times 0.025$ defines the coordinate system of the electromagnetic calorimeter of 200×256 so-called towers. The middle layer constitutes the thickest part of the electromagnetic calorimeter and therefore drives the energy measurement of electromagnetic showers. It is also used to provide fast trigger decisions at the lowest level of the the online readout of the detector where 4×4 towers are combined. The electromagnetic calorimeter is completed by the back layer with a typical granularity of $\Delta\eta \times \Delta\phi = 0.05 \times 0.025$. The energy measurement of electromagnetic showers from cells in all layers are added, where the energy measured in the front and back layer cells spanning several towers are distributed uniformly among the participating elements. A single barrel module of the electromagnetic calorimeter is sketched in Fig. 2.6a together with the lateral and longitudinal size of the cells. Outside the acceptance of the inner detector a reduced granularity of $\Delta\eta \times \Delta\phi = 0.1 \times 0.1$ is realised.

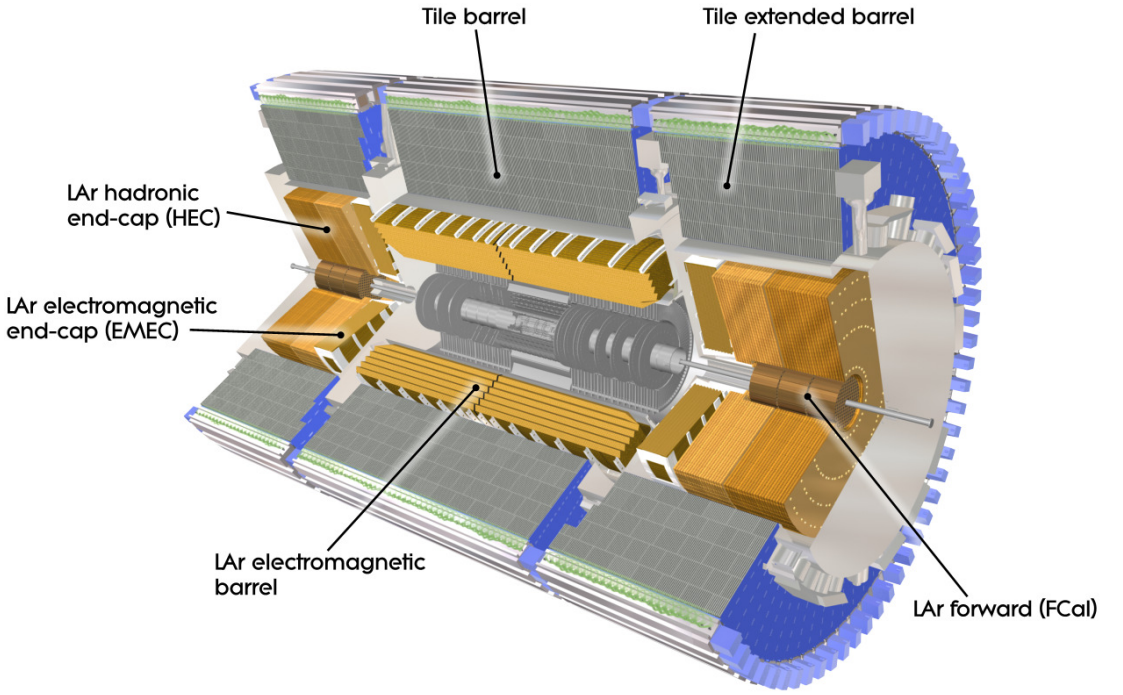

Figure 2.5: Cut-away view of the calorimeter system. The calorimeter system consists of several sampling detectors and extends up to $|\eta| < 4.9$. Taken from Ref. [43].

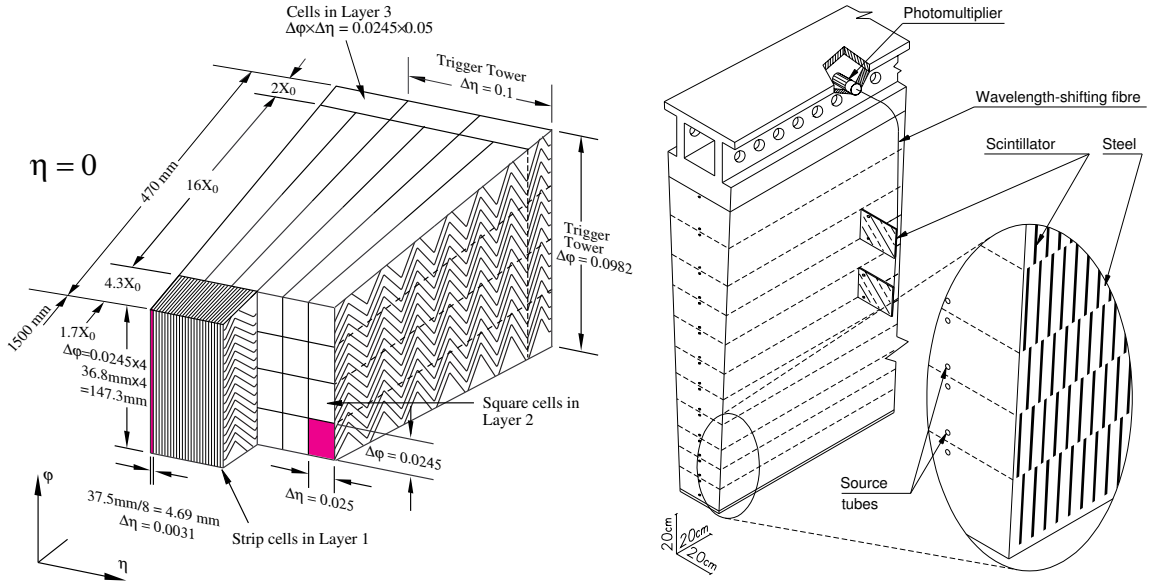

(a) (b)

Figure 2.6: (a) Sketch of a single module of the electromagnetic calorimeter. Each module has several layers of different granularity with the dimensions shown in the figure. (b) Sketch of a single module of the hadronic tile calorimeter. The components of the optical readout are shown. Taken from Ref. [43].

Hadronic Calorimeter

The hadronic calorimetry is made of three sections: a barrel tile calorimeter extending to $|\eta| < 1.7$, hadronic endcap calorimeters covering $1.5 < |\eta| < 3.2$ and forward calorimeters over the range $3.1 < |\eta| < 4.9$. The segmentation of the hadronic calorimeters is much coarser than that of the electromagnetic calorimeters with a cell size of $\Delta\eta \times \Delta\phi = 0.1 \times 0.1$ in the barrel region and increasingly coarser for larger values of η. The tile calorimeter is made of steel absorbers and scintillating tiles assembled in a barrel and two extended barrel modules, each having three longitudinal layers. A single module is sketched in Fig. 2.6b. The modules are read out on two sides by wavelength shifting fibres that end in two photomultiplier tubes.

Two liquid-argon-copper wheels per endcap constitute the hadronic endcap calorimeter. Each contains two longitudinal sections resulting in four layers per endcap. Two forward calorimeters are installed in the range $3.1 < |\eta| < 4.9$. They are equipped with one liquid-argon-copper and two liquid-argon-tungsten modules to provide energy measurements of electromagnetic and hadronic showers, respectively.

2.2.3 Muon Spectrometer

The measurement of muons is based on their deflection in the magnetic field of the toroid magnet system in the r-z plane. The barrel and endcap toroids have eight coils each and cover a pseudorapidity range of $|\eta| < 1.4$ and $1.6 < |\eta| < 2.7$, respectively. A combination of four muon tracking chamber systems is installed between the coils of the barrel toroid magnet and before and after the endcap toroid magnets. For a precise momentum determination Monitored Drift Tube (MDT) chambers are installed over the full range $|\eta| < 2.7$. They consist of three to eight layers of drift tubes that have an average resolution of $80\,\mu$m. The number of MDTs is reduced in the forward region $2.0 < |\eta| < 2.7$ where Cathode-Strip Chambers (CSC) complement the momentum measurement. For a fast trigger of the detector, Resistive Plate Chambers (RPC) are installed in the barrel and Thin Gap Chambers (TGC) in the endcap components ranging up to $|\eta| < 2.4$.

2.2.4 Trigger System

The ATLAS trigger system [52] is designed to select events of pp collisions for readout at a rate which is limited by readout and storage capabilities. The trigger system uses predefined trigger algorithms to reduce the event rate from a design bunch crossing rate of 40 MHz to a value of 200 Hz. The selection of events is based on event topologies and is performed in three steps. In a first step a hardware based trigger, referred to as Level-1, reduces the event rate to ~ 75 kHz using a reduced detector granularity and resolution in the calorimeters and the muon system only. The decision to keep or discard an event at Level-1 is based on either the energy depositions in the electromagnetic and hadronic calorimeters or the track segments in the RPC and TGC detectors of the muon spectrometer. Regions with large energy depositions or hit patterns corresponding to a high transverse momentum are propagated to a processing farm where they are further analysed using software-based algorithms. The software-based selection proceeds in two steps. The Level-2 algorithms refine the anal-

ysis in the regions selected at Level-1 by using an increased detector granularity and by adding information from additional detector components. The Level-2 system allows the reconstruction of tracks in the inner detector and from several segments in the muon spectrometer. Calorimeter clustering algorithms allow an analysis of shapes of electromagnetic and hadronic showers. Matching algorithms between energy depositions and tracks in the inner detector, and tracks in the muon spectrometer and the inner detector are also implemented. In this first, software-based step the rate is reduced to roughly 3 kHz. An event is subsequently further analysed by the so-called Event-Filter, where it is reconstructed using offline-like reconstruction algorithms similar to the ones described in Section 3. With these algorithms the rate can be reduced to the design value of 200 Hz. Examples for trigger algorithms are given in Section 3.2.4 and 3.3.3. Between April 2012 and December 2012 the ATLAS experiment recorded events at a rate of 400 Hz on average, where the storage capacities where improved prior to data taking.

3 Event Reconstruction

The final state particles produced in pp collisions traverse through the ATLAS detector leaving signals in the various components. Event reconstruction algorithms are used to identify individual particles and determine their four momenta. In a first step, tracks and vertices are reconstructed from hits in the inner detector, which is described in Section 3.1. In a second step the information of the individual detector components is combined to reconstruct electrons, muons and jets. The reconstruction of electrons is described in Section 3.2 and the reconstruction of muons is detailed in Section 3.3. The descriptions also includes algorithms used in the online readout of the detector. A summary of the reconstruction of jets is given in Section 3.5, with dedicated algorithms used for jets from b-hadron decays in Section 3.6. As a final step, event properties are reconstructed. The analysis presented in this thesis makes use of the missing transverse momentum, $p_{\mathrm{T}}^{\mathrm{miss}}$, which is discussed in Section 3.7.

3.1 Track and Vertex Reconstruction

The track reconstruction in the inner detector uses a sequence of algorithms [53]. A so-called inside-out algorithm is aiming for the reconstruction of tracks of primary particles produced in the pp collision with a lifetime $\tau > 3 \times 10^{-11}$ s or particles from the subsequent decay of primary particles. A so-called back-tracking algorithm is aiming for the reconstruction of tracks of decay products of long-lived particles. A third algorithm is employed for TRT standalone tracks that have no associated hits in the pixel and SCT detectors.

The inside-out algorithm is seeded by three hits in the silicon detectors. Hits are added to the seed track by moving away from the interaction point with a Kalman filter [54] using the knowledge of the material budget and the magnetic field configuration. Tracks reconstructed by the inside-out algorithm are required to have a transverse momentum of $p_{\mathrm{T}} > 0.4$ GeV. The back-tracking algorithm starts from segments reconstructed in the TRT that are extended to the inner detector. The efficiency of the track reconstruction with the inside-out algorithm is shown in Fig. 3.1a as a function of the pseudorapidity, η, for different values of interactions per bunch-crossing. The track reconstruction efficiency is larger than 80% in the central region of the detector at $|\eta| < 1.0$ and reduced to 60%-70% in the endcap region which has a large material budget. Additional pp collisions in the same or near-by bunch crossing cause a high occupancy in the inner detector. The reconstruction efficiency is stable as a function of the interactions per bunch-crossing, also for the large values up to $\mu = 40$ present in the dataset recorded in 2012.

The reconstructed tracks are used to identify the primary interaction and secondary decay vertices. A vertex seed is taken as the maximum of the distribution of z coordinates of the reconstructed tracks at the beamline. The vertex is fitted using a χ^2 minimisation

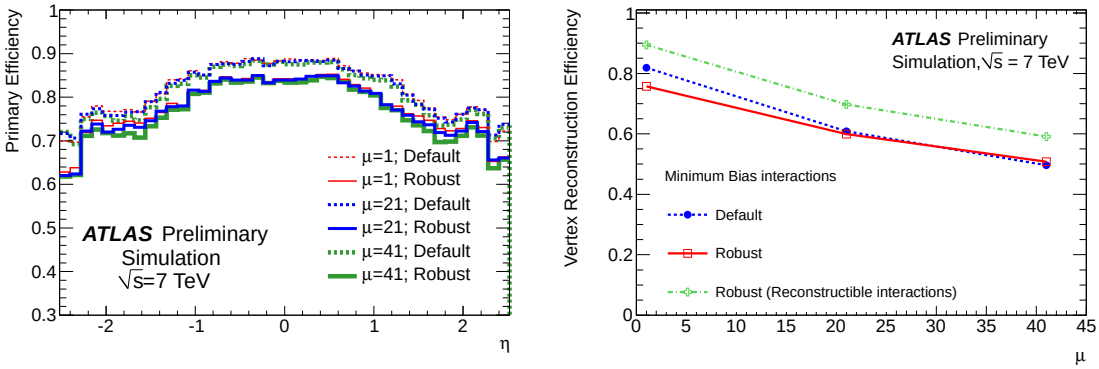

(a) (b)

Figure 3.1: (a) Efficiency of the track reconstruction estimated in simulated event samples as a function of the pseudorapidity, η. The efficiency is shown for several values of interactions per bunch-crossing which result in different occupancies of the inner detector. The solid lines are relevant for the reconstruction in the dataset taken in 2012. (b) Efficiency of the vertex reconstruction measured in simulated event samples. The reconstruction efficiency for events with at least two charged, stable particles are shown in green. Both figures are taken from Ref. [53].

and tracks incompatible by more than seven standard deviations are iteratively removed and used to seed a new vertex. The efficiency to reconstruct a primary vertex from a single interaction is roughly 90% but decreases when additional pp interactions are present as shown in Fig. 3.1b. For a larger number of interactions per bunch-crossing a nearby interaction can prevent the reconstruction of the vertex, resulting in a significant efficiency loss. In those cases several vertices typically cannot be resolved and only one vertex is reconstructed. The probability to assign a single interaction to multiple vertices was found to be lower than 1% [53]. The efficiencies shown in Fig. 3.1b is obtained in simulated events that also contain collisions with low momentum transfer. The efficiency to reconstruct the vertices of the interactions studied in this thesis is close to 100%.

3.2 Electron Reconstruction and Identification

Electrons in the central detector region are reconstructed from energy depositions in the electromagnetic calorimeter that are matched to a track in the inner detector. The reconstruction aims for a high efficiency. In order to differentiate electrons from other particles leaving energy depositions in the electromagnetic calorimeter several sets of identification criteria were developed. These criteria rely on the shapes of the electromagnetic showers, the quality of the tracks and track-to-cluster matching. The identification aims for a high rejection of contributions from background processes. The reconstruction and identification algorithms are described in the following. Only electrons within the acceptance of the inner detector are used throughout this thesis. Electrons in the forward region use different reconstruction and identification algorithms that are described in Ref. [1].

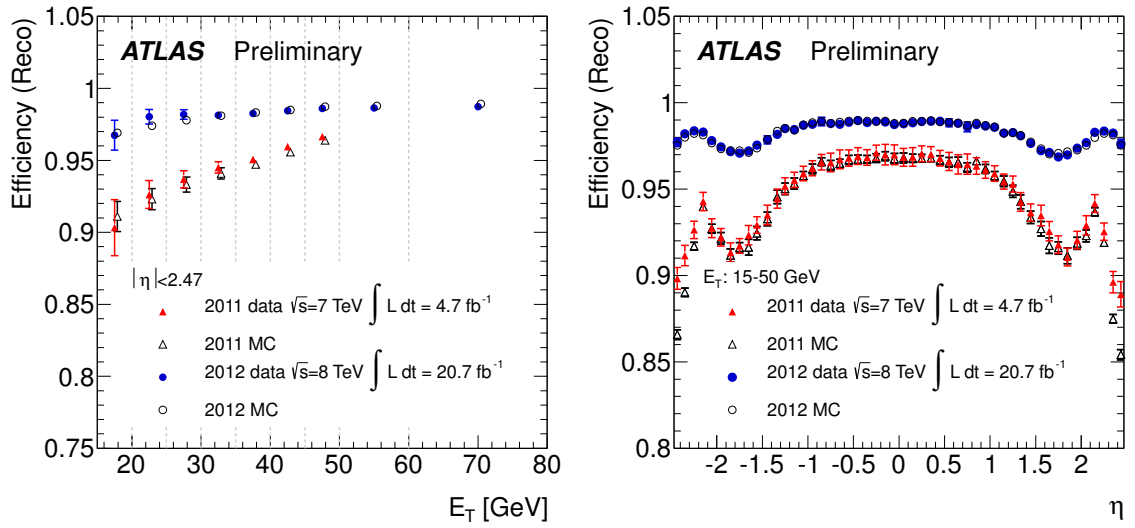

Figure 3.2: Efficiency of the electron reconstruction as a function of transverse energy, E_{T} (left), and pseudorapidity, η (right). The efficiency of the reconstruction algorithms deployed in 2011 and 2012 are shown. Taken from Ref. [2].

3.2.1 Electron Reconstruction

The electron reconstruction algorithm is seeded by energy depositions in the electromagnetic calorimeter with a transverse energy exceeding 2.5 GeV. Electromagnetic clusters are identified by a sliding-window algorithm with a window size of 3×5 middle layer cells in $\eta \times \phi$. Reconstructed tracks are associated to the electromagnetic cluster using the separation in η and ϕ between the cluster barycentre and the track coordinates extrapolated to the calorimeter. Tracks only loosely matched to the electromagnetic cluster are refitted with an improved tracking algorithm, the Gaussian Sum Filter (GSF) [55], accounting for non-linear bremsstrahlung effects. If several tracks are found, a primary track is chosen based on the cluster-track distance and the number of hits in the pixel and first layer of the SCT detectors. The four-momentum of the reconstructed electron candidate is then reconstructed from all three layers of the electromagnetic calorimeter in 3×7 and 5×5 calorimeter cells in the central and endcap region of the detector, respectively, and the momentum direction of the associated track.

The efficiency of the electron track reconstruction and track-to-cluster matching is measured in $Z \rightarrow ee$ events. It is found to be $\sim 99\%$ in the central region of the detector and $\sim 97\%$ in the endcap region [2]. A comparison of the reconstruction efficiencies for the algorithms deployed in 2011 and 2012 is shown in Fig. 3.2, the main difference between both being the use of GSF in 2012 together with loosened requirements on the track-to-cluster matching variables. The use of the Gaussian Sum Filter improves the efficiency of the electron reconstruction particularly in the endcap region where a large amount of passive material has to be traversed in order to reach the electromagnetic calorimeter. The resolution of the transverse momentum and impact parameter measurement is greatly improved as well [55].

3.2.2 Electron Identification

The reconstruction algorithm for electrons is not efficiently discriminating against background processes like hadronic jets that mimic the signature of an electron or electrons from photon conversions. The sample of reconstructed electrons is purified by placing criteria on a set of shower shape variables, track properties and track-to-cluster matching variables [56, 57] defined in Table 3.1. The shower shape variables make use of the fine segmentation of the electromagnetic calorimeter and are mostly defined as longitudinal and lateral ratios of energies measured in the strip layer, middle layer, third layer and the hadronic calorimeter. The track properties include requirements on the number of hits in the pixel and SCT detectors, and particle identification in the TRT. Additional requirements are made on the separation between the cluster position measured in the calorimeter and the coordinates of the track extrapolated to the calorimeter. Electrons are identified by placing a number of sequential selection criteria on these variables or by constructing a likelihood discriminant from these variables.

Three sets of criteria using sequential selection cuts with different efficiencies to reject hadronic jets are defined, loose++, medium++ and tight++, and are optimised [56] in ten bins in $|\eta|$ and eleven bins in E_{T}. From one set to the next the selection criteria on a given variable become stricter and additional variables are added. A fourth set, called multilepton, is optimised for the reconstruction of electrons from $H \to ZZ$ decays and combines a large number of variables with mild requirements on the individual variables.

A second, alternative set of selection criteria is combining the shower shape variables, track properties and track-to-cluster matching variables into a likelihood discriminant $d_{\mathcal{L}}$:

$$d_{\mathcal{L}} = \frac{\mathcal{L}_S}{\mathcal{L}_S + \mathcal{L}_B}, \qquad \mathcal{L}_S(\vec{x}) = \prod_{i=1}^{n} P_{s,i}(x_i) \tag{3.1}$$

where $P_{s,i}(x_i)$ is the signal probability density of variable i, and $\vec{x}$ is the vector of values in these variables for a given electron candidate. The selection on the likelihood discriminant is optimised in nine bins in $|\eta|$ and six bins in E_{T}. Three sets of criteria, loose LH, medium LH and very tight LH, are constructed, each with a separate likelihood discriminant constructed from a different number of variables. The optimisation is performed in data to yield the same efficiency as the criteria based on sequential cuts. Using a likelihood discriminant improves the rejection of background processes by a factor of two [2].

A measurement of the efficiency of the various electron identification sets is described in Chapter 4.

3.2.3 Electron Energy Calibration

The electron energy determined in 3×7 or 5×5 calorimeter cells is corrected for instrumental effects, energy loss in front of the calorimeter, energy depositions outside the cluster (lateral leakage) and beyond the electromagnetic calorimeter (longitudinal leakage). The calibration is based on simulated event samples that are corrected with dedicated measurements of the material budget, the inter-calibration of the different LAr calorimeter layers in data, and measurements of the uniformity in η and ϕ and the stability over time [47]. The

Type	Description	Name
Hadronic leakage	Ratio of E_{T} in the first layer of the hadronic calorimeter and E_{T} of the EM cluster (used over the range $\lvert\eta\rvert < 0.8$ or $\lvert\eta\rvert > 1.37$)	R_{Had1}
	Ratio of E_{T} in the hadronic calorimeter to E_{T} of the EM cluster (used over the range $0.8 < \lvert\eta\rvert < 1.37$)	R_{Had}
Back layer of EM calorimeter	Ratio of the energy in the back layer to the total energy in the EM accordion calorimeter	f_3
Middle layer of EM calorimeter	Lateral shower width in a window of 3×7 cells	$w_{\eta 2}$
	Ratio of the energy in 3×3 cells and the energy in 3×7 cells centred at the electron cluster position	R_ϕ
	Ratio of the energy in 3×7 cells and the energy in 7×7 cells centred at the electron cluster position	R_η
Strip layer of EM calorimeter	Shower width of $\Delta\eta \times \Delta\phi \approx 0.0625 \times 0.2$	w_{stot}
	Ratio of the energy difference of the largest and second largest energy depositions in the cluster and the sum of these energies	E_{ratio}
	Ratio of the energy in the strip layer to the total energy in the EM accordion calorimeter	f_1
Track quality	Number of hits in the b-layer	$n_{b\text{-layer}}$
	Number of hits in the pixel detector	n_{pixel}
	Number of total hits in the pixel and SCT detectors	n_{Si}
	Transverse impact parameter	d_0
	Significance of the transverse impact parameter defined as the ratio of d_0 and its uncertainty	σ_{d_0}
	Momentum lost by the track between the perigee and the last measurement point divided by the original momentum	$\Delta p/p$
TRT	Total number of hits in the TRT	n_{TRT}
	Ratio of the number of high-threshold and total hits in the TRT	F_{HT}
Track-cluster matching	$\Delta\eta$ between the cluster position in the strip layer and the extrapolated track	$\Delta\eta_1$
	$\Delta\phi$ between the cluster position in the middle layer and the extrapolated track	$\Delta\phi_2$
	as $\Delta\phi_2$, but the track momentum is rescaled to the cluster energy before extrapolating the track	$\Delta\phi_{\mathrm{res}}$
	Ratio of the cluster energy to the track momentum	E/p
Conversions	electron candidates matched to converted photons	isConv

Table 3.1: Definition of the discriminating variables used for the identification of electrons. Shower shape, track and track-to-cluster matching variables are used. Depending on the identification criterion a subset of these variables is used. Taken from Ref. [2].

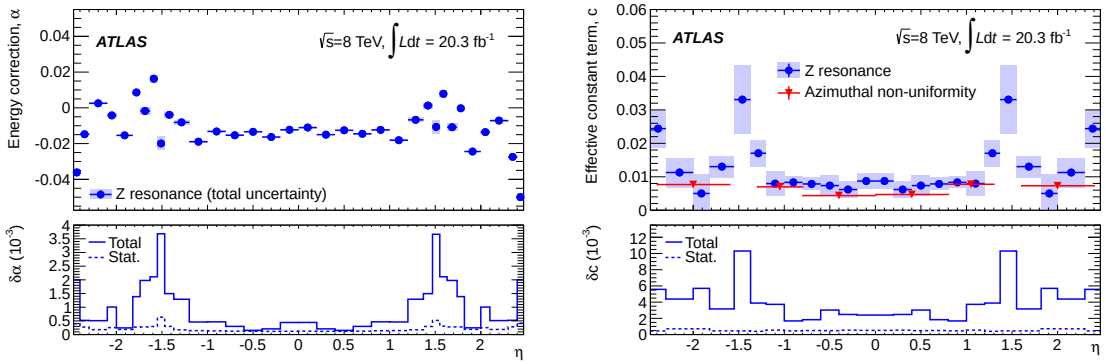

Figure 3.3: Residual energy scale correction α (left) and effective constant term c (right) as determined in $Z \to ee$ events as a function of pseudorapidity, η. The energy scale correction is measured with respect to a previous calibration scheme described in Ref. [56] and defined as $E^{\text{data}} = E^{\text{MC}}(1+\alpha)$. Taken from Ref. [47].

relative energy resolution is parametrised as:

$$\frac{\sigma}{E} = \frac{a}{\sqrt{E}} \oplus \frac{b}{E} \oplus c, \tag{3.2}$$

with the sampling term a, the noise term b and the constant term c. The residual miscalibration is determined in a χ^2 minimisation by comparing the invariant dielectron mass distribution in $Z \to ee$ events observed in data to distributions from simulated event samples with different values for the energy scale α, defined as $E^{\text{data}} = E^{\text{MC}}(1+\alpha)$, and the effective constant term of the resolution c. The procedure is performed differentially in categories of pseudorapidity of the electrons (η_i, η_j) and the resulting values for α and c are shown in Fig. 3.3. The method allows for a determination of the electron energy scale with a precision much better than $\pm 0.1\%$ for most of the pseudorapidity range, with slightly larger values of $\pm 0.15\%$-0.2% close to the calorimeter transition region $1.37 < |\eta| < 1.52$. The effective constant term is determined to be roughly $1-2\%$ over most of the pseudorapidity range.

3.2.4 Electron Trigger

The clean signature of electrons also serves as a good trigger for the online selection of events for readout. The electron trigger algorithms make use of the three-level readout electronics deployed in the ATLAS detector with simplified, fast algorithms used at Level-1 and offline-like reconstruction in the Event-Filter. Electron candidates are formed by a sliding window algorithm operating on arrays of $\Delta\eta \times \Delta\phi = 0.1 \times 0.1$. The energy is reconstructed in 4×4 groups of these arrays. At Level-2, clusters are formed using offline based reconstruction algorithms and a track in the inner detector is required. Identification criteria similar to the loose++ and medium++ criteria described before are implemented at Event-Filter stage [58]. An event is selected for readout by either a single or two electrons. The algorithm based on a single electron requires an electromagnetic cluster of $E_{\text{T}} > 18$ GeV with less than 1 GeV deposited in the hadronic calorimeter or an electromagnetic cluster

of $E_{\mathrm{T}} > 30$ GeV at Level-1 and Level-2. The selection at Event-Filter stage requires the electron candidates that meet the requirements at Level-1 and Level-2 to have a transverse energy exceeding $E_{\mathrm{T}} = 24$ GeV and $E_{\mathrm{T}} = 60$ GeV, respectively, and to satisfy the medium++ identification requirement. An alternative algorithm selects events for readout if two electromagnetic clusters satisfy $E_{\mathrm{T}} > 10$ GeV with less than 1 GeV deposited in the hadronic calorimeter. At Event-Filter stage the threshold is increased to $E_{\mathrm{T}} > 12$ GeV for both electrons and loose++ identification criteria are applied. Another algorithm requires an electron with the same criteria in combination with a muon. For a typical luminosity of $7 \cdot 10^{33}$ s^{-1}cm^{-1} at the beginning of a LHC fill in 2012 these triggers are operating at a rate of 18 kHz and 6.2 kHz for the algorithms based on a single and two electrons, respectively. The rate is reduced to 100 Hz and 11 Hz at Event-Filter stage.

The efficiency of the electron readout is measured in $Z \rightarrow ee$ events in data [59]. The efficiency to select an event by a single electron is found to be 95%-98% in the barrel and 85%-88% in the endcap. For the dielectron algorithms the efficiency is 95%-98% per electron.

3.3 Muon Reconstruction

Muons lose only a small fraction of their energy due to ionisation when traversing the inner detector, the electromagnetic and the hadronic calorimeters. They are reconstructed from tracks in the inner detector (ID) and additional hits in the muon spectrometer (MS) which corresponds to the outermost layers of the detector. Other reconstruction algorithms relying on the MS or the ID alone are discussed in Ref. [60].

3.3.1 Muon Reconstruction

Muons are measured independently in the ID and the MS. The reconstruction of tracks in the MS is seeded by driftcirles in the MDTs or clusters in the CSCs [61]. Track candidates are formed by iteratively adding track segments from single MDT or CSC station and a track fit is performed. A set of quality requirement is made on tracks reconstructed in the ID. Tracks from the ID and the MS are then matched based on their combined χ^2 and a muon candidate is formed using a statistical combination of both tracks [62].

The efficiency of the muon reconstruction is measured in $Z \rightarrow \mu\mu$ and $J/\psi \rightarrow \mu\mu$ decays. It is shown as a function of the pseudorapidity, η, in Fig. 3.4a. Efficiencies between 95% and 98% are reached over most of the pseudorapidity range. The region at $\eta \sim 0$ contains the services for the ID and the calorimeters, as well as support structures. It is therefore only partially equipped with muon chambers, causing a loss of reconstruction efficiency in that region. A second region of low efficiency is the transition region between barrel and positive endcap, $1.1 < \eta < 1.3$, where only part of the chambers were fully installed.

3.3.2 Muon Momentum Scale and Resolution

The muon momentum is inferred from the curvature and coordinates of the reconstructed track. Both the momentum resolution and scale are determined independently in the ID

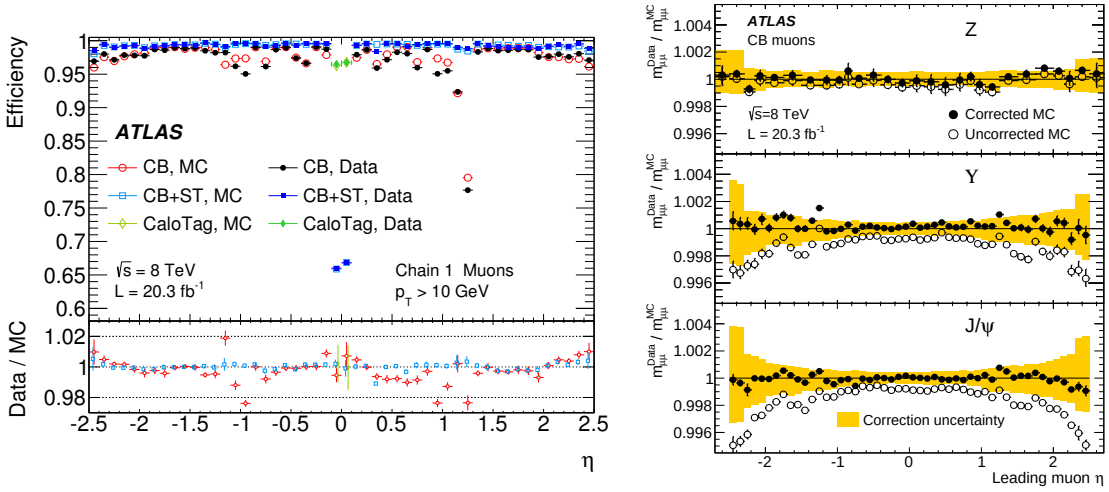

(a) (b)

Figure 3.4: (a) Efficiency of the muon reconstruction as a function of the pseudorapidity, η, measured in $Z \to \mu\mu$ decays for muons with a transverse momentum of $p_{\mathrm{T}} > 10$ GeV. The efficiency of the reconstruction algorithm using both ID and MS is denoted CB and compared to alternative reconstruction algorithms. (b) Ratio of the invariant dimuon mass measured in data and simulated event samples as a function of the transverse momentum of the leading muon. The measurement is performed in $J/\psi \to \mu\mu$, $\Upsilon \to \mu\mu$ and $Z \to \mu\mu$ decays. The ratio is shown for simulated event samples with and without applying corrections based on the momentum scale and resolution measurements in data. Taken from Ref. [60].

and MS. The muon momentum scale accounts mainly for the imperfect knowledge of the detector material that needs to be traversed to reach the MS and the energy loss linked to this. Corrections to the muon momentum are typically below $\sim 0.1\%$. The resolution of the reconstructed muon momentum is affected by fluctuations of the energy loss in the traversed material, proportional to $1/p_{\mathrm{T}}$, multiple scattering and inhomogeneities in the magnetic field, constant in p_{T}, and the uncertainty of the spatial resolution and misalignment, proportional to p_{T} [60]. The muon momentum scale and resolution are measured in $J/\psi \to \mu\mu$, $\Upsilon \to \mu\mu$ and $Z \to \mu\mu$ decays. The ratio of the measured invariant mass of the dimuon system in data and simulated event samples is shown in Fig. 3.4b.

3.3.3 Muon Trigger

Just as electrons, muons provide a clean signature for the online selection of events for readout and the muon trigger algorithms make use of the three-level readout electronics. All trigger algorithms discussed here use a single muon at Level-1. A coincidence of hits in three layers in the RPCs or TGCs forms a muon candidate. The transverse momentum of the muons is estimated from the deviation of the hit pattern from a straight line and is

required to be larger than 15 GeV. A track is reconstructed at Level-2 adding information from the MDTs and then combined with the closest track in the inner detector. The primary algorithm to record events containing muons uses a single muon to trigger the readout [63]. At Event-Filter muons are required to be isolated from other tracks, c.f. Section 3.4.2, such that the transverse momenta of additional tracks in a cone $\Delta R = 0.2$ around the muon sum to less than 12% of the transverse momentum of the muon. In addition, the transverse momentum is required to be larger than 24 GeV. The isolation requirement is removed if $p_{\mathrm{T}} > 36$ GeV. The rate after applying these algorithms is typically 8.5 kHz at Level-1 and it is reduced to 65 Hz at the Event-Filter stage. An alternative trigger algorithm relies on two muons to record the event, one of which satisfies the Level-1 and Level-2 requirements discussed before and $p_{\mathrm{T}} > 18$ TeV at Event-Filter. The other muon only is required to be reconstructed at Event-Filter stage with $p_{\mathrm{T}} > 8$ GeV. In combination with an electron of $p_{\mathrm{T}} > 12$ GeV, a muon of $p_{\mathrm{T}} > 8$ GeV can also trigger the readout.

The efficiency of the trigger algorithms is measured in $Z \to \mu\mu$ events. The efficiency for a single muon to trigger the readout of the event is $\sim 70\%$ and $\sim 86\%$ for muons with $p_{\mathrm{T}} > 25$ GeV in the barrel and endcap region of the detector, respectively, where the efficiency is measured with respect to muons reconstructed offline. The efficiency loss is mainly driven by the Level-1 algorithm. A similar efficiency is reached for the muon that triggers the dimuon readout at Level-1. The efficiency to select the additional muon is higher than 98%.

3.4 Calorimeter and Track Isolation

The lepton identification criteria described above do not make any requirements on the presence of other particles although they typically exclude a large fraction of cases with close-by activity. In particular leptons inside jets that originate from non-prompt decays of c- and b-hadrons have a high probability to be reconstructed by these criteria. They can efficiently be removed by making requirements on additional tracks in the inner detector or energy depositions in the calorimeter around the reconstructed lepton, so-called isolation requirements.

3.4.1 Calorimeter Isolation

The calorimeter isolation, $E_{\mathrm{T}}^{\mathrm{cone}}$, measures the energy deposited in the calorimeter in a cone of ΔR around the lepton candidate. It is defined as the sum of transverse energies, E_{T}, of topological clusters [64] with positive energy in that cone, calibrated on the electromagnetic scale [3]. In case of electrons, the rectangular electromagnetic cluster is not included in the sum and leakage outside this cluster is corrected for. In case of muons, the estimated energy loss when traversing the calorimeter is subtracted [61]. Energy depositions from additional pp collisions and the underlying event are corrected for on an event-by-event basis [65].

3.4.2 Track Isolation

Similar to the calorimeter isolation, the track isolation, $p_{\mathrm{T}}^{\mathrm{cone}}$, is defined as the sum of transverse momenta, p_{T}, of all tracks associated to the primary vertex and satisfying a set of quality requirements. The tracks associated with the electron or muon are not included in the sum, i.e. the primary track and in case of electrons also associated tracks from converted bremsstrahlung photons. Particles from additional pp collisions are excluded from the track isolation due to the requirement of the tracks being association to the primary vertex. In contrast to the calorimeter isolation, the track isolation is only sensitive to charged particles but has the advantage that additional pp interactions can efficiently be suppressed.

3.5 Jet Reconstruction

Quarks and gluons produced in the pp collision with high transverse momenta undergo soft and collinear showering and then hadronise. The experimental signature of quarks and gluons therefore is a group of energy depositions with associated tracks. These are reconstructed using the anti-k_t jet algorithm [66] from topological clusters formed in the calorimeter, where a distance parameter of $\Delta R = 0.4$ is used throughout this thesis. The topological clusters are built from energy depositions in the calorimeter cells and calibrated using a classification of electromagnetic and hadronic showers, the so-called local cell signal weighting (LCW) method [67]. The average energy depositions from additional pp collisions occurring in the same or near-by bunch-crossing are corrected for and jets are calibrated based on simulated event samples. The average jet response is shown in Fig. 3.5a. An alternative calibration is discussed in Ref. [67]. The residual jet-energy scale and resolution are determined in data using the energy balance of jets recoiling against other jets [68], or against photons or Z bosons with well measured energies [69]. The jet energy scale is determined to a precision of $\pm 1\%$ for jets with $150\ \mathrm{GeV} < p_{\mathrm{T}} < 1500\ \mathrm{GeV}$ in the central region of the detector. The uncertainty increases to $\pm 4\%$ for jets with $p_{\mathrm{T}} \sim 25\ \mathrm{GeV}$ [70].

To remove reconstructed jets induced by noise in the calorimeter, cosmic rays or beam-induced background a set of quality requirements with an efficiency of typically 99.8% are applied [67, 71]. Within the acceptance of the tracking detectors, energy depositions can moreover be associated to the primary vertex which allows to remove jets from additional pp collisions. For jets satisfying $p_{\mathrm{T}} < 50\ \mathrm{GeV}$ and $|\eta| < 2.4$, a certain fraction of the scalar sum of the p_{T} of all tracks contained within $\Delta R = 0.4$ of the jet axis is therefore required to be from tracks associated to the primary vertex. This procedure rejects jets from local energy depositions due to additional pp collisions and is referred to as jet-vertex fraction (JVF) requirement [72].

3.6 Identification of b-jets

With a typical lifetime of $\tau \sim 1.5$ ps, hadrons containing b-quarks have a flight path of a few mm before they decay. This allows an identification of jets from b-hadron decays based on the transverse and longitudinal impact parameters of the tracks, or reconstructed secondary vertices associated with the jet. Both are used for the identification of jets from b-

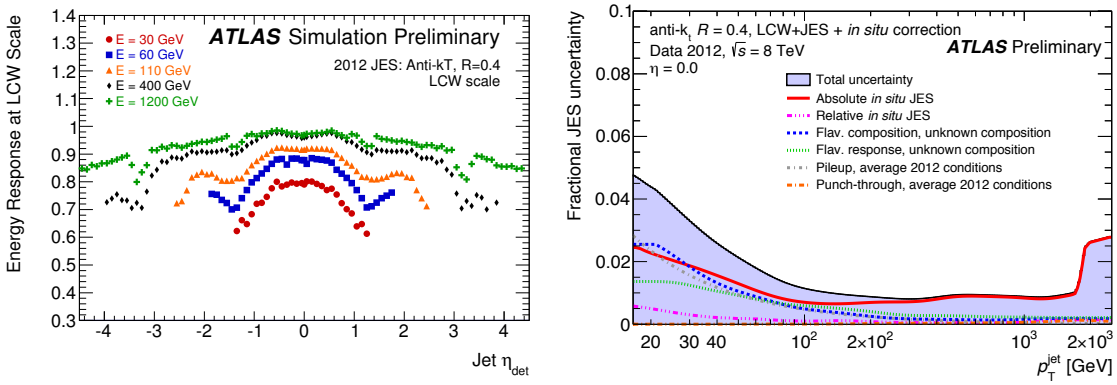

(a) (b)

Figure 3.5: (a) Average response of jets formed from topological clusters and calibrated using the local cell signal weighting (LCW) method. The response is defined as the ratio of the reconstructed jet energy and the energy of jets defined on particle level in simulated event samples. (b) Uncertainty on the jet energy scale as a function of the transverse momentum of the jet. The uncertainty is shown for jets with $|\eta| < 0.8$. Taken from Ref. [70].

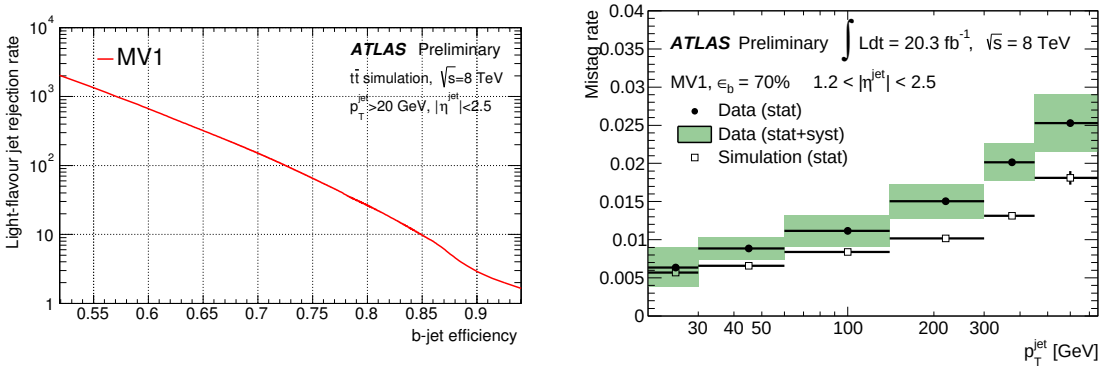

(a) (b)

Figure 3.6: (a) Rate at which light-flavour hadrons are rejected as a function of the efficiency of the b-jet identification. (b) Rate of the misidentification of light-flavour jets as b-jets. The rate is measured in a sample of multijet events in data and simulated event samples and shown here for the operating point corresponding to a b-tagging efficiency of 70%. Taken from Ref. [73].

quark decays. The reconstruction of the secondary decay vertex allows a reconstruction of b-hadron properties, e.g. its invariant mass. The efficiency of the identification algorithms based on secondary decay vertices are limited by the vertex reconstruction efficiency and the vertex resolution which is low if the b-hadron is produced with low transverse momentum. Reconstruction algorithms based on the impact parameter do not rely on the vertex reconstruction but rely on the track parameters. These perform better than the vertex based algorithms for low transverse momentum jets. A third approach makes use of the full decay topology, using also tertiary decay vertices from c-hadrons produced in the b-hadron decay. Several of these algorithms are combined using an artificial neural network [74]. The use of the complementary signatures allows an efficient discrimination of jets from b-hadron decays and light-flavour jets over a large kinematic range.

The efficiency of the b-jet identification is chosen to be 85%, 80%, 70% or 60% resulting in different rates for the rejection of jets from c-hadron decays and of light-flavour jets as shown in Fig. 3.6a for simulated events of top-quark pair production. The efficiency of these operating points is measured in data in dijet and $t\bar{t}$ events [74, 75]. The rate at which light-flavour and c-jets are misidentified as b-jets is measured in data. It is shown for light-flavour jets in Fig. 3.6b for the operating point corresponding to a b-tagging efficiency of 70% [73]. The rate of the misidentification is 0.5%-1.5% for jets with $p_{\mathrm{T}} < 300$ GeV.

3.7 Missing Transverse Momentum

Purely weakly interacting particles such as neutrinos or certain hypothetical particles do not leave signals when traversing the detector. Their presence can be inferred from the momentum imbalance in transverse direction. While the momentum of the initial partons that participate in the hard scatter are unknown in z direction, their transverse momentum is small compared to typical electroweak energies. Consequently, purely weakly interacting particles introduce an imbalance in the vectorial sum of the transverse momenta of the detectable particles, the so-called missing transverse momentum, $p_{\mathrm{T}}^{\mathrm{miss}}$. Two alternative measurements of the missing transverse momentum are described in the following, based on energy depositions in the calorimeter and the tracks reconstructed in the inner detector. The missing momentum in x and y direction is calculated as:

$$p_x^{\mathrm{miss}} = -\sum_i p_i \sin\theta_i \cos\phi_i \tag{3.3}$$

$$p_y^{\mathrm{miss}} = -\sum_i p_i \sin\theta_i \sin\phi_i \tag{3.4}$$

where different energy depositions or reconstructed momenta are summed for the calorimeter and track-based measurement. From these quantities the missing transverse momentum $p_{\mathrm{T}}^{\mathrm{miss}}$ and its azimuthal direction ϕ^{miss} is calculated as:

$$p_{\mathrm{T}}^{\mathrm{miss}} = \sqrt{\left(p_x^{\mathrm{miss}}\right)^2 + \left(p_y^{\mathrm{miss}}\right) 2} \tag{3.5}$$

$$\phi^{\mathrm{miss}} = \arctan\left(p_y^{\mathrm{miss}} \Big/ p_x^{\mathrm{miss}}\right). \tag{3.6}$$

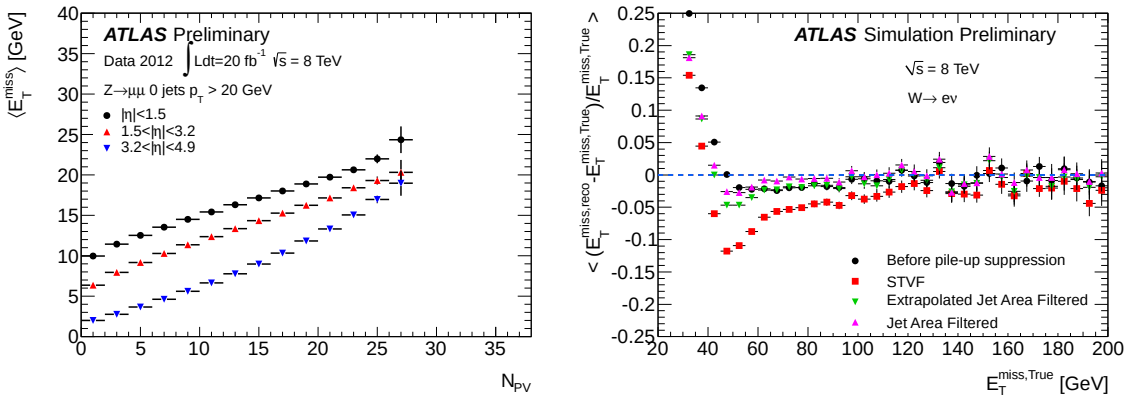

(a) (b)

Figure 3.7: (a) Average missing transverse momentum reconstructed in $Z \rightarrow \mu\mu$ events as a function of the number of reconstructed primary vertices. Shown is the calorimeter-based measurement with different pseudorapidity boundaries. Taken from Ref. [77]. (b) Linear response of the reconstructed missing transverse momentum, defined as the relative deviation of the reconstructed missing transverse momentum from the true value. The calorimeter-based measurement is compared to several alternative computations using techniques to suppress pile-up contributions. Taken from Ref. [78].

When referring to the reconstructed missing transverse momentum $E_{\mathrm{T}}^{\mathrm{miss}}$ and $p_{\mathrm{T}}^{\mathrm{miss}}$ are used to denote the calorimeter and track-based measurement.

3.7.1 Calorimeter-Based Measurement

The calorimeter-based missing transverse momentum is measured according to Eqs. 3.3-3.5 by summing the energy depositions in calorimeter cells. Cells associated with a reconstructed and identified electron, photon, hadronically decaying τ-lepton, jet or muon are excluded and the reconstructed four momenta of these particles are added instead. The contribution from the remaining calorimeter cells, called cell-out term, receives a set of adjustments to improve the resolution of the measurement. Contributions from calorimeter noise are suppressed by considering only cells that belong to three-dimensional topological clusters [64] calibrated at the LCW scale. Topological clusters that have an associated track reconstructed in the inner detector are replaced by the track in the cell-out term. Particles with a transverse momentum too low to reach the calorimeter are accounted for by adding tracks regardless of whether they are associated to a topological cluster [76].

Since all energy depositions in the detector affect the reconstruction of the missing transverse momentum, the resolution is highly affected by additional pp collisions in the event. In $Z \rightarrow \mu\mu$ events no missing transverse momentum is expected and its presence is mostly an effect of the limited resolution. It is shown as a function of the number of reconstructed vertices in Fig. 3.7a. The conditions present in the dataset recorded in the year 2012 with on average of $n_{\mathrm{vtx}} = 11$ reconstructed primary vertices introduce a missing transverse momentum of roughly $E_{\mathrm{T}}^{\mathrm{miss}} = 15$ GeV on average. This causes deviations of the missing transverse

momentum from its true value in particular for low values of $E_{\mathrm{T}}^{\mathrm{miss}}$ as shown in Fig. 3.7b.

3.7.2 Track-Based Measurement

The track-based missing transverse momentum is measured according to Eqs. 3.3-3.5 by summing the tracks reconstructed in the inner detector and originating from the primary interaction vertex. As for the calorimeter-based measurement the reconstructed four momenta of electrons and muons replace the associated tracks. For other particles, in particular for jets, this distinction is not made. The tracks are required to have a minimal transverse momentum of $p_{\mathrm{T}} > 500\,\mathrm{MeV}$, to satisfy a set of quality requirements and to have a maximum transverse momentum of $p_{\mathrm{T}} < 200$ GeV and $p_{\mathrm{T}} < 120$ GeV in the barrel and endcap regions, respectively. The association of tracks to the primary interaction vertex efficiently removes contribution from pile-up interactions in the reconstruction of the missing transverse momentum and thus the track-based measurement has a considerably better resolution than the calorimeter-based measurement. Since neutral particles are by construction excluded from the measurement unless they convert or decay early on, the response of the track-based measurement is worse than that of the calorimeter-based measurement.

4 Measurement of Electron Identification Efficiencies

Isolated, high-energy electrons cannot be produced in pure QCD processes and thus provide a clean and unambiguous signature of electroweak processes at hadron-collider experiments. A precise knowledge of the efficiency to correctly reconstruct and identify the measured electrons is crucial to state detector independent results of these processes. The measurement of electron identification efficiencies in $Z \to ee$ decays as well as the statistical combination with complementary measurements is described in this chapter.

4.1 Methodology of Efficiency Measurements

In order to perform a measurement of the electron reconstruction and identification efficiencies in data, a clean sample of genuine electrons is required. Such electrons are produced at a high rate as the decay products of the J/ψ meson, W-boson and Z-boson resonances. The efficiency of a certain selection criterion can be measured with these electrons by counting the number of electrons satisfying the criterion and relating it to the total number of electrons under investigation:

$$\varepsilon_{\text{criterion}} = \frac{N_{\text{electrons, satisfying criterion}}}{N_{\text{all electrons}}}. \tag{4.1}$$

The investigated sample of electrons has to be unbiased with respect to the criterion of interest. In the ATLAS experiment the efficiency to reconstruct and identify an electron is not measured as a single quantity but factorised into several components:

$$\varepsilon_{\text{total}} = \varepsilon_{\text{reconstruction}} \cdot \varepsilon_{\text{identification}} \cdot \varepsilon_{\text{trigger}} \cdot \varepsilon_{\text{additional}}, \tag{4.2}$$

i.e. the total efficiency is given by the product of reconstruction, identification and trigger efficiency, and the efficiency of additional selection requirements. With this factorisation the efficiency to identify genuine electrons is measured with respect to reconstructed electrons with the definitions introduced in Section 3.2.2. Additional requirements can be e.g. criteria on the isolation defined in Section 3.4.

A set of unbiased electrons is selected using a so-called tag-and-probe method. Candidate events for $J/\psi \to ee$ and $Z \to ee$ decays are selected by applying strict constraints on only one of the electrons (tag), the second electron is used for the efficiency measurement (probe). Additional requirements on event properties and the invariant mass of the tag-and-probe system are applied. The use of two different processes allows a differential measurement of electron efficiencies over a large kinematic range: $J/\psi \to ee$ decays are

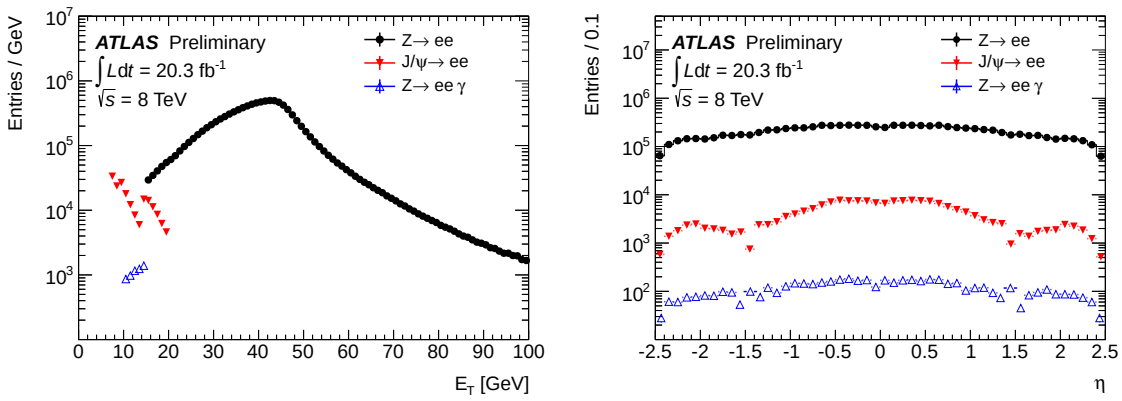

Figure 4.1: Distributions of the transverse energy, E_{T} (left), and the pseudorapidity, η^{cl} (right), for probe electrons selected in data for the measurement of electron identification efficiencies that satisfy the tight++ identification criterion. The electrons are selected in $J/\psi \to ee$ and $Z \to ee$ decays. Previously published in Ref. [2].

used for the measurement of electrons with a transverse energy of 7 GeV $< E_{\mathrm{T}} <$ 20 GeV; the range of $E_{\mathrm{T}} > 10$ GeV is accessible with electrons from $Z \to ee$ decays, where radiative $Z \to ee\gamma$ decays are selected for electrons with 10 GeV $< E_{\mathrm{T}} <$ 15 GeV to enhance the purity of the event sample. In radiative decays, one of the electrons has undergone significant energy loss due to final state radiation and the invariant mass used to select the event sample is calculated from three objects, two electrons and the photon. The number of probe electrons selected in data and satisfying the tight++ identification requirements is shown in Fig. 4.1. The discontinuities in the distribution of the probe electrons from $J/\psi \to ee$ events are caused by the trigger algorithms used to record the events.

The efficiency of the electron identification highly depends on the transverse energy, E_{T}, and pseudorapidity reconstructed in the calorimeter, η^{cl}, of the electrons since the identification criteria are optimised and applied in bins of E_{T} and η^{cl}. The large event yields in $Z \to ee$ and $J/\psi \to ee$ events allow a double differential measurement of efficiencies in $E_{\mathrm{T}} \times \eta^{\mathrm{cl}}$. The measurement of identification efficiencies is performed in 12 bins in E_{T} and in up to 20 bins in η^{cl}. The bin boundaries of the efficiency measurements are chosen to closely match the boundaries of the optimisation of the identification criteria. Additional boundaries are added for areas where the detector geometry changes, which can affect the shower shape variables and their modelling in the event simulation:

$$
\begin{aligned}
\left|\eta(E_{\mathrm{T}} < 20\ \mathrm{GeV})\right| &: [\,0, 0.1, 0.8, 1.37, 1.52, 2.01, 2.47\,] \\
\left|\eta(E_{\mathrm{T}} > 20\ \mathrm{GeV})\right| &: [\,0, 0.1, 0.6, 0.8, 1.15, 1.37, 1.52, 1.81, 2.01, 2.37, 2.47\,] \\
E_{\mathrm{T}}\ [\mathrm{GeV}] &: [\,4, 7, 10, 15, 20, 25, 30, 35, 40, 45, 50, 60, 80, \infty\,]
\end{aligned}
$$

where for electrons with $E_{\mathrm{T}} > 20$ GeV the measurement in η is performed in the positive and negative hemisphere of the detector separately.

In addition to the sensitivity to the detector geometry, identification efficiencies are found to be sensitive to event properties like the amount of pile-up, close-by hadronic activity, kinematic constraints used to select the events and others. Efficiencies are moreover

not universal for different processes. Electrons reconstructed with $E_{\mathrm{T}} = 15$ GeV and originating from a Z boson decay will more likely have undergone some form of energy loss than an electron of the same transverse energy produced in a low mass resonance. Energy loss due to bremsstrahlung will typically widen the shower shape variables and impact the track-to-cluster matching. In order to provide process-independent results, ratios of efficiencies from data and simulated event samples are calculated. These can be used to correct the efficiencies to identify electrons produced in simulated event samples of any arbitrary process to the efficiencies in data.

4.2 Efficiency Measurement in $Z \to ee$ Events

Efficiency measurements in $Z \to ee$ decays are performed in order to provide efficiencies for electrons with transverse energies of $E_{\mathrm{T}} > 15$ GeV. The transverse energies of electrons from $Z \to ee$ decays lie in the kinematic range most important for precision measurements using W bosons, Z bosons and top quarks. Data corresponding to an integrated luminosity of $\mathcal{L} = 20.3\,\mathrm{fb}^{-1}$ are used in the measurement. Only data runs with stable proton–proton collisions in which all relevant detector components were operating normally are used. Events are selected by at least one of two trigger algorithms that require a single electron with thresholds of 24 GeV or 60 GeV, and meeting the medium++ or loose++ identification criteria, respectively.

At least two electron candidates are required to be reconstructed in the event. Strict criteria are placed on one of the electrons that is defined as the *tag* electron and the other electron serves as a *probe*. The tag electron is required to have triggered the readout of the event in order to avoid a bias on the probe electron from the identification criteria imposed in the trigger algorithms. To reject contributions from background processes, events are rejected if the tag electron falls into the calorimeter transition region $1.37 < \left|\eta^{\mathrm{cl}}\right| < 1.52$ or has a transverse energy of $E_{\mathrm{T}} < 25$ GeV. In addition, tag electrons are required to satisfy the tight++ identification criterion and strict criteria on the calorimeter and track-based measurement of the isolation, and the transverse and longitudinal impact parameters. For each event, all possible tag-and-probe pairs are considered in the efficiency measurement. They are required to have opposite electric charge and their invariant mass is restricted to lie within 15 GeV of the Z boson mass. The selection described above yields a total of 12.2 million probe electrons in data.

For the measurement of efficiencies in simulated events a sample of $Z \to ee$ events is used. It is produced with the PowHeg [79–82] event generator interfaced to Pythia8 [83]. Information at the event generation stage is used to remove electrons that do not originate from $Z \to ee$ decays. For additional studies, a sample of $W \to e\nu$ events was simulated with the same settings and a dijet sample was simulated with Pythia8. All simulated event samples have been processed through the full ATLAS detector simulation [84] based on Geant4 [85]. The effects of photon radiation are modelled with Photos [86]. Additional inelastic, minimum-bias like pp collisions (pile-up) are generated using Pythia8 and overlaid. The electron identification efficiencies are sensitive to the number of average interactions per bunch-crossing as well as the z-position of the reconstructed primary vertex, z_{vtx}. The distributions in simulated event samples are therefore corrected to the distribution mea-

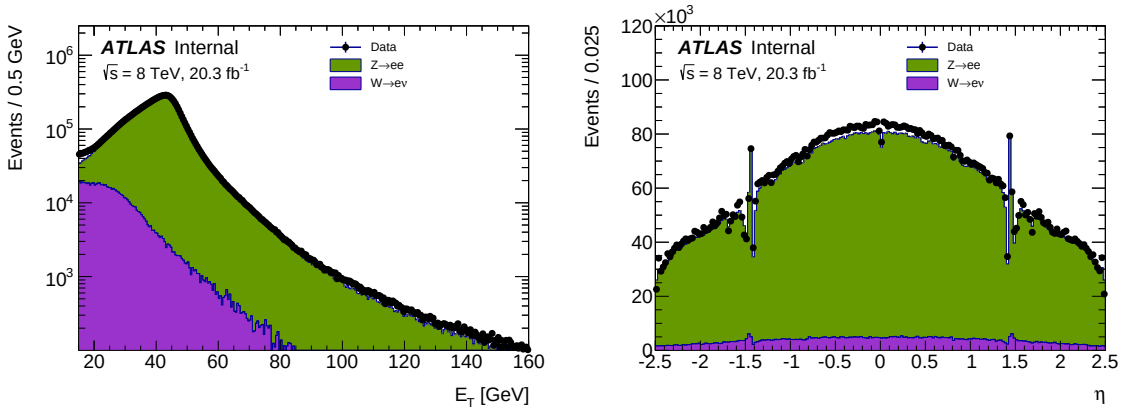

Figure 4.2: Distributions of the transverse energy, E_{T} (left), and pseudorapidity reconstructed in the calorimeter, η^{cl} (right), for probe electrons selected in $Z \to ee$ events. The data are shown with contributions from $Z \to ee$ and $W \to e\nu$ events estimated from simulated event samples. The difference between the data and simulated event samples can be accounted to multijet background for which no simulated events are shown.

sured in data.

4.3 Background Estimation

The event sample selected for the measurement of the efficiency for reconstructed electrons to meet the different identification criteria has large contributions from background processes. In $Z \to ee$ events, background contributions mainly arise from W+jets and multijet events. In both cases the contributions are due to hadronic jets that are reconstructed as electrons. The distributions of the transverse energy, E_{T}, and the pseudorapidity reconstructed in the calorimeter, η^{cl}, are shown in Fig. 4.2 for the selected probe electrons in data and simulated $Z \to ee$ and $W \to e\nu$ events. The difference between the data and simulated events can be accounted to multijet background for which no simulated event samples are shown. The dominant background is due to W+jets production. The figure illustrates that background contributions from misidentified electrons are sizeable for low transverse energies of the probe electron where background contributions can be as large as 40%. For transverse energies close to the Jacobian peak of the Z boson at $E_{\mathrm{T}} \sim 45$ GeV contributions from genuine electrons are more than two orders of magnitude larger than contributions from hadronic jets. Additional processes that produce genuine electrons, e.g. diboson production, are not accounted for. Those electrons are allowed to contribute to the measurement of efficiencies.

Two complementary methods for the subtraction of background are used. Both use a side-band to normalise a template built from data and enriched in misidentified electrons to estimate the background contributions. In one method the side-band is in the high invariant mass of the tag-and-probe pair, in the other the side-band is in the high calorimeter isolation of the probe electron, $E_{\mathrm{T}}^{\mathrm{cone}}$, and is presented here. The technique based on the

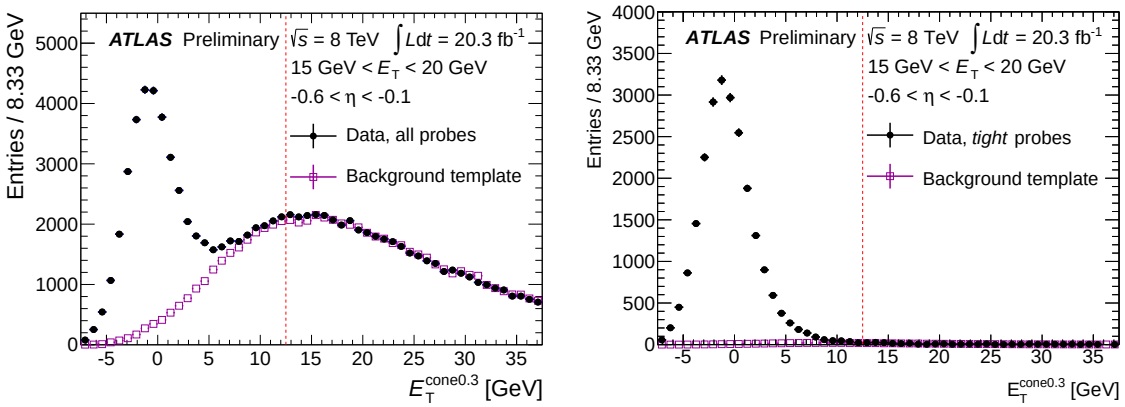

Figure 4.3: Distributions of the calorimeter isolation in a cone of $\Delta R = 0.3$, $E_{\mathrm{T}}^{\mathrm{cone}}(0.3)$ for reconstructed electrons (left) and electrons satisfying the tight++ identification criterion (right). The distributions are shown in a specific kinematic region, defined by 15 GeV $< E_{\mathrm{T}} <$ 20 GeV and $-0.6 < \eta < -0.1$. The figure illustrates the method used for the estimation of contributions from misidentified electrons. A template constructed from data is normalised in the high $E_{\mathrm{T}}^{\mathrm{cone}}(0.3)$ side-band, chosen here to be $E_{\mathrm{T}}^{\mathrm{cone}}(0.3) > 12.5$ GeV. Previously published in Ref. [2].

calorimeter isolation was first introduced in Ref. [56] and originally used for measurements in $W \rightarrow e\nu$ decays, as described in detail in Ref. [87]. The calorimeter isolation $E_{\mathrm{T}}^{\mathrm{cone}}$ is defined in Section 3.4.

The side-band subtraction is illustrated in Fig. 4.3. A template enriched in contributions from misidentified electrons is selected in data and normalised to data in the region of large values of $E_{\mathrm{T}}^{\mathrm{cone}} > 12.5$ GeV, assumed to be free of contributions from genuine electrons. The criteria used to select the templates are described in Section 4.4. To assess the systematic uncertainty of the efficiency determination a set of parameters used in the measurement are varied. The selection criteria for the tag electron are varied by removing the isolation and impact parameter requirements. This results in an increase of the background from multijet production and is considered to assess the effect of template selection criteria on the relative composition of W+jets and multijet events. Furthermore, the threshold for the side-band subtraction is varied at values of 10 GeV, 12.5 GeV and 15 GeV. The criterion placed on the invariant mass of the tag-and-probe pair is varied to lie within 10 GeV, 15 GeV and 20 GeV of the nominal Z boson mass, mainly since electrons that lost part of their energy due to final state radiation cause the invariant mass of the tag-and-probe pair to be lower. At the same time they usually have a lower identification efficiency. The relative composition of the W+jets and multijet background is also affected by this variation. For additional systematic studies of the background estimation, two different templates and two different distributions of the calorimeter isolation, $E_{\mathrm{T}}^{\mathrm{cone}}$, calculated in a cone of $\Delta R =$ 0.3 and 0.4, are used.

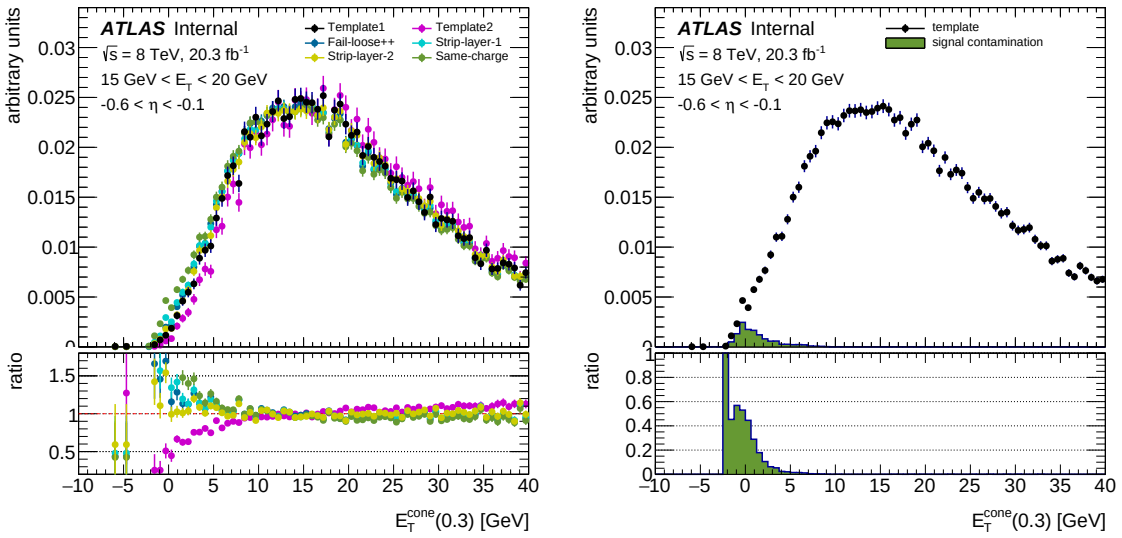

(a) (b)

Figure 4.4: (a) Distribution of the calorimeter isolation in a cone of $\Delta R = 0.3$, $E_{\mathrm{T}}^{\mathrm{cone}}(0.3)$, for various background templates under study. The lower panel is calculated with respect to "Template1". The figure illustrates the bias on the isolation shape which is introduced by requiring the reconstructed electrons to fail identification criteria. The criteria used to select the templates are described in the text. (b) The same distribution is shown for the template "Same-charge" together with the contamination from genuine electrons which is estimated from simulated $Z \to ee$ samples.

4.4 Background Template Studies

The estimation of the background from W+jets and multijet production uses a fully data-driven side-band subtraction. Templates enriched in background contributions are constructed by placing requirements on combinations of selection criteria used in the electron identification, but failing the selection criteria instead of fulfilling them. Several different templates are considered and their quality is studied in the following. The main figure of merit for the quality are a possible bias of the calorimeter isolation, caused by the requirements used to select the templates, and the contributions to the templates from genuine electrons.

4.4.1 Template Definitions

The selection of reconstructed electrons allows to construct background enriched templates by using variables also used in the identification criteria. To reject contributions from genuine electrons the tag-and-probe pair is required to have the same electric charge. The data sample used to select the background templates is thus statistically independent of the sample used for the efficiency measurement where the tag-and-probe pair is required to have opposite electrical charge. A total of six templates are studied which are selected

with the following criteria:

Template1	fail f_{HT} *and* fail w_{stot};
Template2	fail f_{HT}, fail w_{stot} *and* fail R_{ϕ};
Fail-loose++	fail *any* loose++ criterion;
Strip-layer-1	fail *one* of strip variables F_{side}, ΔE, w_{s3} and E_{ratio};
Strip-layer-2	fail *two* of the criteria listed for "Strip-layer-1";
Same-charge	no additional criteria.

The variables used in the definition are introduced in Section 3.2.2, except for those listed for the "Strip-layer" templates. Those are properties defined in the strip layer of the calorimeter and used in the identification of photons, as described in Ref. [88]. The criteria listed above are not defined in all bins of η, in particular the ratio of high threshold hits in the TRT, f_{HT}, can only be used in $|\eta| < 2.01$. For larger values of η the template constructed in the last valid bin is used.

The background-enriched templates are compared in Fig. 4.4a. Only small differences are seen for large values of $E_{\mathrm{T}}^{\mathrm{cone}}$ and the templates are found to properly describe the selected probe electrons in the high $E_{\mathrm{T}}^{\mathrm{cone}}$ region. The templates show large differences for values $E_{\mathrm{T}}^{\mathrm{cone}}(0.3) < 10$ GeV which is the region with large contributions from genuine electrons. This is due to differences in the composition of the templates with events from multijet and W+jets background and due to correlations of the calorimeter isolation $E_{\mathrm{T}}^{\mathrm{cone}}$ and the shower shape variables used to select the templates. The features can be understood from the requirements put on the identification variables when selecting the templates. Probe electrons are required to fail each of the two and three criteria used to define "Template1" and "Template2", respectively. For templates "Fail-loose++" and "Strip-layer-1" only a single criterion out of a larger set is required to fail, and two criteria out of a larger set are required to fail for template "Strip-layer-2". For the "Same-charge" template no additional criteria are used to enhance the contribution from background electrons. The number of criteria placed in the template selection also causes the different template definitions to differ in their efficiency to select background events. This impacts the statistical precision of the efficiency measurement.

4.4.2 Bias from the Template Selection

The criteria placed to select the background templates cause differences in the calorimeter isolation distributions. This bias is quantified by comparing the $E_{\mathrm{T}}^{\mathrm{cone}}(0.3)$ distributions of simulated event samples of misidentified electrons with and without applying the template selection criteria. A sample of simulated multijet events is used to estimate the impact on the distribution for multijet events. Only a single reconstructed electron is required in the studies using the simulated multijet event sample. The impact on W+jets events is studied in simulated W+jets events where the tag-and-probe selection criteria listed above are applied but with a relaxed requirement on the invariant tag-and-probe mass. For systematic studies the requirement on the charge product of the tag-and-probe pair is removed.

A template is considered unbiased if no further selection is applied on the reconstructed electrons. For W+jets events only, the tag-and-probe pair is considered unbiased if it has

	multijet	W+jets		
		opposite charge	same charge	all
Template1 •	1.28	1.25	1.40	1.31
Template2 •	1.54	1.44	1.61	1.51
Fail-loose++ •	1.08	1.06	1.13	1.09
Strip-layer-1 •	1.06	1.06	1.13	1.09
Strip-layer-2 •	1.11	1.11	1.18	1.14
Same-charge •	—	—	1.06	1.03

Table 4.1: Bias b on the distribution of the calorimeter isolation of the background-enriched template from reverting identification criteria. The bias is estimated on simulated W+jets and multijet samples by comparing distributions of the calorimeter isolation $E_{\mathrm{T}}^{\mathrm{cone}}$ to the distribution of unbiased templates. The coloured markers in the first column indicate the colour used in Fig. 4.4a.

opposite electric charge. The reason for the latter requirement is a charge correlation in some W+jets diagrams that is discussed in detail in Section 7.4. The bias b is estimated by calculating ratios of events that pass and fail a selection of $E_{\mathrm{T}}^{\mathrm{cone}}(0.3) < 12.5$ GeV for templates with selection criteria applied and unbiased templates:

$$b = \frac{N_{\mathrm{template}}^{\mathrm{pass}}}{N_{\mathrm{template}}^{\mathrm{fail}}} \Bigg/ \frac{N_{\mathrm{unbiased}}^{\mathrm{pass}}}{N_{\mathrm{unbiased}}^{\mathrm{fail}}}. \tag{4.3}$$

The bias estimated with this method is shown in Table 4.1 for probe electrons with $15\ \mathrm{GeV} < E_{\mathrm{T}} < 20$ GeV and integrated over η. The background templates show a clear hierarchy. If strict selection criteria are applied, a large bias is introduced. If only a few criteria out of a larger set are required, the bias is smaller. The requirement of the same electric charge of the tag-and-probe pair, that is common to all templates, introduces a bias of 6% for background from W+jets production. Since the selection on the tag electron significantly varies the composition of the W+jets and multijet background the second and fourth column of Table 4.1 can be considered lower and upper limits on the bias.

4.4.3 Contributions from Genuine Electrons

The contribution from genuine electrons to the background templates can be estimated by applying the same selection criteria to simulated $Z \to ee$ samples. This is illustrated in Fig. 4.4b for the "Same-charge" template. For the specific kinematic region of E_{T} and η shown, the overall contribution from genuine electrons is 1.3%. The contribution is centred at low values of $E_{\mathrm{T}}^{\mathrm{cone}}$ where contributions from genuine electrons are expected. In the region with large contributions from genuine electrons, $E_{\mathrm{T}}^{\mathrm{cone}}(0.3) < 12.5$ GeV, it reaches up to 3.9%. This can only be a very rough estimate. Especially shower shape variables are known to be mismodelled since the template selection criteria aim at rejecting genuine electrons by placing a selection in extreme parts of the distribution.

The estimated contributions from genuine electrons in the low $E_{\mathrm{T}}^{\mathrm{cone}}$ region are listed for all templates in selected ranges of E_{T} in Table 4.2 integrated over the full pseudorapidity

E_T [GeV]		[15, 20]	[25, 30]	[40, 45]
Template1	•	0.039%	0.17%	0.89%
Template2	•	0.034%	0.11%	0.53%
Fail-loose++	•	0.70 %	3.5 %	16 %
Strip-layer-1	•	3.7 %	19 %	55 %
Strip-layer-2	•	2.7 %	15 %	56 %
Same-charge	•	6.9 %	36 %	86 %

Table 4.2: Contributions from genuine electrons to the templates selected in data. The contributions are estimated in the region with large contributions from genuine electrons, $E_T^{cone}(0.3) < 12.5$ GeV, by applying the selection criteria to simulated $Z \to ee$ samples. The coloured markers in the first column indicate the colour used in Fig. 4.4a.

range. The templates with smallest signal contributions are those that place the strictest selection criteria. The templates "Strip-layer-1" and "Strip-layer-2" that only use variables defined in the strip layer of the calorimeter have only a poor rejection of contributions from genuine electrons. The estimated contributions exhibit a dependence on the pseudorapidity that is not shown in the table. In the endcap region the electrons have to traverse a large amount of material causing them to lose energy due to bremsstrahlung. This leads to a large charge-misidentification rate and the requirement of the same electric charge in the selection of all templates is less effective in rejecting contributions from genuine electrons. To reduce the contributions from genuine electrons at high η the template constructed in $2.01 < |\eta| < 2.37$ is also used in the outermost bin.

4.4.4 Template Choice

The choice of the templates used in the efficiency measurement is based on the studies discussed in Sections 4.4.2 and 4.4.3. Clearly, the "Same-charge" template is preferred due to its small bias. It does, however, show large contributions from genuine electrons which can be larger than the bias due to the template selection criteria in other templates. A combination of two templates is therefore used, one with a small kinematic bias and one with a small contribution from genuine electrons. Since both features affect the shape of the distribution of the calorimeter isolation in an opposite way the templates are expected to yield an estimated background contribution higher and lower than the true value. Different templates are used at low values of E_T, where the background contributions are large and a precise estimation of the background is needed, and for high values of E_T, where the background contributions are small. Here, the low E_T region is defined for transverse momenta of 15 GeV $< E_T <$ 20 GeV in the endcap and calorimeter transition regions, and 15 GeV $< E_T <$ 25 GeV in the central detector region. The templates "Same-charge" and "Strip-layer-2" are used at low E_T; the templates "Template1" and "Strip-layer-2" are found to be good choices at high E_T. From Tables 4.1 and 4.2 the template "Fail-loose++" is found to be preferable over the template "Strip-layer-2". This template was only added to the studies after the results in Section 4.6 were derived and is therefore not used for the measurement. It will improve future measurements of the electron efficiencies in the ATLAS

experiment.

The background estimation is performed in both the numerator and denominator of Eq. 4.1. Since the calorimeter isolation is highly correlated to some of the variables used in the identification criteria, in particular to the hadronic leakage fraction, $R_{\mathrm{Had(1)}}$, the distribution of the background templates do not agree well with the distribution of the probe electrons meeting the identification criteria. Agreement is retained by adding the $R_{\mathrm{Had(1)}}$ requirement that is used in the identification criteria also to the background template used to estimate the numerator of Eq. 4.1.

4.5 Statistical Analysis

The central value of the measurement in each bin and its uncertainty is calculated from a set of values obtained by varying the parameters used for systematic studies in every possible combination. For the measurement described above this results in a set of $2{\cdot}2{\cdot}2{\cdot}3{\cdot}3 = 72$ values, for two different criteria on the tag electron, the use of two different discriminating variables and two templates for the side-band subtraction, three different thresholds for the side-band, and three different constraints on the dilepton invariant mass. The central value is obtained as the arithmetic mean of these values, the statistical uncertainty is obtained by calculating the arithmetic mean of the individual statistical uncertainties, and the systematic uncertainty is obtained as the standard deviation of the values in this set, calculated with respect to the arithmetic mean.

The measurements using different methods for the evaluation of the W+jets and multijet background, and the measurements performed in $Z \to ee$ and $J/\psi \to ee$ final states are combined using statistical methods. Ratios of efficiencies measured in data and simulated events are used in the combination. Efficiency ratios generally have lower uncertainties since some of the effects probed by the systematic variations yield large differences in the measured efficiencies but are found to be well reproduced in simulation and therefore cancel when taking the ratio. As discussed before, only efficiency ratios are comparable between $Z \to ee$ and $J/\psi \to ee$ events, or any arbitrary process. The combination of measurements obtained with different methods for the evaluation of background contributions is described in Section 4.5.1, the combination of results from $Z \to ee$ and $J/\psi \to ee$ events is detailed in Section 4.5.2.

4.5.1 Combined results from $Z \to ee$ Decays

The estimation of background from W+jets and multijet production in $Z \to ee$ decays is performed using the invariant mass of the tag-and-probe pair or the calorimeter isolation of the probe electron as a discriminating variables. The results from the individual methods are statistically correlated. They are also systematically correlated since part of the systematic variations are shared between methods.

To combine both results they are considered as systematic variations. The combined central value and the associated uncertainties are calculated from the sum of values obtained as described above, i.e. the combined results from $Z \to ee$ decays is calculated from a set of every possible combination of systematic variations of the invariant mass and calorimeter

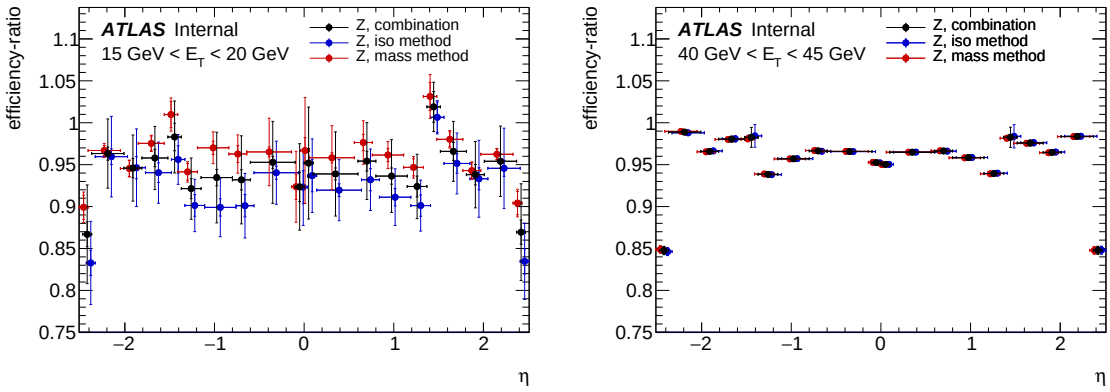

Figure 4.5: Ratios of efficiencies in data and simulated event samples measured in $Z \to ee$ events with the invariant mass and calorimeter isolation-based background estimation methods and the combined result. The efficiency ratios are shown as a function of pseudorapidity, η, for transverse energies of 15 GeV $< E_{\mathrm{T}} <$ 20 GeV (left) and 40 GeV $< E_{\mathrm{T}} <$ 45 GeV (right) of the probe electron. Shown are numbers for the very tight LH identification criterion. The inner error bars show the statistical and the outer ones show the combined statistical and systematic uncertainties.

isolation-based methods. Since both methods use different numbers of systematic variations the values are weighted accordingly. A comparison of the results for the ratio of efficiencies in data and simulated event samples from the individual methods and the combined value is shown in Fig. 4.5 as a function of the pseudorapidity, η, for the very tight LH identification criterion in two selected bins of E_{T}.

The uncertainty of the combined result does not well cover the envelope of the individual results in some cases. This is most visible for probe electrons with a transverse energy of 15 GeV $< E_{\mathrm{T}} <$ 20 GeV but in fact it is consistently seen also at higher values of E_{T}. To assure that the systematic uncertainty accounts for differences between the results obtained with both methods, the uncertainty is inflated such that the overall $\chi^2 = 1$, similar to the prescription used in Ref. [25]. It was found that inflating the uncertainties of the measurements by 20% accounts for the differences observed between the methods.

4.5.2 Combined results from $Z \to ee$ and $J/\psi \to ee$ decays

The procedure of combining the results from $Z \to ee$ and $J/\psi \to ee$ events is as follows: first the systematic correlations between bins in $E_{\mathrm{T}} \times \eta$ are calculated, then a statistical combination is carried out. The correlation information of the measurements between different bins is needed for a correct treatment of correlations in differential measurements and the measurements of ratios. In addition, the knowledge of the correlations between bins can reduce the uncertainty compared to the assumption of full correlation. The measurements from $Z \to ee$ and $J/\psi \to ee$ final states are then combined using a χ^2 minimisation.

Similar to the independent techniques used for the estimation of W+jets and multijet background in $Z \to ee$ decays, two methods exist for $J/\psi \to ee$ decays that both use the in-

variant mass distribution to discriminate genuine and falsely reconstructed electrons but a different treatment of non-prompt J/ψ meson decays. One method uses a fit to the measured lifetime, τ, to estimate the fraction of non-prompt decays, the other only considers events with a short lifetime. The method using events with short lifetime therefore uses a subset of the data of the method estimating the number of events with short lifetime in a fit. The individual results from $J/\psi \to ee$ decays are combined in the same way as the individual $Z \to ee$ results and are found to be in good agreement.

The systematic correlation between measurements x in two bins k and l is described by the covariance matrix V_{kl}:

$$V_{kl} = \sum_i \left(x(k)_i - \bar{x}(k)\right)\left(x(l)_i - \bar{x}(l)\right) \tag{4.4}$$

where the sum runs over all systematic variations i. A transformation of variables is performed to obtain a set of uncorrelated systematic uncertainties, i.e. the covariance matrix for the transformed variables U_{ij} is diagonal. The linear transformation is:

$$y_i = \sum_j^N A_{ij} x_j. \tag{4.5}$$

The columns of the transformation matrix A_{ij} are given by the eigenvectors of the covariance matrix V_{kl}. The covariance matrices in the old and new basis also are related via the transformation matrix, $V_{ij} = \sum_{k,l}^N A_{ik} U_{kl} A_{lj}^\intercal$. Both the old and the new basis have the same dimensionality which is given by the number of bins $N = n_{E_\mathrm{T}} \times n_\eta$. To reduce the amount of information, part of the correlation is neglected by truncating the sum:

$$\tilde{V}_{ij} = \sum_{k,l}^{N'} A_{ik} U_{kl} A_{lj}^\intercal + \delta_{ij} \sum_{k=N'+1}^{N} A_{ik} U_{kk} A_{ki}^\intercal. \tag{4.6}$$

The sum is truncated for entries corresponding to small eigenvalues. For this truncated part, the uncertainties are treated as uncorrelated between bins by setting the off-diagonal elements to zero. The cut-off N' is determined from the size of the eigenvalues corresponding to the individual eigenvectors. Only for the uncertainties corresponding to the largest 99% of the sum of all eigenvalues the correlation information is propagated correctly. For the remaining 1% the information is dropped. This approach reduces the number of systematic uncertainty sources from $N = n_{E_\mathrm{T}} \times n_\eta$ to typically $N' \leq 10$. The correlation coefficient $\rho_{ij} = U_{ij}/\sqrt{U_{ii}U_{jj}}$ is shown for efficiencies of the very tight LH identification criterion measured in $Z \to ee$ events in Fig. 4.6a. The bin-by-bin correlation in η is large for $20\ \mathrm{GeV} < E_\mathrm{T} < 30\ \mathrm{GeV}$ where contributions from misidentified electrons are large. The measurement at low E_T exhibits only little correlation with the measurement at high E_T because different templates are used in the different kinematic regions. A similar distinction between low and high E_T is made in the method based on the high invariant-mass side-band where the threshold for the side-band is different for transverse energies above and below $E_\mathrm{T} = 30\ \mathrm{GeV}$. The largest N' eigenvalues of the covariance matrix are shown in Fig. 4.6b for the very tight LH identification criterion. The number of uncertainty sources is

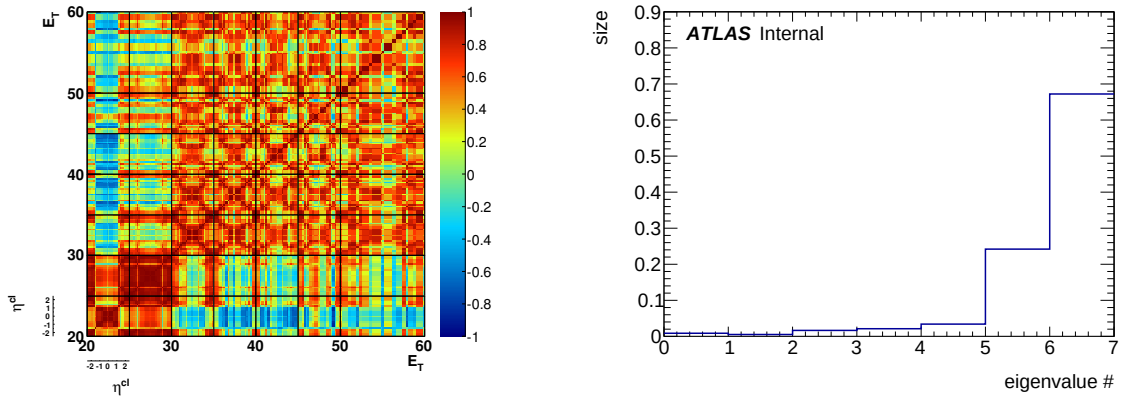

(a) (b)

Figure 4.6: (a) Bin-by-bin correlation coefficients of efficiency ratios measured in $Z \to ee$ decays for the very tight LH identification criterion. Each bin in E_T is subdivided into η bins as indicated by the additional axis for 20 GeV $< E_T <$ 25 GeV. The E_T axes are cut-off at 60 GeV for better visibility. (b) Size of the eigenvalues of the covariance matrix. The first bin shows the sum of $N-N'$ eigenvalues corresponding to the uncertainties for which the correlation information is neglected. The remaining bins show the largest N' eigenvalues.

reduced from $N = 180$ to $N' = 6$ by neglecting contributions from systematic uncertainties corresponding to small eigenvalues. The sum of $N - N' = 174$ eigenvalues corresponding to the neglected uncertainties are shown in the first bin of Fig. 4.6b.

The measurements of the identification efficiencies in $Z \to ee$ and $J/\psi \to ee$ events are combined using a χ^2 minimisation. The χ^2 function is defined as the sum of χ^2 values in all bins i and channels c:

$$\chi^2 = \sum_{i,c} \left(\frac{m_i - \bar{x}_i^c}{\Delta_i^c} \right)^2 \tag{4.7}$$

with the new central values of the measurement m_i, the measurements $\bar{x}_i^c$ and total uncertainty Δ_i^c in the individual bins and channels. Expressing the uncertainties in terms of relative statistical, and relative uncorrelated and correlated systematic uncertainties, $\delta_{i,\text{stat}}^c$, $\delta_{i,\text{uncor}}^c$ and $\gamma_{\alpha,i}^c$, and accounting for the effects of systematic uncertainties with nuisance parameters, b_α, the χ^2 function takes the form in Ref. [89]:

$$\chi^2 = \sum_{i,c} \frac{\left[m_i - \sum_\alpha \gamma_{\alpha i}^c m_i b_\alpha - \bar{x}_i^c \right]^2}{\left(\delta_{i,\text{stat}}^c \right)^2 \bar{x}_i^c \left(m_i - \sum_\alpha \gamma_{\alpha i}^c m_i b_\alpha \right) + \left(\delta_{i,\text{uncor}}^c m_i \right)^2} + \sum_\alpha b_\alpha^2. \tag{4.8}$$

The nuisance parameters b_α are constrained by a penalty term $\sum_\alpha b_\alpha^2$ that is added to the χ^2 function. Compared to Eq. 4.7 the uncertainty is expressed in terms of fitted values m_i.

Since independent measurements from the different final states $Z \to ee$, $Z \to ee\gamma$ and $J/\psi \to ee$ only exist in 10 GeV $< E_T <$ 20 GeV an actual combination is only performed in this region. The measurements are split into a low and high E_T region at $E_T = 20$ GeV. Below this threshold, the measurements in $Z \to ee$, $Z \to ee\gamma$ and $J/\psi \to ee$ events are combined using

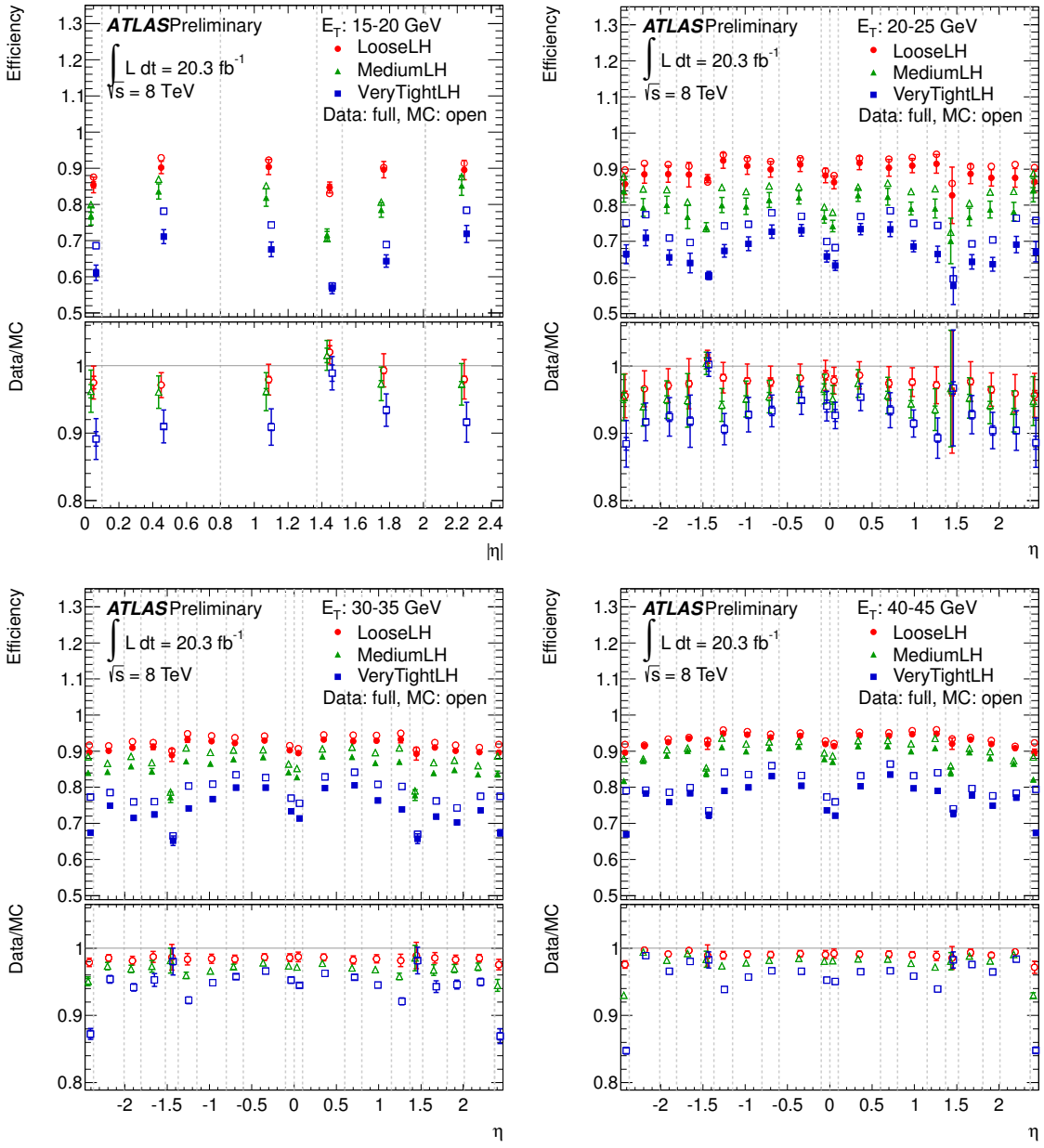

Figure 4.7: Electron identification efficiency for the identification criteria using a likelihood discriminant as a function of pseudorapidity, η, in selected E_{T} bins. The efficiencies are determined by applying the efficiency ratios from the double differential measurement to samples of simulated $Z \to ee$ events. The lower panels display the efficiency ratios obtained in the statistical combination. Two sets of uncertainties are shown. The inner error bars represent the statistical and the outer ones the combined statistical and systematic uncertainties. Taken from Ref. [2].

the methodology described above. For larger transverse energies the plain measurement from $Z \to ee$ events is used. Since the bin boundaries in η were chosen differently for the two final states the measurements from $Z \to ee$ events are merged by calculating the weighted average of measurements within the bin boundaries of the coarser binning chosen for $J/\psi \to ee$ final states. The precision of the combined result is improved compared to the individual results as is seen by comparing Figs. 4.5 and 4.7.

4.6 Results

The identification efficiency is shown in Fig. 4.7 as a function of the pseudorapidity, η, for the identification criteria based on a likelihood discriminant and for four selected bins in transverse energy, E_{T}. They are obtained from samples of simulated $Z \to ee$ events with an arbitrary selection placed on the $Z \to ee$ events. The corresponding data efficiencies are derived by applying the efficiency ratios obtained by combining results from $Z \to ee$ and $J/\psi \to ee$ events to kinematic distributions of simulated $Z \to ee$ events in bins of $E_{\mathrm{T}} \times \eta$. The efficiency ratios resulting from the statistical analysis are shown in the lower panels of Fig. 4.7.

Efficiencies are systematically lower in data than in simulated events which mostly arises from a known mismodelling of calorimeter shower shapes in the Geant4 detector simulation. Deviations from unity in the efficiency ratios therefore depend on how strict the requirements on shower shape variables in the identification criteria are. With higher transverse momenta the criteria become less strict because electrons are better separated from background in many shower shape variables. The efficiency ratios thus deviate less from unity for large values of E_{T}. The shape of the efficiencies and the efficiency ratios as a function of the pseudorapidity is driven by the detector design.

The combined reconstruction and identification efficiencies are shown in Fig. 4.8 as a function of transverse energy, E_{T}, integrated over η, and pseudorapidity, η, integrated over E_{T}. The distributions are obtained by projecting the double differential distributions of efficiencies from simulated events to the E_{T}- or η-axes, where the efficiencies in simulated events are corrected with the measurements in data. The resulting efficiencies therefore represent the efficiencies in data as a function of these variables and illustrate the precision of the efficiency measurement. The identification criteria have different identification efficiencies and are therefore suited for the analysis of wide range of processes and event topologies. The combined electron reconstruction and identification efficiency ranges from 88%–95% for the multilepton and loose LH operating points. For the tight++ and very tight LH operating points the efficiency ranges from 65%–85%. Electrons with lower transverse energy have a lower probability to be identified by the criteria.

The uncertainties are a few per-cent in the low E_{T} range. For transverse energies $E_{\mathrm{T}} > 30$ GeV a precision of better than one per-cent is reached and at the Jacobian peak of the Z boson of $E_{\mathrm{T}} \sim 45$ GeV a precision of roughly one per-mille is achieved. The efficiencies of the electron identification based on sequential cuts and based on a likelihood discriminant are very similar as intended. Dedicated measurements performed in Ref. [2] show that the rejection of background from misidentified electrons is better by a factor of two in the likelihood-based criteria.

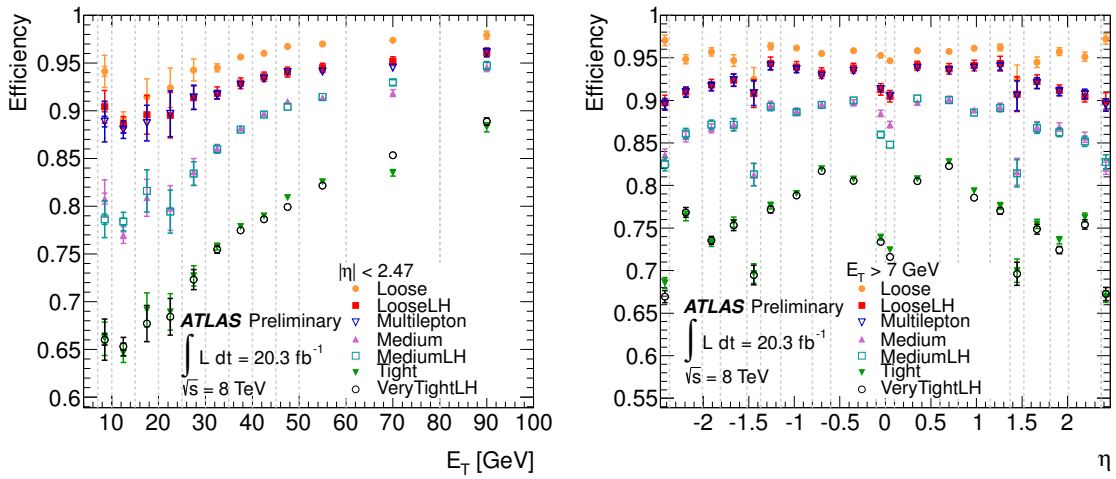

Figure 4.8: Combined electron reconstruction and identification efficiency in $Z \to ee$ events as a function of transverse energy, E_{T}, integrated over η (left), and pseudorapidity, η, integrated over E_{T} (right). The efficiencies are determined by applying the efficiency ratios from the double differential measurement to samples of simulated $Z \to ee$ events. The efficiencies therefore correspond to data efficiencies and the uncertainties reflect the precision achieved in the double differential measurement. Taken from Ref. [2].

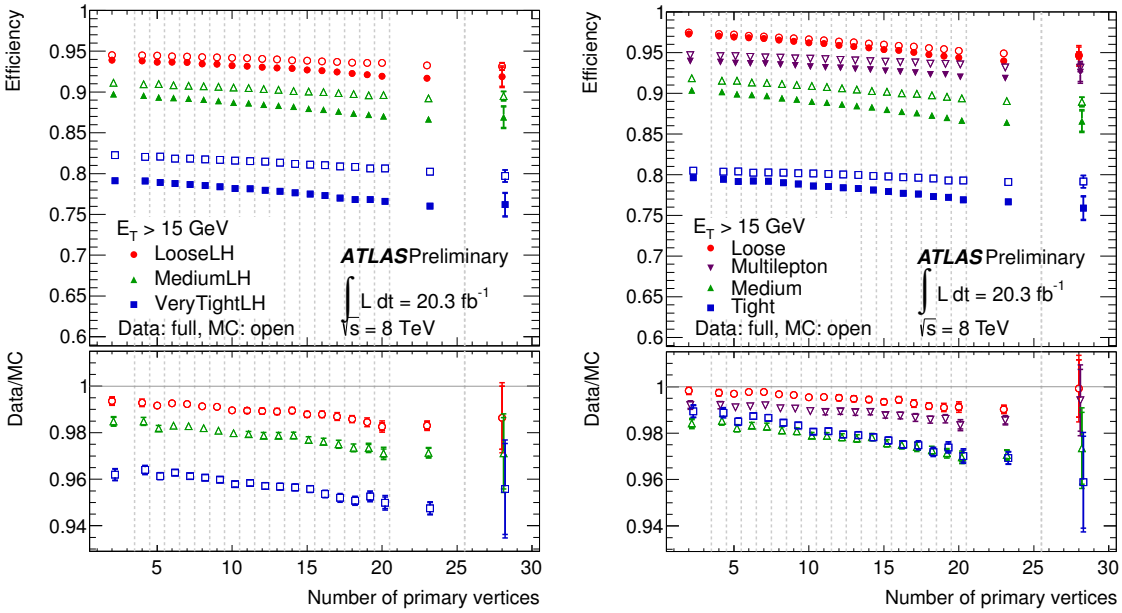

Figure 4.9: Electron identification efficiency as a function of the number of reconstructed primary vertices, n_{vtx}, for the identification criteria using a likelihood discriminant (left) and using sequential selection cuts (right). The efficiency decrease in data compared to simulated events is mainly caused by inefficiencies in the TRT that increased with time. The instantaneous luminosity was also increased with time. Taken from Ref. [2].

The electron identification efficiencies are shown as a function of the number of reconstructed primary vertices, n_{vtx}, in Fig. 4.9 for the identification criteria using sequential selection cuts and the criteria based on a likelihood discriminant. The measurement is performed inclusively in η and E_{T}. The efficiencies in simulated event samples only decrease slightly for environments with a high number of primary vertices n_{vtx}. For the cut-based identification criteria this was achieved by manually adjusting the criteria placed on the individual identification variables in the optimisation of the identification criteria. For the identification criteria based on the likelihood discriminant the requirement on the likelihood discriminant is adjusted depending on n_{vtx}. The efficiencies in data show a larger decrease for high pile-up environments. This is caused by radiation damages in the readout system of the TRT. Since the instantaneous luminosity was steadily increased with time, inefficiencies in the TRT introduce the trend seen in the figure. Nevertheless, the figure illustrates a high robustness of the identification criteria in high pile-up environments.

5 W Boson Pair Production

In the following an overview of the theoretical aspects specific to W boson pair production is presented. An introduction to the electroweak theory is given in Section 1.1.4. This chapter describes how these basic principles relate to W boson pair production. In addition, a review of the recent progress in perturbative calculations related to W boson pair production is given. Finally, the results of previous measurements at ATLAS and other experiments are summarised.

5.1 W Boson Pair Production in the Standard Model

The primary production mechanisms for $pp \to W^+W^-$ production are the s- and t-channel scattering of $q\bar{q}$ initial states as shown in Fig. 5.1. The s-channel diagram involves the exchange of a Z/γ^* boson and a three gauge-boson vertex for the subsequent decay into a pair of W bosons. The relevant terms in the Lagrangian density of the electroweak theory, $\mathcal{L}_{\text{EW}}$, introduced in Section 1.1.4 can be expressed in terms of the physical fields $W^{\pm}_{\mu}$, Z_{μ} and A_{μ} and are given in the following. Higher-order diagrams are discussed in Section 5.2. The production of W bosons as shown in Fig. 5.1a is given by the coupling to quarks in the Lagrangian density:

$$\mathcal{L}_{\text{CC}} = ie_W \left[W^+_{\mu} \left(V_{ij} \bar{u}_i \gamma^{\mu} (1 - \gamma_5) d_j \right) + W^-_{\mu} \left((V^{\dagger})_{ij} \bar{d}_i \gamma^{\mu} (1 - \gamma_5) u_j \right) \right], \tag{5.1}$$

where the operator $(1 - \gamma_5)$ projects the fermion fields on their left-handed component. The self-interaction of the $W^{\pm}$ bosons, the Z boson and the photon γ shown in Fig. 5.1b is given by the term $\frac{1}{4} W^a_{\mu\nu} W^{\mu\nu}_a$ in Eq. 1.14, more specifically by the cubic terms that contain the structure constants ε_{abc} which are non-zero in non-Abelian gauge theories:

$$\begin{aligned}
\mathcal{L}_{\text{self-coupling}} &= -\frac{1}{2} g \varepsilon_{abc} W^a_{\mu\nu} W^{\mu}_b W^{\nu}_c \\
&= \mathcal{L}_{WW\gamma} + \mathcal{L}_{WWZ}, \text{ with} \\
\mathcal{L}_{WW\gamma} &= ie \left[W^+_{\mu\nu} W^{-\mu} A^{\nu} - W^-_{\mu\nu} W^{+\mu} A^{\nu} + W^+_{\mu} W^-_{\nu} F^{\mu\nu} \right] \qquad (5.2) \\
\mathcal{L}_{WWZ} &= ie_Z \left[W^+_{\mu\nu} W^{-\mu} Z^{\nu} - W^-_{\mu\nu} W^{+\mu} Z^{\nu} + W^+_{\mu} W^-_{\nu} Z^{\mu\nu} \right]. \qquad (5.3)
\end{aligned}$$

The coupling constants e and e_Z are given further below. Relevant in the context of W boson pair production are further the couplings of quarks to the Z boson and the photon γ, $\mathcal{L}_{\text{em}}$

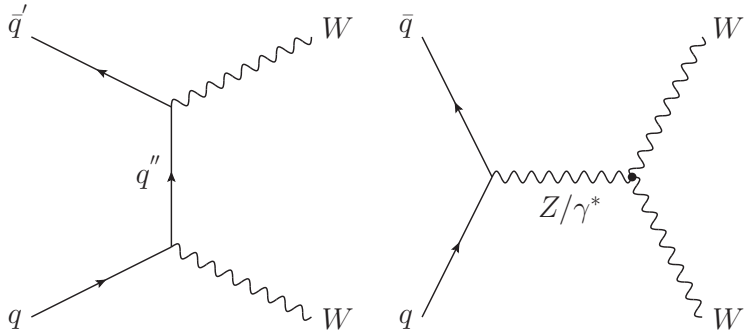

(a) t-channel (b) s-channel

Figure 5.1: Leading-order diagrams for W boson pair production from $q\bar{q}$ initial states. Shown are (a) the t-channel diagram where two W boson are scattered off of the initial quarks, (b) the s-channel diagram with an exchange of a Z boson or a virtual photon and a three gauge-boson vertex.

and $\mathcal{L}_{\mathrm{NC}}$, in order to allow the exchange of the mediators in Fig. 5.1b:

$$\mathcal{L}_{\mathrm{em}} = ie \sum_q A_\mu \bar{q}\gamma^\mu Q_q q \tag{5.4}$$

$$\mathcal{L}_{\mathrm{NC}} = ie_N \sum_q Z_\mu \bar{q}\gamma^\mu \left(g_V^q - \gamma_5 g_A^q\right) q, \tag{5.5}$$

where the sum runs over all up and down-type quark fields q. Compared to Eq. 1.14, the term $\mathcal{L}_{\mathrm{em}}$ is modified to contain the electrical charge of the quark Q_q. The neutral current interactions $\mathcal{L}_{\mathrm{NC}}$ exhibit a (vector–axial-vector) structure ($V - A$) with $g_V = \frac{1}{2}I_3 - Q\sin^2\theta_W$ and $g_A = \frac{1}{2}I_3$. The third component of the weak isospin I_3 and the electrical charge of the quark fields Q are listed in Table 1.2. The coupling constants are predicted in the electroweak theory, expressed in terms of the electromagnetic coupling constant e, take the values:

$$e_W = \frac{e}{2\sqrt{2}\sin\theta_W}, \quad e_N = \frac{e}{\sin 2\theta_W} \quad \text{and} \quad e_Z = e\cot\theta_W. \tag{5.6}$$

The cross section for the production of two W bosons from a pair of fermions f, $f_i\bar{f}_i \to W^+W^-$, was first calculated in Ref. [90] for the leading order diagrams shown in Figs. 5.1a and 5.1b. The analytic form of the cross section exhibits a dependence on the centre-of-mass energy of the parton–parton interaction $\hat{s}$ of $\hat{\sigma}(q\bar{q} \to W^+W^-) \sim (1/\hat{s})\ln\hat{s}$. This scaling behaviour with energy highly depends on the inter-relationship of the couplings given in Eqs. 5.1 to 5.5. Additional terms linear and constant in $\hat{s}$ that originate from longitudinally polarized W bosons appear and let the cross section grow infinitely large with energy. These divergent terms cancel exactly between t- and s-channel diagrams if:

$$Q_i e^2 + e_Z e_N g_V^i - 2Q_i e_W^2 \sum_j \left|V_{ij}\right|^2 = 0 \tag{5.7}$$

$$\text{and} \quad e_Z e_N g_A^i - 2Q_i e_W^2 \sum_j \left|V_{ij}\right|^2 = 0 \tag{5.8}$$

i.e. if the factors in Eq. 5.6 take the relations predicted in the Standard Model and the CKM matrix is unitary. The measurement of the W^+W^- production cross section therefore provides a test of the inner structure of the Standard Model. In particular, the $WW\gamma$ and WWZ interactions that originate from the non-Abelian nature of the electroweak theory are necessary to preserve unitarity in these diagrams.

The divergences in W boson pair production only cancel exactly in the limit of massless fermions. For finite fermion masses the exchange of a scalar particle with a coupling proportional to mass, i.e. the Higgs boson, is required in the s-channel diagrams [91].

5.2 Phenomenology of W Boson Pair Production

The calculation of theoretical predictions for $pp \to W^+W^-$ production cross sections was a very active field in the past years. Both corrections from QCD and electroweak contributions to $q\bar{q} \to W^+W^-$ production are available at various orders of the perturbative expansion. Due to the high gluon luminosity in high energy pp collisions, the production of two W bosons from $\overset{(-)}{q}g$ and gg initial states have sizeable contributions in addition to the qq initial states discussed in Section 5.1. An overview of the different production mechanisms and the recent progress in the calculation of cross sections is given in the following.

5.2.1 Higher-Order Corrections

For comparisons with measurements at hadron-collider experiments, calculations using perturbative QCD are essential. The diagrams discussed in Section 5.1 correspond to the lowest order of the perturbative expansion. In addition to the production from $q\bar{q}$ initial states, the W^+W^- final state can be produced from qg, $\bar{q}g$ and gg initial states. The production from qg scattering occurs at $O(\alpha_s)$ and necessarily includes a final state quark since W bosons do not couple to gluons directly. Corrections at NLO were calculated in Refs. [92, 93] and include the effects of the spin correlations between the W bosons and effects of off-shell W bosons. Also available are corresponding NLO calculations for W^+W^-+jets production [94, 95], where up to three jets were included [96].

The production of W boson pairs from gg initial states occurs at $O(\alpha_s^2)$, corresponding to a NNLO correction to $q\bar{q} \to W^+W^-$ production. The production mechanism does not necessarily feature jets in the final state if quark loops are involved as shown in Fig. 5.2a. Due to the high gluon density in the proton at a centre-of-mass energy of $\sqrt{s} = 8$ TeV, the production from gg initial states gives sizeable contributions. The production cross section for $gg \to W^+W^-$ production was first calculated in Ref. [97] at LO ($O(\alpha_s^2)$). Effects from off-shell W bosons and the leptonic decay of the W bosons were included in the calculation in Ref. [98]. Moreover, $gg \to W^+W^-$ production can occur as a resonant process via the exchange of a Higgs boson, produced from a top-quark loop at $O(\alpha_s^2)$, that subsequently decays into two W bosons. The corresponding diagram is shown in Fig. 5.2b. Diagrams where a Z/γ^* boson is exchanged in the s-channel instead of the Higgs boson do not contribute at LO. The diagrams cancel due to C invariance (γ and vector-Z coupling) and in the limit of $m_u = m_d$ (axial-Z coupling) [97].

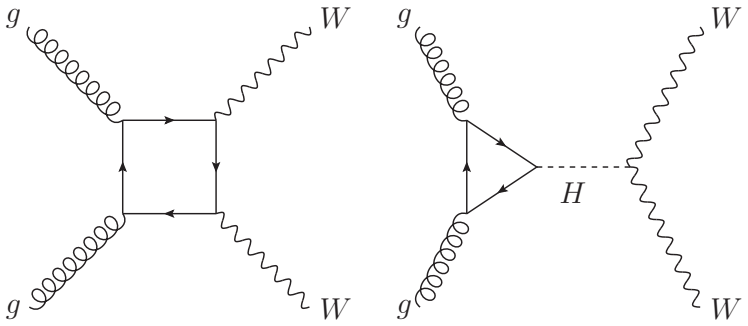

(a) gluon fusion (b) Higgs boson production

Figure 5.2: Diagrams for W boson pair production from gg initial states. (a) The non-resonant production from gg initial states, (b) resonant W boson pair production from Higgs boson decays.

The processes $q\bar{q}, qg$ and $\bar{q}g \rightarrow W^+W^-$, which in the following are denoted simply as $q\bar{q} \rightarrow W^+W^-$, until recently were calculated up to NLO ($O(\alpha_s)$) only [99]. The $q\bar{q} \rightarrow W^+W^-$ production cross section at NLO with a centre-of-mass energy of $\sqrt{s} = 8$ TeV amounts to:

$$\sigma_{\text{tot}}^{\text{NLO}}(pp \rightarrow WW) = 53.2^{+2.3}_{-1.9}\,(\text{scale})^{+1.0}_{-1.1}\,(\text{PDF})\ \text{pb}, \tag{5.9}$$

where the renormalisation and factorisation scales are dynamically set to $\mu = m_{WW}/2$ and the MSTW [28] parton-distribution function (PDF) is used. Recent fixed-order calculations for on-shell W bosons provide theoretical predictions up to NNLO [100], resulting in an increase of the production cross section to:

$$\sigma_{\text{tot}}^{\text{NNLO}}(pp \rightarrow WW) = 59.1^{+1.2}_{-1.0}\,(\text{scale})^{+0.9}_{-0.9}\,(\text{PDF})\ \text{pb}, \tag{5.10}$$

which includes contributions from gg initial states and interference effects with off-shell Higgs boson production. Contributions from off-shell W bosons do not have a significant impact on the theoretical cross section [101].

For pp collisions at a centre-of-mass energy of $\sqrt{s} = 8$ TeV the cross section of non-resonant $gg \rightarrow W^+W^-$ production at LO is $\sigma_{gg\rightarrow WW} = 1.4^{+0.3}_{-0.2}$ pb [99]. Effects from order $O(\alpha_s^3)$, i.e. NLO corrections, were included in Ref. [102]. They are found to increase the cross section to $\sigma_{gg\rightarrow WW} = 2.78^{+0.20}_{-0.26}$ pb where the renormalisation and factorisation scales are set to $\mu = m_W$. The total cross section resulting from the sum of the NNLO cross section and the $gg \rightarrow W^+W^-$ sub-process at NLO is calculated to:

$$\sigma_{\text{tot}}^{\text{nNNLO}}(pp \rightarrow WW) = 60.8^{+1.2}_{-1.1}\ \text{pb} \tag{5.11}$$

where both calculations are added with a consistent scale choice of $\mu_F = \mu_R = m_W$. The alternative scale choice increases Eq. 5.10 to $59.8^{+1.3}_{-1.1}$ pb. The total production cross section of a Higgs boson from gg initial states for a mass of the Higgs boson of $m_H = 125$ GeV is $\sigma_{gg\rightarrow H} = 19.3^{+1.4}_{-1.5}\,(\text{scale})^{+1.4}_{-1.3}\,(\text{PDF})$ pb [103] at NNLO ($O(\alpha_s^4)$) for a centre-of-mass energy of $\sqrt{s} = 8$ TeV. More recently it was computed up to NNNLO [104] in the limit of a large top-

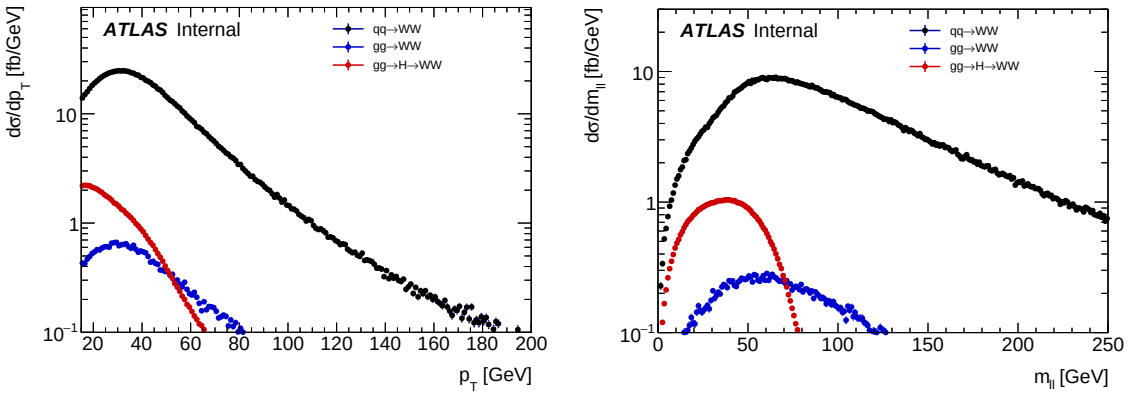

Figure 5.3: Differential fiducial $pp \to W^+W^- \to e^\pm\nu\mu^\mp\nu$ production cross sections as a function of the transverse momentum of the leading lepton, p_T (left), and the invariant mass of the dilepton system, $m_{\ell\ell}$ (right). The distributions are shown separately for W^+W^- events produced from qq initial states, and the resonant and non-resonant production from gg initial states. The transverse momenta of the leptons are restricted to $p_\mathrm{T} > 15$ GeV.

quark mass. The branching fraction for the Higgs boson decay to a pair of W bosons is $\mathcal{B}\left(H \to W^+W^-\right) = 0.215^{+0.09}_{-0.09}$ [103] for $m_H = 125$ GeV.

Electroweak contributions to $q\bar{q} \to W^+W^-$ production were calculated at NLO ($O\left(\alpha^3_\mathrm{EW}\right)$) for stable, on-shell W bosons [105, 106] and including off-shell effects with the W bosons decaying to a lepton and its corresponding neutrino [107, 108]. While these contributions have a minor effect of $< 1\%$ on the total W^+W^- cross section, differential cross sections can be reduced by several 10% for high energies of the leptons or the dilepton system.

For the modelling of kinematic distributions event generators are used. The measurement presented in this thesis mostly relies on the PowHeg [79–82] program for the modelling of $q\bar{q} \to W^+W^-$ production, where Pythia8 is used for the modelling of the underlying event and hadronisation. Contributions up to NLO QCD ($O(\alpha_\mathrm{s})$) are included. Events from $gg \to W^+W^-$ production are modelled with the gg2ww [109] event generator with a simulation of the matrix element at LO ($O(\alpha^2_\mathrm{s})$) interfaced to Jimmy. The modelling of $gg \to H \to W^+W^-$ production is implemented in the PowHeg event generator at NLO, including electroweak contributions to NLO, and corrected to reproduce the p^H_T distribution from a resummed calculation at NNLO+NLL [110]. The differential $pp \to W^+W^-$ production cross section with leptonically decaying W bosons is shown in Fig. 5.3 as a function of the transverse momentum, p_T, of a lepton, and as a function of the invariant mass of the dilepton system, $m_{\ell\ell}$. The dominant process is the production from $q\bar{q} \to W^+W^-$ initial states, followed by resonant $gg \to H \to W^+W^-$ production and non-resonant $gg \to W^+W^-$ production. The leptons from the W boson decay are restricted to a transverse momentum of $p_\mathrm{T} > 15$ GeV. The resonant $gg \to H \to W^+W^-$ production results in smaller transverse momenta and lower invariant masses. This is due to the fact that one of the W bosons is off-shell. Another difference between resonant and non-resonant W^+W^- production is the angular correlation between the decay leptons. The $(V - A)$ structure of the $W \to \ell\nu$

decay preserves the information of the spin of the incident particles. The resonant production via the exchange of the scalar Higgs boson causes the leptons from the W boson decay to be emitted in the same direction whereas leptons from $q\bar{q} \to W^+W^-$ and non-resonant $gg \to W^+W^-$ production are emitted in opposite direction.

5.2.2 Resummation for $q\bar{q} \to W^+W^-$ Production

Previous measurements of W boson pair production at hadron-collider experiments were performed by requiring the absence of hadronic jets in the final state, c.f. Sections 5.4.2 and 5.4.3, the so-called jet veto. While the production of W boson pairs introduces a mass scale of m_{WW}, the jet-veto requirement introduces another mass scale at the jet-veto threshold $p_{\mathrm{T}}^{\mathrm{veto}}$. It is therefore not obvious, which value to choose for the renormalisation and factorisation scales, $\mu_{\mathrm{R}} = \mu_{\mathrm{F}} = m_{WW}$ or $\mu_{\mathrm{R}} = \mu_{\mathrm{F}} = p_{\mathrm{T}}^{\mathrm{veto}}$.

The cross section of W^+W^- production with zero hadronic jets is shown in Fig. 5.4a as a function of the jet-veto threshold for the two alternative choices of $\mu_{\mathrm{R}} = \mu_{\mathrm{F}} = \mu$, $\mu = p_{\mathrm{T}}^{\mathrm{veto}}$ and $\mu = m_W$. The cross sections differ significantly for low values of $p_{\mathrm{T}}^{\mathrm{veto}}$ and converge as $p_{\mathrm{T}}^{\mathrm{veto}}$ increases and therefore gets closer to m_W. At NLO the transverse momentum of outgoing quarks and gluons is directly correlated with the transverse momentum of the W^+W^- system, p_{T}^{WW}. In the calculation of differential cross sections as a function of p_{T}^{WW} the perturbative expansion acquires terms:

$$\frac{\mathrm{d}\sigma}{\mathrm{d}p_{\mathrm{T}}^{WW}} \sim \alpha_s^n \log^m \left(\frac{(m_{WW})^2}{\left(p_{\mathrm{T}}^{WW}\right)^2} \right). \tag{5.12}$$

The presence of large logarithms causes the perturbative series to converge slower. The dependence of the cross section on the choice of μ can be reduced by resumming the logarithmic terms in Eq. 5.12. This was done up to the next-to-leading logarithm (NLL) and next-to-next-to-leading logarithms (NNLL) for the calculation at NLO with two alternative approaches [111, 112] . It is claimed in Ref. [113] that both yield consistent results. For the calculation at NNLO the terms were resummed to NNLL [114]. A comparison of the results based on resummed calculations at various orders is given in Fig. 5.4b. Including higher order and resummation contributions result in lower jet-veto efficiencies.

The distribution of the transverse momentum of the W^+W^- system is compared in Fig. 5.5 for the NLO+NNLL and NNLO+NNLL calculations, and the distribution obtained at NLO with PowHeg and Pythia8. The calculation at NLO+NNLL yields lower values of p_{T}^{WW} than the NLO calculation with parton-shower modelling, resulting in lower selection efficiencies of the jet-veto requirement. This seems in contradiction with the behaviour shown in Fig. 5.4 where a fixed-order calculation at NLO yields the highest efficiencies. A possible underestimation of the jet-veto efficiency in the PowHeg+Pythia8 event simulation was pointed out in Ref. [115]. However, when comparing to higher-order calculations the distributions from PowHeg+Pythia8 and the fixed order calculation with resummation at NNLO+NNLL agree well.

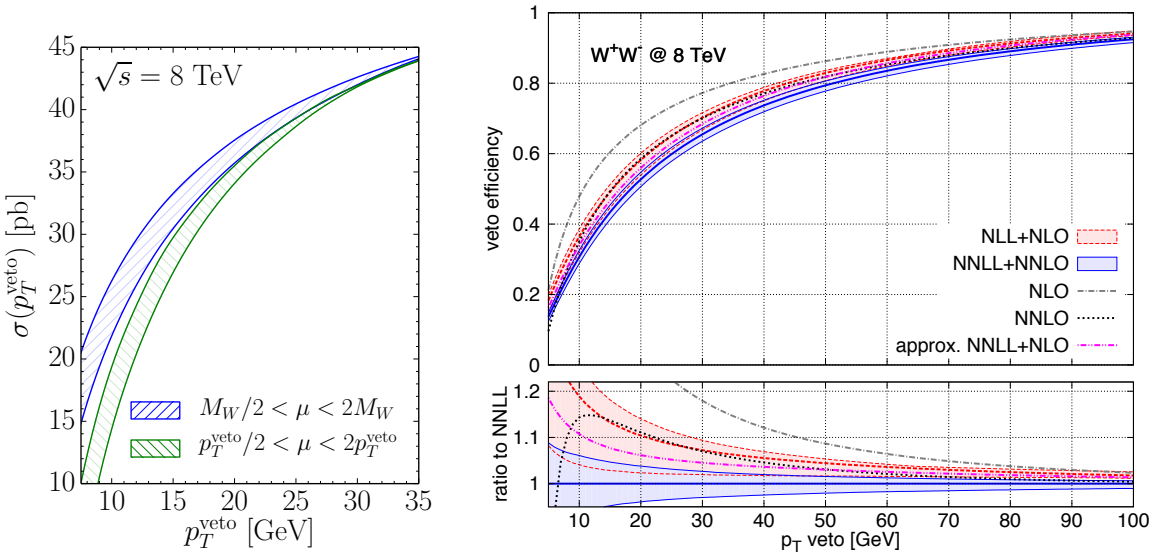

(a) (b)

Figure 5.4: (a) Cross section in the fiducial region defined by the absence of a hadronic jet as a function of the jet-veto threshold for two different choices of μ_R and μ_F at NLO. Taken from Ref. [112]. (b) Efficiency of the jet-veto requirement as a function of the jet-veto threshold from theoretical calculations at various perturbative orders. Taken from Ref. [114]. Both figures show $pp \to W^+W^-$ production at $\sqrt{s} = 8$ TeV.

5.3 Anomalous Triple Gauge Couplings

The most striking feature in W boson pair production is the cancellation between the s- and t-channel diagrams, as discussed in Section 5.1. Although the specific form of the gauge boson self-interaction was validated in the measurements described in Section 5.4.1 there are compelling reasons to believe that the Standard Model is the low-energy limit of a more fundamental theory [116]. Additional contributions beyond the Standard Model modify the high energy behaviour of W boson pair production and can be parametrised in a model-independent way by generalising the electroweak Lagrangian density. The most general extension of the WWV interaction Lagrangian density, $V = \gamma, Z$, that conserves CP, C and P is given in Ref. [117] by:

$$\mathcal{L} = ig_{WWV}\left[g_1^V\left(W^+_{\mu\nu}W^{-\mu}V^{\nu} - W^-_{\mu\nu}W^{+\mu}V^{\nu}\right) + \kappa_V W^+_{\mu}W^-_{\nu}V^{\mu\nu} + \frac{\lambda_V}{m_W^2}V^{\mu\nu}W^{+\rho}_{\nu}W^-_{\rho\mu}\right], \quad (5.13)$$

with the coupling parameters $g_{WW\gamma} = e$ and $g_{WWZ} = e\cot\theta_W$. This generalised Lagrangian reduces to Eqs. 5.2 and 5.3 for $g_1^Z = g_1^\gamma = \kappa_Z = \kappa_\gamma = 1$ and $\lambda_Z = \lambda_\gamma = 0$. Deviations from the Standard Model can therefore be expressed in terms of $\Delta g_1^V = 1 - g_1^V$ and $\Delta\kappa_V = 1 - \kappa_V$ and λ_V. The parameter $\Delta g_1^\gamma = 0$ is required by electromagnetic gauge invariance. Non-zero values of the five free parameters, Δg_1^Z, $\Delta\kappa_V$ or λ_V, would indicate new interactions not described in the Standard Model.

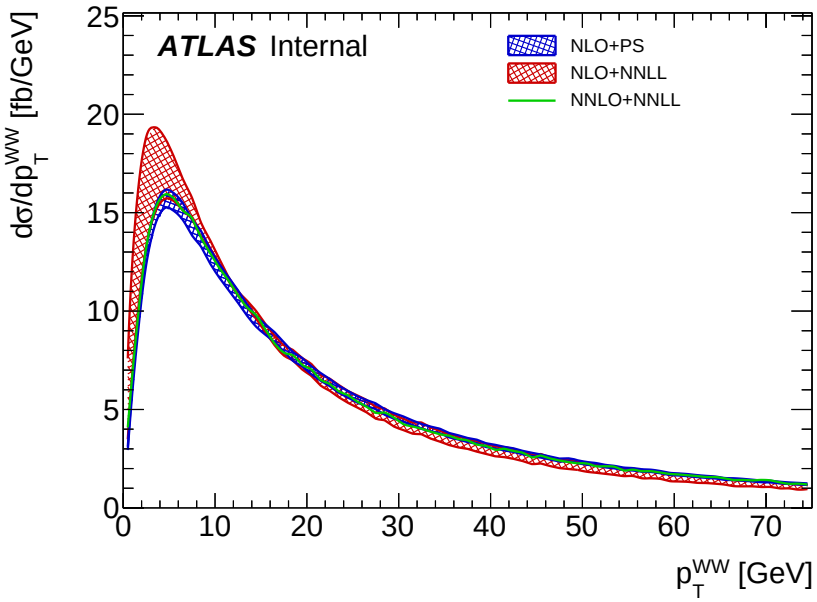

Figure 5.5: Differential fiducial $pp \to W^+W^- \to e^\pm\nu\mu^\mp\nu$ production cross section as a function of the transverse momentum of the W^+W^- system $\mathrm{d}\sigma_{\mathrm{fid}}/\mathrm{d}p_{\mathrm{T}}^{WW}$ in the phase space defined by the $e\mu$ selection criteria. The distributions are obtained by reweighting the p_{T}^{WW} distribution of simulated PowHeg+Pythia8 samples, denoted NLO+PS, to the distribution calculated in Ref. [111], denoted NLO+NNLL, and Ref. [114], denoted NNLO+NNLL. The bands show the envelope of the uncertainties from studying the dependence on renormalisation and factorisation scales (NLO+PS) and renormalisation, factorisation and resummation scales (NLO+NNLL). For the NNLO+NNLL calculation no uncertainties are shown.

Further constraints can be imposed on the effective Lagrangian. Requiring Eq. 5.13 to be invariant under an $\mathrm{SU}(2)_L \otimes \mathrm{U}(1)_Y$ gauge transformation is of particular interest and leads to:

$$\kappa_Z = g_1^Z - \left(\kappa_\gamma - 1\right)\tan^2\theta_W, \tag{5.14}$$

$$\lambda_Z = \lambda_\gamma. \tag{5.15}$$

and reduces the number of free parameters from five to three. The constraints in Eq. 5.14 and 5.15 are referred to as the LEP scenario.

The Lagrangian in Eq. 5.13 describes an effective theory, i.e. it can only be an approximation of a more fundamental theory. The theory is not renormalisable and exhibits unphysical behaviour at higher orders and high energies. Threshold effects at the scale of new physics are introduced in the model by adding form factors Λ to the coupling constants:

$$\alpha \to \frac{\alpha}{\left(1 + \hat{s}/\Lambda^2\right)^2}, \tag{5.16}$$

where $\alpha = \Delta g_1^V, \Delta\kappa_V, \lambda_V$. Without these form factors the theoretical cross section of W^+W^- production would rise unphysically large around the threshold of new physics. In return, this can lead to an overestimation of the experimental sensitivity when limits on anomalous triple gauge couplings are set [118].

Anomalous triple gauge couplings can also be probed e.g. in WZ events (WWZ couplings) and $W\gamma$ events ($WW\gamma$ couplings).

5.4 Previous Measurements at LEP, Tevatron and LHC

Measurements of the production of pairs of W bosons were performed previously in e^+e^- collisions in the second phase of the LEP program, in $p\bar{p}$ collisions at the Tevatron experiments and in pp collisions at the LHC. These measurements are summarised in the following sections.

5.4.1 LEP

The measurement of W boson pair production was one of the main scientific goals of the LEP II program [36]. Between 1995 and 2000 the centre-of-mass energy of the LEP collider was steadily increased from 130.3 GeV to 208.0 GeV with an integrated luminosity of $\mathcal{L} \sim 0.75\ \mathrm{fb}^{-1}$ recorded by each of the LEP experiments, ALEPH [119], DELPHI [120], L3 [121] and OPAL [122].

In e^+e^- collisions the W^+W^- production mechanism is analogous to Fig. 5.1 but substituting the quarks q, q' by e^+, e^-. It involves the t-channel scattering of W bosons with the exchange of a neutrino ν_e and the annihilation of the initial electron-positron pair to a Z/γ^* boson with a subsequent decay to two W bosons in the s-channel. Measurements of $e^+e^- \to W^+W^-$ were performed using both hadronic and leptonic decays of the W bosons. The combination of results from the four LEP experiments from $\sim$ 10,000 W^+W^- candidate

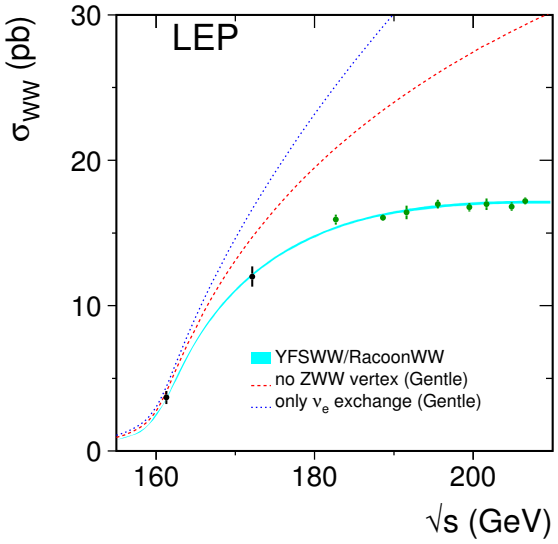

Figure 5.6: Measurement of the W boson pair production cross section in e^+e^- collisions at LEP II. The damping of the cross section as a function of the centre-of-mass energy, $\sqrt{s}$, is a consequence of the non-Abelian structure of the electroweak theory. The dashed lines show the theoretical calculation in the absence of γWW and ZWW vertices, thus only the t-channel production (blue), and in absence of only the ZWW vertex (red). Taken from Ref. [123].

events collected by each experiment is described in Ref. [123] and results in cross sections determined with a precision of typically ±(1-2)%. The measured cross sections are shown as a function of the centre-of-mass energy, $\sqrt{s}$, in Fig. 5.6. The measured cross sections are compared to theoretical calculations in the absence of the γWW and ZWW vertices, in absence of only the ZWW vertex, and including all diagrams predicted by the Standard Model. The measurements clearly favour the scenario predicted by the Standard Model. The damping of the cross section as a function of $\sqrt{s}$ represents the first clear proof of electroweak gauge boson self interaction, i.e. the non-Abelian structure of the electroweak interaction.

The coupling parameters of the effective electroweak Lagrangian were determined to be $g_1^Z = 0.984^{+0.018}_{-0.020}$, $\kappa_\gamma = 0.982^{+0.042}_{-0.042}$ and $\lambda_\gamma = -0.022^{+0.019}_{-0.019}$ [123] using the constraints in Eqs. 5.14 and 5.15 and were found to be in agreement with the values of the Standard Model. For the determination of a single parameter, the other two parameters were set to their Standard Model values. The measurement of the coupling parameters can be translated to limits on anomalous triple gauge couplings of $-0.054 < \Delta g_1^Z < 0.021$, $-0.099 < \Delta\kappa_\gamma < 0.066$ and $-0.059 < \lambda_\gamma < 0.017$ at 95% confidence level.

5.4.2 Tevatron

The first measurements of W boson pair production at hadron-collider experiments were performed by the CDF [124] and D0 experiments [125] in $p\bar{p}$ collisions at $\sqrt{s} = 1.96$ TeV at the Tevatron [126]. Only final states with at least one of the W bosons decaying to an electron or muon were used for the measurement. The most precise results were obtained in the fully leptonic decay modes, i.e. both W bosons decay leptonically into an electron or muon. The W^+W^- cross sections measured by the D0 and CDF experiments were, respectively:

$$\sigma^{\text{tot}}(p\overline{p} \to WW) = 11.5 \pm 2.1\,(\text{stat.+syst.}) \pm 0.7\,(\text{lumi.})\ \text{pb} \qquad [127] \qquad (5.17)$$

$$\sigma^{\text{tot}}(p\overline{p} \to WW) = 12.1 \pm 0.9\,(\text{stat.})^{+1.6}_{-1.4}\,(\text{syst.})\ \text{pb} \qquad [128] \qquad (5.18)$$

obtained in 3.6 fb^{-1} and 1.1 fb^{-1} of data, respectively. The results are in agreement with the theoretical calculation at NLO of $\sigma^{\text{tot}}(p\overline{p} \to WW) = 12.0 \pm 0.7$ pb [129]. Both analyses use different selection criteria to suppress background from top-quark pair production. Whereas a selection on the vectorial sum of lepton transverse momenta and missing transverse momentum is used in Ref. [127], the fiducial phase space requires the absence of any hadronic jet with $E_{\text{T}} > 15$ GeV and $|\eta| < 2.5$, reconstructed in a cone of $\Delta R = 0.4$, in Ref. [128]. The measurement of the total cross section is therefore sensitive to effects discussed in Section 5.2.2.

More recently the W^+W^- cross section was updated by the CDF and D0 collaborations using a larger dataset corresponding to an integrated luminosity of 9.7 fb^{-1} and the selection criteria were reconsidered. The results are:

$$\sigma^{\text{tot}}(p\overline{p} \to WW) = 11.6 \pm 0.4\,(\text{stat.}) \pm 0.6\,(\text{syst.})\ \text{pb} \qquad [130] \qquad (5.19)$$

$$\sigma^{\text{tot}}(p\overline{p} \to WW) = 14.0 \pm 0.6\,(\text{stat.})^{+1.2}_{-1.0}\,(\text{syst.}) \pm 0.8\,(\text{lumi.})\ \text{pb} \qquad [131] \qquad (5.20)$$

The analysis presented in Ref. [130] is performed with a requirement on the number of reconstructed hadronic jets $n_{\text{jets}} \leq 1$ where a jet is defined by $p_{\text{T}} > 20$ GeV and $|\eta| < 2.4$, reconstructed in a cone of $\Delta R = 0.5$. The measurement presented in Ref. [131] is performed differentially in bins of the number of reconstructed jets, where a jet is defined by $p_{\text{T}} > 15$ GeV and $|\eta| < 2.5$, reconstructed in a cone of $\Delta R = 0.4$. Within the uncertainties of ±20% and ±35% the jet-binned cross sections of 1-jet and ≥2-jet are found to be in agreement with fixed-order calculations and calculations using a parton shower.

Limits on anomalous trilinear gauge couplings were obtained from fully leptonic and semi leptonic final states based on 8.6 fb^{-1} of data in Ref. [132] and set to be $-0.034 < \Delta g_1^Z < 0.084$, $-0.158 < \Delta\kappa_\gamma < 0.255$ and $-0.036 < \lambda_\gamma < 0.044$ at 95% confidence level using a form factor of $\Lambda = 2$ TeV and the constraints in Eqs. 5.14 and 5.15. The corresponding limits from Ref. [128] from fully leptonic final states based on 3.6 fb^{-1} of data are $-0.22 < \Delta g_1^Z < 0.30$, $-0.57 < \Delta\kappa_\gamma < 0.65$ and $-0.14 < \lambda_\gamma < 0.15$.

The measurements are summarised in Figs. 5.7 and 5.8 where they are compared to measurements at the LHC.

5.4.3 LHC

Measurements of the W^+W^- cross section in pp collisions were performed at a centre-of-mass energy of $\sqrt{s} = 7$ TeV by the ATLAS and CMS collaborations at the LHC. The resulting total cross section measured based on 4.6 fb^{-1} and 4.9 fb^{-1} of data are, respectively:

$$\sigma^{\text{tot}}(pp \to WW) = 51.9 \pm 2.0\,(\text{stat.}) \pm 3.9\,(\text{syst.}) \pm 2.0\,(\text{lumi.})\ \text{pb} \qquad [133] \qquad (5.21)$$

$$\sigma^{\text{tot}}(pp \to WW) = 52.4 \pm 2.0\,(\text{stat.}) \pm 4.5\,(\text{syst.}) \pm 1.2\,(\text{lumi.})\ \text{pb} \qquad [134]. \qquad (5.22)$$

The measured cross section are consistently higher, yet compatible, with the theoretical calculation at NLO of $\sigma^{\text{tot}}(pp \to WW) = 44.7^{+2.1}_{-1.9}$ pb. Events were required to be free of hadronic jets, reconstructed with $E_{\text{T}} > 30$ GeV and $|\eta| < 5.0$ in a cone of $\Delta R = 0.5$ [134] or $p_{\text{T}} > 25$ GeV and $|\eta| < 4.5$ in a cone of $\Delta R = 0.4$ [133]. The measurement by the ATLAS collaboration also included the differential cross section as a function of the transverse momentum of the leading lepton. Limits on anomalous triple gauge couplings of $-0.036 < \Delta g_1^Z < 0.066$ and $-0.045 < \Delta\kappa_Z < 0.044$ and $-0.062 < \lambda_\gamma < 0.065$ at 95% C.L. were obtained using a form factor of $\Lambda = 6$ TeV. The corresponding limits from Ref. [134] are $-0.095 < \Delta g_1^Z < 0.095$, $-0.21 < \Delta\kappa_Z < 0.22$ and $-0.048 < \lambda_\gamma < 0.048$.

A measurement of the W^+W^- cross section in pp collisions at a centre-of-mass energy of $\sqrt{s} = 8$ TeV was also performed by the CMS collaboration on a partial dataset of 5.3 fb^{-1}, leading to:

$$\sigma^{\text{tot}}(pp \to WW) = 69.9 \pm 2.8\,(\text{stat.}) \pm 5.6\,(\text{syst.}) \pm 3.1\,(\text{lumi.})\ \text{pb}\ [135]. \qquad (5.23)$$

The measurements discussed above were conducted without considering the resonant $gg \to H \to WW$ production. Contributions of typically 3% are expected [133] but were neither subtracted nor treated in the extrapolation from the fiducial to the total phase space. The measured cross sections are therefore systematically higher than those predicted in the theoretical calculations.

Very recently the measurement was updated based on 19.4 fb^{-1} of data [136]. The measurement was extended to include events containing up to one hadronic jet. Resummation effects were taken into account in the extrapolation from the fiducial to the total cross section by reweighing the p_{T}^{WW} distribution to the calculation in Ref. [111]. This results in a measured cross section of:

$$\sigma^{\text{tot}}(pp \to WW) = 60.1 \pm 0.9\,(\text{stat.}) \pm 3.2\,(\text{syst.}) \pm 3.1\,(\text{theo.}) \pm 1.6\,(\text{lumi.})\ \text{pb}\ [136] \qquad (5.24)$$

Contributions from non-resonant $gg \to H \to WW$ were accounted for by subtracting the contributions expected from event simulation. In addition, differential cross sections were measured in $e\mu$ + 0-jet final states for the transverse momentum of the leading lepton, the transverse momentum of the dilepton system, the invariant mass of the dilepton system, and the angular separation in the transverse plane between both leptons. Limits on anomalous triple gauge couplings were set in a different parameter basis than that introduced in Section 5.3. Following Ref. [118] the limits translate to $-0.015 < g_1^Z < 0.032$,

$-0.022 < \kappa_Z < 0.027$ and $-0.024 < \lambda_\gamma < 0.024$.

The results of the measurements at the LHC are summarised in Figs. 5.7 and 5.8. The results are compared to measurements at the Tevatron. The recent measurement by the CMS collaboration as well as the measurement presented in this thesis are not shown.

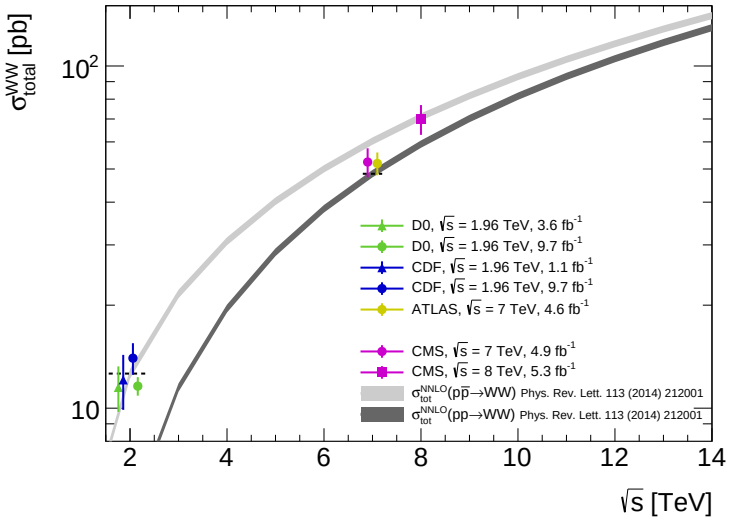

Figure 5.7: Comparison of previous measurements of the total W^+W^- production cross sections at the Tevatron and the LHC. The results of the measurements presented in this thesis and the comparable measurements by the CMS collaboration discussed in the text are not shown. The measurements are compared to the theoretical cross sections at NNLO where a dashed line indicates the theoretical prediction when markers are shifted for better readability. Contributions from non-resonant $gg \rightarrow H \rightarrow W^+W^-$ production are not included.

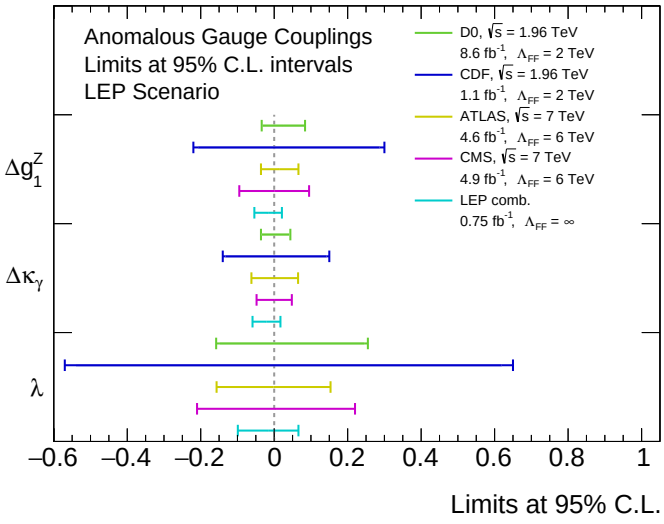

Figure 5.8: Limits on anomalous triple gauge couplings obtained at LEP, the Tevatron and the LHC. Only limits derived from W^+W^- production are shown.

6 Event Selection and Background Determination

For the measurement of W^+W^- production, candidate events are selected from the data recorded by the ATLAS experiment where both W bosons decay leptonically to $W \to \ell\nu$, $\ell = e, \mu$. The fully leptonic final state gives the cleanest signature at hadron-collider experiments. In the following, the data sample as well as simulated event samples of signal and processes constituting a background to this signature are described. The simulated event samples are used to derive requirements on particle and event properties that are used to select a clean sample of W^+W^- candidate events in data. They are also used in the estimation of contributions from background processes which is also discussed.

6.1 Introduction

The analysis presented here aims at performing measurements of W boson pair production in fully leptonic W boson decays, i.e. both W bosons decay to either an electron or a muon and the corresponding neutrino, $W \to \ell\nu$, $\ell = e, \mu$. The experimental signature of W boson pair production thus is the presence of two isolated leptons with opposite electric charge and missing transverse momentum, $p_{\mathrm{T}}^{\mathrm{miss}}$, from the neutrinos that leave the detector without interacting. The data sample is separated into the possible final states $e\mu$, ee and $\mu\mu$. Criteria for the selection of W^+W^- candidate events are chosen for each of the three final states individually.

The distribution of the invariant mass of the dilepton system is shown for events selected with exactly two isolated leptons with opposite electric charge in Fig. 6.1 for the sum of ee and $\mu\mu$ final states, and for $e\mu$ final states. The data sample is dominated by contributions from background processes, namely background from $Z \to \ell\ell$, top quark, W+jets and diboson production.

The dominant production mechanism for dilepton final states in pp collisions is the Drell-Yan process, $q\bar{q} \to Z/\gamma^* \to \ell\ell$. The cross section of Drell-Yan production is more than three orders of magnitude larger than that of W^+W^- production. Due to lepton flavour conservation, the Drell-Yan process only produces pairs of leptons of the same generation, i.e. ee, $\mu\mu$ or $\tau\tau$ final states. Drell-Yan production therefore represents a large background to ee and $\mu\mu$ final states. Contributions to $e\mu$ final states can only occur via non-prompt τ lepton decays, $\tau \to \ell\nu_\ell\nu_\tau$. Consequently, the contribution from Drell-Yan production in ee or $\mu\mu$, and $e\mu$ final states differs in absolute size and depending on the final states involved. Decays with prompt electrons or muons can be fully reconstructed. Their invariant mass corresponds to the mass of the Z boson with $m_Z = 91.1876 \pm 0.0021$ GeV [25]. These contributions can effectively be rejected by requiring missing transverse momentum $p_{\mathrm{T}}^{\mathrm{miss}}$ in the event. The decay to $e\mu$ final states also contains neutrinos and therefore features genuine missing transverse momentum although in smaller magnitude as the W^+W^- signal.

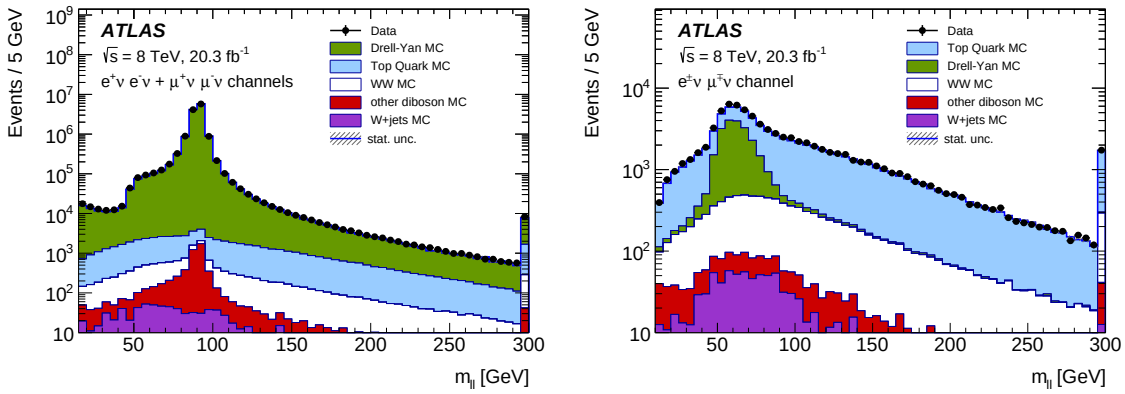

Figure 6.1: Distributions of the invariant mass of the dilepton system, $m_{\ell\ell}$, for the sum of ee and $\mu\mu$ (left), and for $e\mu$ final states (right). Shown are the events selected in data together with the expected contributions from W^+W^- and background production as estimated from simulated event samples. Only statistical uncertainties are shown. Previously published in Ref. [5].

Background from top-quark production mainly originates from top quark pair production, $t\bar{t}$, where each top quark decays into a W boson and a down-type quark. The probability for a top quark to decay into quarks of a certain flavour q is proportional to the square of the corresponding CKM matrix element $\mathcal{B}(t \to Wq) \sim \left|V_{tq}\right|^2$. This causes top quarks to decay almost exclusively to a W boson and a b-quark, $\mathcal{B}(t \to Wb)/\mathcal{B}(t \to Wq) = 0.99830^{+0.00006}_{-0.00009}$ [137]. Since the decay involves two genuine, on-shell W bosons, the experimental signature of top quark pair production only differs from W^+W^- production by additional hadronic jets from the b-quarks produced in the top-quark decay. A production mechanism with a cross section of similar size as top quark pair production is the t-channel production of a single top quark. Contributions to W^+W^- events are highly suppressed since the experimental signature consists of only a single isolated lepton in the final state. Background from top-quark production can be largely reduced by requiring the absence of hadronic jets in the event or by rejecting events with jets identified as originating from b-quarks.

Multiboson production, in particular the production of a pair of Z bosons and the production of a W boson in association with an off-shell Z/γ^* or a on-shell Z boson, constitutes a background process if the W and Z bosons decay leptonically. The process $ZZ \to \ell\ell\nu\nu$ results in the same particles in the final states as W^+W^- production.

The above processes mostly contain two genuine leptons. Another class of backgrounds contain so-called misidentified leptons, i.e. hadronic jets or converted photons that are falsely identified as leptons. The probability of a hadronic jet to be misidentified as a lepton is small. However, the processes contributing have production cross-sections much larger than that of $pp \to W^+W^-$ production. In the context of dilepton measurements, W+jets and multijet production where one or both of the selected leptons are misidentified give sizeable contributions. These contributions can be rejected by imposing strict identification criteria on the leptons and additional requirements on the calorimeter and track isolation. Additional requirements on the transverse and longitudinal impact parameters help rejecting contributions from non-isolated electrons produced in the decay of jets containing b-

or c-quarks. Background from the production of a W boson in association with a photon, $W\gamma$, contributes if the photon is misidentified as an electron.

The rejection of background processes drives the choice of kinematic constraints used to select a clean sample of W^+W^- events. The cross sections times branching fractions of the various background processes are listed in Table 6.1.

6.2 Event Samples from Data and Simulation

The data sample recorded by the ATLAS detector between April and December 2012 at a centre-of-mass energy of $\sqrt{s} = 8$ TeV is used for the analysis. Only data recorded with stable proton–proton collisions in which all detector components are operating under nominal conditions are considered. The analysed data correspond to an integrated luminosity of $\mathcal{L} = 20.3$ fb^{-1}.

Events from $q\bar{q} \to W^+W^-$ production are simulated with the PowHeg [79–82] event generator using Pythia8 [83] for the simulation of the underlying event and hadronisation processes. For the simulation of $gg \to W^+W^-$ events, the gg2ww [109] event generator is used and interfaced to Herwig+Jimmy [138, 139]. Resonant $gg \to H \to W^+W^-$ production is simulated with PowHeg+Pythia8 with the Higgs boson mass set to $m_H = 125$ GeV. The three samples use the CT10 [140] parton-distribution-function. The simulated signal samples are normalised to a cross section times branching fraction of 5.58 pb for $q\bar{q} \to W^+W^-$ [99], to 0.153 pb for non-resonant $gg \to H \to W^+W^-$ [103] and 0.435 pb for $gg \to W^+W^-$ [99]. The sum of these contributions correspond to a total W^+W^- cross-section of $58.7^{+4.2}_{-3.8}$ pb.

For the simulation of the production of top quarks, two sets of event generators are used for the results presented in Chapter 10 and 11, respectively. The first set relies on the Mc@Nlo [141] generator for the calculation of the hard interaction and Jimmy for the parton-shower and the underlying event model in the simulation of $t\bar{t}$ production, single top production in the s-channel, and the associated production of a W boson with a top quark. The second set employs PowHeg+Pythia8 in the simulation of these processes. In both sets the AcerMC [142] generator is used in the calculation of single top production in the t-channel, together with Pythia6 [143] for the parton shower model. The parton-distribution-functions are taken from CT10 for the Mc@Nlo and PowHeg samples and from CTEQ6L1 [144] for the AcerMC sample.

Events from Z/γ^* and W+jets production are modelled with Alpgen [145]. The generator is interfaced to Pythia6 for the simulation of W+jets and $Z/\gamma^* \to \ell\ell$ events with $m_{\ell\ell} > 60$ GeV, and to Herwig+Jimmy for the simulation of $Z/\gamma^* \to \ell\ell$ events with $m_{\ell\ell} < 60$ GeV. These simulated event samples are produced with the CTEQ6L1 parton-distribution-functions, but for $Z/\gamma^* \to \ell\ell$ production they are reweighted to the CT10 PDF.

The production of two gauge bosons WZ and ZZ is simulated with the PowHeg+Pythia8 generator, the simulation of $W\gamma^*$ production is using the Sherpa [146] generator. Overlap between WZ and $W\gamma^*$ is removed on generator level by requiring the invariant mass of the Z/γ^* decay products to be above or below $m_{\ell\ell} = 7$ GeV. The events are simulated using the CT10 PDF. A sample of $W\gamma$ events is simulated using Alpgen+Herwig with the CTEQ6L1 PDF.

Process		Generator	$\sigma \cdot \mathcal{B}$	Calculation
$WW \to \ell\nu\ell\nu$				
$q\bar{q} \to W^+W^-$		PowHeg+Pythia8	5.58	NLO [99]
$gg \to W^+W^-$		gg2ww+Herwig	0.153	LO [109]
$gg \to H \to W^+W^-$		PowHeg+Pythia8	0.435	NNLO [103]
Top quark (0-jet category)				
$t\bar{t}$		Mc@Nlo+Herwig	26.6	NNLO+NNLL [147]
Wt		Mc@Nlo+Herwig	2.35	NNLO+NNLL [148]
Single top t-channel		AcerMC+Pythia6	28.4	NNLO+NNLL [149]
Single top s-channel		Mc@Nlo+Herwig	1.82	NNLO+NNLL [150]
Top quark (1-jet category)				
$t\bar{t}$		PowHeg+Pythia8	26.6	NNLO+NNLL [147]
Wt		PowHeg+Pythia8	2.35	NNLO+NNLL [148]
Single top t-channel		AcerMC+Pythia6	28.4	NNLO+NNLL [149]
Single top s-channel		PowHeg+Pythia8	1.82	NNLO+NNLL [150]
$Z \to \ell\ell$				
$Z \to ee/\mu\mu$	($m_{\ell\ell} > 60$ GeV)	Alpgen+Pythia6	16500	NNLO [151]
$Z \to \tau\tau$	($m_{\ell\ell} > 60$ GeV)	Alpgen+Pythia6		
$Z \to \ell\ell$	(10 GeV $< m_{\ell\ell} <$ 60 GeV)	Alpgen+Herwig		
Other diboson				
$W\gamma$	($p_{\mathrm{T}}^{\gamma} > 8$ GeV)	Alpgen+Herwig	369.0	NLO [99]
$WZ(/\gamma^*)$	($m_{\ell\ell} > 7$ GeV)	PowHeg+Pythia8	12.7	NLO [99]
$WZ(/\gamma^*)$	($m_{\ell\ell} < 7$ GeV)	Sherpa	12.9	NLO [99]
$ZZ \to 4\ell$	($m_{\ell\ell} > 4$ GeV)	PowHeg+Pythia8	0.733	NLO [99]
$ZZ \to \ell\ell\nu\nu$	($m_{\ell\ell} > 4$ GeV)	PowHeg+Pythia8	0.504	NLO [99]

Table 6.1: Simulated event samples of various signal and background processes. Information on the event generator and parton-shower model used to simulate the process, the theoretical cross section times branching fraction, $\sigma \cdot \mathcal{B}$ at $\sqrt{s} = 8$ TeV, to which samples are normalised and the corresponding perturbative order are quoted. The branching fraction $\mathcal{B}$ includes the decays $t \to Wq$, $W \to \ell\nu$, and $Z \to \ell\ell$. The decay of one Z boson to neutrinos is considered for the process $ZZ \to \ell\ell\nu\nu$. Two sets of simulated samples for top quark production are shown, used in different parts of the analysis.

A summary of the event generators used for simulation of signal and background production is given in Table 6.1 together with the cross section times branching fraction from theoretical calculations that are used to normalise the event samples. Minimum bias events generated with Pythia8 are overlaid in all samples to model additional pp collisions (pile-up). The simulated events are processed through the ATLAS detector simulation [84]. The simulation of the PowHeg+Pythia8 event samples of $t\bar{t}$ production is based on Geant4 [85] combined with a parametrised Geant4-based calorimeter simulation [152]. The simulation of the remaining event samples is based on Geant4. The radiation of photons is modelled by Photos [86].

6.3 Selection of W^+W^- Candidate Events

The criteria imposed on the data in order to select a clean sample of W^+W^- candidate events are described in the following. Since the decay products of top quark production are two W bosons accompanied by hadronic jets, the dataset is categorised into jet multiplicities of 0-jet and 1-jet and analysed separately.

6.3.1 Pre-Selection

Events are required to have a reconstructed primary vertex with at least three tracks with a transverse momentum of $p_{\mathrm{T}} \geq 400$ MeV. If several primary vertices are found, the one with the largest value of $\sum (p_{\mathrm{T}})^2$ is chosen, where the transverse momenta of all tracks associated with the vertex are considered. Only events containing exactly two leptons with opposite electric charge are selected. These are required to have triggered the readout of the event. For $e\mu$ final states this can be either the single-lepton or dilepton trigger algorithms described in Sections 3.2.4 and 3.3.3. The trigger algorithms require transverse momenta of $p_{\mathrm{T}} > 24$ GeV for a single electron *or* single muon together with requirements on identification criteria and their track isolation, or transverse momenta of $p_{\mathrm{T}} > 12$ GeV *and* $p_{\mathrm{T}} > 8$ GeV for the electron and muon, respectively, with less strict requirements on identification criteria. The selection of ee and $\mu\mu$ final states always relies on both leptons, where transverse momenta of $p_{\mathrm{T}} > 12$ GeV are required for electrons, and $p_{\mathrm{T}} > 18$ GeV and $p_{\mathrm{T}} > 8$ GeV for the leading and sub-leading muon. The chosen trigger scheme has an efficiency of $99 - 100\%$ to select W^+W^- signal events with respect to the offline lepton selection criteria outlined below.

6.3.2 Particle Selection

The selection of electrons and muons is crucial for the rejection of background from misidentified leptons from W+jets and multijet processes. In a first step events are selected if at least two leptons with a transverse momentum exceeding $p_{\mathrm{T}} > 7$ GeV are present.

Only electrons reconstructed in the central region of the detector $|\eta| < 2.47$, excluding the calorimeter transition region $1.37 < |\eta| < 1.52$, are used in the analysis. They are required to meet the very tight LH identification criterion. Additional criteria are placed on the associated track, for which the transverse impact parameter divided by its significance

is required to satisfy $|d_0|/\sigma_{d_0} < 3.0$, and the longitudinal impact parameter is required to satisfy $|z_0 \sin\theta| < 0.4$ mm. Electrons are further required to be isolated by placing a selection on the ratio of the calorimeter or track-based measurement of the isolation and the transverse momentum of the lepton. The isolation is calculated in a cone of $\Delta R = 0.3$ in the calorimeter, and of $\Delta R = 0.4$ or $\Delta R = 0.3$ in the inner detector for electrons with $p_{\mathrm{T}} < 15$ GeV and $p_{\mathrm{T}} > 15$ GeV, respectively. The ratio of isolation and transverse momentum is required to be less than 0.20, 0.24 or 0.28 in the calorimeter, and 0.06, 0.08 or 0.10 in the inner detector, for electrons with transverse momenta of $p_{\mathrm{T}} < 15$ GeV, 15 GeV $< p_{\mathrm{T}} < 20$ GeV and $p_{\mathrm{T}} > 20$ GeV, respectively.

Muons are required to satisfy $|\eta| < 2.4$. As for electrons, additional impact parameter and isolation requirements are applied but at different values. Muon tracks are required to satisfy $|d_0|/\sigma_{d_0} < 3.0$ and $|z_0 \sin\theta| < 1.0$ mm. The ratio of isolation and transverse momentum are required to be less than 0.06, 0.12 or 0.18 in the calorimeter, and 0.06, 0.08 or 0.12 in the inner detector, using the same cone sizes and transverse momentum boundaries as for electrons.

The selection criteria on isolation and associated tracks are taken from Ref. [153]. Events containing more than two leptons that fulfil the identification criteria are rejected. This way the selection on leptons also affects the contribution from processes with genuine leptons, i.e. multilepton processes that produce more than two leptons such as WZ or ZZ production. For the selection of W^+W^- candidate events the two selected leptons are further required to have a transverse momentum of $p_{\mathrm{T}} > 25$ GeV and $p_{\mathrm{T}} > 20$ GeV for the leading and trailing lepton, respectively.

The selection criteria placed on jets are crucial to differentiate events from W^+W^- and top-quark production. Jets are selected if their transverse momentum exceeds $p_{\mathrm{T}} > 25$ GeV and if their pseudorapidity is $|\eta| < 4.5$. To suppress contributions from additional pp interactions in the event, more than 50% of the scalar sum of the transverse momenta of all tracks contained within $\Delta R = 0.4$ of the jet axis are required to be from tracks associated to the primary vertex (JVF) if the jet satisfies $p_{\mathrm{T}} < 50$ GeV and $|\eta| < 2.4$ [72].

To remove ambiguities where a single particle is reconstructed by several particle reconstruction algorithms, a so-called overlap removal procedure is applied. Jets found within a cone of $\Delta R = 0.3$ of an electron are removed, electrons are removed if found within $\Delta R = 0.3$ of a muon, and muons are removed if found within $\Delta R = 0.3$ of a jet.

6.3.3 Kinematic Selection in 0-jet Final States

Roughly $1.3 \cdot 10^7$ events are selected in data by requiring the presence of two isolated leptons with transverse momenta of $p_{\mathrm{T}} > 25/20$ GeV and by imposing the criteria described throughout Sections 6.3.1 and 6.3.2. The majority of these events consist of events from $Z/\gamma^* \to \ell\ell$ production as is shown in Fig. 6.1. The amount of background highly depends on the flavour of the final state leptons. The dataset is categorised into $e\mu$ and $ee + \mu\mu$ final states to find criteria on the kinematic properties of the decay products for an efficient selection of W^+W^- events and a high rejection of background contributions.

In the absence of hadronic jets in the final state the main concern of these selection criteria is the rejection of background from $Z/\gamma^* \to \ell\ell$ production. Criteria for the selection of

W^+W^- candidate events are chosen by finding the optimal combination of selection criteria on a set of variables, determined as the combination that yields a maximum significance $Z = s\Big/\sqrt{s+b+\sigma_b^2}$. Here, s is the number of expected signal events, b is the number of expected background events, σ_b corresponds to the assumed uncertainties in the determination of background contributions. The optimisation is performed separately for $e\mu$+0-jet, and the sum of ee and $\mu\mu$+0-jet final states. The uncertainties on the estimation of background contributions are assumed to be ±30% for background from W+jets production, ±10% and ±30% for background from $Z \to \ell\ell$ production in $e\mu$ and $ee + \mu\mu$ final states, respectively, ±20% for background from diboson production and ±10% for background from top quark production.

In the optimisation a set of kinematic variables that can discriminate between signal and background processes are considered. The invariant mass of the dilepton system is optimised to reject contributions from low-mass resonances like $J/\psi \to \ell\ell$ or $\Upsilon \to \ell\ell$. Moreover, contributions from resonant $Z \to \ell\ell$ production to $ee + \mu\mu$ final states can be efficiently removed by rejecting events with an invariant mass close to the nominal Z boson mass, $|m_{\ell\ell} - m_Z|$. Criteria on several alternative calculations of the missing transverse momentum, $p_{\mathrm{T}}^{\mathrm{miss}}$, have been studied as well as combinations of these variables. The optimal choice is found to be a combination of missing transverse momentum variables, with the cell-out term calculated from energy depositions in the calorimeter and calculated purely from tracks reconstructed in the inner detector, referred to as $E_{\mathrm{T}}^{\mathrm{miss}}$ and $p_{\mathrm{T}}^{\mathrm{miss}}$ in the following. The reconstruction of both variables is described in Section 3.7. To reduce the sensitivity of the reconstruction to fluctuations in the measurement of the energy of electrons and muons, the relative missing transverse momentum, $E_{\mathrm{T,\,Rel}}^{\mathrm{miss}}$, is used which is defined as the projection of the $E_{\mathrm{T}}^{\mathrm{miss}}$ 2-vector on leptons:

$$E_{\mathrm{T,\,Rel}}^{\mathrm{miss}} = \begin{cases} E_{\mathrm{T}}^{\mathrm{miss}} \cdot \sin\Delta\phi_\ell & \text{if } \Delta\phi_\ell < \pi/2 \\ E_{\mathrm{T}}^{\mathrm{miss}} \cdot \sin\Delta\phi_\ell & \text{otherwise} \end{cases} . \tag{6.1}$$

where $\Delta\phi_\ell$ is the separation of $E_{\mathrm{T}}^{\mathrm{miss}}$ and the closest lepton in the transverse plane. The two alternative measures of the missing transverse momentum, $E_{\mathrm{T,\,Rel}}^{\mathrm{miss}}$ and $p_{\mathrm{T}}^{\mathrm{miss}}$, are shown in Fig. 6.2 in a kinematic region defined by restricting the invariant mass of the dilepton system to lie within 15 GeV of the nominal Z boson mass. Good agreement between data and the simulated event samples is seen within the uncertainties assigned. A further selection criterion considered in the optimisation of kinematic selection criteria is the azimuthal separation between the calorimeter and track-based measurements of the missing transverse momentum, $\Delta\phi(E_{\mathrm{T}}^{\mathrm{miss}}, p_{\mathrm{T}}^{\mathrm{miss}})$. Since both variables use completely independent detector systems for the calculation of the cell-out term this variable is sensitive to experimental effects in the measurement of the cell-out term.

The significance Z defined above is calculated for all possible combinations of constraints on these variables, where steps of 5 GeV are used for $m_{\ell\ell}$, $|m_{\ell\ell} - m_Z|$, $E_{\mathrm{T,\,Rel}}^{\mathrm{miss}}$ and $p_{\mathrm{T}}^{\mathrm{miss}}$. For $\Delta\phi(E_{\mathrm{T}}^{\mathrm{miss}}, p_{\mathrm{T}}^{\mathrm{miss}})$ steps of 0.3 are chosen. The procedure is illustrated in Fig. 6.3 where the significance is shown as a function of lower bounds on the variables $E_{\mathrm{T,\,Rel}}^{\mathrm{miss}}$ and $p_{\mathrm{T}}^{\mathrm{miss}}$ with all other criteria applied as resulting from the optimisation. The combination of the two

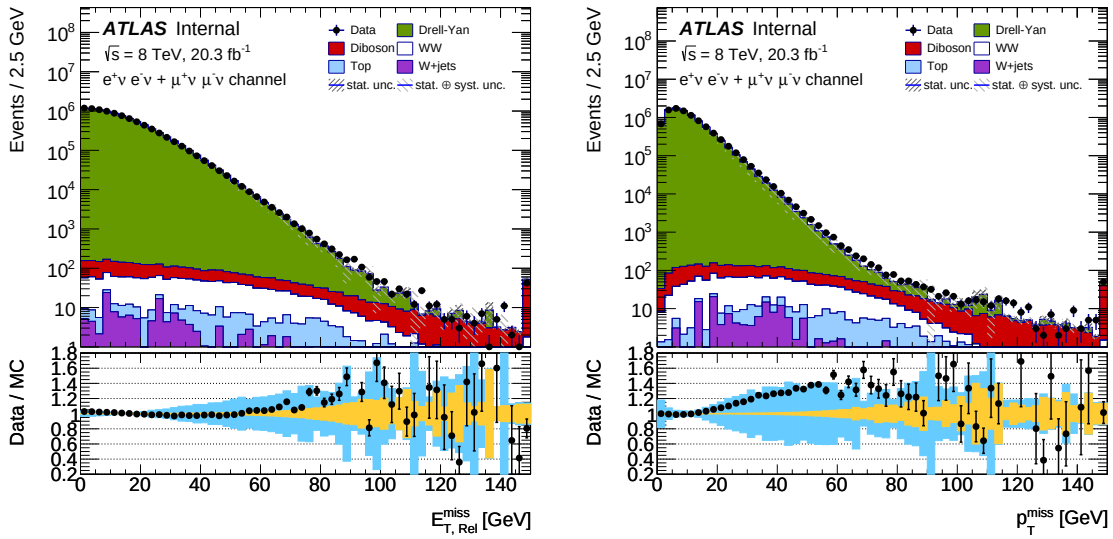

Figure 6.2: Distributions of the relative missing transverse momentum, $E_{\mathrm{T,\,Rel}}^{\mathrm{miss}}$ (left), and the track-based measurement of the missing transverse momentum, $p_{\mathrm{T}}^{\mathrm{miss}}$ (right), in the kinematic region of the Z boson resonance, $\left|m_{\ell\ell} - m_Z\right| < 15$ GeV. The distributions are shown for the sum of ee and $\mu\mu$+0-jet final states. Data are shown together with contributions from W^+W^- and background production as estimated from simulated event samples. Statistical uncertainties are shown separately from uncertainties on the scale and resolution of the $E_{\mathrm{T}}^{\mathrm{miss}}$ and $p_{\mathrm{T}}^{\mathrm{miss}}$ measurements. A good description of the selected data by simulated event samples is seen within the uncertainties assigned.

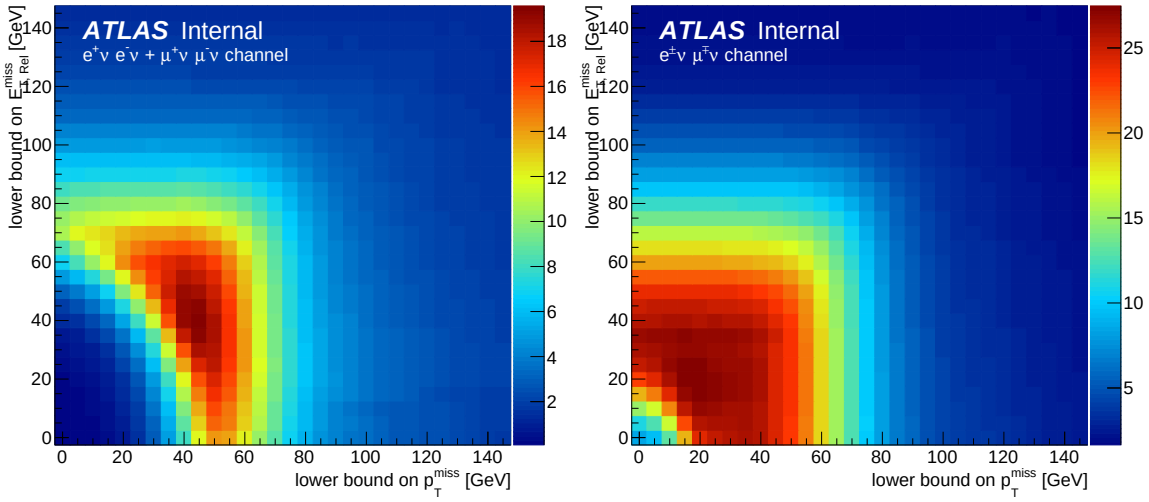

Figure 6.3: Distributions of the significance $Z = s\Big/\sqrt{s+b+\sigma_b^2}$ as a function of a lower bound on the variables $E_{\mathrm{T,\,Rel}}^{\mathrm{miss}}$ and $p_{\mathrm{T}}^{\mathrm{miss}}$. Assumptions on the uncertainty of the background processes, σ_b, are made as described in the text. The significance is shown for the sum of ee and $\mu\mu$+0-jet final states (left), and for $e\mu$+0-jet final states (right). All selection criteria except for the criteria on the two variables shown are applied.

variables yields a larger significance than using only one of them. Based on such studies selection criteria of $p_{\mathrm{T}}^{\mathrm{miss}} > 20$ GeV, $E_{\mathrm{T,\,Rel}}^{\mathrm{miss}} > 15$ GeV for $e\mu$ final states, and $p_{\mathrm{T}}^{\mathrm{miss}} > 45$ GeV, $E_{\mathrm{T,\,Rel}}^{\mathrm{miss}} > 45$ GeV for ee and $\mu\mu$ final states are chosen. The resulting kinematic selection criteria are summarized in Table 6.2. For $e\mu$ final states, additional selection criteria of $m_{\ell\ell} > 10$ GeV and $\Delta\phi(E_{\mathrm{T}}^{\mathrm{miss}}, p_{\mathrm{T}}^{\mathrm{miss}}) < 0.6$ are imposed. For ee and $\mu\mu$ final states those selection criteria are chosen to be $m_{\ell\ell} > 15$ GeV, $\left|m_{\ell\ell} - m_Z\right| > 15$ GeV and $\Delta\phi(E_{\mathrm{T}}^{\mathrm{miss}}, p_{\mathrm{T}}^{\mathrm{miss}}) < 0.3$. The event yields expected from simulated event samples are shown in Table 6.3. A high rejection of events from $Z \to \ell\ell$ production is reached. In ee and $\mu\mu$ final states the expected contributions from $Z \to \ell\ell$ production are reduced by a factor of $\sim 5 \cdot 10^4$ to $\sim 4\%$ of the sum of expected signal and background contributions. For $e\mu$ final states a rejection of only ~ 120 is needed to bring down the expected contributions from $Z \to \ell\ell$ production to $\sim 3\%$ of the expected event yields. The largest expected contribution to the selected data is from W^+W^- production, followed by background from top quark production. The jet multiplicity distribution is shown in Fig. 6.4 with the requirement on the number of reconstructed jets removed. The efficiency of the 0-jet requirement is $\sim 70\%$ for events from W^+W^- production and $3 - 4\%$ for events from top quark production. The distribution of the reconstructed jets allows to efficiently separate signal and background from top-quark production. Rejecting events with hadronic jets in the event yields an event sample of high purity. Rejecting the contributions from top-quark production in $e\mu$+1-jet final states is discussed in Section 6.3.4.

Events with higher jet multiplicity are not considered for analysis. The number of ex-

	$e\mu$+0-jet	ee and $\mu\mu$+0-jet	$e\mu$+1-jet
p_{T}^{ℓ} (leading and sub-leading)	$> 25/20$ GeV		
η^{ℓ}	$\lvert\eta^{\mu}\rvert < 2.4$ and $\lvert\eta^{e}\rvert < 2.47$, excluding $1.37 < \lvert\eta^{e}\rvert < 1.52$		
$m_{\ell\ell}$	> 10 GeV	> 15 GeV	> 10 GeV
$\lvert m_Z - m_{\ell\ell}\rvert$	—	> 15 GeV	—
number of jets with $p_{\mathrm{T}} > 25$ GeV, $\lvert\eta\rvert < 4.5$	0	0	1
$p_{\mathrm{T}}^{\mathrm{miss}}$	> 20 GeV	> 45 GeV	> 20 GeV
$E_{\mathrm{T,\,Rel}}^{\mathrm{miss}}$	> 15 GeV	> 45 GeV	> 15 GeV
$\Delta\phi(E_{\mathrm{T}}^{\mathrm{miss}}, p_{\mathrm{T}}^{\mathrm{miss}})$	< 0.6	< 0.3	< 2.0

Table 6.2: Kinematic constraints used to select the sample of W^+W^- candidate events for $e\mu$, and ee and $\mu\mu$ final states. The criteria are optimised separately for $e\mu$+0-jet and the sum of ee and $\mu\mu$+0-jet final states. For $e\mu$+1-jet final states the criteria are adopted from the $e\mu$+0-jet category.

pected signal events selected with two hadronic jets is only 3% of the yields expected from top-quark production. An analysis of the 2-jet category is therefore extremely challenging. The topology of two W bosons with the same electrical charge in association with two hadronic jets is studied in Ref. [154] which enhances the selected events in contributions from vector-boson scattering.

6.3.4 Kinematic Selection in 1-jet Final States

A separate analysis is performed where events are selected with exactly one hadronic jet. The analysis in the 1-jet category is performed in $e\mu$ final states only. As shown in Section 6.3.3 the ee and $\mu\mu$ final states suffer from large backgrounds from $Z/\gamma^* \to \ell\ell$ production. The rejection of these contributions results in a low selection efficiency for events from W^+W^- production.

The composition of the selected $e\mu$+1-jet events is shown in Fig. 6.4. The selected 1-jet data are highly contaminated with background from top-quark production which constitutes roughly 80% of the expected event yield. Since top quarks predominantly decay to a W boson and a b-quark the background from top-quark production can be efficiently removed using the b-jet identification criteria described in Section 3.6. The b-jet identification discriminant for the selected jet is shown in Fig. 6.5a for the events selected in data and expected from W^+W^-, top quark and other background production. No selection on the missing transverse momentum is applied. The b-jet identification criterion with the highest efficiency to identify jets from b-quark decays of typically 85%, $w_{\mathrm{MV1}} < 0.1340$, gives the highest rejection of background from top-quark production. Roughly 75% of the contributions are suppressed while only 10% of the expected W^+W^- yield is rejected. To further reject background from top-quark production, the transverse momentum threshold of the jet selection is lowered. By rejecting events with jets with 20 GeV $< p_{\mathrm{T}} <$ 25 GeV that are identified as b-jets, the background from top-quark production can be suppressed by an

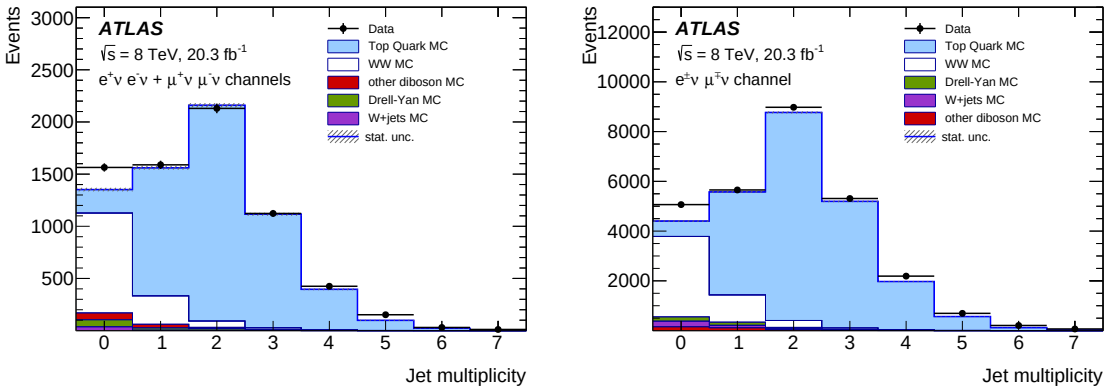

Figure 6.4: Jet multiplicity distributions for the sum of ee and $\mu\mu$ (left), and for $e\mu$ final states (right). Shown are the selected data together with the contributions from W^+W^- and background production estimated from simulated event samples. The yields from W^+W^- production are shown for a total cross section of $58.7^{+4.2}_{-3.8}$ pb. Only statistical uncertainties are shown. Previously published in Ref. [5].

additional 20%, affecting the W^+W^- signal by only 3%, as shown in Fig. 6.5b.

The choice of the remaining selection criteria for the 1-jet category is driven by the desire to combine the results with those obtained in the 0-jet category. The selection criteria should therefore closely match the criteria placed on $e\mu$+0-jet final states. An electron and a muon are selected with opposite electric charge and transverse momenta of $p_{\mathrm{T}} > 25$ GeV and $p_{\mathrm{T}} > 20$ GeV for the leading and sub-leading lepton, respectively. The same selection criteria on the calorimeter and track-based measurement of the missing transverse momentum, $p_{\mathrm{T}}^{\mathrm{miss}}$ and $E_{\mathrm{T}}^{\mathrm{miss}}$, are placed as for $e\mu$+0-jet final states. The selection on the azimuthal separation of the calorimeter and track-based measurements of the missing transverse momentum, $\Delta\phi(E_{\mathrm{T}}^{\mathrm{miss}}, p_{\mathrm{T}}^{\mathrm{miss}})$, loses some of its discriminating power due to the presence of a jet in the event. Calibrated jets are only used in the calorimeter-based measurement. Fluctuations in the jet energy measurement cause the independent measurements to less likely point into the same direction. Thus, a looser selection criterion of $\Delta\phi(E_{\mathrm{T}}^{\mathrm{miss}}, p_{\mathrm{T}}^{\mathrm{miss}}) < 2.0$ is placed for $e\mu$+1-jet final states.

6.3.5 Observed and Expected Signal and Background Yields

The observed events yields at various steps of the selection are shown in Table 6.3 together with the contributions from signal and background processes estimated from simulated event samples with their statistical uncertainties. The simulated event samples are scaled to the cross-sections described in Table 6.1. A total of 5067 events are selected in data in $e\mu$+0-jet final states. This is compared to 594 and 975 events selected in ee+0-jet and $\mu\mu$+0-jet final states, respectively. The $e\mu$ final state has the highest event yield since the cross section times branching fraction is twice as large as for ee or $\mu\mu$ final states and the selection requirements on the calorimeter and track-based measurement of the missing transverse momentum, $p_{\mathrm{T}}^{\mathrm{miss}}$, are less strict. The selection criteria result in a comparable purity

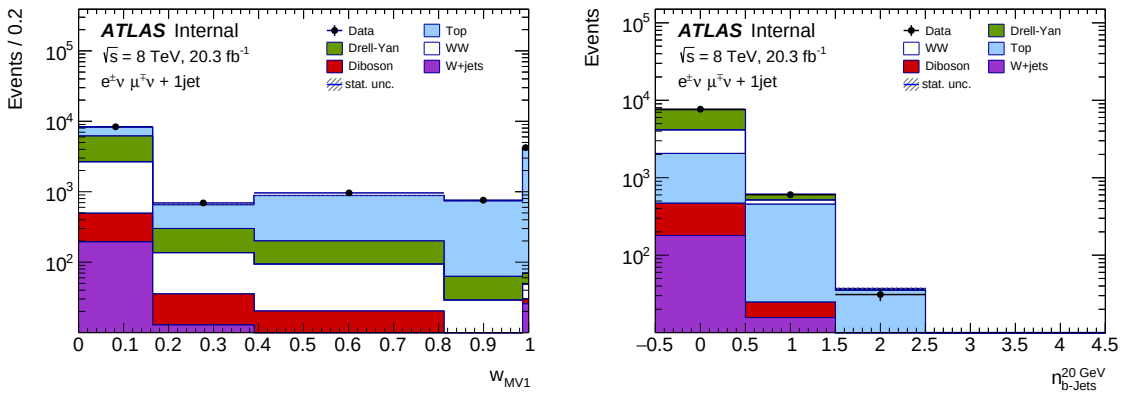

(a) (b)

Figure 6.5: (a) Distribution of the b-quark identification discriminant w_{MV1} for the jet selected in the $e\mu$+1-jet category. (b) Distribution of the number of additional jets identified as originating from b-quarks with a lowered transverse momentum threshold of 20 GeV $< p_{\mathrm{T}} <$ 25 GeV. Only statistical uncertainties are shown.

over the three final states, where 20%-25% of the selected data are expected to originate from background contributions. The expected signal yields are shown for a total production cross section of 58.7 pb and are the largest individual contribution to the expected event yields. Compared to the estimated contributions from simulated event samples an excess of roughly 15% is seen in data consistently in all final states of the 0-jet category. A total of 3458 events are observed in $e\mu$+1-jet final states where roughly 50% of the selected data are expected to originate from background contributions. In $e\mu$+1-jet final states a smaller excess of 5% is seen.

In all categories considered in the analysis, the agreement between data and the sum of contributions from signal and background processes is much better before applying kinematic selection criteria, i.e. if the event sample mainly consists of contributions from background processes. To ensure that the discrepancies between data and expected contributions result from W^+W^- production the background contributions are studied in Section 6.4. After subtracting the expected background contributions, an excess in data of $\sim$ 20% is seen consistently in all final states of the 0-jet category and an excess of $\sim$ 10% is seen in the 1-jet category where the individual signal processes are scaled to a total cross section of 58.7 pb.

6.4 Background Estimation

The selected sample of W^+W^- candidate events has a high purity but still contains contributions from the background processes described in Section 6.3.2. These processes are studied in the following and their contributions to the selected data are estimated.

		Data	W^+W^-	$Z \to \ell\ell$	top	diboson	W+jets	Data/MC
$e\mu$+0-jet	$m_{\ell\ell} > 10$ GeV	82999 ± 288	8720 ± 16	19235 ± 156	50590 ± 93	880 ± 9	825 ± 41	1.03 ± 0.00
	$n_{\text{jets}} = 0$	21981 ± 148	5283 ± 13	13704 ± 141	878 ± 15	305 ± 5	419 ± 34	1.07 ± 0.01
	$E_{\text{T, Rel}}^{\text{miss}} > 15$ GeV	10773 ± 104	4199 ± 11	4509 ± 79	751 ± 14	227 ± 5	293 ± 27	1.08 ± 0.01
	$p_{\text{T}}^{\text{miss}} > 20$ GeV	6059 ± 78	3721 ± 11	398 ± 24	708 ± 13	192 ± 4	270 ± 26	1.15 ± 0.02
	$\Delta\phi(E_{\text{T}}^{\text{miss}}, p_{\text{T}}^{\text{miss}}) < 0.6$	5067 ± 71	3234 ± 10	163 ± 15	618 ± 12	150 ± 4	225 ± 24	1.15 ± 0.02
ee +0-jet	$m_{\ell\ell} > 15$ GeV	4916163 ± 2217	3323 ± 10	4909111 ± 4098	20107 ± 58	2118 ± 10	369 ± 38	1.00 ± 0.00
	$\lvert m_{\ell\ell} - m_{\text{Z}}\rvert > 15$ GeV	412615 ± 642	2563 ± 9	375618 ± 1011	15778 ± 51	604 ± 7	267 ± 29	1.05 ± 0.00
	$n_{\text{jets}} = 0$	280409 ± 530	1530 ± 7	261502 ± 950	274 ± 8	245 ± 4	148 ± 27	1.06 ± 0.00
	$E_{\text{T, Rel}}^{\text{miss}} > 45$ GeV	4449 ± 67	588 ± 4	3326 ± 93	146 ± 6	53 ± 2	42 ± 15	1.07 ± 0.03
	$p_{\text{T}}^{\text{miss}} > 45$ GeV	798 ± 28	459 ± 4	52 ± 7	129 ± 6	37 ± 2	24 ± 10	1.14 ± 0.05
	$\Delta\phi(E_{\text{T}}^{\text{miss}}, p_{\text{T}}^{\text{miss}}) < 0.3$	594 ± 24	346 ± 3	26 ± 6	92 ± 5	27 ± 1	23 ± 10	1.16 ± 0.06
$\mu\mu$+0-jet	$m_{\ell\ell} > 15$ GeV	8354789 ± 2890	5441 ± 13	8296666 ± 5524	30172 ± 73	2913 ± 10	400 ± 23	1.00 ± 0.00
	$\lvert m_{\ell\ell} - m_{\text{Z}}\rvert > 15$ GeV	721731 ± 850	4185 ± 12	661160 ± 1363	23412 ± 65	603 ± 4	296 ± 20	1.05 ± 0.00
	$n_{\text{jets}} = 0$	492407 ± 702	2561 ± 9	460953 ± 1277	382 ± 10	323 ± 3	160 ± 15	1.06 ± 0.00
	$E_{\text{T, Rel}}^{\text{miss}} > 45$ GeV	8180 ± 90	1038 ± 6	6235 ± 129	203 ± 7	71 ± 2	48 ± 8	1.08 ± 0.02
	$p_{\text{T}}^{\text{miss}} > 45$ GeV	1323 ± 36	807 ± 5	94 ± 9	178 ± 7	50 ± 1	20 ± 5	1.15 ± 0.03
	$\Delta\phi(E_{\text{T}}^{\text{miss}}, p_{\text{T}}^{\text{miss}}) < 0.3$	975 ± 31	613 ± 4	42 ± 6	133 ± 6	38 ± 1	14 ± 4	1.16 ± 0.04
$e\mu$+1-jet	$n_{\text{jets}} = 1$	14995 ± 122	2384 ± 9	3832 ± 56	7900 ± 15	343 ± 6	247 ± 18	1.02 ± 0.01
	b-veto	7664 ± 88	2093 ± 8	3386 ± 53	1592 ± 7	288 ± 5	179 ± 15	1.02 ± 0.01
	$E_{\text{T, Rel}}^{\text{miss}} > 15$ GeV	4882 ± 70	1692 ± 7	1349 ± 33	1343 ± 7	218 ± 4	132 ± 13	1.03 ± 0.02
	$p_{\text{T}}^{\text{miss}} > 20$ GeV	3693 ± 61	1527 ± 7	414 ± 17	1256 ± 6	194 ± 4	117 ± 12	1.05 ± 0.02
	$\Delta\phi(E_{\text{T}}^{\text{miss}}, p_{\text{T}}^{\text{miss}}) < 2.0$	3458 ± 59	1486 ± 7	288 ± 14	1223 ± 6	185 ± 4	114 ± 12	1.05 ± 0.02

Table 6.3: Number of events observed in data and expected from W^+W^-, $Z/\gamma^* \to \ell\ell$, top quark, diboson and W+jets production at various steps of the kinematic selection. The signal and background contributions are estimated from simulated event samples. The yields from W^+W^- production are shown for a total cross section of $58.7^{+4.2}_{-3.8}$ pb. Only statistical uncertainties are shown.

6.4.1 Background from W+jets, multijet and $Z \to \ell\ell$ Production

The production of W+jets and multijet background contributes to the W^+W^- candidate events if hadronic jets are incorrectly identified as an electron or muon. The rate of the misidentification is very small and the contributions from W+jets and multijet production to the selected events in data are estimated from data. A detailed description is given in Chapter 7. Similarly, background from $Z/\gamma^* \to \ell\ell$ production contains only small genuine missing transverse momentum, $p_{\mathrm{T}}^{\mathrm{miss}}$, and mainly contributes due to fluctuations in the energy measurement of hadronic jets or the cell-out term. The background from $Z/\gamma^* \to \ell\ell$ production is estimated from a kinematic region dominated by $Z/\gamma^* \to \ell\ell$ events in data, described in Chapter 8.

6.4.2 Background from Top-Quark Production

Background from top-quark production is typically accompanied by two hadronic jets from the top-quark decay and contributes to the selected W^+W^- candidate events in the 0-jet category if the hadronic jets fall outside the kinematic acceptance of the jet selection. In the 1-jet category, b-jet identification criteria are placed on the selected jet and on additional jets with transverse momenta 20 GeV $< p_{\mathrm{T}} <$ 25 GeV. Contributions to the selected W^+W^- events can occur due to inefficiencies in the b-jet identification and if one jet falls outside the acceptance of the inner detector $|\eta| < 2.5$. Due to the different nature of the contributions to both categories the estimation of background is performed using different methods in the 0-jet and 1-jet categories.

The methods used for the estimation of the background from top-quark production rely on control samples selected in data that are enriched in contributions from top-quark production. The contributions to the selected W^+W^- candidate events are extrapolated from these control samples with extrapolation factors α determined in data:

$$N_{\mathrm{top}}^{\mathrm{data}}(\mathrm{SR}_i) = N_{\mathrm{top}}^{\mathrm{data}}(\mathrm{CR}_i) \cdot \alpha_i. \tag{6.2}$$

For the estimation of the contributions from top-quark production to the 0-jet category ($\mathrm{SR}_{0\text{-jet}}$), the control sample ($\mathrm{CR}_{0\text{-jet}}$) is defined by the nominal selection criteria but instead of requiring the absence of a hadronic jet in the event any number of hadronic jets is allowed. The extrapolation factor α is the efficiency of the jet-veto requirement. It is determined in simulated event samples but the probability p of a jet falling outside of the detector acceptance is corrected for by measurements in data. The probability p is measured in yet another sample in data where one of the jets is required to be identified as a b-jet. The b-jet requirement enriches the sample in events from top-quark production. This method was first suggested in Ref. [155]. In the context of the present analysis, the control sample receives large contributions from W^+W^- production. It is therefore purified by a criterion on the scalar sum of the transverse momenta of leptons and jets, $H_{\mathrm{T}} > 130$ GeV, for which another correction factor, $\varepsilon_{H_{\mathrm{T}}}^{\mathrm{MC}}$ is calculated in simulated event samples. The efficiency of the $H_{\mathrm{T}} > 130$ GeV requirement is 95% for events from top-quark production. The

full extrapolation factor takes the form:

$$\alpha_{0\text{-jet}} = \frac{\varepsilon^{\text{MC}}_{\text{jet-veto}}}{\varepsilon^{\text{MC}}_{H_{\text{T}}}} \cdot \left(\frac{p^{\text{data}}}{p^{\text{MC}}} \right)^2 , \tag{6.3}$$

where the square of the jet-veto probability accounts for the fact that top quark pair production is typically accompanied by two jets from b-hadron decays.

The control sample ($\text{CR}_{1\text{-jet}}$) for the estimation of contributions from top-background production in the 1-jet category ($\text{SR}_{1\text{-jet}}$) is defined by requiring the selected jet to be identified as a b-jet instead of rejecting them. This method was used e.g. in Ref. [153]. The extrapolation factor is given by the efficiency of the b-jet identification criterion which is measured in data in events selected with exactly two jets, either of them required to be identified as a b-jet. The efficiency of the b-jet identification is determined from the second jet such that the extrapolation factor α takes the form:

$$\alpha_{1\text{-jet}} = \frac{1 - f \cdot \varepsilon^{\text{data}}_{2\text{j}}}{f \cdot \varepsilon^{\text{data}}_{2\text{j}}}. \tag{6.4}$$

The factor $f = \varepsilon^{\text{data}}_{1\text{j}} \big/ \varepsilon^{\text{data}}_{2\text{j}}$ accounts for differences between the event sample with exactly two jets and the region with one hadronic jet. It is determined from simulated event samples.

Systematic uncertainties arise from the correction factors from simulated event samples, i.e. the factors $\varepsilon^{\text{MC}}_{\text{jet-veto}}$, $\varepsilon^{\text{MC}}_{H_{\text{T}}}$ and p^{MC} in the 0-jet category and the factor f in the 1-jet category. Experimental uncertainties arise mainly from uncertainties on the jet energy scale and resolution, and uncertainties in the b-jet identification efficiency. These propagate to uncertainties of ±5% and ±3% on the estimated background from top-quark production in the 0-jet and 1-jet categories, respectively. Theoretical uncertainties are assigned by studying the dependence of the estimated yield on the renormalisation and factorisation scale, the uncertainties on the parton distribution functions used to simulate the event samples, and by comparing simulated event samples produced with different generators and parton shower models. The relative normalisation of contributions from single top and top quark pair production is varied by 30% and interference effects are studied. The systematic studies result in theoretical uncertainties on the estimated background form top-quark production of ±7% in the 0-jet category and ±2.5% in the 1-jet category. Additional methodical uncertainties arise from the assumption of two jets in an event from top-quark production in the 0-jet category. These are assessed by varying the exponent in the ratio $(p^{\text{data}}/p^{\text{MC}})^2$ to 1.5 or 2.5 which results in an effect on the estimated yield of less than 1%.

The statistical uncertainty of the estimated background from top-quark production is the sum in quadrature of the statistical uncertainties in the data and the simulated event samples, resulting in a statistical uncertainty of ±2% in the 0-jet category and ±3.5% in the 1-jet category. Kinematic distributions of events selected for the control samples are shown in Fig. 6.6.

The background from top-quark production is estimated to be 609 ± 18(stat) ± 52(syst) events for $e\mu$+0-jet final states, 92 ± 7(stat) ± 8(syst) events for ee+0-jet final states and 127 ±

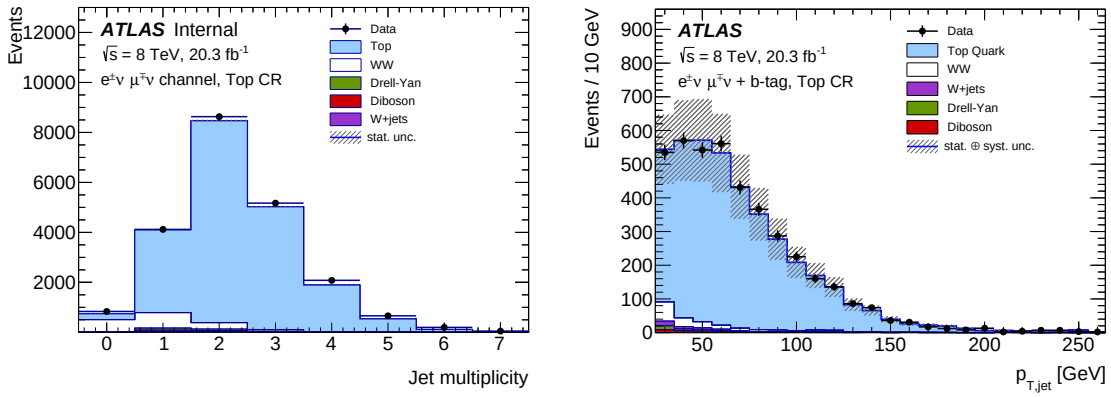

Figure 6.6: Events selected in the control sample used for the estimation of the background from top-quark production. The jet multiplicity distribution in the top quark control sample of the 0-jet category (left) and the distribution of the transverse momentum of the selected jet in the 1-jet category are shown (right). Statistical uncertainties are shown for the 0-jet category and both statistical and systematic uncertainties are shown for the 1-jet category. Previously published in Ref. [6].

9(stat) ± 11(syst) events for $\mu\mu$+0-jet final states. For $e\mu$+1-jet final states where top-quark production represents the background process with the largest individual contribution the yield is estimated to be 1236 ± 43(stat) ± 49(syst) events.

6.4.3 Background from Other Diboson Processes

Possible contributions from diboson production other than W^+W^- arise from the $W\gamma$, ZZ and WZ/γ^* processes. These are estimated from simulated event samples. The event samples are normalised to cross sections calculated with MCFM [99] at NLO. The event generators and cross sections are summarised in Table 6.1. Uncertainties are assigned on the cross sections used to normalise the simulated event samples and the acceptance of the kinematic selection. Furthermore, experimental uncertainties are assigned in the same way as described in Section 9.2 for the signal.

Background from $W\gamma$ production arises if the W boson decays leptonically and the photon is falsely identified as an electron. Hence, this background contributes to ee and $e\mu$ final states only. Events are generated using the Alpgen+Herwig event generator. An uncertainty on the cross section of ±6% is assigned. In the 0-jet category an additional uncertainty of ±30% is assigned to account for possible higher-order effects based on differences between the measurement of $W\gamma$ production at $\sqrt{s} = 7$ TeV [156] and theoretical calculations at NLO. For the background from $W\gamma$ production in the 1-jet category a K-factor of $K = 1.2$ is derived from Ref. [157]. Uncertainties on the acceptance of ±50% are assigned in the 1-jet category based on studies performed in Ref. [153].

The diboson process that constitutes the largest background is the production of a W boson with an off-shell Z/γ^* or an on-shell Z boson. The contribution arises mainly if one of the leptons is not identified or falls outside of the acceptance of the kinematic constraints

applied on the leptons. The Sherpa event generator is used for the $W\gamma^*$ process, whereas PowHeg+Pythia is used for WZ production. Overlap between simulated event samples is removed using information at the event generation stage. The invariant mass of the dilepton system of the Z/γ^* decay products is restricted to $m_{\ell\ell} < 7$ GeV and $m_{\ell\ell} > 7$ GeV in the two samples, respectively. The theoretical uncertainties on the cross-section calculations are ±7% for $W\gamma^*$ and ±8% for WZ production. The uncertainty on the WZ cross section is increased to ±15% in the 1-jet category to account for possible higher-order effects based on the results in Refs. [158, 159]. Uncertainties of ±7% and ±30% are assigned on the $W\gamma^*$ acceptance which originate from jet-binned correction factors derived for the simulated event sample in Ref. [153]. The acceptance uncertainty for WZ production is derived from the uncertainties assigned to W^+W^- production in Section 9.3.

The production of two Z bosons can have the same decay products as W^+W^- production in the ee and $\mu\mu$ final states if one of the Z bosons decays leptonically $Z \to \ell\ell$ and the other to neutrinos $Z \to \nu\nu$. These contributions are small since the leptons reconstruct to $\left|m_{\ell\ell} - m_Z\right| < 15$ GeV and are therefore removed by the kinematic selection. Most of the contributions arise from events where both Z bosons decay leptonically and of each Z boson one lepton falls outside the acceptance or fails the selection criteria. Simulated event samples are produced using PowHeg+Pythia8. An uncertainty of ±13% is assigned on the cross section based on differences between calculations at NLO and NNLO where only fiducial NNLO cross sections for on-shell Z bosons have been calculated [160, 161]. As for WZ production, the same acceptance uncertainty as for W^+W^- signal events is assigned to the background from ZZ production.

The contributions to the selected W^+W^- event sample estimated to originate from diboson production sum up to 150±4 (stat)±30 (syst) for $e\mu$+0-jet final states, 27±1 (stat)±5 (syst) for ee+0-jet final states, 38 ± 1 (stat) ± 5 (syst) for $\mu\mu$+0-jet final states and 195 ± 5 (stat) ± 53 (syst) for $e\mu$+1-jet final states. A validation of the estimated yields is performed in data in the course of the estimation of contributions from W+jets and multijet production and discussed in Section 7.7. For this qualitative validation $e\mu$ final states are selected with the nominal selection criteria but with a requirement on both leptons to have the same electric charge. Background from $W\gamma$ and WZ/γ^* is equally likely to contribute to the nominal selection criteria with opposite electric charge as to the same charge control sample. The production of a Z boson with initial or final state photon radiation, $Z\gamma$, is estimated together with background from Z/γ^* production in Section 8. Since the additional photon will typically also be reconstructed as a jet, no differentiation is needed between these processes. Contributions from triboson production have been estimated and are found to have a negligible contribution to the selected data.

7 Estimation of the W+jets and Multijet Backgrounds

Single W boson production can contribute to the selected W^+W^- candidate events when an associated hadronic jet is misidentified as a lepton. Multijet events can also contribute if two hadronic jets are misidentified and sufficiently large missing transverse momentum is induced by a mismeasurement of the jet energy.

The rate of this misidentification is very small and these background processes containing misidentified leptons only have significant contributions since the cross sections of W+jets and multijet production are many orders of magnitude larger than that of W boson pair production. Since the misidentification is very rare it is difficult to be simulated with high accuracy. Therefore, the contributions from W+jets and multijet events are estimated from data. The method is described in the following.

7.1 Introduction to the Matrix Method

The estimation of the W+jets and multijet backgrounds relies on a control sample that is enriched in misidentified leptons. It is selected with relaxed criteria on the selection of leptons applied, e.g. relaxed identification criteria, impact parameter and isolation requirements. Other criteria such as those on the kinematic variables are imposed as in the nominal selection. The number of dilepton events in this sample with different combinations of genuine (real) and misidentified leptons (fake) can be calculated from the number of events selected with the relaxed, so-called *loose* (L), criteria and the nominal, so-called *tight* (T) criteria. The relation is given by the following system of linear equations:

$$
\begin{aligned}
N^{\mathrm{LL}} &= N^{\mathrm{LL}}_{\mathrm{fake,fake}} + N^{\mathrm{LL}}_{\mathrm{real,fake}} + N^{\mathrm{LL}}_{\mathrm{fake,real}} + N^{\mathrm{LL}}_{\mathrm{real,real}} && (7.1)\\
N^{\mathrm{LT}} &= \varepsilon_{\mathrm{fake}} N^{\mathrm{LL}}_{\mathrm{fake,fake}} + \varepsilon_{\mathrm{fake}} N^{\mathrm{LL}}_{\mathrm{real,fake}} + \varepsilon_{\mathrm{real}} N^{\mathrm{LL}}_{\mathrm{fake,real}} + \varepsilon_{\mathrm{real}} N^{\mathrm{LL}}_{\mathrm{real,real}} && (7.2)\\
N^{\mathrm{TL}} &= \varepsilon_{\mathrm{fake}} N^{\mathrm{LL}}_{\mathrm{fake,fake}} + \varepsilon_{\mathrm{real}} N^{\mathrm{LL}}_{\mathrm{real,fake}} + \varepsilon_{\mathrm{fake}} N^{\mathrm{LL}}_{\mathrm{fake,real}} + \varepsilon_{\mathrm{real}} N^{\mathrm{LL}}_{\mathrm{real,real}} && (7.3)\\
N^{\mathrm{TT}} &= \varepsilon^2_{\mathrm{fake}} N^{\mathrm{LL}}_{\mathrm{fake,fake}} + \varepsilon_{\mathrm{real}}\varepsilon_{\mathrm{fake}} N^{\mathrm{LL}}_{\mathrm{real,fake}} + \varepsilon_{\mathrm{fake}}\varepsilon_{\mathrm{real}} N^{\mathrm{LL}}_{\mathrm{fake,real}} + \varepsilon^2_{\mathrm{real}} N^{\mathrm{LL}}_{\mathrm{real,real}} && (7.4)
\end{aligned}
$$

where N^{LL}, N^{LT}, N^{TL} and N^{TT} denote the number of events with leptons satisfying the loose and tight criteria. The first and second index corresponds to the leading and sub-leading lepton, respectively, and $\varepsilon_{\mathrm{real}}$ and $\varepsilon_{\mathrm{fake}}$ are the efficiencies for genuine and misidentified leptons, respectively, selected with the loose criteria to also meet the tight criteria.

By counting the number of events that fulfil different combinations of the loose and tight criteria the number of events with genuine and misidentified leptons can be obtained

with the knowledge of the efficiencies $\varepsilon_{\text{real}}$ (henceforth simply denoted efficiency) and $\varepsilon_{\text{fake}}$ (henceforth denoted misidentification rate) by solving the above system of linear equations. This can be conveniently done by writing Eqs. 7.1-7.4 in matrix form which explains why the method is frequently referred to as matrix method. It has previously been used e.g. in Refs. [162, 163].

The number of W+jets events in the sample selected with loose criteria then is the number of events with one misidentified and one genuine lepton $N^{\text{LL}}_{\text{real,fake}} + N^{\text{LL}}_{\text{fake,real}}$. The number of events with two misidentified leptons $N^{\text{LL}}_{\text{fake,fake}}$ corresponds to the number of multijet events. The contributions to the nominal event sample with tight lepton criteria are obtained as:

$$N_{W\text{+jets}} = N^{\text{LL}}_{\text{real,fake}} \cdot \varepsilon_{\text{real}}\varepsilon_{\text{fake}} + N^{\text{LL}}_{\text{fake,real}} \cdot \varepsilon_{\text{fake}}\varepsilon_{\text{real}} \tag{7.5}$$

$$N_{\text{QCD}} = N^{\text{LL}}_{\text{fake,fake}} \cdot \varepsilon^2_{\text{fake}}. \tag{7.6}$$

7.2 Definition of the Loose Criterion

For the definition of the loose lepton criteria a large difference between $\varepsilon_{\text{fake}}$ and $\varepsilon_{\text{real}}$ is desirable as factors $1/(\varepsilon_{\text{real}} - \varepsilon_{\text{fake}})$ occur when solving Eqs. 7.1-7.4. The difference between efficiency and misidentification rate occurs in every term and uncertainties on efficiencies and misidentification rates are leveraged when propagated to the final estimate. In practice, the definition of the loose lepton criteria is driven by the necessity of being able to select a data sample with the loose criteria, i.e. it is limited by the criteria imposed in the trigger algorithms used to record the event sample.

The loose lepton criteria are defined as the nominal lepton selection criteria discussed in Section 6.3.2 but removing the requirements on the calorimeter and track isolation, and the impact parameter requirements. In addition, electrons are required instead of satisfying the very tight LH identification to only satisfy medium LH, thus effectively relaxing the criteria placed on tracking variables and calorimeter shower-shapes.

For this analysis, electron identification criteria based on a likelihood discriminant are used in combination with trigger algorithms that use sequential cuts on shower shape and tracking variables. Moreover, the trigger algorithms for single leptons explicitly use track isolation criteria. This causes the selection in the trigger algorithm being not necessarily looser than the selection imposed offline. Consequently, the event sample is biased with respect to the loose selection criteria. To account for this bias, the events selected with looser criteria on the leptons are categorised according to which of the leptons triggered the readout system. Efficiencies and misidentification rates are determined individually for each category and the appropriate trigger requirements are added to the loose lepton definition.

Using the loose lepton criteria to select events results in a sample of 900 ee+0-jet events, 1076 $\mu\mu$+0-jet events, 5876 $e\mu$+0-jet events and 1076 $e\mu$+1-jet events. The event yield is 50-70% higher than for the nominal selection criteria for ee and $e\mu$ events. For $\mu\mu$ events the yield is only 10% higher. The fraction of W+jets and multijet events in the event sample selected with loose lepton selection criteria impacts the uncertainty of the background estimation. The distributions of the relative missing transverse momentum, $E^{\text{miss}}_{\text{T, Rel}}$, are shown

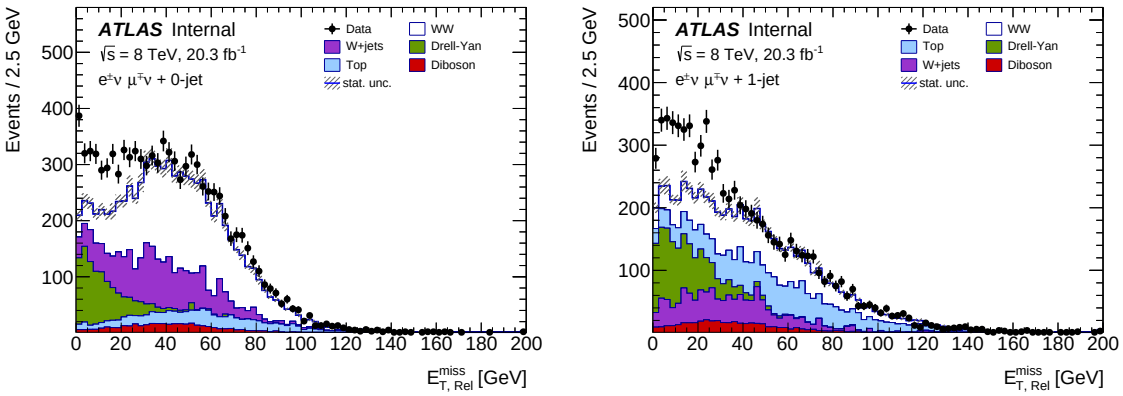

Figure 7.1: Distributions of $E_{\mathrm{T,\,Rel}}^{\mathrm{miss}}$ for the event sample selected with the loose lepton selection criteria. Shown are $e\mu$ final states without hadronic jets (left) and with one hadronic jet (right). The kinematic selection criteria of the nominal analysis are applied except for the selection on the relative missing transverse momentum $E_{\mathrm{T,\,Rel}}^{\mathrm{miss}}$. Reasonable agreement between data and the yields estimated from simulated event samples is seen at high values of $E_{\mathrm{T,\,Rel}}^{\mathrm{miss}}$. The difference between data and estimated yields for low values of $E_{\mathrm{T,\,Rel}}^{\mathrm{miss}}$ can be attributed to multijet background for which no simulated event samples are shown.

in Fig. 7.1 for the $e\mu$ final state where all nominal kinematic selection requirements are applied except for $E_{\mathrm{T,\,Rel}}^{\mathrm{miss}}$. Differences between data and the yields estimated from simulated event samples are seen at low values of $E_{\mathrm{T,\,Rel}}^{\mathrm{miss}}$. This can be attributed to multijet background for which no simulated event samples are shown. If the selection on $E_{\mathrm{T,\,Rel}}^{\mathrm{miss}}$ is applied as well, 20% and 15% of the selected data are expected to originate from W+jets production in the $e\mu$+0-jet and $e\mu$+1-jet event sample, respectively. In the ee ($\mu\mu$) final states the contributions are 15% (7%) for background from W+jets production. Lower fractions of multijet background are expected since the requirements of $E_{\mathrm{T,\,Rel}}^{\mathrm{miss}}$ and $p_{\mathrm{T}}^{\mathrm{miss}}$ are much more stringent than for $e\mu$ final states.

7.3 Measurement of Efficiencies and Misidentification Rates

The determination of efficiencies and misidentification rates is described in the following. Simulated event samples are used to determine the efficiencies $\varepsilon_{\mathrm{real}}$ as described in Section 7.3.1. The measurement of misidentification rates $\varepsilon_{\mathrm{fake}}$ in data is discussed in Section 7.3.2.

7.3.1 Measurement of Efficiencies of Genuine Leptons

Efficiencies are generally not process-independent. This means that they cannot be determined in $Z \to ee$ events, as described in Section 4.1, when used for the estimation of the background from W+jets and multijet production. Efficiencies have to be determined for the processes relevant in the kinematic region of interest individually. A tag-and-probe

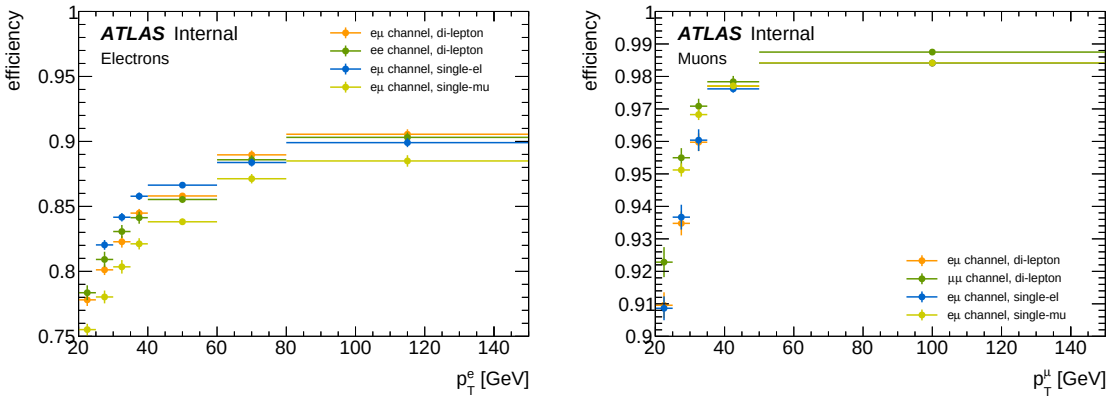

Figure 7.2: Efficiencies for genuine loose leptons to satisfy the nominal selection criteria. These serve as an input to the data-driven estimation of the W+jets and multijet background. Efficiencies for the 0-jet category are shown for electrons (left) and muons (right) as a function of the transverse momentum, p_{T} with their statistical uncertainties only.

method is used on simulated event samples of the W^+W^- and background processes. They are corrected with the efficiency ratios measured in data such that efficiency in simulated event samples corresponds to the efficiency is data. The same kinematic selection as for the nominal analysis is applied but with the requirements on $E_{\mathrm{T,\,Rel}}^{\mathrm{miss}}$, $p_{\mathrm{T}}^{\mathrm{miss}}$ and $\Delta\phi(E_{\mathrm{T}}^{\mathrm{miss}}, p_{\mathrm{T}}^{\mathrm{miss}})$ relaxed in order to achieve a higher statistical precision. The procedure is performed for $e\mu$+0-jet, ee+0-jet, $\mu\mu$+0-jet and $e\mu$+1-jet final states separately. The different contributions from W^+W^-, $Z/\gamma^* \to \ell\ell$, top quark production and the other diboson processes are weighted according to the composition in the W^+W^- candidate event sample. For the calculation of efficiencies used in the estimation of background to the 0-jet category the W^+W^- processes are scaled up by 21% with respect to the theory prediction of 58.7 pb to be in agreement with the measured yield.

To account for bias from the trigger algorithms, several sets of efficiencies are measured where the criteria imposed in the different trigger algorithms are explicitly added to the selection. The efficiencies for the individual sets are shown in Fig. 7.2 as a function of the transverse momentum, p_{T}. Three sets are calculated for $e\mu$ final states where each lepton can trigger the single-lepton or the dilepton readout but is not required to do so if the other lepton triggers the single-lepton readout. The largest bias results from the case where the single-lepton readout is triggered. Since this algorithm requires track isolation it yields the highest efficiency. For ee and $\mu\mu$ final states the trigger decision is unambiguous and only a single set is needed per final state.

In practise efficiencies are evaluated double differentially as a function of transverse momentum and pseudorapidity. The double differential efficiencies for electrons and muons are shown in Fig. 7.3 for $e\mu$ events that triggered the dilepton readout.

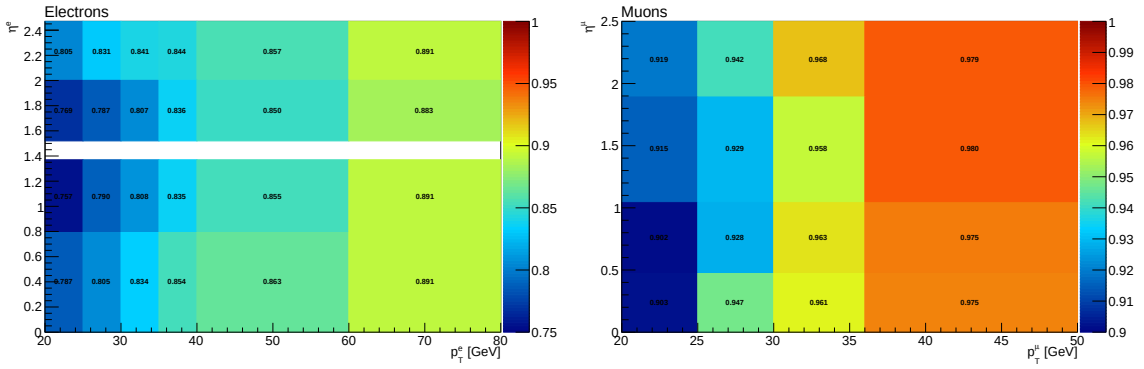

Figure 7.3: Efficiencies for genuine loose leptons to satisfy the nominal selection criteria as a function of transverse momentum, p_T, and pseudorapidity, η. Shown are double differential efficiencies for electrons (left) and muons (right) that triggered the dilepton readout in the $e\mu$+0-jet final state. These serve as an input to the data-driven estimation of the W+jets and multijet background.

7.3.2 Measurement of Efficiencies of Misidentified Leptons

Due to the lack of a clean W+jets sample that allows a measurement of misidentification rates directly, misidentification rates are measured in dijet events. Selecting events with exactly one loose lepton already yields an event sample dominated by dijet production. However, large contributions from genuine leptons, mainly $W \to \ell\nu$ and $Z/\gamma^* \to \ell\ell$ decays, are also present and become the dominant contribution once tight lepton criteria are applied. To enrich the event sample in dijet events one hadronic jet with $p_T > 30$ GeV in opposite azimuthal direction, i.e. satisfying $\Delta\phi(\ell, \text{jet}) > 2$, is required. For a further rejection of contributions from $W \to \ell\nu$ production the missing transverse momentum is required to be $E_T^{\text{miss}} < 30$ GeV and the transverse mass of the lepton-p_T^{miss} system is required to be $m_T < 40$ GeV. The transverse momentum distributions in the selected dijet events are shown in Fig. 7.4 for misidentified electrons and muons. Contributions from genuine leptons are still large and subtracted using simulated event samples of $W \to \ell\nu$, $Z/\gamma^* \to \ell\ell$ and $t\bar{t}$ production.

As for the measurement of the efficiency of genuine leptons, several sets of misidentification rates are measured with the criteria imposed in the different trigger algorithms explicitly added. Since misidentification rates are measured in data with a single reconstructed lepton, a set of trigger algorithms requiring a single lepton are used that implement the same criteria otherwise used in the dilepton algorithms. Such algorithms are implemented but the bandwidth of the readout is limited. For a selection equivalent to the dilepton algorithms a set of trigger algorithms with transverse momentum thresholds at $p_T > 15$ GeV, $p_T > 22$ GeV and $p_T > 60$ GeV is used where the bandwidth was limited to record a fraction of $6 \cdot 10^{-4}$-$3 \cdot 10^{-2}$ of all events. Differences in the algorithms compared to those used to record the W^+W^- candidate events are small and well within the uncertainty assigned to the measurement of the misidentification rates. Algorithms that require an electromagnetic cluster with $p_T > 20$ GeV and $p_T > 24$ GeV with a rate limited to a fraction of 10^{-4} and $6 \cdot 10^{-6}$ are used for the measurement of misidentification rates of unbiased

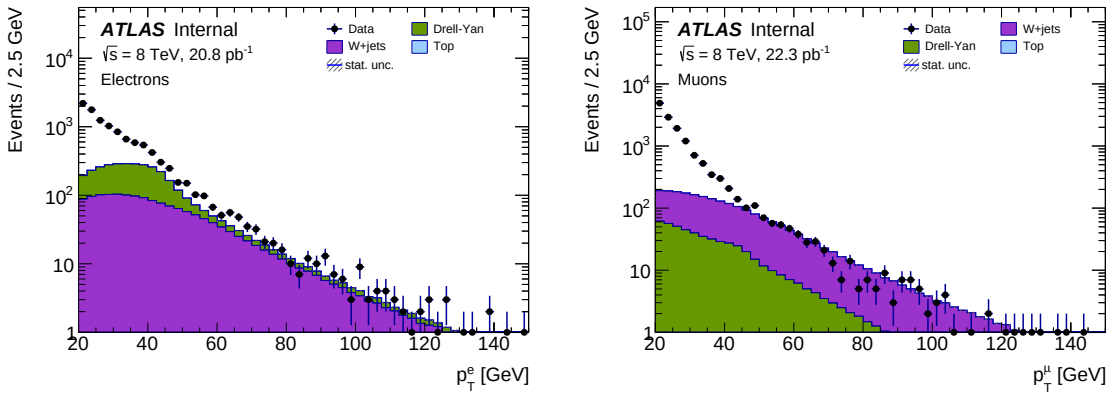

Figure 7.4: Distribution of the transverse momentum, p_{T}, of the misidentified lepton candidates selected for the measurement of misidentification rates in dijet events. The tight criteria are applied for electrons (left) and muons (right). Shown are the events recorded with a specific single lepton trigger algorithm where the p_{T} threshold set to 15 GeV.

loose electron candidates. For muons an algorithm with a transverse momentum threshold of $p_{\mathrm{T}} > 15$ GeV and a bandwidth limited to a fraction of 10^{-3} is used and suitable for the measurement of misidentification rates for all loose muon candidates that did not trigger the readout and that triggered the dilepton readout. Furthermore, misidentification rates are measured with the single-lepton algorithms used to record the W^+W^- candidate events and used in the corresponding category.

A systematic uncertainty on the subtraction of contributions from genuine leptons is assigned by varying the normalisation by ±5%. Varying the normalisation accounts for uncertainties on the luminosity determination and the cross section used to normalise the simulated $W \to \ell\nu$, $Z \to \ell\ell$ and top quark event samples. In addition, systematic uncertainties are assigned for a possible bias from the kinematic selection by removing separately the $E_{\mathrm{T}}^{\mathrm{miss}}$ and m_{T} requirements in the selection. The sample of dijet events was recorded with much lower pile-up conditions than the nominal event sample as the bandwidth of the readout used to select the samples is limited and increases towards the end of an LHC fill. The uncertainty on this effect is assessed by restricting the number of reconstructed primary vertices n_{vtx} to be less or more than $n_{\mathrm{vtx}} \leqslant 20$. The symmetrised difference to the nominal misidentification rate is assigned as a systematic uncertainty.

The resulting misidentification rates are shown in Fig. 7.5 for electrons and muons in the barrel and endcap regions. The bias from the readout algorithms is clearly visible, in particular the requirement on track isolation implemented in the single-lepton algorithms causes higher misidentification rates.

7.3.3 Kinematic Dependence of Efficiencies and misidentification rates

Both the efficiencies and the misidentification rates strongly depend on the transverse momentum and the pseudorapidity of the lepton, and only mildly on other variables. To al-

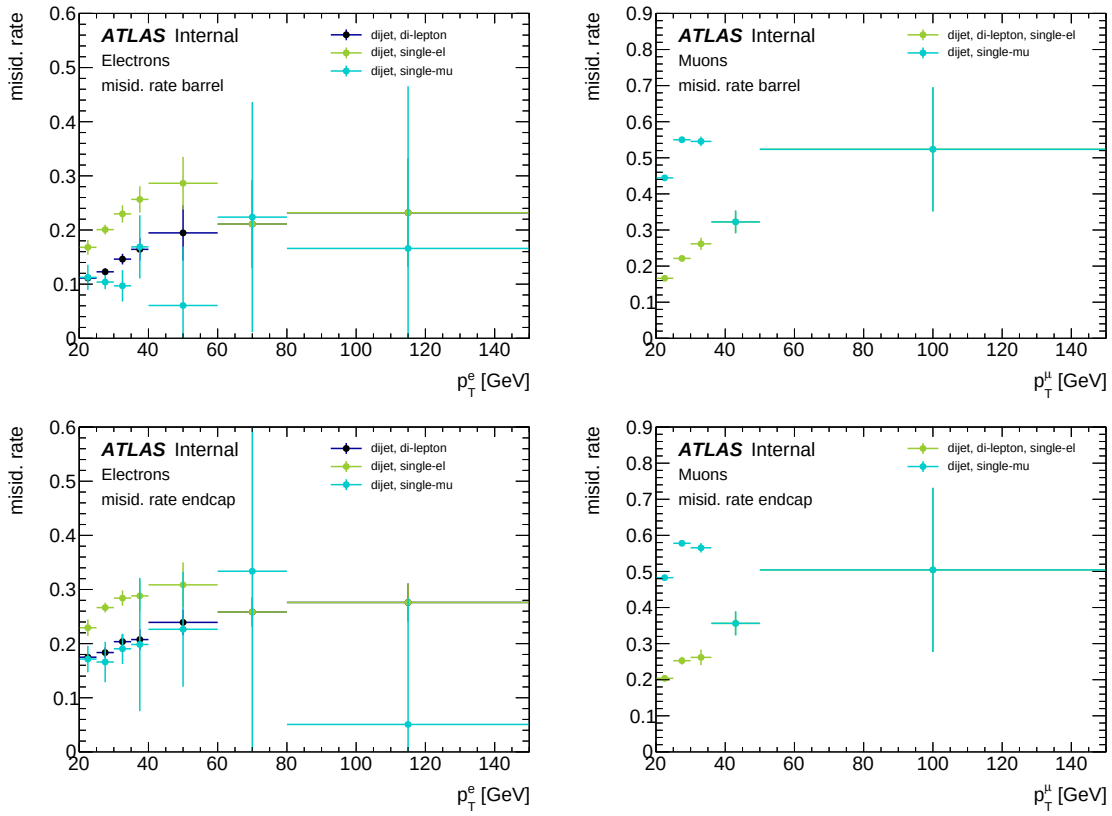

Figure 7.5: Misidentification rates measured in data that serve as input to the data-driven estimation of the background from W+jets and multijet production for electrons (left) and muons (right). The misidentification rates are shown separately for the barrel (top) and endcap regions (bottom) with their systematic uncertainty. The sample dependence uncertainty discussed in Section 7.4 is not included.

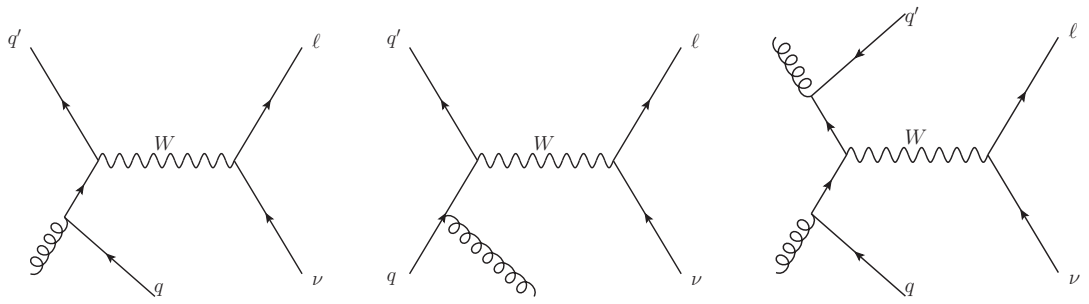

Figure 7.6: Leading order diagrams for W+jets production for different combinations of initial partons. Shown are qg initial states (7.6a) and $q\bar{q}$ initial states (7.6b) with one additional jet. Production of a W boson from gg initial states (7.6c) is associated with at least two jets.

low a correct determination of differential W+jets and multijet distributions from data, efficiencies and misidentification rates are determined in bins of these variables. The bin boundaries are oriented at the detector geometry and the optimisation of the lepton reconstruction and identification criteria. Seven bins in p_{T} and four bins in η are used for the measurement of efficiencies of electrons, five bins in p_{T} and four bins in η are used for muons. In the measurement of misidentification rates the number of η bins is reduced to two.

7.4 Sample Dependence Uncertainty

In general, jets from heavy-flavour decays have a higher probability to be misidentified as leptons than light flavour jets since heavy-flavour decays can involve genuine, but non-isolated leptons. A sample of loose misidentified leptons will thus be enriched in heavy-flavour decays with respect to the relatively lower production cross section. On the other hand there are dedicated selection criteria to reject background from heavy-flavour decays, namely the selection criteria on the impact parameter and the isolation. Due to the long lifetime of heavy-flavour hadrons in the order of ~ 1.5 ps they have secondary decay vertices and thus the decay leptons have large impact parameters. Events from W+jets production typically contain a larger fraction of heavy-flavour jets than events from multijet production. As a result, misidentification rates for dijet and W+jets events differ and the differences need to be accounted for with a systematic uncertainty, referred to as the sample dependence uncertainty.

7.4.1 W+jets Production

The leading order diagrams of W+jets production are shown in Fig. 7.6. Events from W+jets production can be produced from qg, qq and gg initial states. The relative contributions to W+1-jet production are 65% from qg initial states and 35% from qq initial states [164]; gg initial states do not contribute to W+1-jet production as they produce at least two jets. In

W+2-jet production the contributions are 60-65% from qg initial states, 30-35% from qq and $\sim 5\%$ from gg initial states. A selection on the charge product of the genuine and misidentified leptons can change these ratios. The processes with qg initial states in Fig. 7.6a exhibit a charge correlation between the lepton and the outgoing quark while the processes with qq and gg initial states in Figs. 7.6b and 7.6c do not. Requiring genuine and misidentified leptons to have opposite electric charge will thus enrich the background from W+jets production with contributions from qg initial states and the requirement of the same electric charge will largely suppress these processes.

For the interpretation in the context of the measurement of W^+W^- production it is important to note that a jet misidentified as an electron is usually removed in the overlap removal procedure, i.e. the W+1-jet events contribute to the 0-jet category. Muons are required to be isolated from jets. Jets misidentified as muon typically fall below the transverse momentum threshold of the jet selection. Events from W+2-jet production analogously contribute to the 1-jet category.

The charge correlation in the diagram in Fig. 7.6a, together with the high probability of heavy flavour jets to be misidentified as a lepton, causes $\sim 80\%$ of the expected background from W+jets production in the $e\mu$+0-jet category to originate from $W + c$ production.

7.4.2 Determination of the Sample-Dependence Uncertainty

The uncertainty originating from the sample dependence is determined by comparing simulated multijet samples, generated with Pythia8, and W+jets samples, generated with Alpgen and showered with Pythia6. The misidentification rates evaluated from data and from the two simulated event samples are shown as a function of transverse momentum, p_{T}, for $W + \ell_{\mathrm{fake}}$+0-jet events in Fig. 7.7. The misidentified lepton is required to not originate from a W boson, Z boson or top quark decay. For the estimation of misidentification rates in W+jets events, the misidentified lepton is further required to have the opposite electric charge as the generated W boson.

Calculating an inclusive sample dependence uncertainty was found to underestimate the difference between dijet and W+jets events since their jet p_{T} spectra are different. The sample dependence uncertainty is evaluated differentially in p_{T}. In order to reduce the effect from statistical fluctuations in the simulated event samples the weighted average of the difference in p_{T} is assigned as the final sample dependence uncertainty. In the 0-jet category this amounts to an uncertainty of $\pm$(50-60)% for the electron misidentification rates and $\pm$(35-60)% for the muon misidentification rates. In the 1-jet category the uncertainty reduces to $\pm$40% for both lepton flavours. The misidentification rates as shown in Fig. 7.8 reflect the change in contributions from heavy-flavour jets for higher jet multiplicities which results in lower sample dependence uncertainties. The sample dependence uncertainty is always calculated with respect to the same dijet misidentification rate.

For a qualitative validation of these numbers in data, the measurement of misidentification rates is repeated with strict b-jet identification requirements placed on the tagging jet, thus enriching the sample in heavy flavour, mainly $b\bar{b}$, events. Indeed, the sample enriched in misidentified leptons from heavy-flavour decays yields significantly lower misidentification rates as shown in Fig. 7.9. The effect is found to lie within the sample dependence uncertainty assigned to the misidentification rates by comparing simulated event samples.

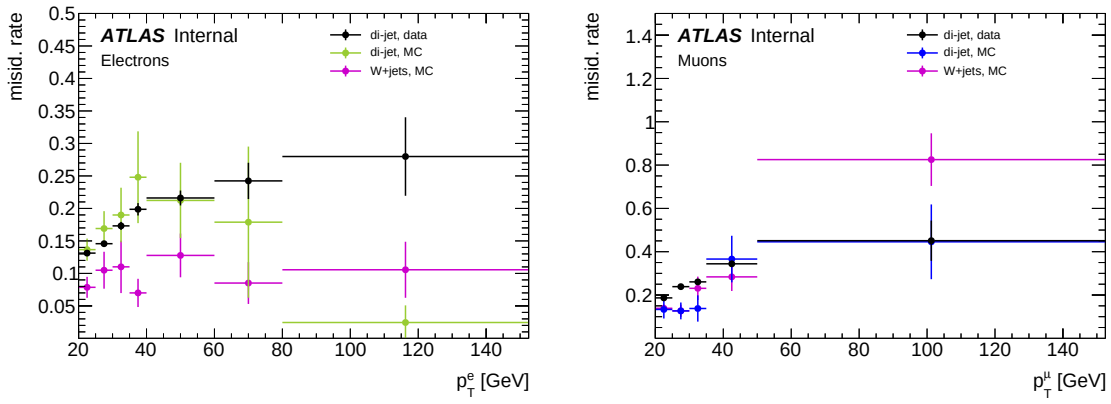

Figure 7.7: Misidentification rates estimated in dijet events in data and in simulated dijet and W+fake+0-jet events for electrons (left) and muons (right). The difference between the two simulated event samples is assigned to the measured misidentification rates used in the estimation of the W+jets background as a systematic uncertainty. Only statistical uncertainties are shown.

Jets from b-hadrons typically have larger impact parameters and thus are easier to reject than jets from c-hadrons. Therefore, the qualitative validation can be considered as conservative.

The misidentification rate obtained in the simulated W+jets event sample can be used to perform a test of the background estimation technique. It is applied to a loose control sample of simulated W+jets events and found to reproduce the yields in the same sample selected with the tight criteria within the uncorrelated part of the statistical uncertainty.

7.5 Results

The method described above is capable of estimating contributions to the selected W^+W^- events from two misidentified leptons and contributions from one misidentified and one genuine lepton. For the latter case there are two non-negligible processes that contribute to the analysis, the W+jets background and the associated production of a W boson with a photon, $W\gamma$. Photons exhibit misidentification rates very different from jets or the efficiency of genuine leptons. Contamination from $W\gamma$ events can neither be avoided, nor can the method correctly account for their contributions. The contamination from $W\gamma$ production is accounted for by applying the method to simulated $W\gamma$ events and subtracting the estimated contribution to the W+jets yield.

The results of the data-driven estimation of the W+jets and multijet background are shown in Table 7.1 for the 0-jet category and the 1-jet category with a detailed breakdown of systematic uncertainties. The uncertainties on the estimated W+jets yield are derived by propagating the uncertainties described in Section 7.3 and 7.4 to Eqs. 7.1-7.4. The total systematic uncertainties are obtained by averaging the up and downward uncertainties of the individual sources and adding them quadratically. It should be noted that the uncertainty assigned on the pure multijet background cannot be considered complete as the presence of

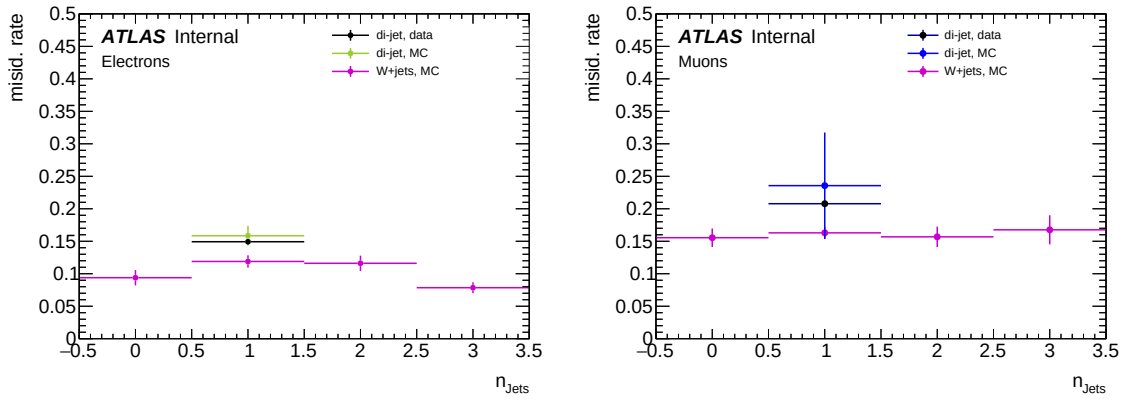

Figure 7.8: Misidentification rates estimated in dijet events in data and in simulated dijet and W+jet events for electrons (left) and muons (right) as a function of the jet multiplicity. The jet multiplicity is counted after lepton-jet overlap removal. The sample dependence uncertainty for the 0-jet and 1-jet category are calculated with respect to the same dijet misidentification rate. Statistical uncertainties are shown for simulated event samples, the combined statistical and systematic uncertainty is shown for the data samples.

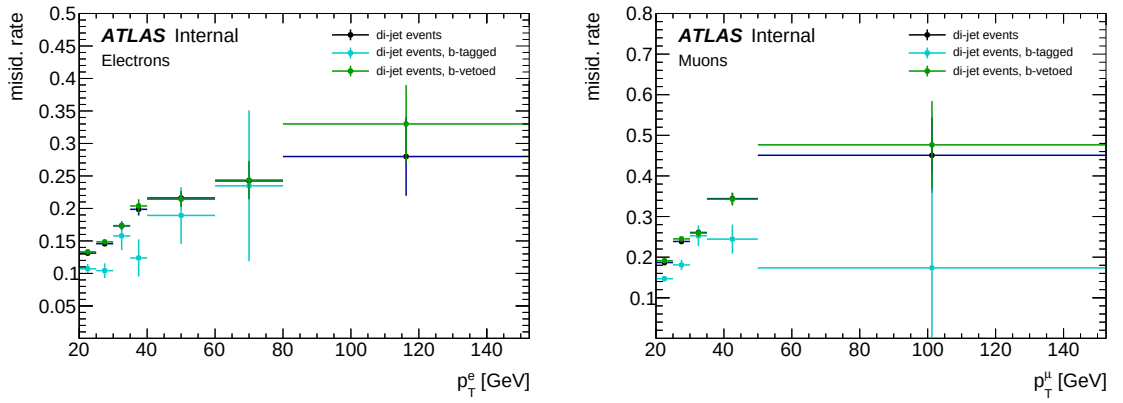

Figure 7.9: Misidentification rates estimated in dijet events in data for electrons (left) and muons (right) as a function of the transverse momentum, p_{T}. In order to have a qualitative comparison of the sample dependence evaluated in simulated events, strict b-jet identification requirements are placed on the tagging jet. The requirement is chosen to have a b-jet identification efficiency of 60% and 85% for the b-jet identification and b-jet veto requirement, respectively. The combined statistical and systematic uncertainties are shown.

two misidentified leptons enriches the sample in heavy-flavour contributions for which no uncertainty is assigned. The effect was shown to be smaller than the uncertainty assigned due to the sample dependence in W+jets events in Ref. [153] and the uncertainty assigned to the combined W+jets and multijet yield is considered to account for the effect.

The W+jets and multijet contributions are estimated to be $250 \pm 20\,(\text{stat}) \pm 140\,(\text{syst})$ for $e\mu$+0-jet final states, $14 \pm 5\,(\text{stat}) \pm 14\,(\text{syst})$ for ee+0-jet final states and $6 \pm 5\,(\text{stat}) \pm 12\,(\text{syst})$ for $\mu\mu$+0-jet final states. The analysis of the 1-jet category is only conducted in $e\mu$+1-jet final states and the estimated sum of the W+jets and multijet contribution is $120 \pm 15\,(\text{stat}) \pm 50\,(\text{syst})$. The contribution to ee and $\mu\mu$ final states from multijet background is insignificant. For $e\mu$+0-jet final states it is roughly 10% of the estimated W+jets and multijet yield. The stricter selection criteria on $E_{\text{T, Rel}}^{\text{miss}}$, $p_{\text{T}}^{\text{miss}}$ and $\Delta\phi(E_{\text{T}}^{\text{miss}}, p_{\text{T}}^{\text{miss}})$ in same-flavour final states effectively remove the multijet contribution. For $e\mu$+1-jet final states the multijet contribution is at the level of 25% which is larger than for $e\mu$+0-jet final states because of the reduced $E_{\text{T}}^{\text{miss}}$ resolution due to the presence of a jet. The systematic uncertainties on the estimated yields are dominated by the sample dependence uncertainty. Uncertainties from lepton efficiencies can also be large, e.g. in $\mu\mu$+0-jet final states. This is because the loose lepton sample has only little contributions from misidentified muons. The larger fraction of W+jets events in the 0-jet category compared to the 1-jet category translates to relatively lower uncertainties from the lepton efficiency.

7.6 Estimation of Differential W+jets Distributions

For the measurement of differential cross sections and for setting limits on anomalous gauge couplings the background from W+jets and multijet production needs to be estimated differentially. The differential distributions are also determined in a fully data-driven way. Since Eqs. 7.1-7.4 are linear, the background from W+jets and multijet production can be evaluated in single bins of the differential distributions measured. The efficiencies and misidentification rates must not show any dependence on the variable of which the differential cross section is measured. As described in Section 7.3 they are already determined in bins of transverse momentum and pseudorapidity of the leptons.

The lepton identification criteria are known to be sensitive to activity from close-by particles. This is particularly relevant for the angular separation variables $\Delta\phi_{\ell\ell}$ and $\Delta\eta_{\ell\ell}$. For both variables the dependence has been checked and was found to be negligible compared to the overall uncertainty assigned to efficiencies and misidentification rates. Efficiencies as a function of $\Delta\phi_{\ell\ell}$ and $\Delta\eta_{\ell\ell}$ and misidentification rates as a function $\Delta\phi_{\ell,\text{jet}}$ and $\Delta\eta_{\ell,\text{jet}}$ are shown in Fig. 7.10.

Any dependence on further variables can be attributed to a dependence on p_{T}, η, $\Delta\phi_{\ell\ell}$ or $\Delta\eta_{\ell\ell}$. Hence, no further correction or uncertainty is assigned to the shapes of the W+jets and multijet background used for the measurement of the differential W^+W^- production cross sections.

	$e\mu$+0-jet		ee+0-jet		$\mu\mu$+0-jet		$e\mu$+1-jet	
W+jets and multijet	250 ± 140		14 ± 15		6 ± 13		121 ± 52	
simulation (±stat.)	225 ± 24		22.6 ± 9.7		13.6 ± 4.3		114 ± 12	
Source	Uncertainty		Uncertainty		Uncertainty		Uncertainty	
	+	−	+	−	+	−	+	−
statistical	15	15	4.9	4.9	5.0	5.0	15	15
efficiency	37	39	3.2	3.3	9.9	10	22	22
misidentification rate	16	37	3.4	2.9	1.4	6.5	25	33
sample dependence	140	120	18	7.7	3.4	1.8	31	36
total syst.	150	130	19	8.9	11	12	45	54
multijet	22 ± 14		0.20 ± 0.49		1.9 ± 3.6		32 ± 15	
simulation (±stat.)	—		—		—		—	
Source	Uncertainty		Uncertainty		Uncertainty		Uncertainty	
	+	−	+	−	+	−	+	−
statistical	2.2	2.2	0.41	0.41	1.4	1.4	2.6	2.6
efficiency	1.2	1.2	0.05	0.04	0.03	0.02	0.66	0.54
misidentification rate	22	5.2	0.35	0.18	5.3	1.3	21	9.4
sample dependence	—		—		—		—	
total syst.	22	5.3	0.35	0.18	5.3	1.3	21	9.5

Table 7.1: Data-driven estimation of the background from W+jets and multijet production with their statistical and systematic uncertainties. The top part of the table shows the sum of the estimated W+jets and multijet yield, the bottom part shows the estimated multijet yield separately. The uncertainties on misidentification rates are shown separately for the uncertainty of the measurement of misidentification rates and the uncertainty due to sample dependence. The total systematic uncertainty on the estimated yields is obtained by averaging the up and downward uncertainties of the individual sources and adding them quadratically. The estimated yields are shown for $e\mu$, ee and $\mu\mu$ final states for the 0-jet category and for $e\mu$ final states for the 1-jet category.

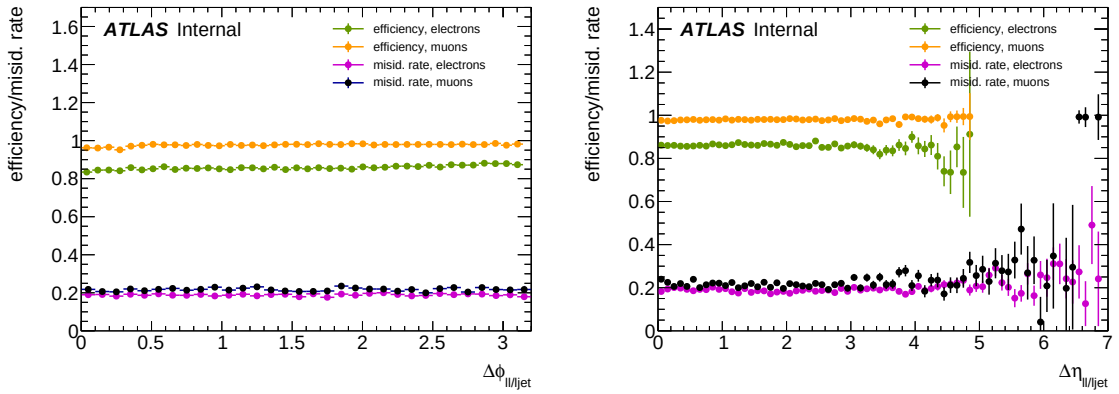

Figure 7.10: Efficiencies and misidentification rates measured as a function of $\Delta\phi_{\ell\ell/\ell\text{jet}}$ (left) and $\Delta\eta_{\ell\ell/\ell\text{jet}}$ (right) for electrons and muons. For the measurement of efficiencies the separation to the other lepton in the event is shown, for the measurement of misidentification rates the separation to the tagging jet is shown.

7.7 Same Charge Control Sample

For a qualitative validation of the estimated W+jets and multijet yields a control sample is defined by replacing the requirement of opposite electric charge between leptons by a requirement of both leptons to have the same electric charge. To avoid contamination from processes that enter the selection when the electron was reconstructed with the wrong charge assignment, electrons are restricted to a pseudorapidity range of $\left|\eta^{e}\right| < 2.01$. As can be seen from Fig. 2.4a the amount of material from the pixel detectors, crucial for discriminating electron tracks and tracks from converted photons, rises for larger values. The resulting data sample has relatively large contributions from W+jets events. Additional contributions originate from diboson processes. The composition of the diboson background is changed with respect to the nominal selection with opposite electrical charge.

Efficiencies are recalculated for this same charge control sample while the central values of the misidentification rates remain unchanged. The sample dependence uncertainty is re-evaluated as well. The $W + c$ production process contributing $\sim 80\%$ to the nominal selection does not contribute to the same charge sample. Therefore the flavour composition in the same charge region differs significantly from that in the nominal selection. The sample dependence uncertainty reduces to $\pm$(10-15)% for electrons and $\pm$18% for muons. Contributions from charge misidentification are treated in the same way as background from $W + \gamma$, i.e. the method is applied to simulated event samples and the resulting yield is subtracted from the yield in the actual estimation. Since charge misidentification cannot be simulated accurately, a systematic uncertainty of $\pm 100\%$ is assigned.

The estimated W+jets and multijet background yields in the same charge sample are shown in Table 7.2 for the 0-jet and 1-jet categories. They are found to be $90 \pm 8\,(\text{stat}) \pm 22\,(\text{syst})$ for $e\mu$+0-jet final states, $14.9 \pm 2.8\,(\text{stat}) \pm 5.3\,(\text{syst})$ for ee+0-jet final states and $7.2 \pm 2.0\,(\text{stat}) \pm 5.4\,(\text{syst})$ for $\mu\mu$+0-jet final states. A quantitative comparison of the estimated yields to the nominal selection with a requirement of opposite electrical charge is difficult since the control sample does not cover the same kinematic phase space. However, the W+jets yield is expected to be significantly lower since gq initial states play a less important role, in particular the $W + c$ contribution is largely reduced when applying a same charge selection. For $e\mu$+1-jet final states the estimated yield is $67 \pm 8\,(\text{stat}) \pm 20\,(\text{syst.})$. The estimation of the background from other diboson processes is purely based on simulated event samples. Systematic uncertainties on the normalisation of these samples are assigned, as described in Section 6.4.3. The yields for the individual diboson processes with their statistical and systematic uncertainties are shown in Table 7.3.

The distributions of the missing transverse momentum, $E_{\mathrm{T}}^{\mathrm{miss}}$, and invariant mass, $m_{\ell\ell}$, in the same charge control region are shown in Figs. 7.11 and 7.12 for the 0-jet and 1-jet categories, respectively. A good overall agreement is found between data and the estimated yield for W+jets, multijet and diboson production.

	$e\mu$+0-jet		ee+0-jet		$\mu\mu$+0-jet		$e\mu$+1-jet	
W+jets and multijet	90 ± 23		14.9 ± 6.0		7.2 ± 5.8		67 ± 21	
simulation (±stat.)	142 ± 35		10.1 ± 5.0		2.5 ± 2.0		52 ± 11	
Source	Uncertainty		Uncertainty		Uncertainty		Uncertainty	
	+	–	+	–	+	–	+	–
statistical	7.8	7.8	2.8	2.8	2.0	2.0	8.1	8.1
charge-fakes	4.8	4.8	0.67	0.67	4.8	4.8	16	16
efficiency	2.0	2.2	0.42	0.55	0.41	0.44	5.3	6.9
misidentification rate	17	14	5.2	3.6	2.0	0.93	3.2	6.7
sample dependence	15	14	2.9	2.6	2.0	1.7	5.4	9.9
total syst.	23	20	6.0	4.5	5.6	5.2	18	21

Table 7.2: Data-driven estimation of the background from W+jets and multijet production in the same charge control sample with their statistical and systematic uncertainties. The uncertainties on misidentification rates are split into the uncertainty of the measurement of misidentification rates and the uncertainty due to sample dependence. The uncertainty on the estimated yields is obtained by averaging the up and downward uncertainties of the individual sources and adding them quadratically. The estimated yields are shown for $e\mu$, ee and $\mu\mu$ final states for the 0-jet category and for $e\mu$ final states for the 1-jet category.

	$e\mu$+0-jet	ee+0-jet	$\mu\mu$+0-jet	$e\mu$+1-jet
data	208 ± 14	11.0 ± 3.3	22.0 ± 4.7	223 ± 15
WZ	62.5 ± 1.8 ± 5.0	2.84 ± 0.39 ± 0.23	16.8 ± 0.92 ± 1.4	85 ± 2 ± 21
$W\gamma^*$	39.1 ± 2.1 ± 7.1	3.36 ± 0.61 ± 0.60	2.93 ± 0.59 ± 0.53	27.1 ± 1.8 ± 8.3
$W\gamma$	31.1 ± 2.4 ± 9.3	2.39 ± 0.63 ± 0.72	—	27 ± 2 ± 14
ZZ	1.56 ± 0.07 ± 0.20	0.06 ± 0.03 ± 0.01	0.41 ± 0.03 ± 0.05	4.7 ± 0.1 ± 1.1
non-prompt	4.54 ± 0.86 ± n.a.	0.81 ± 0.21 ± n.a.	0.41 ± 0.42 ± n.a.	9.3 ± 1.6 ± n.a.
W+jets	90 ± 8 ± 22	14.9 ± 2.8 ± 5.3	7.2 ± 2.0 ± 5.4	67 ± 8 ± 20

Table 7.3: Contributions from other diboson processes to the same charge control region with statistical and systematic uncertainties. The yields are estimated from simulated event samples. Systematic uncertainties are assigned on the cross sections and acceptances of the diboson processes and identical to those discussed in Section 6.4.3. The estimated W+jets and multijet yield is also shown.

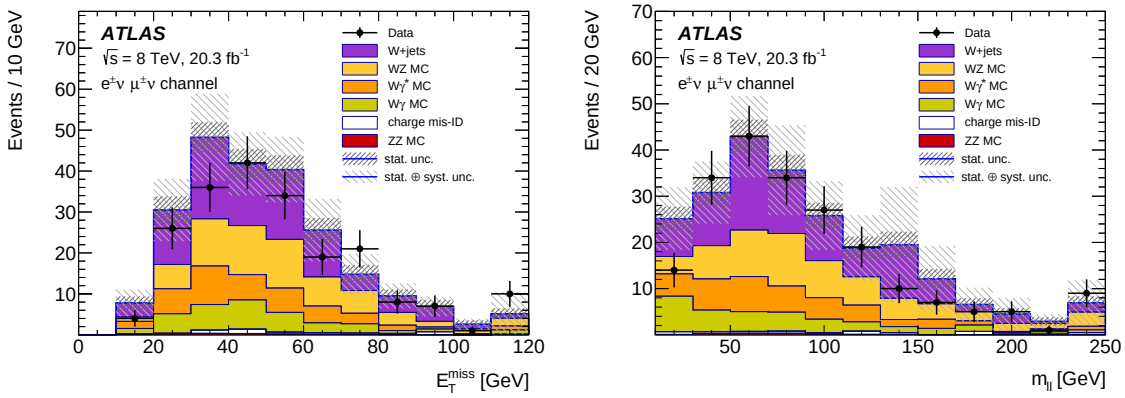

Figure 7.11: Distributions of the missing transverse momentum $E_{\mathrm{T}}^{\mathrm{miss}}$ (left) and invariant mass $m_{\ell\ell}$ (right) in the same charge control sample for the 0-jet category. The uncertainty bands show statistical and systematic uncertainties on the estimation of the W+jets and multijet background as well as the theoretical systematic uncertainties assigned on the cross sections and acceptances of the diboson processes. Experimental systematic uncertainties for the diboson processes are not included. Previously published in Ref. [5].

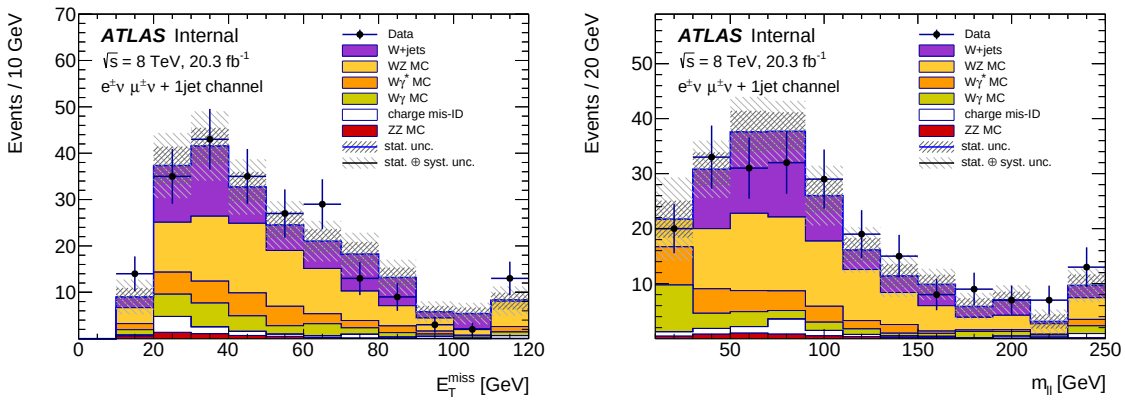

Figure 7.12: Distributions of the missing transverse momentum $E_{\mathrm{T}}^{\mathrm{miss}}$ (left) and invariant mass $m_{\ell\ell}$ (right) in the same charge control sample for the 1-jet category. The uncertainty bands show statistical and systematic uncertainties on the estimation of the W+jets and multijet background as well as the theoretical systematic uncertainties assigned on the cross sections and acceptances of the diboson processes. Experimental systematic uncertainties for the diboson processes are not included.

8 Estimation of the $Z \to \ell\ell$ Background

Background from $pp \to Z/\gamma^* \to \ell\ell$ production represents a significant fraction of the total background. The choice of kinematic event selection criteria for the analysis is largely driven by the need to reject contributions from this process.

The nature of the contribution of the $Z/\gamma^* \to \ell\ell$ process to the selected W^+W^- candidate events is different for the measurement in different final states. The ee and $\mu\mu$ final states involve prompt leptons from Z/γ^* decays while $e\mu$ final states receive contributions from $Z \to \tau\tau$ decays mainly. The production rate for $Z \to \tau\tau$ events with a subsequent decay to leptons $\tau \to \ell\nu_\ell\nu_\tau$ is only roughly 3% of the $Z \to ee$ or $\mu\mu$ production rates. For the decay modes involving prompt electrons and muons, events can only contribute to the selected W^+W^- candidate events if large missing transverse momentum is induced by fluctuations due to pile-up. If electrons and muons are produced in τ-lepton decays, the events feature non-prompt electrons and muons and genuine missing transverse momentum, $p_{\mathrm{T}}^{\mathrm{miss}}$, from neutrinos.

8.1 Methodology

The estimation of the background from $pp \to Z/\gamma^* \to \ell\ell$ production, which in the following is referred to as $Z \to \ell\ell$, relies on a kinematic region that is enriched in $Z \to \ell\ell$ events and that is statistically independent of the nominal W^+W^- sample. An auxiliary fit of simulated signal and background events is performed in the samples defined by the nominal selection requirements, the signal sample (SR), and the sample enriched in events from $Z \to \ell\ell$ production, the so-called control sample (CR). The approach can be expressed by:

$$n^{\mathrm{data}}_{Z\to\ell\ell}(\mathrm{SR}) = n^{\mathrm{data}}_{Z\to\ell\ell}(\mathrm{CR}) \cdot \beta. \tag{8.1}$$

The number of $Z \to \ell\ell$ events in the signal sample $n^{\mathrm{data}}_{Z\to\ell\ell}(\mathrm{SR})$ is obtained from the number of $Z \to \ell\ell$ events in the control sample $n^{\mathrm{data}}_{Z\to\ell\ell}(\mathrm{CR})$ by multiplying with an extrapolation factor defined as the ratio of $Z \to \ell\ell$ events in signal and control samples:

$$\beta = \frac{n^{\mathrm{MC}}_{Z\to\ell\ell}(\mathrm{SR})}{n^{\mathrm{MC}}_{Z\to\ell\ell}(\mathrm{CR})}. \tag{8.2}$$

The calculation of the extrapolation factor β relies on simulated event samples.

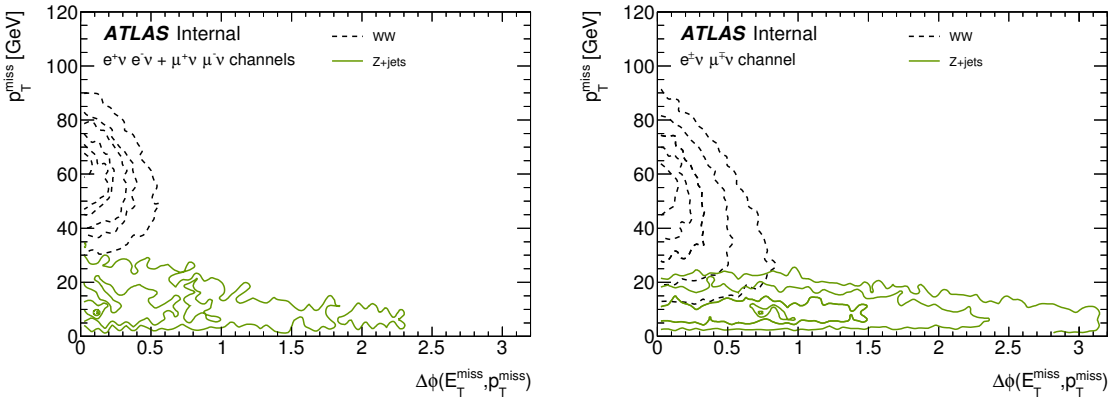

Figure 8.1: Distribution of simulated events of W^+W^- and $Z \to \ell\ell$ production as a function of the track-based measurement of the missing transverse momentum, $p_{\mathrm{T}}^{\mathrm{miss}}$, and the angular separation between track and calorimeter-based measurement, $\Delta\phi(E_{\mathrm{T}}^{\mathrm{miss}}, p_{\mathrm{T}}^{\mathrm{miss}})$. The distributions are shown as contours. All selection requirements are applied except for those on the two variables shown. The distributions for the combined $ee + \mu\mu$ (left) and $e\mu$ final states (right) are shown for the 0-jet category. Both variables exhibit only little correlation and a high level of discrimination between signal and $Z \to \ell\ell$ background.

8.2 Definition of Signal and Control Samples

The choice of the criteria used to select the control sample is driven by the desire to have a precise estimate. In order to achieve this, small statistical uncertainties on the $Z \to \ell\ell$ yield in the control sample $n_{Z\to\ell\ell}^{\mathrm{data}}(\mathrm{CR})$ and small systematic uncertainties on the extrapolation factor β are necessary. The latter is met by choosing the control sample with selection criteria similar to the the selection criteria of the signal sample. A convenient way to enrich the control sample in events from $Z \to \ell\ell$ production is by reverting the requirement on the track-based measurement of the missing transverse momentum, $p_{\mathrm{T}}^{\mathrm{miss}} < 20$ GeV and $p_{\mathrm{T}}^{\mathrm{miss}} < 45$ GeV for $e\mu$ and $ee/\mu\mu$ final states, respectively. In addition, a lower bound on $p_{\mathrm{T}}^{\mathrm{miss}} > 5$ GeV is introduced and the requirement on the angular separation between calorimeter and track-based measurement of the missing transverse momentum is removed. Reverting either of the requirements on the missing transverse momentum yields a data sample with large contributions from $Z \to \ell\ell$ events. The purity of the event sample is higher when reverting the criterion on the track-based measurement of the missing transverse momentum and it is therefore favoured for the definition of the control sample. In addition, the track-based measurement is less sensitive to uncertainties in the jet energy scale and resolution since only the tracks of the jets are used in the calculation. Both variables used to define the control samples are found to be modelled well by simulated event samples and exhibit only little correlation as can be seen in Fig. 8.1.

The purity of the control samples in contributions from $Z \to \ell\ell$ production is roughly 85% for $e\mu$+0-jet final states and 95% for ee and $\mu\mu$+0-jet final states. For $e\mu$+1-jet final states the purity is slightly reduced to 75% due to the additional contributions from top-quark production.

8.3 Simulated Event Samples and Systematic Uncertainties

The simulated event samples used for the estimation of background from $Z \to \ell\ell$ production are produced separately for low values of the invariant mass $10 < m_{\ell\ell} < 60$ GeV and high values $m_{\ell\ell} > 60$ GeV. Both sets of simulated event samples are generated with Alpgen but with different parton shower models. For ee and $\mu\mu$ final states the event samples with low invariant mass are produced with Herwig and event samples with high invariant mass are produced with Pythia6. The same settings are used for the simulated $Z \to \tau\tau$ samples in the 1-jet category. In the 0-jet category a large simulated $Z \to \tau\tau$ sample is necessary to obtain differential distributions with high statistical precision in order to measure differential cross sections. A large sample of simulated Alpgen+Herwig events is available and used to model $Z \to \tau\tau$ decays in the 0-jet category.

Systematic uncertainties enter the estimation of the background from $Z \to \ell\ell$ production via the extrapolation factor β defined in Eq. 8.2. Systematic uncertainties common to signal and control sample cancel in the ratio, in particular uncertainties on the overall $Z \to \ell\ell$ normalisation. Since missing transverse momentum is introduced in $Z \to \ell\ell$ events by experimental effects, experimental systematic uncertainties are expected to dominate the estimation of the $Z \to \ell\ell$ background. Nevertheless, a theoretical uncertainty of $\pm 3.5\%$ is assigned from variations of renormalisation and factorisation scales. As there is no genuine missing transverse momentum in $Z \to \ell\ell$ events, the same uncertainty is assigned in both the signal and the control samples and no impact on the $\Delta\phi(E_{\mathrm{T}}^{\mathrm{miss}}, p_{\mathrm{T}}^{\mathrm{miss}})$ distribution is expected. The effect of the choice of the parton shower model is tested by exchanging the event samples simulated with Alpgen+Pythia by event samples simulated with Alpgen+Herwig and vice versa.

Experimental systematic uncertainties are assigned on the reconstruction and calibration of leptons, jets and the calorimeter and track-based measurements of the missing transverse momentum. These uncertainties are assigned in a correlated way to the simulated W^+W^- and $Z \to \ell\ell$ event samples in the signal and control samples. Additional uncertainties arise from the background from the production of top, W+jets and other diboson processes. The same uncertainties as in the nominal analysis are assigned in the signal region. An uncertainty of $\pm 20\%$ and $\pm 100\%$ is assigned to the top and W+jets backgrounds in the control samples, respectively. For the diboson processes theoretical uncertainties are assigned as described in Section 6.4.3.

8.4 Fit of the $Z \to \ell\ell$ Yield and Results

The methodology described in Eq. 8.1 is implemented in a fit of the W^+W^- and $Z \to \ell\ell$ yields performed simultaneously in the signal and the control samples. The control sample is dominated by $Z \to \ell\ell$ events but receives significant contributions from signal events. It is for this reason that the fit is performed in the signal and control samples simultaneously, including both the normalisation of signal and $Z \to \ell\ell$ background as free parameters. The approach avoids any assumption on the absolute signal normalisation which is measured

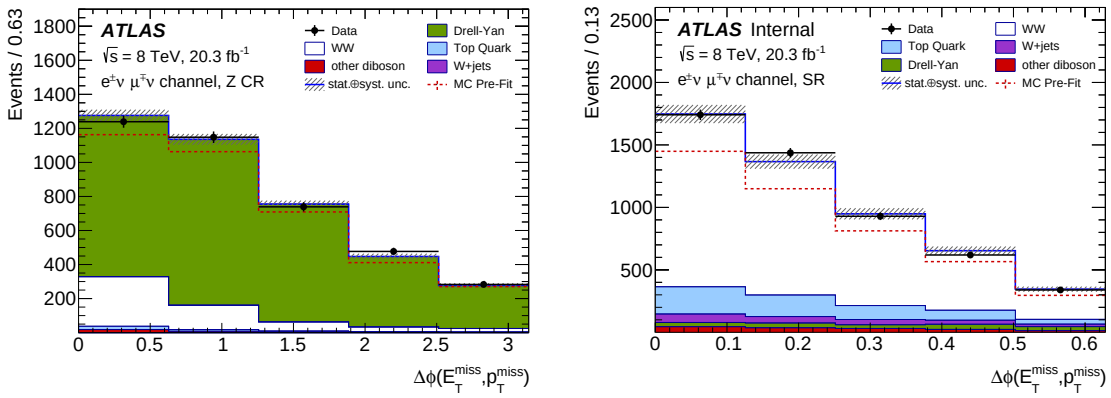

Figure 8.2: The $\Delta\phi(E_{\mathrm{T}}^{\mathrm{miss}}, p_{\mathrm{T}}^{\mathrm{miss}})$ distributions in the control sample (left) and in the sample of W^+W^- candidate events (right) used for the estimation of the background from $Z \to \ell\ell$ production in $e\mu$+0-jet final states. The distributions of simulated event samples are constrained by the likelihood fit. The sum of these distributions before the fit are overlaid as dashed red line. The post-fit distributions give an improved description of the data. The W^+W^- signal contribution is left to float in the fit. Previously published in Ref. [5].

in this analysis. The fit is performed in five bins of the distribution of the azimuthal separation of the calorimeter-based and the track-based measurements of the missing transverse momentum, $\Delta\phi(E_{\mathrm{T}}^{\mathrm{miss}}, p_{\mathrm{T}}^{\mathrm{miss}})$, to have a further discrimination of the W^+W^- and $Z \to \ell\ell$ production processes.

The fit is based on a profile likelihood approach. The likelihood function is of a similar form as Eq. 9.17. It is given by the product of Poisson probabilities in the signal and control samples for $n_{\mathrm{sig}} + n_{Z\to\ell\ell}$ to produce $n_{\mathrm{data}}^{\mathrm{SR}}$ and $n_{\mathrm{data}}^{\mathrm{CR}}$ events. The variables n_{sig} and $n_{Z\to\ell\ell}$ are the numbers of signal and $Z \to \ell\ell$ events, respectively, and $n_{\mathrm{data}}^{\mathrm{SR}}$ and $n_{\mathrm{data}}^{\mathrm{CR}}$ are the numbers of events observed in data in the signal and control samples, respectively. Systematic uncertainties are included in the likelihood function as nuisance parameters constrained by Gaussian distributions. Only the $Z \to \ell\ell$ yield is obtained in this fit and used further in the analysis.

The kinematic distributions, before and after the fit in the signal and control samples, are shown in Figs. 8.2-8.4. The simultaneous fit improves the agreement with data both by adjusting the normalisation of the simulated event samples and by adjusting the central values of the nuisance parameters accounting for systematic uncertainties. The $Z \to \ell\ell$ yields estimated in data are compared in Table 8.1 to the yields expected from simulated event samples together with the normalisation factor obtained in the fit. The estimated yields for the background from $Z \to \ell\ell$ production for the 0-jet category are $175 \pm 3(\mathrm{stat.}) \pm 18(\mathrm{syst.})$ for $e\mu$ final states, $28 \pm 1(\mathrm{stat.}) \pm 13(\mathrm{syst.})$ for ee final states and $33 \pm 1(\mathrm{stat.})) \pm 17(\mathrm{syst.})$ for $\mu\mu$ final states. The estimated $Z \to \ell\ell$ yield for $e\mu$+1-jet final states is $267 \pm 12(\mathrm{stat.})) \pm 49(\mathrm{syst.})$.

The fitted $Z \to \ell\ell$ yield differs from the product of fitted normalisation parameter and the $Z \to \ell\ell$ yield expected from simulated event samples since the fit also includes the

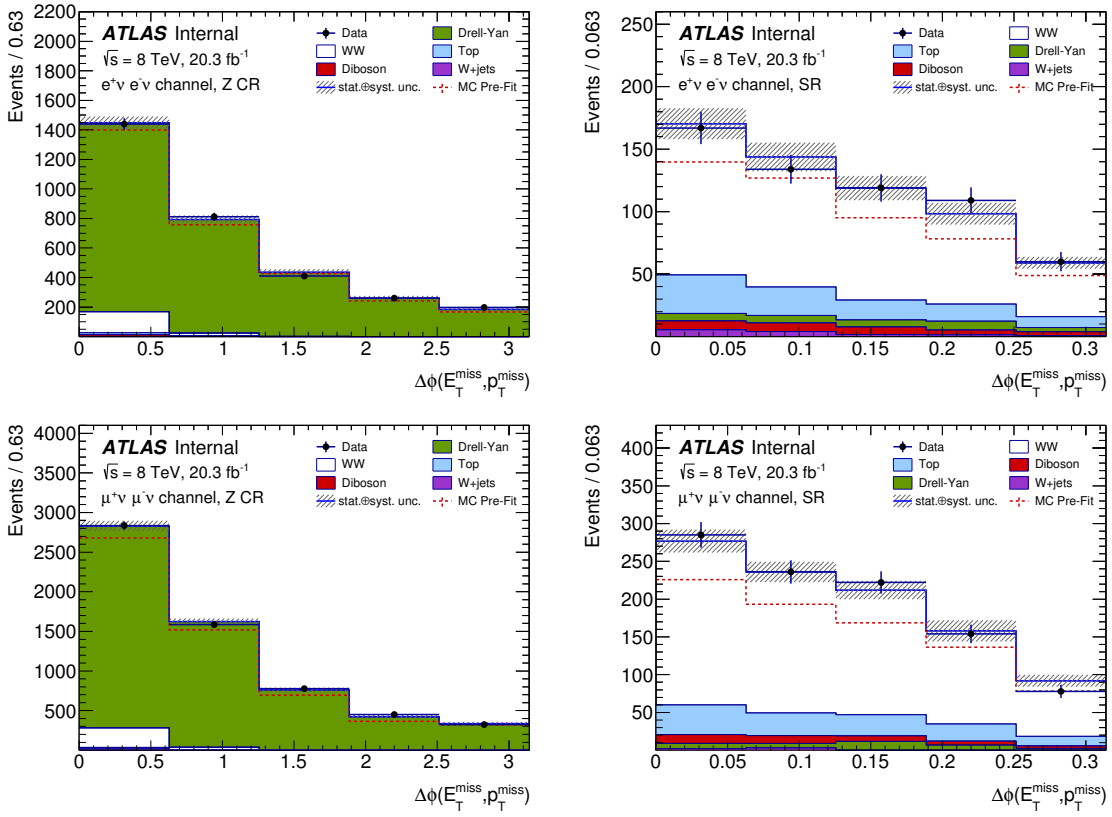

Figure 8.3: The $\Delta\phi(E_{\mathrm{T}}^{\mathrm{miss}}, p_{\mathrm{T}}^{\mathrm{miss}})$ distributions in the control sample (left) and in the sample of W^+W^- candidate events (right) used for the estimation of the background from $Z \to \ell\ell$ production in ee+0-jet final states (top) and $\mu\mu$+0-jet final states (bottom). The distributions of simulated event samples are constrained by the likelihood fit. The sum of these distributions before the fit are overlaid as dashed red line. The post-fit distributions give an improved description of the data. The W^+W^- signal contribution is left to float in the fit.

	$e\mu$+0-jet	ee+0-jet	$\mu\mu$+0-jet	$e\mu$+1-jet
simulation	173 ± 23	26 ± 19	42 ± 22	288 ± 77
fitted $Z \to \ell\ell$ yield	175 ± 18	28 ± 13	33 ± 17	267 ± 50
fitted normalisation factor	$1.06^{+0.09}_{-0.08}$	$0.95^{+0.18}_{-0.14}$	$1.11^{+0.23}_{-0.17}$	$1.02^{+0.16}_{-0.14}$

Table 8.1: Contributions from $Z \to \ell\ell$ production to the selected W^+W^- candidate events. The yields expected from simulated event samples and estimated in the simultaneous fit are shown, as well as the fitted normalisation factors. Since the nuisance parameters are allowed to vary in the fit the yield predicted by simulation and the fitted normalisation factor do not factorise to the fitted yield.

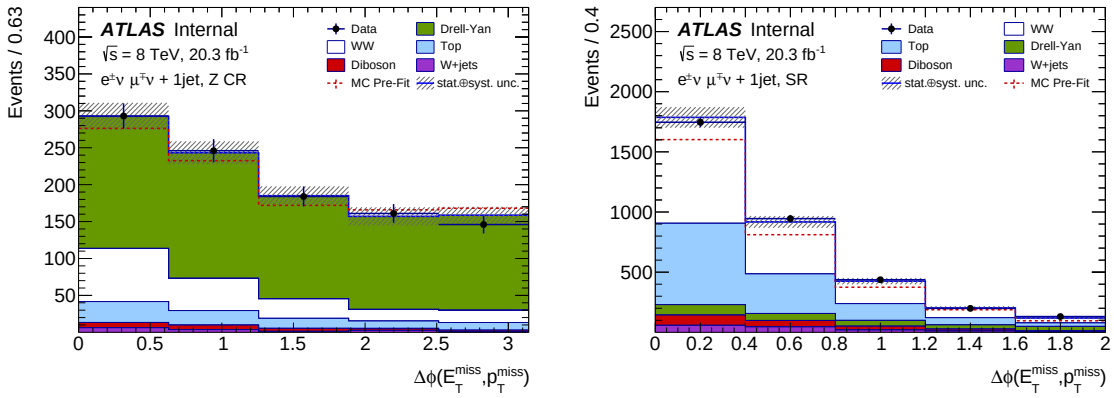

Figure 8.4: The $\Delta\phi(E_{\mathrm{T}}^{\mathrm{miss}}, p_{\mathrm{T}}^{\mathrm{miss}})$ distributions for the control sample (left) and the W^+W^- candidate samples (right) used for the estimation of the $Z \to \ell\ell$ background in $e\mu$+1-jet final states. The distributions of simulated event samples is constrained by the likelihood fit. The sum of these distributions before the fit are overlaid as dashed red line. The post-fit distributions give an improved description of the data. The W^+W^- signal contribution is left to float in the fit.

systematic uncertainties as nuisance parameters. If nuisance parameters are fitted to values different from their nominal value they affect the fitted yield, e.g. a nuisance parameter corresponding to a systematic uncertainty of ±5% will alter the yield by ±1% if fitted at $\hat{\theta}_{\mathrm{NP}} = 0.2$. This feature is most apparent for $e\mu$+1-jet final states where the fitted $Z \to \ell\ell$ yield is lower than the yield predicted in simulation although the normalisation factor is larger than unity. The uncertainty from parton shower modelling corresponds to a ∓18% uncertainty prior to fitting. The corresponding nuisance parameter is fitted at a value of $\hat{\theta} = 0.85^{+0.76}_{-0.78}$ which together with the $Z \to \ell\ell$ normalisation factor of $\mu = 1.02$ roughly results in the estimated yield.

The statistical and systematic uncertainties on the estimated yield from $Z \to \ell\ell$ production are shown together with the shifts of the corresponding nuisance parameters in Tables 8.2 and 8.3. The statistical uncertainty shown is due to the limited amount of data in the control sample. It is determined by repeating the fit with nuisance parameters fixed at their fitted values and only the signal and $Z \to \ell\ell$ normalisation factors are left floating. The systematic uncertainty originating from a certain source is assessed by varying the corresponding nuisance parameter within the uncertainty and repeating the fit. The dominant systematic uncertainties are from jet energy scale and resolution, calorimeter and track-based missing transverse momentum scale and resolution, and the parton-shower model used for the simulation of $Z \to \ell\ell$ events. The estimated $Z \to \ell\ell$ yields in the ee and $\mu\mu$ final states are found to have much larger uncertainties than those in $e\mu$ final states since the requirements made on the missing transverse momentum are much stricter. Other systematic uncertainties can be of the same size as some of those shown in Tables 8.2 and 8.3, e.g. lepton reconstruction uncertainties for the ee and $\mu\mu$ final states. They are, however, small compared to the uncertainties shown on $E_{\mathrm{T}}^{\mathrm{miss}}$ and not shown in the tables.

	$e\mu$+0-jet			ee+0-jet			$\mu\mu$+0-jet		
Source	Uncertainty [%]		Shift	Uncertainty [%]		Shift	Uncertainty [%]		Shift
	+	−	$\hat{\theta}(\sigma)$	+	−	$\hat{\theta}(\sigma)$	+	−	$\hat{\theta}(\sigma)$
statistical	1.92	1.92		1.94	1.94		1.38	1.38	
JES Np1	0.62	0.71		1.08	1.45		1.45	1.38	
JES Np2	1.40	1.36		8.36	9.09		11.24	12.29	
JES Np3	0.53	0.65		1.40	1.91		3.58	3.00	
JES Np4	0.09	0.40		1.89	2.17		1.28	2.20	
JES Np5	0.03	0.09		0.98	1.06		0.12	0.43	
JES Np6	0.02	0.11		0.04	0.04		0.12	0.02	
JER	1.08	1.05		41.17	41.89		35.41	21.43	
$E_{\mathrm{T}}^{\mathrm{miss}}$ reso.	1.11	2.10		4.55	7.37		3.30	3.23	
$E_{\mathrm{T}}^{\mathrm{miss}}$ scale	4.55	6.54		10.94	10.26		7.69	6.42	
$p_{\mathrm{T}}^{\mathrm{miss}}$ reso.	0.24	1.60		13.48	15.42		6.10	3.87	
$p_{\mathrm{T}}^{\mathrm{miss}}$ scale	5.02	5.18		10.24	10.53		40.92	38.70	
parton-shower	4.48	4.61		4.24	4.95		2.01	2.98	
			-1 0 1			-1 0 1			-1 0 1

Table 8.2: Systematic uncertainties in the estimation of background from $Z \to \ell\ell$ production in the 0-jet category for $e\mu$, ee and $\mu\mu$ final states. The first two columns for a given final state show the systematic uncertainty on the estimated $Z \to \ell\ell$ yield, the third column shows the value at which the corresponding nuisance parameter is fitted with its uncertainty. The statistical uncertainty originating from the limited amount of data in the control sample is shown in the first row. Systematic uncertainties on the jet energy scale (JES) and resolution (JER), scale and resolution of the calorimeter and track-based measurement of $p_{\mathrm{T}}^{\mathrm{miss}}$, and from parton shower modelling are also shown.

	$e\mu$+1-jet		
Source	Uncertainty [%]		Shift
	+	−	$\hat{\theta}(\sigma)$
statistical	4.49	4.49	
JES Np1	1.70	1.74	
JES Np2	3.53	3.72	
JES Np3	0.32	0.38	
JES Np4	1.01	0.84	
JES Np5	0.03	0.02	
JES Np6	0.95	1.07	
JER	1.32	1.60	
$E_{\mathrm{T}}^{\mathrm{miss}}$ reso.	3.71	4.08	
$E_{\mathrm{T}}^{\mathrm{miss}}$ scale	0.63	0.65	
$p_{\mathrm{T}}^{\mathrm{miss}}$ reso.	5.47	6.32	
$p_{\mathrm{T}}^{\mathrm{miss}}$ scale	2.68	3.15	
parton-shower	11.45	13.03	
			-1 0 1

Table 8.3: Systematic uncertainties in the estimation of background from $Z \to \ell\ell$ production in the 1-jet category for $e\mu$ final states. The first two columns for a given final state show the systematic uncertainty on the estimated $Z \to \ell\ell$ yield, the third column shows the value at which the corresponding nuisance parameter is fitted with its uncertainty. The statistical uncertainty originating from the limited amount of data in the control sample is shown in the first row. Systematic uncertainties on the jet energy scale (JER) and resolution (JES), scale and resolution of the calorimeter and track-based measurement of $p_{\mathrm{T}}^{\mathrm{miss}}$, and from parton shower modelling are also shown.

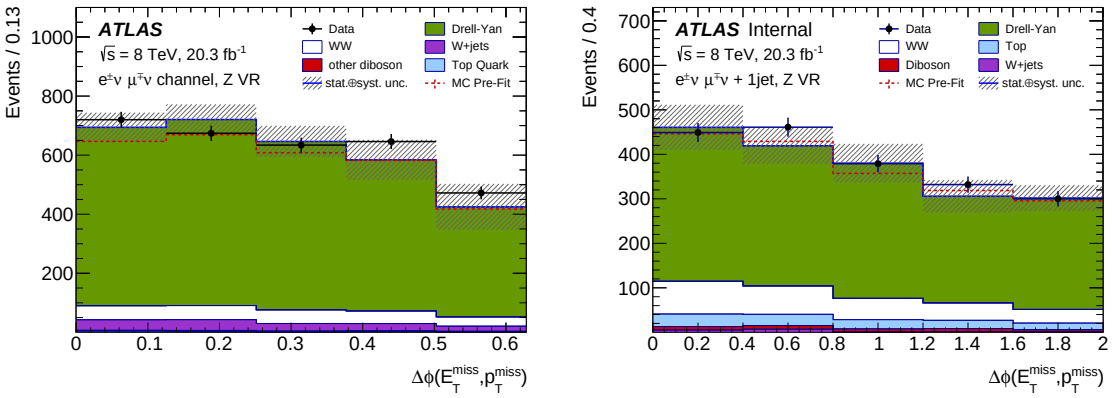

Figure 8.5: Estimated background from $Z \to \ell\ell$ production in the validation sample. The $Z \to \ell\ell$ distributions are obtained by applying the normalisation factors and nuisance parameters from the nominal fit to simulated samples. The distributions are shown for $e\mu$ final states in the 0-jet category (left) and the 1-jet category (right). Previously published in Ref. [5].

8.5 Validation in a Second Control Sample

The method used to estimate the background from $Z \to \ell\ell$ production is validated in a third sample which is statistically independent of both the signal and the control samples. It is selected by reverting the criteria on the calorimeter and the track-based measurements of the missing transverse momentum. This second control sample is further referred to as the validation sample. The fitted values of the normalisation factors and nuisance parameters obtained in the fit in the signal and control samples are applied to the simulated events selected in the validation sample. Reverting the calorimeter-based measurement of the missing transverse momentum give a validation of the fitted nuisance parameters for scale and resolution, in particular. The resulting $\Delta\phi(E_{\mathrm{T}}^{\mathrm{miss}}, p_{\mathrm{T}}^{\mathrm{miss}})$ distribution in the validation sample is shown in Fig. 8.5 for $e\mu$+0-jet and $e\mu$+1-jet final states. Within the systematic uncertainties good agreement between the distributions in data and simulated background events is observed.

8.6 Estimation of Differential $Z \to \ell\ell$ Distributions

For the measurement of differential cross sections, differential $Z \to \ell\ell$ distributions are estimated. A method similar to the validation procedure described in Section 8.5 is used, i.e. normalisation factors and nuisance parameters obtained in the $Z \to \ell\ell$ background estimation are applied to kinematic distributions from simulated $Z \to \ell\ell$ events. The resulting differential transverse momentum distribution is shown in Fig. 8.6 in the signal sample and the validation sample. For the signal sample, the distribution of the leading lepton, p_{T}, is compared before and after applying the normalisation factors and nuisance parameters resulting from the fit to the distribution predicted by simulation. The uncertainties shown include uncertainties propagated from the fit. The $Z \to \ell\ell$ distribution in the valida-

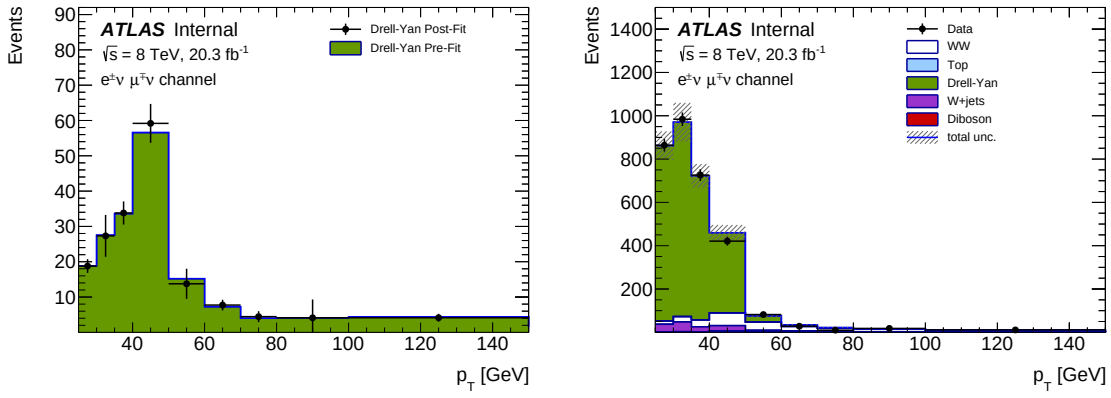

(a) (b)

Figure 8.6: Distributions of the transverse momentum of the transverse momentum of the leading lepton, p_{T}. (a) Shown is a comparison of simulated $Z \to \ell\ell$ events selected with the nominal W^+W^- criteria with and without applying the normalisation factors and nuisance parameters resulting from the fit used to estimate the yield from $Z \to \ell\ell$ production. (b) Comparison of data and the estimated differential $Z \to \ell\ell$ yield in the validation sample.

tion sample is shown with backgrounds from other processes and compared to data. Good overall agreement is seen between data and simulated event samples. Bins with larger differences receive significant contributions from other background processes, too.

9 Cross-Section Measurement

The event yields measured by the ATLAS detector need to be translated into detector-independent observables. The methodology used to calculate experimental results is presented in Section 9.1. Furthermore, the sources of uncertainties in the determination of the results are discussed in Sections 9.2 and 9.3. The methodology of the combination of results from different final states is presented in Section 9.4. Whenever a different treatment is needed for the analyses based on 0-jet and 1-jet final states, references are made to Chapters 10 and 11. Chapter 10 describes the results from 0-jet final states, Chapter 11 concentrates on $e\mu$+1-jet final states and combined results together with $e\mu$+0-jet final states.

9.1 Methodology

The calculation of the cross sections is performed in two steps. First, cross sections are calculated for each of the individual final states in the fiducial phase space defined by the kinematic constraints imposed in the selection of W^+W^- candidate events. The fiducial cross sections are then extrapolated to the total phase space and combined between measurements from individual final states.

9.1.1 Fiducial and Total Cross Sections

Both, total cross sections and fiducial cross sections for W boson pair production are measured. The fiducial cross sections are determined individually for the $e\mu$, ee and $\mu\mu$ final states from the number of W^+W^- candidate events observed in data, N^{obs}, and the estimated number of events from background contributions, N^{bkg}, or the number of signal events, $N^{\text{sig}} = N^{\text{obs}} - N^{\text{bkg}}$:

$$\sigma^{\text{fid}}\left(pp \to WW \to \ell\nu\ell'\nu\right) = \frac{N^{\text{obs}} - N^{\text{bkg}}}{C_{WW\to\ell\nu\ell'\nu} \times \mathcal{L}} = \frac{N^{\text{sig}}}{C_{WW\to\ell\nu\ell'\nu} \times \mathcal{L}} \tag{9.1}$$

with the efficiency correction factor $C_{WW\to\ell\nu\ell'\nu}$ and the integrated luminosity $\mathcal{L}$. The efficiency correction factor $C_{WW\to\ell\nu\ell'\nu}$ accounts for detector effects in the event reconstruction, e.g. efficiencies of the particle reconstruction and the detector response. It is defined in Section 9.1.2.

Based on the measured fiducial cross sections, the total $pp \to W^+W^-$ production cross

section is calculated from the fiducial cross sections as:

$$\sigma^{\text{tot}}(pp \to WW) = \frac{\sigma^{\text{fid}}\left(pp \to WW \to \ell\nu\ell'\nu\right)}{A_{WW\to\ell\nu\ell'\nu} \times \mathcal{B}^2(W \to \ell\nu)} \tag{9.2}$$

$$= \frac{N^{\text{obs}} - N^{\text{bkg}}}{A_{WW\to\ell\nu\ell'\nu} \times C_{WW\to\ell\nu\ell'\nu} \times \mathcal{B}^2(W \to \ell\nu) \times \mathcal{L}}\,. \tag{9.3}$$

The kinematic constraints from the selection criteria imposed in the analysis are accounted for in the acceptance correction factor $A_{WW\to\ell\nu\ell'\nu}$ that is introduced in Section 9.1.3. While the fiducial cross sections are defined as the cross sections of W boson pair production with a subsequent leptonic decay, $W \to \ell\nu$, the total cross section is corrected for the $W \to \ell\nu$ branching fraction $\mathcal{B}(W \to \ell\nu) = 0.1083$ [123].

9.1.2 Experimental Efficiency C_{WW}

The efficiency correction factor $C_{WW\to\ell\nu\ell'\nu}$ accounts for experimental effects. It is calculated on simulated event samples as the ratio of the number of events that are reconstructed and satisfy the W^+W^- selection criteria, $N_{\text{reco}}^{WW\to\ell\nu\ell'}$, and the number of events generated in the fiducial phase space $N_{\text{gen, fid}}^{WW\to\ell\nu\ell'\nu}$:

$$C_{WW\to\ell\nu\ell'\nu} = \frac{N_{\text{reco}}^{WW\to\ell''\nu\ell'''}}{N_{\text{gen, fid}}^{WW\to\ell\nu\ell'\nu}}, \quad \text{with } \ell, \ell' = e, \mu \text{ and } \ell'', \ell''' = e, \mu, \tau. \tag{9.4}$$

The efficiency correction factor $C_{WW\to\ell\nu\ell'\nu}$ accounts for detector inefficiencies, resolution and migration effects. Most notably, the numerator contains all simulated events from $W \to \ell\nu$, $\ell = e, \mu, \tau$, decays while the denominator only contains events from prompt $W \to \ell\nu$, $\ell = e, \mu$, decays into $e\mu$, ee and $\mu\mu$ final states. Thus, the correction factor implies a subtraction of the relative fraction of $WW \to \ell\nu\tau\nu$, $\ell = e, \mu, \tau$, events contributing to the selected W^+W^- candidate events. The approach relies on the correct modelling of the $W \to \tau\nu$ branching fraction and the kinematic properties of these decays. Assumptions on the cross section $\sigma^{\text{tot}}(pp \to WW)$ are not made unlike in the alternative approach of subtracting the number of events predicted by simulated event samples which is frequently used in other analyses, e.g. in Ref. [165].

For the definition of the fiducial phase space the selection criteria listed in Section 6.1 are translated to generator level quantities and shown in Table 9.1. For the constraints on the lepton and dilepton quantities equivalent selection criteria are placed on the generated leptons which are merged with collinear photons from final state radiation. Whereas the quantities of the reconstructed missing transverse momentum, $E_{\text{T, Rel}}^{\text{miss}}$ and $p_{\text{T}}^{\text{miss}}$, are calculated as the negative vectorial sum of all energy depositions in the detector, the corresponding quantity at the event generation stage is defined as the vectorial sum of the transverse momenta of the neutrinos. The selection requirement on the azimuthal separation between the calorimeter and track-based measurements of the missing transverse momentum, $\Delta\phi(E_{\text{T}}^{\text{miss}}, p_{\text{T}}^{\text{miss}})$, is not included in the definition of the fiducial phase space since both quantities are identical at the event generation stage. The selection criteria on

	$e\mu$+0-jet	ee and $\mu\mu$+0-jet	$e\mu$+1-jet
p_{T}^{ℓ} (leading and sub-leading)	$> 25/20$ GeV		
η^{ℓ}	$\lvert\eta^{\mu}\rvert < 2.4$ and $\lvert\eta^{e}\rvert < 2.47$, excluding $1.37 < \lvert\eta^{e}\rvert < 1.52$		
$m_{\ell\ell}$	> 10 GeV	> 15 GeV	> 10 GeV
$\lvert m_Z - m_{\ell\ell}\rvert$	—	> 15 GeV	—
number of jets with $p_{\mathrm{T}} > 25$ GeV, $\lvert\eta\rvert < 4.5$	0	0	1
$\lvert\sum \vec{p}_{\mathrm{T}}^{\,\nu_i}\rvert$	> 20 GeV	> 45 GeV	> 20 GeV
$\lvert\sum \vec{p}_{\mathrm{T}}^{\,\nu_i}\rvert$ ($\times \sin(\Delta\phi_\ell)$ if $\Delta\phi_\ell < \pi/2$)	> 15 GeV	> 45 GeV	> 15 GeV

Table 9.1: Kinematic constraints that define the fiducial phase space for $e\mu$, ee and $\mu\mu$ final states. Criteria equivalent to the selection criteria on the reconstructed leptons and the dilepton system are applied on quantities defined using information at the event generation stage. The missing transverse momentum at the event generation stage is defined as the vectorial sum of the transverse momenta of the neutrinos $\lvert\sum \vec{p}_{\mathrm{T}}^{\,\nu_i}\rvert$. For an equivalent selection to $E_{\mathrm{T,\,Rel}}^{\mathrm{miss}}$ the vectorial sum of the transverse momenta of the neutrinos is projected on the closest lepton, where $\Delta\phi_\ell$ is the azimuthal separation to this lepton.

generator level closely correspond to the detector level selection. The efficiency correction factor C_{WW} and the measured fiducial cross sections therefore exhibit only minimal dependence on theoretical calculations. The numerical values of the efficiency correction factors C_{WW} are shown in Table 9.2.

The efficiency correction factor C_{WW} also account for events generated outside of the fiducial phase space but reconstructed in the kinematic phase space. This can cause a bias in the measurement of fiducial cross sections if these migrations are large and are not described properly by simulation. Migration effects are typically particularly large for differential measurements. They can be implemented in Eq. 9.1 by replacing the efficiency correction factor C_{WW} by a matrix R_{ij} that in addition describes the migration of events generated in interval j and reconstructed in interval i. The fiducial cross section in interval j is given by:

$$\sigma_j^{\mathrm{fid}}\left(pp \to WW \to \ell\nu\ell'\nu\right) = \frac{1}{\mathcal{L}} \sum_i R_{ij}^{-1} N_i^{\mathrm{sig}} \tag{9.5}$$

and depends on the observed event yields in all intervals i. The matrix R_{ij} is defined as the probability to reconstruct events generated with a value t to be reconstructed with a value r in the intervals Δt and Δr. Analogously to the efficiency correction factor C_{WW} in Eq. 9.4, the matrix R_{ij} is calculated on simulated event samples as the ratio of reconstructed and generated events but using information at the event generation stage in both the denominator and the numerator. In the present case migration effects need to be considered between

	$e\mu$+0-jet		ee+0-jet		$\mu\mu$+0-jet		$e\mu$+1-jet	
	A_{WW}	C_{WW}	A_{WW}	C_{WW}	A_{WW}	C_{WW}	A_{WW}	C_{WW}
$q\bar{q} \to W^+W^-$	0.235	0.514	0.087	0.292	0.095	0.477	0.093	0.583
$gg \to W^+W^-$	0.306	0.536	0.147	0.334	0.163	0.482	0.143	0.597
$gg \to H \to W^+W^-$	0.104	0.435	0.041	0.218	0.046	0.393	0.065	0.513
Total ($pp \to W^+W^-$)	0.228	0.512	0.086	0.291	0.093	0.474	0.092	0.580

Table 9.2: Efficiency correction factors C_{WW} and acceptance correction factors A_{WW} for the $q\bar{q} \to W^+W^-$, $gg \to W^+W^-$ and $gg \to H \to W^+W^-$ processes, and for the total $pp \to W^+W^-$ production. The correction factors are shown for the different categories $e\mu$+0-jet, ee+0-jet, $\mu\mu$+0-jet and $e\mu$+1-jet. The efficiency correction factors C_{WW} account for detector effects and the geometrical acceptance factors A_{WW} account for the kinematic requirements used to select W^+W^- candidate events defined in Table 9.1.

$e\mu$+0-jet and $e\mu$+1-jet final states and the parameters t and r take discrete values:

$$R_{ij} = p\left(r \in \Delta r_i | t \in \Delta t_j\right) = \frac{N_{\text{reco}}^{WW\to\ell''\nu\ell'''}\left(n_{\text{jets}}^{\text{reco}} = i, n_{\text{jets}}^{\text{gen}} = j\right)}{N_{\text{gen, fid}}^{WW\to\ell\nu\ell'\nu}\left(n_{\text{jets}}^{\text{gen}} = j\right)} \tag{9.6}$$

The matrix R_{ij} for the measurement of fiducial cross section in $e\mu$+0-jet and $e\mu$+1-jet final states is shown in Fig. 9.1a. The probability of migrations is $\sim 10\%$ which can be estimated by comparing R_{ij} and the values for C_{WW}.

Since information at the event generation stage is used in the numerator of Eq. 9.6, this approach does not reduce to Eq. 9.4 in the limit of a single bin. If differential distributions are measured with upper or lower boundaries, events falling outside these boundaries also need to be accounted for. In the present case of measuring jet multiplicities this concerns values of $N_{\text{reco}}^{WW\to\ell''\nu\ell'''}$, $j \geq 2$. Those migrations are accounted for by including them in the matrix elements R_{i1} corresponding to the jet bin $j = 1$ yielding the migration matrix shown in Fig. 9.1b. Including the contributions from outside the upper boundaries is a small correction.

The simulated W^+W^- event samples also include contributions from b-hadron decays, mainly from the process $g \to b\bar{b}$ occurring in the Pythia8 parton shower. The b-jet veto requirement included in the W^+W^- selection does not have an equivalent in the definition of the fiducial phase space and therefore is accounted for in R_{ij}. It was found that including this would affect the measured cross section by less than 1%.

9.1.3 Geometrical Acceptance A_{WW}

The fiducial phase space is defined by the geometrical and kinematic acceptance of the detector and the event selection criteria used to select the W^+W^- candidate events. The factor $A_{WW\to\ell\nu\ell'\nu}$ accounts for these acceptance effects and is used to extrapolate from the fiducial to the total phase space. It is calculated on simulated event samples as the ratio of events

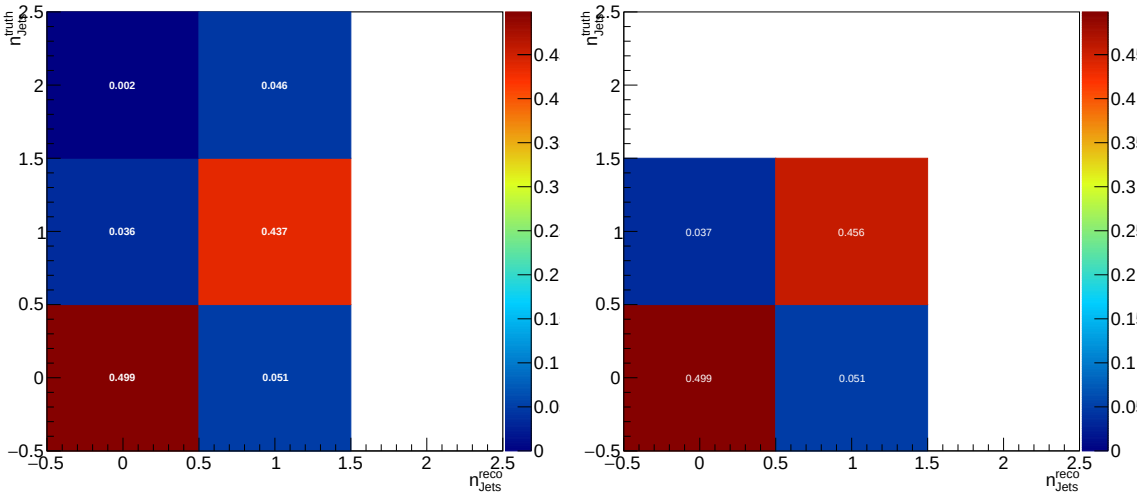

(a) (b)

Figure 9.1: Graphical representation of the matrix R_{ij} accounting for migration effects between the $e\mu$+0-jet and $e\mu$+1-jet final states. Shown are the probabilities for events produced with $n_{\text{jets}}^{\text{truth}}$ to be reconstructed with $n_{\text{jets}}^{\text{reco}}$. (a) The migration matrix in the usual definition. (b) The migration matrix corrected for migrations from outside the upper boundaries of $n_{\text{jets}} = 1$.

generated in the fiducial volume $N_{\text{gen, fid}}^{WW\to\ell\nu\ell'\nu}$ and all generated events $N_{\text{gen, all}}^{WW\to\ell\nu\ell'\nu}$:

$$A_{WW\to\ell\nu\ell'\nu} = \frac{N_{\text{gen, fid}}^{WW\to\ell\nu\ell'\nu}}{N_{\text{gen, all}}^{WW\to\ell\nu\ell'\nu}}, \quad \text{with } \ell,\ell' = e,\mu, \tag{9.7}$$

where the fiducial volume is defined such that it reflects the kinematic constraints applied on reconstructed events. The numerical values of the acceptance correction factors are derived from the simulated event samples introduced in Section 6.2 and are listed in Table 9.2 for the individual W^+W^- production processes and final states.

9.2 Experimental Efficiencies and Systematic Uncertainties

Uncertainties on the reconstruction efficiencies and calibration of electrons, muons, jets and the measurements of the missing transverse momentum are assigned to the efficiency correction factors C_{WW} or the migration matrix R_{ij}. Further uncertainties arise from the modelling of additional pp collisions. Since C_{WW} and R_{ij} are obtained from simulated event samples they also have theoretical uncertainties.

Dedicated measurements of the reconstruction efficiencies and the energy scale and resolution resulting from the detector calibration are discussed in Chapters 3 and 4. The uncertainties associated with these measurements are propagated to the simulated event samples by varying the corresponding parameters in the event simulation. The procedure is

described in Sections 9.2.1 and 9.2.2. The systematic uncertainties on the measured event yields are probed by comparing C_{WW} factors or the matrix R_{ij} calculated with nominal and varied parameters. The residual theoretical dependence is evaluated in Section 9.2.3. Furthermore, the systematic uncertainties in the determination of background contributions enter the measurement through the term $N^{\text{obs}} - N^{\text{bkg}}$. The estimated background contributions are summarised in Section 9.2.4.

A summary of the experimental systematic uncertainties is given in Table 9.3. The largest sources of experimental uncertainties are the jet-energy scale and jet-energy resolution. These affect the measured event yields in the 0-jet category due to the jet-veto requirement. In the 1-jet category they also enter through the jet requirement but in addition they highly affect the reconstruction of the missing transverse momentum. Since ee+0-jet and $\mu\mu$+0-jet final states rely on both leptons to trigger the readout of the event, the associated uncertainties represent another large source. The $e\mu$ final states particularly suffer from the large uncertainties on the estimation of background from W+jets and multijet production. When combining 0-jet and 1-jet categories and accounting for the experimental systematic correlations between the two categories the uncertainty in the determination of the W+jets and multijet background represents the largest source of uncertainty in the measurement.

9.2.1 Energy Scale and Resolution

The reconstruction of the particle four momenta is calibrated separately for electrons, muons, jets and the cell-out term of the missing transverse momentum reconstruction. The energy scale and resolution of these objects affect the efficiency of the W^+W^- candidate selection mainly through the migration of events above and below the threshold of the kinematic constraints. The uncertainty in the energy-scale determination is propagated to the measurement by varying the energy scale of the objects in simulated event samples within the uncertainty of the energy scale in data. The uncertainty in the energy resolution is propagated by widening the energy response in simulated event samples using pseudo-experiments.

9.2.2 Particle Reconstruction Efficiency

The simulated event samples are corrected with measurements of the reconstruction and identification efficiencies of electrons, muons and b-jets in data. This is done by weighting each particle with appropriate efficiency ratios measured in data and event simulation as introduced in Section 4.1. The uncertainty in the measurement of the reconstruction efficiencies is propagated by varying the efficiency ratios within their uncertainties. Each individual efficiency measurement is propagated separately with the factorisation introduced in Eq. 4.2. For b-jets, dedicated efficiency measurements exist for jets from light flavour hadrons, and from c- and b-hadrons. The uncertainty of the selection criteria on the jet-vertex fraction is evaluated by varying the nominal constraint of JVF > 0.5 by $\pm 6\%$ [72].

	$e\mu$+0-jet	ee+0-jet	$\mu\mu$+0-jet	$e\mu$+1-jet
Experimental uncertainties [%]				
Integrated luminosity	±2.0	±2.0	±2.0	±2.2
Pile-up	±1.4	±2.0	±2.0	±0.6
Trigger	±0.4	±2.8	±3.0	±0.4
Electron energy scale	±0.4	±1.5	—	±0.3
Electron energy resolution	<0.1	±0.2	—	<0.1
Electron ID and reconstruction	±1.0	±2.2	—	±1.2
Electron isolation	±0.2	±0.5	—	±0.3
Muon momentum scale	±0.1	—	±0.4	±0.5
Muon momentum resolution (ID)	±0.6	—	±1.7	±0.2
Muon momentum resolution (MS)	±0.1	—	±0.2	±0.4
Muon ID and reconstruction	±0.4	—	±0.8	±0.6
Muon isolation	±0.6	—	±1.2	±0.8
Jet vertex fraction	±0.2	±0.3	±0.2	±0.1
Jet energy scale	±4.1	±3.9	±4.4	±4.2
Jet energy resolution	±1.4	±1.3	±1.5	±1.0
$E_{\mathrm{T}}^{\mathrm{miss}}$ scale cell-out term	±1.1	±2.1	±1.9	±0.1
$E_{\mathrm{T}}^{\mathrm{miss}}$ resolution cell-out term	±0.3	±0.4	±0.5	±0.1
$p_{\mathrm{T}}^{\mathrm{miss}}$ scale cell-out term	±0.2	±0.4	±0.4	±0.4
$p_{\mathrm{T}}^{\mathrm{miss}}$ resolution cell-out term	±0.1	±0.2	±0.1	±0.3
b-tagging	—	—	—	±2.9
Background uncertainties [%]				
Top-quark background	±1.4	±1.8	±1.4	±3.9
W+jets & multijet background	±3.6	±3.1	±2.0	±3.4
Drell–Yan background	±0.5	±3.0	±2.3	±3.7
Statistical uncertainty (top, W+jets, DY)	±0.6	±2.0	±1.4	±3.6
Other diboson cross sections	±0.7	±1.0	±0.6	±4.2
Statistical uncertainty (other diboson)	±0.1	±0.3	±0.2	±0.3

Table 9.3: Experimental systematic uncertainties in the determination of fiducial cross sections from event reconstruction and the estimation of background contributions. The uncertainty sources are shown for $e\mu$+0-jet, ee+0-jet, $\mu\mu$+0-jet and the $e\mu$+1-jet final states. The uncertainties apply to both fiducial and total cross sections. Correlations between C_{WW} or R_{ij} and the background from diboson production are taken into account. For $e\mu$+1-jet final states correlations to $e\mu$+0-jet final states that enter in the migration matrix R_{ij} are taken into account.

9.2.3 Theoretical Uncertainties

The evaluation of theoretical systematic uncertainties is discussed in the context of the acceptance correction factor A_{WW} in Section 9.3. The fiducial phase space is constructed such that the efficiency correction factor C_{WW} or the migration matrix R_{ij} exhibit only a minimal dependence on the theoretical description of the kinematic distributions.

Residual theoretical uncertainties on the efficiency correction factors are evaluated in simulated $q\bar{q} \to W^+W^-$ events by studying the scale dependence and comparing the results to the nominal efficiency correction factors. The renormalisation and factorisation scales μ_R and μ_F are varied coherently by factors of one-half and two. A further theoretical uncertainty is assigned by comparing the nominal values and values calculated with alternative choices of the generator and parton shower model. The scale dependence of C_{WW} is found to be $\pm 0.6\%$. By comparing the efficiency correction factors obtained with the simulated PowHeg+Pythia8 sample and a sample simulated with Mc@Nlo+Herwig an uncertainty on the choice of the generator and parton-shower model is found to range between $\pm 0.35\%$ and $\pm 0.92\%$ in the 0-jet category.

The uncertainties on the migration matrix are derived in the same way as for C_{WW}. In general, the off-diagonal elements of the migration matrix R_{01} and R_{10} show larger theoretical uncertainties. Very small uncertainties result for the diagonal elements R_{00} and R_{11} since in contrast to C_{WW} the migration matrix is independent of the relative 0-jet and 1-jet normalisation. An additional uncertainty arises when accounting for contributions from $\geq$ 2-jets. It is assessed by varying the $\geq$ 2-jet contributions based on the studies discussed in Section 9.3.2. The overall theoretical uncertainties assigned to the migration matrix are 0.8% for R_{01}, 2.2% for R_{11}, 5.3% for R_{10} and 23% for R_{01}.

Other effects were studied and found to have a negligible effect. The uncertainties on C_{WW} and R_{ij} derived from simulated event samples of $q\bar{q} \to W^+W^-$ production are also assigned to the correction factors for the $gg \to W^+W^-$ and $gg \to H \to W^+W^-$ sub-processes.

9.2.4 Uncertainties on Background Determination

The uncertainties on the background contributions estimated in Section 6.4 and Chapters 7 and 8 are translated into relative uncertainties on the estimated signal yield in data. The absolute yields and their uncertainties are summarised in Table 9.4. Since the background from diboson production is estimated using event simulation, they are subject to reconstruction uncertainties. Correlations between the efficiency correction factor C_{WW} or the migration matrix R_{ij}, and the estimated diboson yields are considered in Table 9.3. For the estimation of the other background processes, data-driven techniques are used and the residual reconstruction uncertainties are treated as uncorrelated with C_{WW} or R_{ij}. The largest background contribution is from top-quark production. In the 0-jet category it is, however, estimated with a relatively high precision. The largest source of uncertainty is the estimation of the contributions of the background from W+jets and multijet production. It is particularly large for $e\mu$+0-jet final states where the uncertainty is roughly twice the size of the uncertainties of all other background contributions combined.

	$e\mu$+0-jet	ee+0-jet	$\mu\mu$+0-jet	$e\mu$+1-jet
Top quark	$609 \pm 18 \pm 52$	$92 \pm 7 \pm 8$	$127 \pm 9 \pm 11$	$1236 \pm 43 \pm 49$
W+jets and multijet	$250 \pm 20 \pm 140$	$14 \pm 5 \pm 14$	$6 \pm 5 \pm 12$	$121 \pm 15 \pm 50$
$Z \to \ell\ell$	$175 \pm 3 \pm 18$	$28 \pm 0 \pm 13$	$33 \pm 0 \pm 17$	$267 \pm 12 \pm 49$
Other dibosons	$150 \pm 4 \pm 30$	$27 \pm 1 \pm 5$	$38 \pm 1 \pm 5$	$195 \pm 5 \pm 53$

Table 9.4: Estimated background contributions in $e\mu$+0-jet, ee+0-jet, $\mu\mu$+0-jet and the $e\mu$+1-jet final states. Both statistical and systematic uncertainties are shown for each background contribution.

9.3 Geometrical Acceptance and Systematic Uncertainties

The geometrical acceptance is calculated using the simulated event samples introduced in Section 6.2. The calculation requires generator level information which introduces theoretical uncertainties. Since separate W^+W^- event samples are generated for different initial states, the evaluation of the acceptance and the corresponding uncertainties is also performed individually for each sub-process. In a second step a combined acceptance is calculated where the acceptance of each process contributes according to its cross section. The calculation of the geometrical acceptance factor is sensitive to the modelling of the hard interaction, the underlying event and hadronisation, missing higher-order corrections in the perturbative expansion and the parton distribution function (PDF) used in the simulation. Systematic uncertainties are assigned for each of these sources. A summary is given in Table 9.5 for all final states and categories considered. The largest source of theoretical uncertainties is imposed by the categorisation of the analysis into jet-bins, denoted jet-binning uncertainty. The jet-binning still represents the largest individual source of uncertainty when the 0-jet and 1-jet categories are combined. Another large uncertainty is related to the choice of generators for the event simulation, denoted as ME+PS. The evaluation of the individual components is described in the following.

9.3.1 PDF

The simulated event samples used to derive the geometrical acceptance A_{WW} are produced using the CT10 [140] PDF. The uncertainty of this choice is evaluated by comparing the geometrical acceptances obtained from the CT10, MSTW [28] and NNPDF [166] PDF sets and their uncertainties. The uncertainty is assigned as the envelope of the CT10, MSTW and NNPDF error bands as proposed in Ref. [167]. The values are obtained by reweighting the simulated PowHeg+Pythia8 samples for $q\bar{q} \to W^+W^-$ and $gg \to H \to W^+W^-$ production to the different PDF central values and their error sets. The uncertainties for the CT10 set

	$e\mu$+0-jet	ee+0-jet	$\mu\mu$+0-jet	$e\mu$+1-jet	$e\mu$+0/1-jet
$qq \to WW$					
PDF	0.7%	0.9%	0.9%	0.9%	0.7%
jet-binning	2.9%	2.9%	2.9%	18%	3.6%
scale	0.2%	0.2%	0.2%	0.2%	0.2%
ME+PS	1.3%/2.9%	1.3%	1.3%	7.7%	1.2%
EW corrections	0.5%	0.4%	0.5%	—	—
$gg \to WW$					
PDF	1.7%	1.7%	1.7%	1.5%	1.7%
jet-binning	15%/18%	15 %	15 %	43 %	9.5%
scale	0.3%	0.3%	0.3%	0.3%	0.3%
ME+PS	31 %	28 %	29 %	15 %	18 %
$gg \to H \to WW$					
PDF	1.7%	1.7%	1.7%	1.5%	1.7%
jet-binning	15%/18%	15 %	15 %	43 %	9.5%
scale	1.4%	1.4%	1.4%	1.4%	1.4%
ME+PS	6.9%	6.9%	6.9%	2.5%	5.2%
combined					
PDF	0.7%	0.9%	0.9%	0.9%	0.8%
jet-binning	3.4%/3.9%	3.4%	3.4%	20 %	4.0%
scale	0.2%	0.2%	0.2%	0.3%	0.2%
ME+PS	2.5%/5.0%	2.6%	2.7%	7.8%	1.9%
EW corrections	0.5%	0.4%	0.4%	—	—

Table 9.5: Theoretical uncertainties on the geometrical acceptance A_{WW}. The uncertainties are shown separately for the individual processes of $pp \to W^+W^-$ production and for different final states. For the jet-binning and the ME+PS uncertainties two values are given for $e\mu$+0-jet final states, that are used for the results obtained in Chapter 10 and 11, respectively, as described in the text.

	$e\mu$+0-jet	$e\mu$+1-jet	$e\mu$+0/1-jet
$q\bar{q} \to W^+W^-$			
CT10 (nominal)	0.2341±0.0011	0.0931±0.0004	0.3272±0.0015
MSTW	0.2351±0.0005	0.0936±0.0003	0.3287±0.0008
NNPDF	0.2331±0.0006	0.0930±0.0003	0.3261±0.0008
final value	0.2341±0.0016	0.0931±0.0008	0.3272±0.0023
$gg \to H \to W^+W^-$			
CT10 (nominal)	0.1156±0.0012	0.0717±0.0006	0.1873±0.0017
MSTW	0.1157±0.0007	0.0718±0.0003	0.1876±0.0010
NNPDF	0.1169±0.0007	0.0725±0.0003	0.1895±0.0010
final value	0.1156±0.0020	0.0717±0.0011	0.1873±0.0032

Table 9.6: Acceptance correction factors A_{WW} with uncertainties due to the choice of the parton-distribution function (PDF) for the $q\bar{q} \to W^+W^-$ and $gg \to H \to W^+W^-$ processes. Shown is the acceptance obtained with several PDFs and the corresponding uncertainties. The total uncertainty is evaluated as the envelope of the CT10, MSTW and NNPDF error bands.

is obtained according to Ref. [140] by:

$$\delta^+ f = \sqrt{\sum_{i=0}^{N_a} \left[\max\left(f_i^{(+)} - f_0, f_i^{(-)} - f_0, 0\right)\right]^2} \tag{9.8}$$

$$\delta^- f = \sqrt{\sum_{i=0}^{N_a} \left[\max\left(f_0 - f_i^{(+)}, f_0 - f_i^{(-)}, 0\right)\right]^2} \tag{9.9}$$

with the central value f_0 and the up and down variation of $N_a = 26$ eigenvectors $f_i^{\pm}$. Similar prescriptions exist for the other PDF sets. No separate PDF uncertainty is evaluated for non-resonant $gg \to WW$ production. Instead, the uncertainty derived for resonant $gg \to H \to WW$ production is used where the initial states are the same.

9.3.2 Perturbative Expansion and Jet Selection

The uncertainty of an observable due to neglected higher-order corrections in the perturbative series is commonly evaluated studying the scale dependence of the observable. The renormalisation and factorisation scales, μ_R and μ_F, are varied independently by factors of one-half and two. In a jet-binned analysis, however, this approach may underestimate the uncertainty. The underestimation can occur due to accidental cancellations of perturbative corrections leading to large K-factors and perturbative corrections that have logarithmic sensitivity to the jet-bin boundary [168]. The perturbative uncertainty is therefore evaluated separately for the selection of the number of jets and the remaining selection requirements.

An alternative approach for the evaluation of the scale dependence of jet-binned quantities is described in Ref. [168]. It is argued that the uncertainty of exclusive jet-binned cross

sections, $\sigma_{\geq N}$, are uncorrelated. Therefore the relative uncertainties of the acceptance of the selection of exactly zero and one jet, f_0 and f_1, are:

$$\delta(f_0)^2 = \left(\frac{1}{f_0} - 1\right)^2 \left(\delta^2_{\text{total}} + \delta^2_{\geq 1}\right), \tag{9.10}$$

$$\delta(f_1)^2 = \delta^2_{\text{total}} + \left(\frac{1-f_0}{f_1}\right)^2 \delta^2_{\geq 1} + \left(\frac{1-f_0}{f_1} - 1\right)^2 \delta^2_{\geq 2} \tag{9.11}$$

with the relative uncertainties of the total cross section, δ_{total}, and the exclusive cross sections for the production of more than one or two jets, $\delta_{\geq 1}$ and $\delta_{\geq 2}$. Similarly, the uncertainties for any selection on the number of jets and correlation coefficients between different selection criteria on the number of jets can be derived. Relevant are the correlation coefficient between 0-jet and 1-jet category, $\rho(f_0, f_1)$, as well as the combined acceptance, $f_{\leq 1} = f_0 + f_1$:

$$\delta\left(f_{\leq 1}\right)^2 = \left(\frac{1}{f_{\leq 1}} - 1\right)^2 \left(\delta^2_{\text{total}} + \delta^2_{\geq 2}\right), \tag{9.12}$$

$$\rho(f_0, f_1) = -\left(1 + \frac{1-f_0}{f_1}\frac{\delta^2_{\geq 1}}{\delta^2_{\text{total}}}\right)\left(\frac{1}{f_0} - 1\right)\frac{\delta^2_{\text{total}}}{\delta(f_0)\,\delta(f_1)}. \tag{9.13}$$

The correlation coefficient between the efficiencies to select zero and one jet always has a negative sign. Uncertainties due to missing higher-order corrections cancel when combining the two categories.

Inclusive and jet-binned cross sections are shown in Table 9.7 for $q\bar{q} \to W^+W^-$ production for different choices of μ_{R} and μ_{F} with respect to a nominal choice which is dynamically set to $\mu_{\text{R}} = \mu_{\text{F}} = m_{WW}/2$. The scale dependence is evaluated using the fixed order calculation at NNLO provided by Ref. [169] and compared to uncertainties evaluated on simulated PowHeg+Pythia8 events generated at NLO of the perturbative expansion. The negative correlation between f_0 and f_1 results in partial cancellations of uncertainties and relatively smaller uncertainties for the combined acceptance $f_{\leq 1}$. The uncertainty on the acceptance correction is assigned based on the NNLO calculation and is ±2.9% for the 0-jet category and ±3.6% for the combined 0+1-jet final states.

For $gg \to H \to W^+W^-$ production, the uncertainties due to the scale dependence are shown in Table 9.8. Two alternative ways of determining the uncertainty of the jet selection are shown, as derived in Ref. [153]. The approach from Ref. [168] is used to obtain the results presented in Chapter 11. An alternative approach is taken from Refs. [110, 170] and yields slightly smaller uncertainties. It is used when correlations between the 0-jet and 1-jet selections are not needed, i.e. for the results in Chapter 10. The uncertainty derived for $gg \to H \to W^+W^-$ is assigned to both the resonant and non-resonant $gg \to W^+W^-$ production.

The scale dependence of the acceptance of the remaining selection criteria is evaluated by studying the residual acceptance. This residual acceptance is defined by all kinematic constraints of the fiducial phase space except for any selection on the number of jets. It is

	NNLO			PowHeg+Pythia8		
(μ_F, μ_R)	$\sigma_{\text{incl.}}$ [pb]	$\sigma_{\geq 1\text{jet}}$ [pb]	$\sigma_{\geq 2\text{jet}}$ [pb]	$\sigma_{\text{incl.}}^{e\mu,\text{fid}}$ [fb]	$\sigma_{\geq 1\text{jet}}^{e\mu,\text{fid}}$ [fb]	$\sigma_{\geq 2\text{jet}}^{e\mu,\text{fid}}$ [fb]
(1 , 1)	59.13	18.75	6.00	303.1	104.4	29.5
(1 , 2)	59.12	18.68	5.66	306.0	104.5	29.3
(2 , 2)	58.08	17.68	4.66	299.9	101.7	28.4
(2 , 1)	58.04	17.79	4.94	297.9	101.6	28.5
(1 , 0.5)	59.16	18.91	6.37	301.3	104.5	29.7
(0.5, 0.5)	60.38	19.85	7.93	309.2	108.0	30.9
(0.5, 1)	60.27	19.72	7.47	311.7	107.8	30.6
(2 , 0.5)				295.8	101.5	28.7
(0.5, 2)				312.4	107.7	30.4
uncertainty	±2.12%	±5.88%	±32.09%	±3.04%	±3.40%	±4.79%
f_0	0.683 ± 0.020 (± 2.90%)			0.656 ± 0.016 (±2.39%)		
f_1	0.216 ± 0.038 (±17.54%)			0.247 ± 0.015 (±5.93%)		
$f_{\leq 1}$	0.899 ± 0.033 (± 3.63%)			0.9027 ± 0.0055 (±0.61%)		

Table 9.7: Theoretical inclusive and inclusive jet-binned cross sections for $q\bar{q} \rightarrow W^+W^-$ production for different choices of the renormalisation and factorisation scales, μ_R and μ_F. The renormalisation and factorisation scales are dynamically set to $\mu_R = \mu_F = m_{WW}/2$ and varied independently by factors of two. In addition, the jet selection efficiencies are shown for 0-jet, 1-jet and the combined 0/1-jet category together with the uncertainties evaluated from Eqs. 9.10-9.12. Two sets of numbers are shown, calculated at fixed order at NNLO and calculated in simulated PowHeg+Pythia8 events at NLO. The cross sections from PowHeg+Pythia8 are evaluated in $e\mu$ final states within the acceptance of the lepton selection which is why they are much smaller. The numbers for NNLO are calculated in the total phase space and have been provided by Ref. [169]. Contributions from $gg \rightarrow W^+W^-$ have been removed.

(μ_F, μ_R)	$\sigma_{\text{incl.}}$ [pb]	$\sigma_{\geq 1\text{jet}}$ [pb]	$\sigma_{\geq 2\text{jet}}$ [pb]
$(1, 1)$	19.27	7.46	2.87
uncertainty	±18%	±43%	±101%
	jet-veto efficiency [168]		
f_0	0.614 ± 0.084 (±18 %)		
f_1	0.267 ± 0.116 (±43 %)		
$f_{\leq 1}$	0.881 ± 0.085 (± 9.5%)		
	combined-inclusive [110, 170]		
f_0	0.614 ± 0.092 (±15%)		
f_1	0.267 ± 0.072 (±27%)		

Table 9.8: Theoretical inclusive and inclusive jet-binned cross sections for $gg \to H \to W^+W^-$ production for a Higgs boson with a mass of $m_H = 125$ GeV. Only the cross sections corresponding to the nominal choice of renormalisation and factorisation scales of $\mu_R = \mu_F = m_H$ are shown with systematic uncertainties evaluated in Ref. [153]. Two alternative uncertainties for the jet selection efficiency are shown, evaluated with the approaches in Ref. [168] and Refs. [110, 170], respectively.

	A_{WW}	
$qq \to WW$	0.36913 ± 0.00081	(0.2%)
$gg \to WW$	0.4853 ± 0.0015	(0.3%)
$gg \to H \to WW$	0.2248 ± 0.0031	(1.4%)

Table 9.9: Acceptance correction factor $A_{WW\to\ell\nu\ell'\nu}$ for $e\mu$ final states with the uncertainty due to missing higher-order corrections. The relative uncertainty is shown in brackets. The acceptance of the jet selection is not included in the calculation since a dedicated approach is used for the evaluation of the associated systematic uncertainty. The uncertainty of the selection for the $gg \to H \to W^+W^-$ process is taken from Ref. [153]. The uncertainties for ee and $\mu\mu$ final states have the same size and are not shown.

shown in Table 9.9 together with the uncertainty from missing higher-order corrections, evaluated by varying the renormalisation and factorisation scale in the numerator and denominator of Eq. 9.7. The residual acceptance is evaluated on simulated PowHeg+Pythia8 samples for the $q\bar{q} \to W^+W^-$ and $gg \to H \to W^+W^-$ processes. The uncertainty for the residual acceptance of non-resonant $gg \to WW$ production is evaluated using MCFM. The scale dependence of the jet selection efficiency is in all cases larger than the scale dependence of the residual acceptance correction.

9.3.3 Generator, Underlying Event and Hadronisation

The uncertainty related to the choice of the generator and parton-shower model for event simulation is evaluated by comparing the acceptance calculated with event samples that are using alternative choices of the generators and parton-shower models. For $q\bar{q} \to W^+W^-$

	$e\mu$+0-jet	$e\mu$+1-jet	$e\mu$+0/1-jet
Powheg+Pythia8	0.2344	0.093 05	0.3274
Powheg+Jimmy	0.2385	0.092 43	0.3309
MC@NLO	0.2439	0.085 35	0.3292
Δ(Pythia8,Jimmy)	0.0041 (1.7%)	0.0004 (0.7%)	0.0035 (1.1%)
Δ(Powheg,MC@NLO)	0.0054 (2.3%)	0.0071 (7.7%)	0.0017 (0.5%)
uncertainty	0.0068 (2.9%)	0.0071 (7.7%)	0.0039 (1.2%)

Table 9.10: Acceptance correction factors A_{WW} for $e\mu$ final states in the 0-jet, 1-jet and combined 0/1-jet categories evaluated using different samples of simulated $q\bar{q} \to W^+W^-$ events. The theoretical uncertainty due to the choice of the generator and parton-shower model is evaluated based on this table and given in the last row. These uncertainties are used for the results presented in Chapter 11.

production, the nominal simulated event sample is generated with PowHeg+Pythia8 and compared with PowHeg+Jimmy for the evaluation of the systematic uncertainty of the underlying event and hadronisation. For an alternative generator choice the acceptance is calculated with Mc@Nlo. Since only a simulated event sample using Herwig+Jimmy is at hand the difference to PowHeg+Jimmy is quoted as an uncertainty. The uncertainties assigned for the results presented in Chapters 10 and 11 use a different treatment of the selection of jets to evaluate this uncertainty. The restriction on the number of jets is removed to evaluate the uncertainty for the results in Chapter 10. The uncertainties for the results in Chapter 11 use the appropriate selection of 0-jet, 1-jet or ≤1-jets.

For non-resonant $gg \to W^+W^-$ production the simulated event samples are generated with gg2ww using Herwig+Jimmy for the modelling of underlying event and hadronisation. For the evaluation of systematic uncertainties the acceptance is compared to the acceptance calculated with event samples simulated with MCFM and interfaced to Herwig+Jimmy or Pythia8.

The acceptance correction factors calculated with the individual simulated event samples are shown in Table 9.10 for $q\bar{q} \to W^+W^-$ production and Table 9.11 for $gg \to W^+W^-$ production. Only results from $e\mu$ final states are shown. Cancellations between 0-jet and 1-final states result in smaller uncertainties on the combined 0+1-jet acceptance. The uncertainty assigned for the underlying event and hadronisation is 1.2% for the 0+1-jet acceptance in $q\bar{q} \to W^+W^-$ production, but larger for jet-binned acceptances. For $gg \to W^+W^-$ production which is only implemented at leading-order the uncertainty can be as large as 31% for the 0-jet acceptance and represents the largest uncertainty for the 0-jet and 0/1-jet categories. For resonant $gg \to H \to W^+W^-$ production an uncertainty of ±6.4% and 2.5% is assigned for the choice of the generator and parton-shower model in the 0-jet category. In the 1-jet category the corresponding uncertainties are ±2.1% and ±1.4%. They were obtained in Ref. [153] by comparing simulated event samples produced with PowHeg+Pythia8 and PowHeg+Herwig and simulated event samples produced with PowHeg and Mc@Nlo. The uncertainties for $gg \to H \to W^+W^-$ production are considered uncorrelated in the two jet bins. The procedure of deriving uncertainties for the acceptance for the $q\bar{q} \to W^+W^-$ process used in Chapter 10 results in uncertainties of ±1.3% for $e\mu$, ee and $e\mu$ final states.

	$e\mu$+0-jet	$e\mu$+1-jet	$e\mu$+0/1-jet
gg2ww+Herwig	0.306	0.143	0.448
MCFM+Herwig	0.257	0.165	0.422
MCFM+Pythia8	0.189	0.163	0.352
Δ(Herwig,Pythia8)	0.068 (26%)	0.022 (15 %)	0.026 (5.9%)
Δ(gg2ww,MCFM)	0.049 (16%)	0.002 (1.2%)	0.071 (17 %)
uncertainty	0.093 (31%)	0.022 (15 %)	0.080 (18 %)

Table 9.11: Acceptance correction factors A_{WW} for $e\mu$ final states in the 0-jet, 1-jet and combined 0/1-jet categories evaluated using different samples of simulated $gg \to W^+W^-$ events. The theoretical uncertainty due to the choice of the generator and parton-shower model is evaluated based on this table and given in the last row. The uncertainties for ee+0-jet and $\mu\mu$+0-jet final states are evaluated in the same way but are not shown here.

9.3.4 Electroweak Contributions at NLO

Electroweak contributions to $pp \to W^+W^-$ are partially taken into account by post-processing final state leptons with Photos [86]. Dedicated calculations at NLO ($O\left(\alpha_{\mathrm{EW}}^3\right)$) are mentioned in Section 5.2.1 for the $q\bar{q} \to W^+W^-$ sub-process. These are not included in the simulation of the hard interaction in the PowHeg+Pythia8 event samples. A K-factor is derived from Ref. [106] as a function of the Mandelstam variables s and t and applied in the calculation of the acceptance correction factors A_{WW} for the 0-jet category. To account for the fact that Ref. [106] uses a narrow width approximation, a systematic uncertainty as large as the electroweak K-factor itself is assigned for the lack of knowledge if the mass of one of the W bosons differs from the nominal W boson mass m_W by more than 25 GeV. As no mixed QCD and electroweak calculations were performed yet, systematic uncertainties are also assigned for events with high QCD activity, where high QCD activity is quantified by the aplanarity parameter ρ being larger than 0.3. The electroweak correction changes the acceptance correction factor A_{WW} by 0.2% but introduce an uncertainty of ±0.5%. It is, however, much more significant for the related analysis of anomalous triple gauge couplings presented in Section 10.5 where the correction can be as large as 30%.

The impact of mixed QCD and electroweak effects may be enhanced in events with increased QCD activity like studied in the analysis of the 1-jet category. Such phase-space regions are explicitly excluded in related calculations, see e.g. Ref. [171]. The electroweak effects are ignored for the results presented in Chapter 11 in order to avoid an artificial increase of the uncertainty.

9.4 Combination of Results from Different Final States

The number of signal events in a given final state i can be expressed in terms of the cross section and the correction factors discussed in Section 9.1 by transposing Eq. 9.3:

$$N_s^i(\sigma) = \sigma \times \mathcal{B}^2(W \to \ell\nu) \times \mathcal{L} \times A_{WW} \times C_{WW}. \tag{9.14}$$

In order to take into account the impact of systematic uncertainties on the number of signal events a further term $\left(1 + \sum_k x_k S_k^i\right)$ is added to Eq. 9.14 that parametrises the effect of systematic uncertainties k on the expected signal yield. The parameters S_k^i correspond to the relative systematic uncertainties and the parameters x_k are nuisance parameters that are assumed to be normal distributed, i.e. $x_k \sim N(0,1)$. The final form of Eq. 9.14 is:

$$N_s^i(\sigma, \{x_k\}) = \sigma \times \mathcal{B}^2(W \to \ell\nu) \times \mathcal{L} \times A_{WW} \times C_{WW} \times \left(1 + \sum_k x_k S_k^i\right). \tag{9.15}$$

Similarly, the expression for the number of background events is defined as:

$$N_b^i(\{x_k\}) = N_b^i \times \left(1 + \sum_k x_k B_k^i\right). \tag{9.16}$$

The measured cross sections are obtained in a profile likelihood fit. The likelihood function is given by the product of Poisson probabilities in different final states i with $N_{\mathrm{s}}^i(\sigma, \{x_k\}) + N_{\mathrm{b}}^i(\{x_k\})$ expected signal and background events that produce the number of events observed in the data. N_{obs}^i. The corresponding negative log likelihood is given by:

$$-\ln L(\sigma, \{x_k\}) = \sum_i -\ln\left(\frac{e^{-(N_{\mathrm{s}}^i(\sigma,\{x_k\}) + N_{\mathrm{b}}^i(\{x_k\}))} \times (N_{\mathrm{s}}^i(\sigma,\{x_k\}) + N_{\mathrm{b}}^i(\{x_k\}))^{N_{\mathrm{obs}}^i}}{(N_{\mathrm{obs}}^i)!}\right) + \sum_k \frac{x_k^2}{2} \tag{9.17}$$

where the functions of different final states i are summed if measurements are combined. Systematic uncertainties are represented by the nuisance parameters x_k. They are constrained by a Gaussian penalty term $\sum_k \frac{x_k^2}{2}$. For the results presented in Chapter 10 the results of $i = e\mu, ee, \mu\mu$ final states in the 0-jet category are combined. The effect of migrations is implemented in Eq. 9.17 by replacing in Eq. 9.15:

$$\sigma \times C_{WW} \to \sum_j R_{ij}\sigma_j, \tag{9.18}$$

such that the expected signal yield reconstructed in a given final state N_s^i is a function of several cross sections $N_s^i(\sigma_1, \sigma_2, \ldots, \{x_k\})$. This approach is used for the results presented in Chapter 11 where the measurements of $e\mu$ final states in the i = 0-jet, 1-jet category are combined to a fiducial 0/1-jet cross section

10 Results from WW+0-jet Final States

Results from WW+0-jet final states are presented in the following. With the methodology and the yields of data and background events discussed throughout Chapters 6–9 it is possible to compute the $pp \to W^+W^-$ cross section. The observed data and estimated background yields are summarised in Section 10.1. Theoretical predictions of fiducial and total cross sections are derived in Section 10.2. The corresponding measured values are presented in Section 10.3. Furthermore, results for differential cross sections as well as limits on anomalous triple gauge boson couplings are summarised in Section 10.4 and 10.5, respectively.

10.1 Kinematic Distributions of Selected Events

A total of 6636 W^+W^- candidate events are selected in data in the 0-jet category. The event yields in data in different final states are summarised in Table 10.1 together with the contributions from W^+W^- production and background processes as estimated from simulated event samples or determined in data. The number of events observed in data is consistently higher than the sum of the estimated background yields and signal yields expected from the event simulation which correspond to a total $pp \to W^+W^-$ production cross section of $58.7^{+4.2}_{-3.8}$ pb.

Differential distributions of the selected W^+W^- candidate events are shown together with the estimated background contributions and the systematic uncertainties in Figs. 10.1 and 10.2 for the transverse momentum of the leading lepton, p_{T}, the invariant mass of the dilepton system, $m_{\ell\ell}$, the transverse momentum of the dilepton system, $p_{\mathrm{T}}^{\ell\ell}$, and the azimuthal separation of the leptons, $\Delta\phi_{\ell\ell}$. Higher event yields in data are consistently seen over the full kinematic range of the variables shown.

10.2 Theoretical Cross-Section Predictions

For a comparison with the measured value the total cross section is computed as the sum of the individual sub-processes using the highest order calculation available at the time the analysis was performed. The total $pp \to W^+W^-$ production cross section is obtained from the sum of $q\bar{q} \to W^+W^-$at NNLO, which includes $gg \to W^+W^-$ production at LO, and the $gg \to H \to W^+W^-$ cross section at NNLO [103]. It is found to be:

$$\sigma_{\mathrm{tot}} = 63.2^{+2.0}_{-1.8}\ \mathrm{pb} \tag{10.1}$$

and represented the highest order calculation available at the time of the publication of the measurement in Ref. [5]. The renormalisation and factorisation scales for the $q\bar{q} \to W^+W^-$

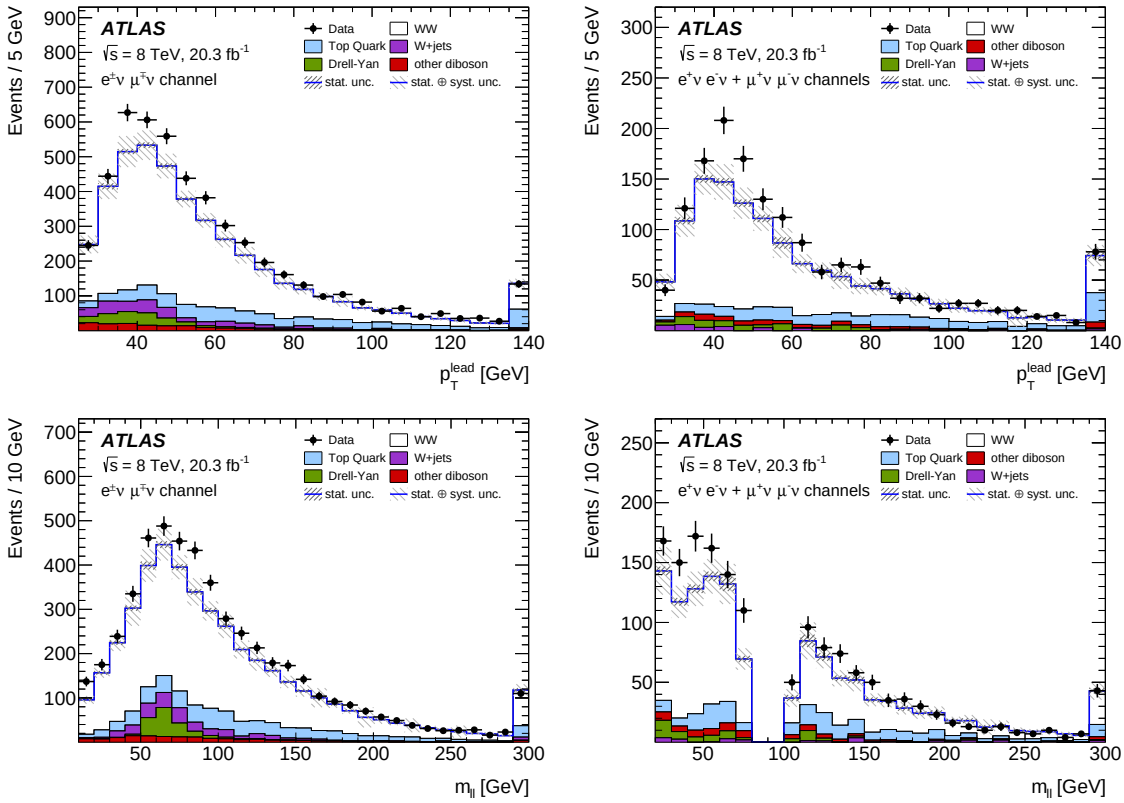

Figure 10.1: Distributions of the transverse momentum of the leading lepton, p_{T} (top), and the invariant mass of the dilepton system, $m_{\ell\ell}$ (bottom), for $e\mu$+0-jet (left) and the sum of ee and $\mu\mu$+0-jet final states (right). Data are shown together with the estimated signal and background contributions. The yields from W^+W^- production are shown for a total cross section of $58.7^{+4.2}_{-3.8}$ pb. The uncertainty bands show statistical and systematic uncertainties. Previously published in Ref. [5].

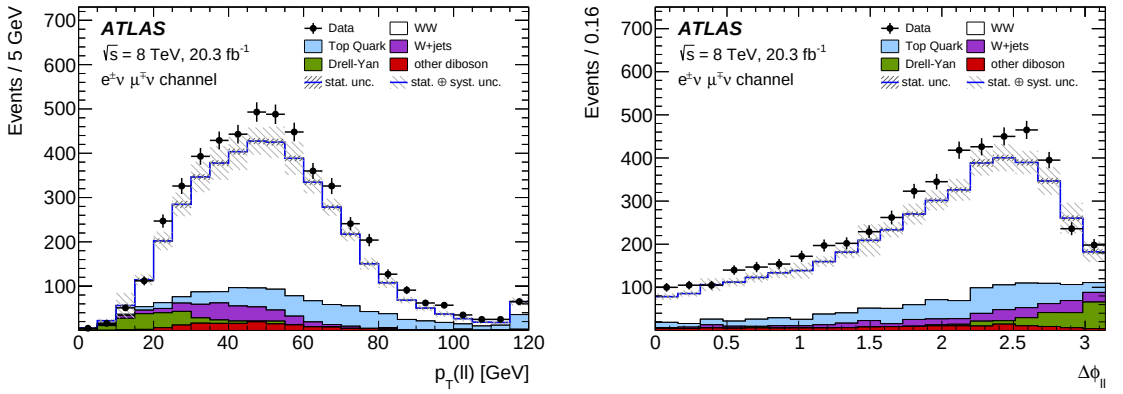

Figure 10.2: Distributions of the transverse momentum of the dilepton system, $p_{\mathrm{T}}^{\ell\ell}$ (left), and the azimuthal separation between the leptons, $\Delta\phi_{\ell\ell}$ (right), for $e\mu$+0-jet final states. Data are shown together with the estimated signal and background contributions. The yields from W^+W^- production are shown for a total cross section of $58.7^{+4.2}_{-3.8}$ pb. The uncertainty bands show statistical and systematic uncertainties. Previously published in Ref. [5].

	$e\mu$+0-jet	ee+0-jet	$\mu\mu$+0-jet
Observed events	5067 ± 71	594 ± 24	975 ± 31
Total expected events	4420 ± 26 ± 319	507 ± 9 ± 39	817 ± 11 ± 65
W^+W^- signal	3240 ± 10 ± 280	346 ± 3 ± 33	613 ± 5 ± 60
Top quark	609 ± 18 ± 52	92 ± 7 ± 8	127 ± 9 ± 11
W+jets and multijet	250 ± 20 ± 140	14 ± 5 ± 14	6 ± 5 ± 12
$Z \to \ell\ell$	175 ± 3 ± 18	28 ± 0 ± 13	33 ± 0 ± 17
Other dibosons	150 ± 4 ± 30	27 ± 1 ± 5	38 ± 1 ± 5
Total background	1180 ± 24 ± 150	161 ± 9 ± 21	205 ± 11 ± 24

Table 10.1: Observed and expected signal and background contributions in $e\mu$+0-jet, ee+0-jet and $\mu\mu$+0-jet final states. The yields from W^+W^- production are shown for a total cross section of $58.7^{+4.2}_{-3.8}$ pb. The estimated event yields are shown with their statistical and systematic uncertainties.

calculation were dynamically set to $\mu = m_{WW}/2$ and independently varied by factors of one-half and two with the constraint $0.5 < \mu_F/\mu_R < 2$ to estimate the effects of missing higher order corrections.

In order to incorporate higher-order corrections also in the theoretical predictions of fiducial cross sections, approximate fiducial cross sections are calculated by multiplying the total $pp \to W^+W^-$ cross section with the acceptance correction factors, A_{WW}, that correspond to a lower order calculation in perturbative QCD. The theoretical uncertainties are considered uncorrelated between the total cross section and the acceptance correction factors. This results in the fiducial cross sections for the individual final states of:

	$e\mu$+0-jet	ee+0-jet	$\mu\mu$+0-jet	
$\sigma_{\text{fid}}^{\text{NLO}}$	311 ± 15 fb	58.5 ± 2.8 fb	63.7 ± 3.1 fb	(10.2)
$\sigma_{\text{fid}}^{\text{NNLO}}$	335 ± 18 fb	63.0 ± 3.4 fb	68.6 ± 3.7 fb.	(10.3)

Fiducial cross sections including resummation calculations are obtained from the simulated $q\bar{q} \to W^+W^-$ samples by reweighting their p_T^{WW} distribution to the calculation at NLO+NNLL [111]. The resulting acceptance correction factors are $A_{WW}^{e\mu} = 0.236 \pm 0.011$, $A_{WW}^{ee} = 0.0889 \pm 0.0041$ and $A_{WW}^{\mu\mu} = 0.0966 \pm 0.0046$. The uncertainties are taken from Section 9.3, except for uncertainties on higher order effects that are assigned based on the dependence on the renormalisation and factorisation scales, and the dependence on the resummation scale. Approximate fiducial NNLO+NNLL cross sections were calculated in Ref. [115] and are also listed here. By incorporating the effects of resummation calcula-

tions the following fiducial cross sections are obtained:

	$e\mu$+0-jet	ee+0-jet	$\mu\mu$+0-jet	
$\sigma_{\text{fid}}^{\text{NLO+NNLL}}$	349 ± 19 fb	65.5 ± 3.6 fb	71.2 ± 4.0 fb	(10.4)
$\sigma_{\text{fid}}^{\text{approx. NNLO+NNLL}}$	358 ± 14 fb	69.0 ± 2.7 fb	75.1 ± 3.0 fb [115].	(10.5)

The fiducial cross sections are consistently enhanced compared to the values given in Eq. 10.3.

10.3 Inclusive Fiducial and Total Cross Sections

Fiducial cross sections are calculated from the event yields for $e\mu$, ee and $\mu\mu$ final states separately using Eq. 9.1. The measured cross sections in the fiducial phase space are calculated to be:

$$\sigma_{\text{fid}}^{e\mu} = 374\ ^{+7}_{-7}\ (\text{stat.})^{+25}_{-23}\ (\text{syst.})^{+8}_{-7}\ (\text{lumi.})\ \text{fb} \tag{10.6}$$

$$\sigma_{\text{fid}}^{ee} = 73.4^{+4.2}_{-4.1}(\text{stat.})^{+6.5}_{-5.6}(\text{syst.})^{+1.5}_{-1.5}(\text{lumi.})\ \text{fb} \tag{10.7}$$

$$\sigma_{\text{fid}}^{\mu\mu} = 80.2^{+3.3}_{-3.2}(\text{stat.})^{+6.4}_{-5.5}(\text{syst.})^{+1.6}_{-1.6}(\text{lumi.})\ \text{fb} \tag{10.8}$$

Comparisons of the measurements and the theoretical fiducial cross sections obtained in Section 10.2 are shown in Fig. 10.3. The measured fiducial cross sections and the corresponding approximate theoretical values differ by roughly one standard deviation. The resummation calculation at NLO+NNLL improves the agreement between measured and theoretical fiducial cross sections. These trends hold for each of the individual final states, i.e. the observed behaviour is not particularly sensitive to the stricter requirements on the missing transverse momentum applied for the same-flavour final states. Even better agreement is observed when comparing the measurement to the approximate calculation at NNLO+NNLL which is based on the p_{T}^{Z} distribution in simulated $Z \to \ell\ell$ events.

Using Eq. 9.3, the fiducial cross sections are used to extrapolate the measurement to the total phase space. Total cross sections are calculated for each of the individual final states and found to be:

$$\sigma_{\text{tot}}^{e\mu} = 70.6^{+1.3}_{-1.3}(\text{stat.})^{+5.8}_{-5.1}(\text{syst.})^{+1.4}_{-1.4}(\text{lumi.})\ \text{pb} \tag{10.9}$$

$$\sigma_{\text{tot}}^{ee} = 73.6^{+4.2}_{-4.1}(\text{stat.})^{+7.5}_{-6.4}(\text{syst.})^{+1.5}_{-1.5}(\text{lumi.})\ \text{pb} \tag{10.10}$$

$$\sigma_{\text{tot}}^{\mu\mu} = 74.0^{+3.0}_{-3.0}(\text{stat.})^{+7.1}_{-5.9}(\text{syst.})^{+1.5}_{-1.5}(\text{lumi.})\ \text{pb}. \tag{10.11}$$

The results from individual final states are found in agreement with each other, even within statistical uncertainties. They are combined to a total cross section of:

$$\sigma_{\text{tot}} = 71.1^{+1.1}_{-1.1}(\text{stat.})^{+5.7}_{-5.0}(\text{syst.})^{+1.4}_{-1.4}(\text{lumi.})\ \text{pb}, \tag{10.12}$$

where the correlations between systematic uncertainties are considered. The statistical uncertainty of the combined result is improved compared to the results obtained from the individual final states. The systematic uncertainties however are largely correlated and therefore do not significantly reduce when combining the results. The measured total cross sec-

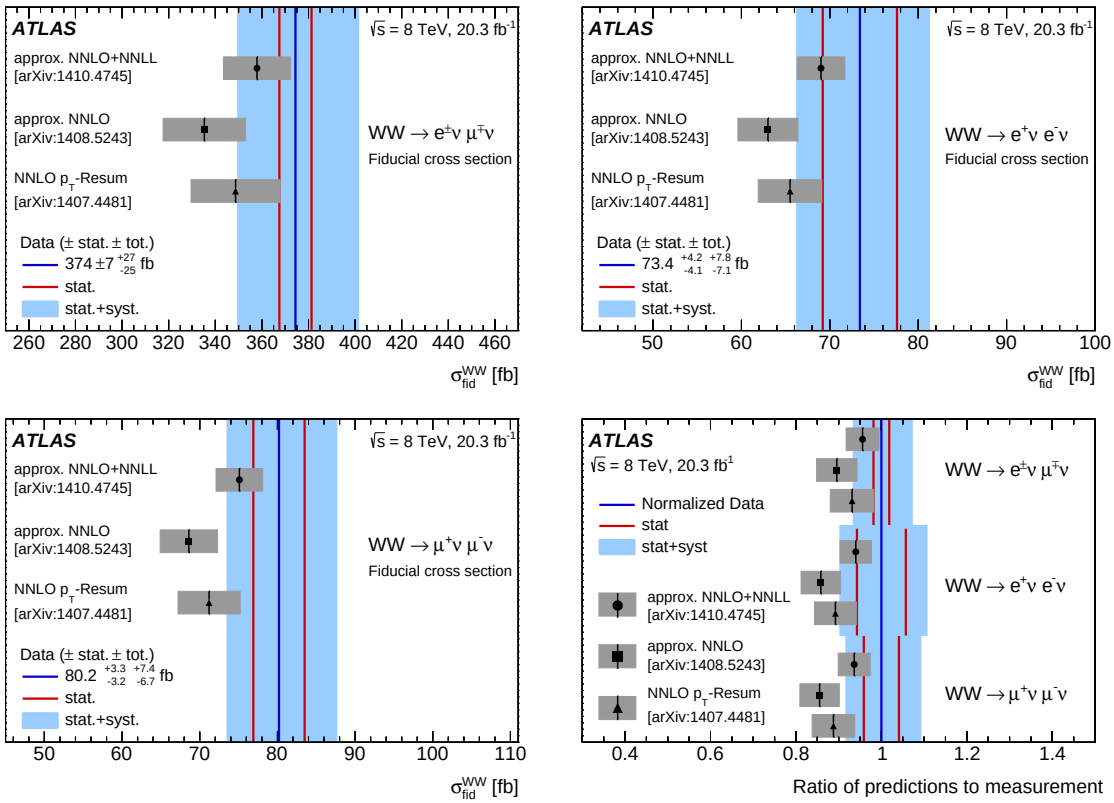

Figure 10.3: Comparison of the measured fiducial cross sections with various theoretical predictions of fiducial cross sections. The comparison is made for the $e\mu$+0-jet (top left), ee+0-jet (top right) and $\mu\mu$+0-jet (bottom left) final states. The ratios of theoretical predictions to the cross sections measured in data are shown as well (bottom right). Previously published in Ref. [5].

tion is compared to the theoretical prediction in Fig. 10.4 where the results obtained from $e\mu$, ee and $\mu\mu$ final states are shown as well. The theoretical calculation agrees with the measured cross section within 1.3 standard deviations.

In an earlier publication of this analysis in Ref. [4] a difference of more than two standard deviations between measurement and theoretical calculation was quoted. Here, the highest order calculation was quoted as the sum of the NLO $q\bar{q} \to W^+W^-$ and LO $gg \to W^+W^-$ cross sections [99], and the NNLO $gg \to H \to W^+W^-$ cross section [103], resulting in a total cross section of $\sigma_{\text{tot}} = 58.7^{+3.0}_{-2.7}$ pb. The tension between the measured and theoretical cross sections initiated speculations about possible signs of physics beyond the Standard Model, which can produce signatures similar to the W^+W^- final state in certain parameter spaces of supersymmetry [172–174]. The measured $pp \to W^+W^-$ cross section can consequently also be used to derive constraints on the parameter space [175].

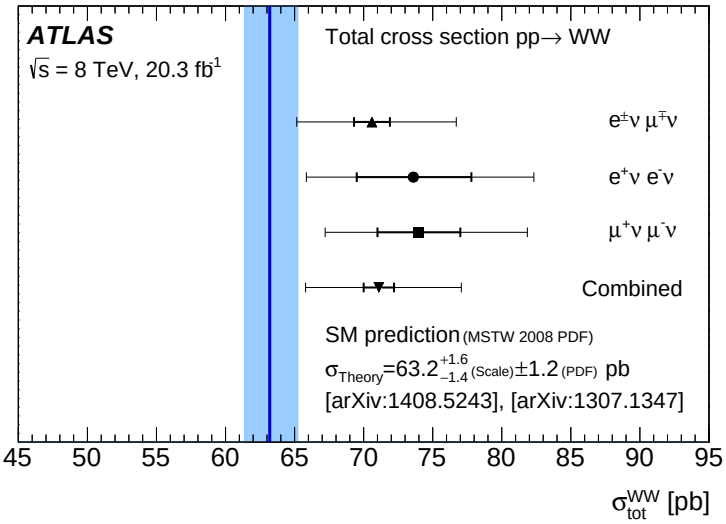

Figure 10.4: The total $pp \to W^+W^-$ production cross section extrapolated from $e\mu$+0-jet, ee+0-jet and $\mu\mu$+0-jet final states as well as the result obtained by combining the three final states. Two sets of error bars are shown: the smaller error bars correspond to the statistical uncertainty, the larger error bars correspond to the combined statistical and systematic uncertainty. The measured cross section is higher than the theoretical calculation at NNLO accuracy by 1.3 standard deviations. Previously published in Ref. [5].

10.4 Differential Cross Sections

To further study the difference between the measured cross sections and the theoretical calculations, measurements of differential cross sections are performed that allow a more thorough comparison. Since the fiducial phase-space regions of $e\mu$, ee and $\mu\mu$ final states differ and the precision of the result in Section 10.3 is largely driven by $e\mu$ final states, only $e\mu$ final states are considered. A Bayesian iterative unfolding approach [176, 177] is employed.

Differential distributions are measured in the fiducial phase space as a function of six different variables. Only quantities of single leptons and the dilepton system are considered since variables involving neutrinos typically have much lower resolution. The transverse momentum of the leading lepton, p_{T}, the transverse momentum of the dilepton system, $p_{\mathrm{T}}^{\ell\ell}$, and the invariant mass of the dilepton system, $m_{\ell\ell}$, are reported. All these variables are correlated with the centre-of-mass energy of the hard interaction and are sensitive to contributions from physics beyond the Standard Model at high values of $\sqrt{\hat{s}}$. The variables p_{T} and $p_{\mathrm{T}}^{\ell\ell}$ also are directly correlated to the transverse momentum of the W^+W^- system. They are therefore sensitive to higher order QCD corrections that affect the p_{T}^{WW} distribution. The azimuthal separation of the dilepton system, $\Delta\phi_{\ell\ell}$, is directly related to the spin correlation of the two W bosons and plays a special role in the measurement of the Higgs boson signal in the decay mode to W bosons [153]. Additional measurements are performed as a function of the rapidity of the dilepton system, $\left|y_{\ell\ell}\right|$, and the observable $\left|\cos\theta^*\right|$. The

rapidity is sensitive to the Lorentz boost of the W^+W^- system along the z-axis and therefore also to the different production modes from qq, qg and gg initial states. The variable $\left|\cos\theta^*\right| = \left|\tanh\left(\Delta\eta_\ell/2\right)\right|$ is suggested in the context of searches for light super-partners of the top quark in W^+W^- signatures in Ref. [173].

The results for the differential cross sections are shown in Fig. 10.5 and compared to theoretical predictions using Mc@Nlo+Jimmy and PowHeg+Pythia8. The theoretical predictions are scaled to the cross section at NNLO and contributions from $gg \to W^+W^-$ and $gg \to H \to W^+W^-$ production are added using the simulated gg2ww and PowHeg event samples. They therefore correspond to the approximate fiducial cross sections calculated in Section 10.2. Also shown are theoretical distributions that are obtained by reweighting the PowHeg+Pythia8 samples to the p_{T}^{WW} distribution calculated at NLO+NNLL [111]. The measured and theoretical cross sections are divided by the bin width to avoid discontinuities in the distributions. The measured differential cross sections have a precision ranging between ±10% and ±30%. They are on average ∼ 15% higher than the theoretical cross sections as shown in the lower panels of Fig. 10.5. The discrepancy is constant for most of the kinematic variables of which differential cross sections are measured. Only for low values of p_{T} and $m_{\ell\ell}$, and high values of p_{T} and $p_{\mathrm{T}}^{\ell\ell}$ larger discrepancies are seen. The distributions of the various theoretical cross sections show only little differences and within the uncertainties of the measurement none of them is preferred by data. Contributions from $gg \to H \to W^+W^-$ production contribute on average 2% and at most 8.5% for $\Delta\phi_{\ell\ell} < \pi/2$ to the cross-section.

10.5 Limits on Anomalous Triple Gauge Couplings

The pair production of W bosons is sensitive to extensions of the Standard Model that modify the WWV, $V = Z, \gamma$, couplings. Contributions from physics beyond the Standard Model can be expressed in terms of anomalous triple gauge couplings (aTGC) parameters as introduced in Section 5.3. Detector level distributions of $e\mu$+0-jet final states are used to set limits on aTGC parameters. The distribution of the transverse momentum of the leading lepton was found to be particularly sensitive and is shown in Fig. 10.6a. Simulated event samples where the anomalous coupling parameters are set to high values are overlaid.

No significant excess over the estimated contributions from Standard Model W^+W^- production and background is seen in data. The distribution is therefore used to set limits on anomalous triple gauge couplings. Confidence intervals at 95% confidence level are determined using a profile-likelihood ratio test statistic. The resulting limits on the coupling parameters Δg_Z, $\Delta\kappa_Z$ and λ_Z, using the constraints in Eqs. 5.14 and 5.15, are found to be:

	Expected	Observed	Expected	Observed	
	$\Lambda = 7$ TeV	$\Lambda = 7$ TeV	$\Lambda = \infty$	$\Lambda = \infty$	
Δg_Z	$[-0.035, 0.041]$	$[-0.017, 0.029]$	$[-0.033, 0.037]$	$[-0.016, 0.027]$	(10.13)
$\Delta\kappa_Z$	$[-0.041, 0.038]$	$[-0.027, 0.021]$	$[-0.037, 0.035]$	$[-0.025, 0.020]$	(10.14)
λ_Z	$[-0.033, 0.033]$	$[-0.020, 0.020]$	$[-0.031, 0.031]$	$[-0.019, 0.019]$,	(10.15)

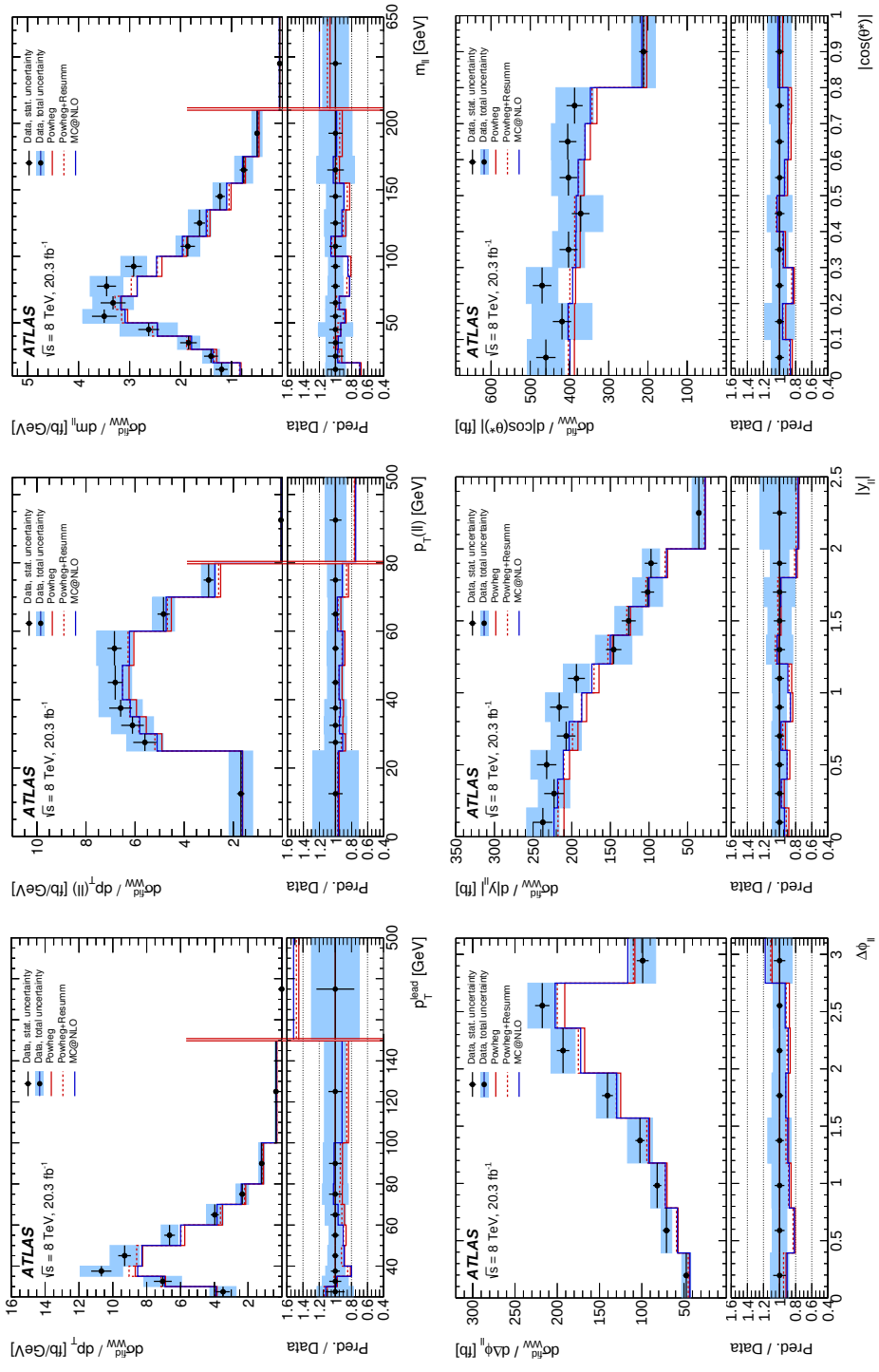

Figure 10.5: Differential cross sections of $pp \to W^+W^-$ production measured in the fiducial phase space of the $e\mu$+0-jet final state. The error bars indicate the statistical uncertainty of the measurement, the blue band indicates the combined statistical and systematic uncertainties. The cross sections are measured for the transverse momentum of the leading lepton, p_{T} (top left), the dilepton transverse momentum, $p_{\mathrm{T}}^{\ell\ell}$ (top middle), the dilepton invariant mass, $m_{\ell\ell}$ (top right), the azimuthal separation of the leptons, $\Delta\phi_{\ell\ell}$ (bottom left), the dilepton rapidity, $|y_{ll}|$ (bottom middle), and the observable $|\cos\theta^*|$, defined in the text (bottom right). Double red lines indicate a change in the axis of abscissae. Taken from Ref. [5]. The theoretical cross sections are scaled to a total cross section of $63.2^{+2.0}_{-1.8}$ pb and therefore correspond to approximate fiducial cross sections.

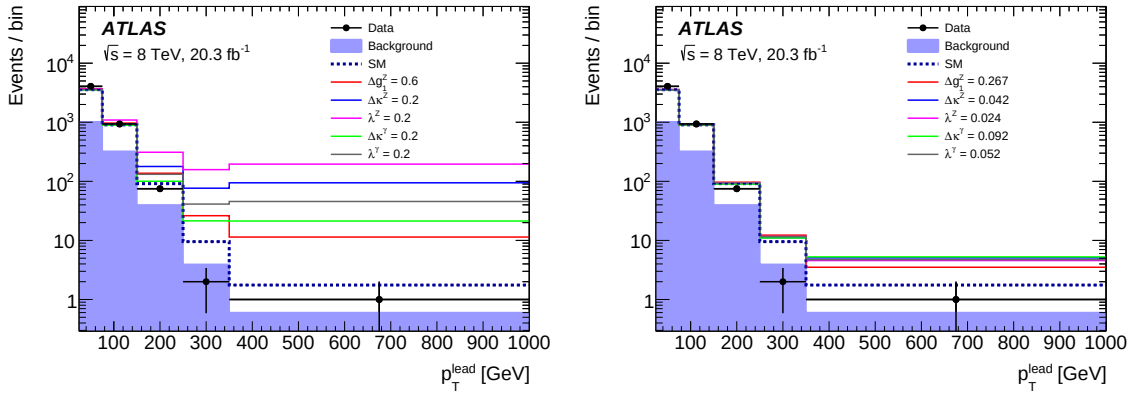

(a) (b)

Figure 10.6: Distribution of the transverse momentum, p_{T}, of the leading lepton used to set limits on anomalous triple gauge couplings (aTGCs). (a) The distributions of events from $e\mu$+0-jet final states in data and simulated event samples are compared to the distributions of simulated event samples with different values of the aTGC parameters. (b) They are also compared to the distributions with the aTGC parameters set to the upper 95% confidence level bound. The constraints in Eqs. 5.14 and 5.15 are *not* used here which is why the values of the parameters differ from the confidence level bounds given in Eqs. 10.13-10.15. The form factor scale is set to infinity. Taken from Ref. [5].

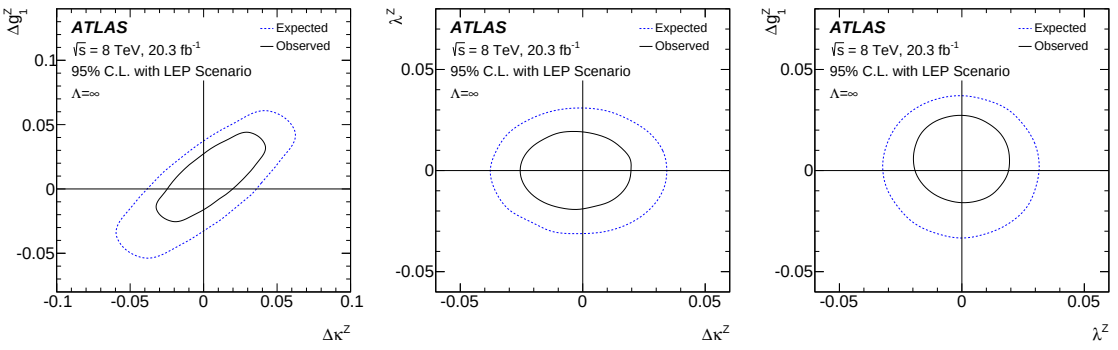

Figure 10.7: The expected and observed 95% confidence level contours for linear combinations of coupling parameters. The parameter not under study is set to zero. The number of anomalous coupling parameters is constrained by Eqs. 5.14 and 5.15, reducing them to three: Δg_Z, $\Delta\kappa_Z$ and λ_Z. The form factor scale is set to infinity. Taken from Ref. [5].

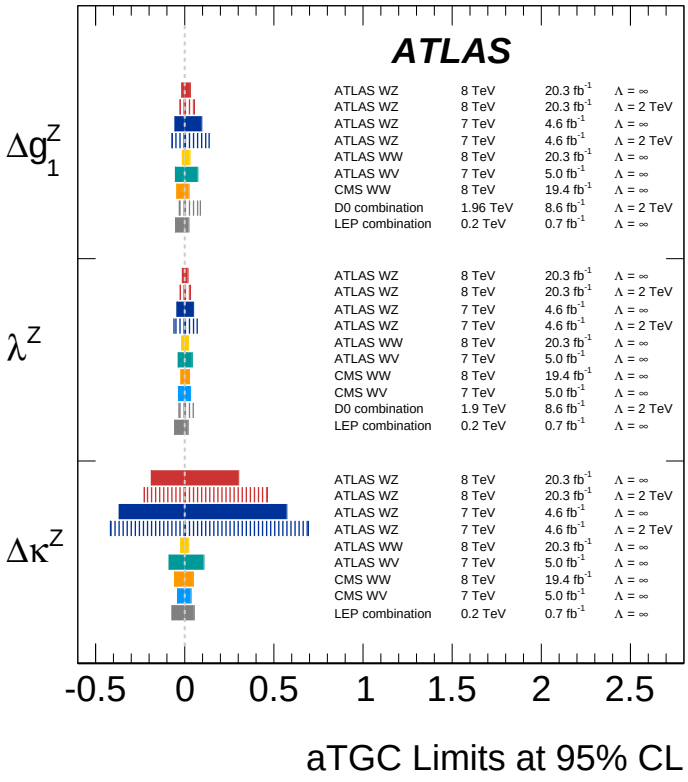

Figure 10.8: Observed 95% confidence level intervals on anomalous triple gauge couplings obtained in different analyses. Shown are limits derived at the LEP collider, the D0 experiment at the Tevatron and in WW and WZ events at the ATLAS and CMS experiments. The number of anomalous coupling parameters is constrained by Eqs. 5.14 and 5.15. The limits denoted WV are obtained in semi-leptonic final states of WW and WZ events, those denoted WW and WZ are derived in fully leptonic final states. Taken from Ref. [158].

and shown here for two choices of the form factor scale of $\Lambda = 7$ TeV and $\Lambda = \infty$. Limits on linear combinations of coupling parameters are shown in Fig. 10.7. Since the estimated contributions from the Standard Model signal and background exceed the data at high values of p_{T} the observed limits are more stringent than expected. The observed 95% confidence level intervals improve on those previously derived in W^+W^- events in $pp \to W^+W^-$ and $p\bar{p} \to W^+W^-$ collisions. The limits derived at LEP and the Tevatron are compared to recent measurements at the LHC in Fig. 10.8. The limits presented in Eqs. 10.13-10.15 are comparable to the limits derived in $pp \to W^{\pm}Z$ production on the same dataset [158] and to those derived at the LEP collider.

11 Results from WW+1-jet Final States and Combination with WW+0-jet

The analysis of events with one hadronic jet in the final state is presented here. For the calculation of the fiducial cross section, migrations from $e\mu$+0-jet final states to the selected $e\mu$+1-jet final states are taken into account with the approach introduced in Chapter 9. Combined results from the 0-jet and 1-jet categories are quoted and an alternative calculation of the total W^+W^- cross section is obtained.

11.1 Event Yields in Data and Theoretical Predictions

A total of 3458 events with one jet are selected in data. The events yields in data are compared to the event yields estimated to originate from W^+W^- production and the individual background contributions in Table 11.1. Only $\sim$ 45% of the events selected in data are attributed to W^+W^- production. The largest individual contribution from background processes is top quark production that constitutes $\sim$ 40% of the selected data. Nevertheless, the estimation of the background from top-quark production introduces similar uncertainties as the estimation of contributions from W+jets and multijet production, $Z \to \ell\ell$ and other diboson production. The systematic uncertainties are in fact of comparable size for all the background contributions and only the statistical component of the uncertainty is larger for background from top-quark production. The signal yield in the 1-jet category in data is similar to the yield expected from event simulation and compatible within the uncertainties assigned. Compared to the 0-jet category, where differences are observed, the uncertainties on the expected signal yields are larger, such that no significant difference is seen. The distribution of the transverse momentum of the selected jet is shown in Fig. 11.1. Good agreement between data and the estimated event yields is seen.

The results presented here are compared to updated theoretical calculations compared to those used throughout Chapter 10. While the total cross section for resonant $gg \to H \to W^+W^-$ production at NNLO was refined [178], the cross section of non-resonant $gg \to W^+W^-$ production was extended to also include NLO ($O(\alpha_s^3)$) effects [102]. The contributions from $gg \to W^+W^-$ production are therefore removed from the $pp \to W^+W^-$ calculation at NNLO and the calculation at NLO is added. For a consistent treatment, the choice of the renormalisation and factorisation scales is changed with respect to the values used throughout Chapter 10 to $\mu_R = \mu_F = m_W$. The sum of these contributions yields a total theoretical $pp \to W^+W^-$ cross section of:

$$\sigma_{\text{tot}} = 65.0^{+1.3}_{-1.4}\ \text{pb}. \tag{11.1}$$

It should be noted that the alternative choice of fixed resummation and factorisation scales

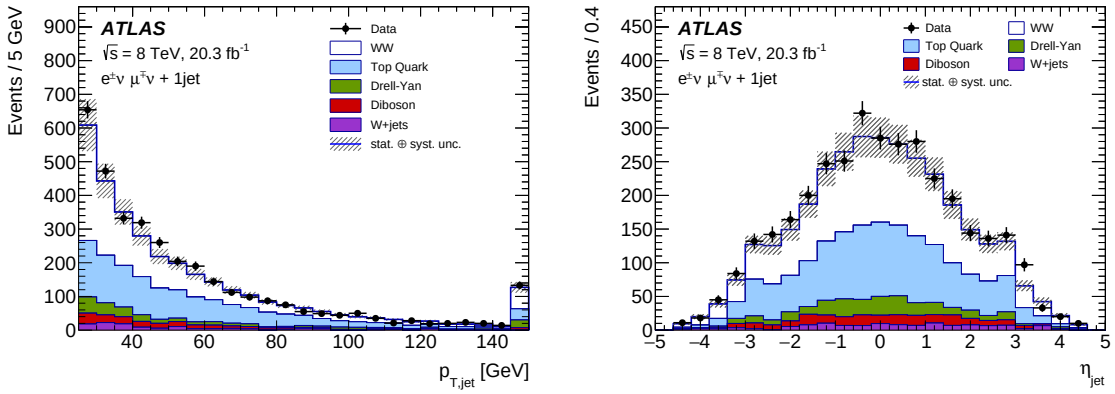

Figure 11.1: Distribution of the transverse momentum, p_{T} (left), and the pseudorapidity, η (right), of the jet selected in $e\mu$+1-jet events. Data are shown together with the estimated signal and background contributions. The yields from W^+W^- production are shown for a total cross section of $58.7^{+4.2}_{-3.8}$ pb. The uncertainty bands show statistical and systematic uncertainties. Previously published in Ref. [6].

	$e\mu$+1-jet
Observed events	3458 ± 59
Total expected events	3305 ± 48 ± 340
W^+W^- signal	1486 ± 7 ± 325
Top quark	1236 ± 43 ± 49
W+jets and multijet	121 ± 15 ± 50
$Z \to \ell\ell$	267 ± 12 ± 49
Other dibosons	195 ± 5 ± 53
Total background	1819 ± 47 ± 101

Table 11.1: Observed and expected signal and background contributions in $e\mu$+1-jet final states. The yields from W^+W^- production are shown for a total cross section of $58.7^{+4.2}_{-3.8}$ pb. The estimated event yields are shown with their statistical and systematic uncertainties.

causes the $pp \to W^+W^-$ cross section to be $\sim$ 1% higher than if the scale is dynamically set. The increase of the total cross section is therefore due to including the improved calculation of non-resonant $gg \to W^+W^-$ production. Approximate fiducial cross sections are calculated following the approach in Section 10.2 by multiplying the total $pp \to W^+W^-$ production cross section with the acceptance correction factor A_{WW}. Corresponding approximate fiducial cross sections at NLO+NNLL are also obtained where the modified acceptance correction factors for $e\mu$ final states in jet bins are $A_{WW}^{0\text{-jet}} = 0.237 \pm 0.013$, $A_{WW}^{1\text{-jet}} = 0.086 \pm 0.018$ and $A_{WW}^{0/1\text{-jet}} = 0.322 \pm 0.015$. The fiducial $e\mu$+0-jet, $e\mu$+1-jet and the combined fiducial $e\mu$+0/1-jet cross sections are found to be:

	$e\mu$+0-jet	$e\mu$+1-jet	$e\mu$+0/1-jet	
$\sigma_{\text{fid}}^{\text{NNLO}}$	346 ± 19 fb	141 ± 30 fb	487 ± 22 fb	(11.2)
$\sigma_{\text{fid}}^{\text{NLO+NNLL}}$	361 ± 21 fb	131 ± 28 fb	491 ± 24 fb.	(11.3)

As seen in Section 10, the calculation at NLO+NNLL enhances the fiducial 0-jet cross section by 4%. Since the calculation does not alter the total cross section, the enhancement in $n_{\text{jets}} = 0$ results in a reduction of the fiducial 1-jet and ≥2-jet cross sections. Both theoretical predictions for the fiducial $e\mu$+0/1-jet cross sections differ by less than 1% which was anticipated and motivated the measurement of 1-jet final states. The direct comparison of Eqs. 11.2 and 11.3 shows that the combined fiducial $e\mu$+0/1-jet cross section is less sensitive to the effects targeted by the resummation calculation. The theoretical predictions for the $e\mu$+0-jet and $e\mu$+1-jet cross sections exhibit larger differences.

In addition, predictions for fiducial cross sections became available at NNLO with the Matrix programme [101]. It allows the calculation of theoretical fiducial cross sections without the use of acceptance correction factors from lower order calculations but includes the non-resonant $gg \to W^+W^-$ production process at leading order only. Contributions from $gg \to H \to W^+W^-$ are added with the approach used above. The fiducial cross sections at NNLO are found to be:

	$e\mu$+0-jet	$e\mu$+1-jet	$e\mu$+0/1-jet	
$\sigma_{\text{fid}}^{\text{Matrix}}$	343 ± 17 fb	124 ± 31 fb	466 ± 38 fb.	(11.4)

Uncertainties are assigned by studying the scale dependence of the cross-sections and treating the cross sections of successive inclusive jet-binned cross sections uncorrelated [168]. The fiducial cross sections are corrected for non-perturbative effects by comparing simulated event samples of Madgraph [179] interfaced with Pythia8 with these effects enabled or disabled and a systematic uncertainty assigned by studying the effect using Madgraph and Herwig++ [180]. The fiducial 0-jet cross section is comparable to the one given in Eq. 11.2 but the 1-jet and 0/1-jet cross sections are generally lower.

11.2 Results from 1-jet and 0+1-jet Final States

The fiducial $e\mu$+1-jet cross section is obtained from Eqs. 9.17 and 9.18. Since migration effects between the 0-jet and 1-jet categories are taken into account, the fiducial $e\mu$+1-jet cross section is a function of the yields in data in both the $e\mu$+0-jet and the $e\mu$+1-jet final states. The cross section in the fiducial phase space defined by the $e\mu$+1-jet selection criteria is measured to be:

$$\sigma_{\text{fid}}^{\text{1-jet}} = 136 \pm 6(\text{stat.}) \pm 14(\text{syst.}) \pm 3(\text{lumi.})\ \text{fb}. \tag{11.5}$$

With the approach from Eqs. 9.17 and 9.18 the fiducial $e\mu$+1-jet cross section is measured simultaneously with the $e\mu$+0-jet cross-section. The result for $\sigma_{\text{fid}}^{\text{0-jet}}$ is found to agree with the previous result shown in Eq. 10.6 within better than 0.1%. The small difference can be understood from migration effects which are very small in $e\mu$+0-jet events. The correlation of the total uncertainties of the measurements of the fiducial $e\mu$+0-jet and $e\mu$+1-jet cross sections is found to be small with a correlation coefficient of $\rho = -0.05$. A list of the individual systematic sources in the 0-jet, 1-jet and the combined 0/1-jet categories is shown in Table 11.2 and illustrates that the small size of the correlation coefficient is a result of cancellations in reconstruction uncertainties on the jet energy scale which yields overall negative correlations. At the same time there are large positive correlations in the remaining reconstruction uncertainties and in the uncertainties on the estimation of background contributions.

The combined fiducial $e\mu$+0/1-jet cross section is obtained from the sum of the individual fiducial $e\mu$+0-jet and $e\mu$+1-jet cross sections considering the correlation between both measurements:

$$\sigma_{\text{fid}}^{\text{0/1-jet}} = 511 \pm 9(\text{stat.}) \pm 26(\text{syst.}) \pm 10(\text{lumi.})\ \text{fb}. \tag{11.6}$$

Compared to the individual fiducial 0-jet and 1-jet cross sections the combined result has the smallest relative uncertainty of ±5.8%. The source of uncertainties with the largest reduction is the jet energy scale that is reduced by a factor of 2.5. Additional uncertainties introduced by rejecting events containing b-jets and increased uncertainties on the estimation of background contributions cause the overall experimental uncertainty to be lower by only $\sim 20\%$ compared to the fiducial $e\mu$+0-jet cross section.

A comparison of the measured fiducial cross sections with their theoretical values from Eq. 11.4 is shown in Fig. 11.2. The measured values of the fiducial 1-jet and 0/1-jet cross sections are found to be slightly larger than the corresponding theoretical values. The missing contributions at NLO from non-resonant $gg \to W^+W^-$ production would likely account for the remaining difference. In comparison with the approximate theoretical fiducial cross sections given in Eqs. 11.2 and 11.3 the measurements and the theoretical predictions agree.

11.3 Ratio of Jet-binned Fiducial Cross Sections

To allow further comparisons independently of the total cross section, the ratio of the jet-binned fiducial cross sections R_1 is calculated, defined as $R_1 = \sigma_{\text{fid}}^{\text{1-jet}} \big/ \sigma_{\text{fid}}^{\text{0-jet}}$ in Ref. [96]. The

	$e\mu$+0-jet	$e\mu$+1-jet	$e\mu$+0/1-jet
Experimental uncertainties [%]			
Integrated luminosity	±2.0	±2.2	±2.0
Pile-up	±1.4	±0.6	±0.8
Trigger	±0.4	±0.4	±0.4
Electron energy scale	±0.4	±0.3	±0.3
Electron energy resolution	<0.1	<0.1	<0.1
Electron ID and reconstruction	±1.0	±1.2	±1.0
Electron isolation	±0.2	±0.3	±0.2
Muon momentum scale	±0.1	±0.5	±0.2
Muon momentum resolution (ID)	±0.6	±0.2	±0.4
Muon momentum resolution (MS)	±0.1	±0.4	±0.1
Muon ID and reconstruction	±0.4	±0.6	±0.4
Muon isolation	±0.6	±0.8	±0.6
Jet vertex fraction	±0.2	±0.1	<0.1
Jet energy scale	±4.1	±4.2	±1.4
Jet energy resolution	±1.4	±1.0	±1.4
$E_{\mathrm{T}}^{\mathrm{miss}}$ scale cell-out term	±1.1	±0.1	±0.7
$E_{\mathrm{T}}^{\mathrm{miss}}$ resolution cell-out term	±0.3	±0.1	±0.1
$p_{\mathrm{T}}^{\mathrm{miss}}$ scale cell-out term	±0.2	±0.4	±0.3
$p_{\mathrm{T}}^{\mathrm{miss}}$ resolution cell-out term	±0.1	±0.3	±0.2
b-tagging	—	±2.9	±0.7
Background uncertainties [%]			
Top-quark background	±1.4	±5.2	±1.3
W+jets & multijet background	±3.6	±3.5	±3.2
Drell–Yan background	±0.5	±3.8	±1.2
Other diboson cross sections	±0.7	±4.2	±1.1

Table 11.2: Experimental systematic uncertainties in the determination of fiducial cross sections in the 0-jet, 1-jet and the combined 0/1-jet categories. The uncertainties for the 0-jet and 1-jet categories are taken from Table 9.3. The uncertainties for the combined 0/1-jet category illustrates the correlations of the systematic uncertainties of the individual sources..

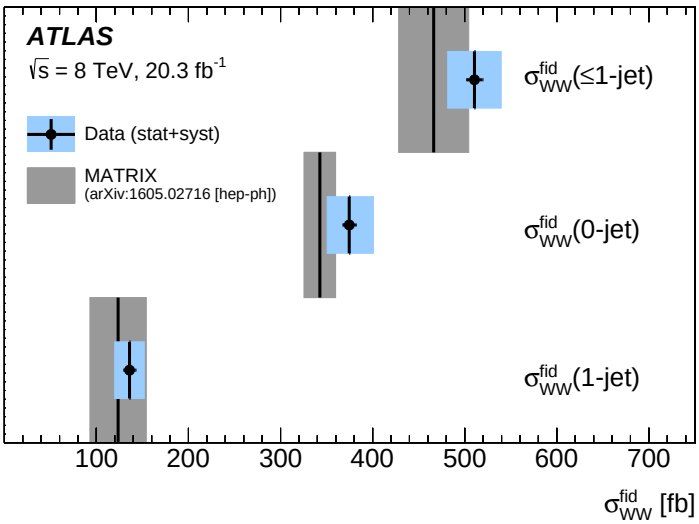

Figure 11.2: Comparison of the measured cross sections in the 0-jet, 1-jet and 0/1-jet fiducial regions with theoretical predictions. The theoretical predictions are obtained with Matrix [101]. For the measured cross sections statistical uncertainties are indicated as horizontal error bars and the combined statistical and systematic uncertainties are shown as a blue band. The uncertainties on theoretical cross sections are shown as a grey band. They are estimated by varying the renormalisation and factorisation scales independently by a factor of two and considering the uncertainties of successive inclusive jet-binned cross sections uncorrelated. Contributions from resonant $gg \to H \to W^+W^-$ production are added using simulated PowHeg+Pythia8 samples. Previously published in Ref. [6].

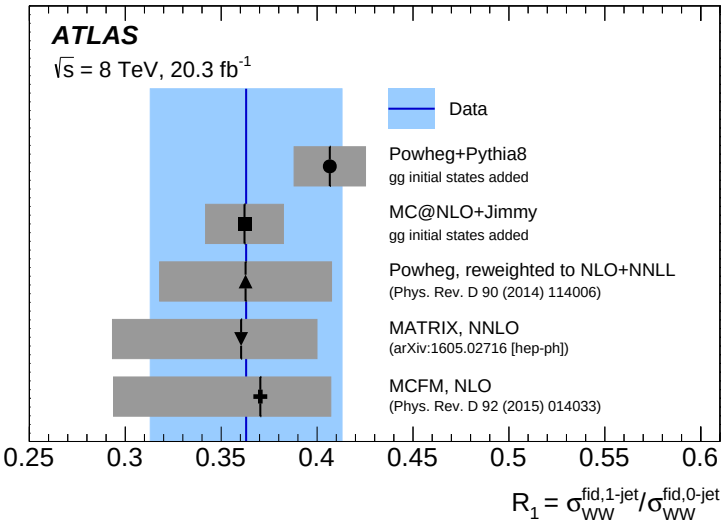

Figure 11.3: Measured and theoretical values for the fiducial jet-binned cross-section ratio R_1. The measured values are compared to theoretical predictions from two different $q\bar{q} \to W^+W^-$ event generators and by reweighting the p_{T}^{WW} distribution from PowHeg+Pythia to the calculation at NLO+NNLL. Contributions from resonant and non-resonant $gg \to W^+W^-$ production are added to all three theoretical values. Also shown are fixed-order calculations at NNLO using Matrix [101] and at NLO using MCFM [95, 99] where contributions from $gg \to H \to W^+W^-$ are added using simulated PowHeg+Pythia8 samples. Previously published in Ref. [6].

quantity R_1 is measured to be:

$$R_1^{\text{fid}} = 0.363 \pm 0.050 \tag{11.7}$$

which is compared to several theoretical calculations in Fig. 11.3. All theoretical values agree well with the measurement within the uncertainties and the measurement does not allow to favour one theoretical value over the others. Theoretical predictions are taken from either the simulated PowHeg+Pythia8 or the simulated Mc@Nlo event samples of $q\bar{q} \to W^+W^-$ production . Theoretical uncertainties are assigned by studying the scale dependence. The renormalisation and factorisation scales are varied independently by factors of one-half and two with the constraint $0.5 < \mu_F/\mu_R < 2$ but simultaneously in the numerator and denominator of R_1. The contributions from resonant and non-resonant $gg \to W^+W^-$ production are in both cases added from the simulated event samples used throughout this thesis. The full effect of omitting the $gg \to W^+W^-$ contributions is assigned as an additional theoretical uncertainty. To investigate the effect of resummation calculations at NLO+NNLL, the simulated PowHeg+Pythia8 event samples are reweighted to reproduce the p_T^{WW} distribution from Ref. [111]. The resummation scale is varied in addition to the renormalisation and factorisation scales. Finally, theoretical values for R_1 are obtained using the fixed-order calculations from Matrix at NNLO [101] and MCFM at NLO. The latter uses the implementations of inclusive W^+W^- production [99] and W^+W^- +1-jet production [95]. In both these calculations the renormalisation and factorisation scales are set to $\mu_F = \mu_R = m_W$ and non-perturbative effects are estimated based on Madgraph using the approach described in Section 11.1. Contributions from resonant $gg \to H \to W^+W^-$ are included using the simulated PowHeg+Pythia8 event samples.

11.4 Total Cross Section

To profit from the reduced uncertainties in the combined $e\mu$+0/1-jet fiducial cross section, the result is extrapolated to the total phase space using the appropriate acceptance correction factor that can be calculated from Table 9.2:

$$\sigma_{\text{tot}} = 68.2 \pm 1.2(\text{stat.}) \pm 3.4(\text{syst.}) \pm 2.8(\text{theo.}) \pm 1.4(\text{lumi.})\ \text{pb}, \tag{11.8}$$

where uncertainties arising from the jet-binning in the migration matrix R_{ij} and A_{WW} are treated correlated and slightly reduce the theoretical uncertainty. The measured total cross section is found to be in agreement with the theoretical calculation of $\sigma_{\text{tot}} = 65.0^{+1.2}_{-1.1}$ pb. The agreement is improved compared to the result presented in Chapter 10 since the measured value is lower by 4% and the theoretical calculation increased by including NLO corrections to $gg \to W^+W^-$ production. Apart from the change in the central value, the measured cross section improved in precision. Comparing the results in Eqs. 10.12 and 11.8 the uncertainties are reduced by $\sim 12\%$ from $\pm 8\%$ to $\pm 7\%$. The main reason for the reduction is the cancellation of uncertainties from the jet energy scale and resolution. Additional uncertainties are introduced by the rejection of jets from b-quark decays and the large amount of background from top-quark production in the 1-jet category. While the largest sources of uncertainty in the previous result are originating from the jet energy scale and the scale dependence of the acceptance correction factor, the new result is dominated by uncertain-

ties on the background estimation. The measurement of the total cross section still heavily relies on theoretical calculations, resulting in large uncertainties on the acceptance correction factor. The factors $A_{WW}^{0\text{-jet}}$ as used in Chapter 10 and $A_{WW}^{0/1\text{-jet}}$ in fact have comparable total uncertainties. The overall reduction of uncertainties makes the result in Eq. 11.8 the most precise measurement of the total W^+W^- cross section achieved at a hadron-collider experiment so far.

Summary

The large dataset corresponding to an integrated luminosity of 20.3 fb^{-1} of proton–proton collisions recorded by the ATLAS experiment at a centre-of-mass energy of $\sqrt{s} = 8$ TeV in the year 2012 allowed a precise measurement of the diboson production processes. In this thesis, measurements of W^+W^- production in final states with two leptons and missing transverse momentum are presented. The measurements provide a test of the gauge structure of the electroweak theory of the Standard Model.

In order to provide detector independent results for a comparison to theoretical calculations, the knowledge of the efficiency to reconstruct particles in the ATLAS experiment is crucial. In the course of this thesis the efficiency of the electron identification was determined and has been published in Refs. [1–3]. A method previously used to measure efficiencies in $W \to e\nu$ decays is adapted to $Z \to ee$ decays. Detailed studies of the W+jets and multijet background are necessary to account for changes in the electron reconstruction in the year 2012 in order to continue to provide results with high precision. At energies of electroweak processes that produce electrons with transverse momenta of typically 30 GeV $< p_{\text{T}} <$ 50 GeV the efficiency of the electron identification is known with a precision of better than ±0.5%. For electrons with lower transverse energies the precision is better than ±2.5%. This allows to perform precise measurements in the electroweak sector of the Standard Model at the ATLAS experiment using electron final states. The studies presented here have served as an important ingredient to all measurements by the ATLAS collaboration using electron final states.

The $pp \to W^+W^-$ production cross section is measured in final states with exactly one electron and one muon of opposite electric charge, or with pairs of electrons and muons. The studies presented here have resulted in three publications [4–6]. A first measurement of the total production cross section had a precision of ±8%, at that time representing the most precise measurement of this process at a hadron collider experiment. Due to the high precision achieved, a difference of more than two standard deviations is seen between the resulting total cross section and the corresponding theoretical calculations. This has subsequently elicited a large number of theoretical publications on an improved description of the jet-veto requirement but also phenomenological publications speculating about signs of physics beyond the Standard Model that have a W^+W^- signature. In parallel to the measurement, theorists have significantly improved the calculations of the total cross sections. The initial tension of two standard deviations is reduced by comparing the measurement to updated theoretical calculations. The comparison of fiducial cross sections with various theoretical calculations further shows that the resummation of large logarithms introduced by the restriction of the phase space to 0-jet final states can improve the agreement. In addition, differential cross-section measurements are presented and limits on anomalous trilinear gauge couplings are set.

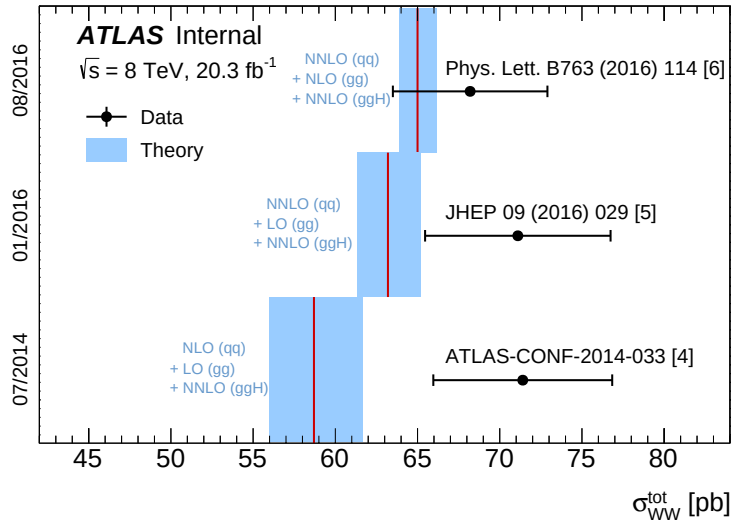

Figure 11.4: The total $pp \to W^+W^-$ cross section and its evolution with time. Shown are the measured values and theoretical calculations quoted in three publications conducted in the context of this thesis. The different analyses have been published in July 2014 [4], in January 2016 [5], and in August 2016 [6].

The largest sources of theoretical and experimental uncertainties in the measurement are related to the requirement of the absence of hadronic jets in the final state. Together with the discussion on the modelling of the jet-veto requirement, this gave the initial motivation to study W^+W^- production in final states with one hadronic jet. It constitutes the first measurement of the jet-associated W boson pair production cross section at the ATLAS experiment. In combination with the previous measurement that was restricted to 0-jet final states, the first measurement of the ratio of jet-binned fiducial cross sections is performed. It allows for a comparison of theoretical calculations independently of the total cross section. The cross sections in the fiducial 0-jet and 1-jet regions are combined and extrapolated to the total phase space. The total $pp \to W^+W^-$ production cross section is measured to be:

$$\sigma_{\text{tot}} = 68.2 \pm 1.2(\text{stat.}) \pm 3.4(\text{syst.}) \pm 2.8(\text{theo.}) \pm 1.4(\text{lumi.})\ \text{pb}. \tag{11.9}$$

This provides a measurement of the total cross section from a larger phase space region than that considered before. By expanding the phase space, the experimental uncertainties due to uncertainties on the jet-energy scale are considerably reduced. It is also found that the sensitivity on the theoretical modelling of the jet multiplicity is reduced. Compared to the previous measurement, the value of the total cross section is measured to be 4% lower. The measured cross section is found in good agreement with the theoretical calculation which is also updated with respect to the previous measurement. The comparison of measured and theoretical total W^+W^- cross sections quoted in three publications conducted in the course of this thesis is shown in Fig. 11.4.

The total W^+W^- cross section extrapolated from ≤1-jet final states represents the most

precise measurement conducted at a hadron collider experiment so far. It is also more precise than the measurement by the CMS collaboration that includes 1-jet final states as well. The largest individual source of uncertainty remains the restriction to ≤1-jet final states. Future measurements could possibly improve the precision by extending the measurement to also include 2-jet final states. However, this is extremely challenging due to the large background from top-quark pair production. There are also large experimental uncertainties, in particular from the estimation of the contributions from W+jets production. A future improvement of the measurement could be achieved by further rejecting W+jets events using improved lepton identification criteria, or developing novel techniques for the estimation of the contributions from misidentified leptons to the selected data.

In conclusion, the $pp \to W^+W^-$ production cross section is measured with a high precision. The phase-space region is extended compared to previous measurements which reduces the sensitivity of the measurement to theoretical calculations. Improved theoretical calculations of the total production cross section agree well with the measurement. Differential distributions are also measured and found to be well described by theoretical calculations. Deviations from the Standard Model can be expressed in terms of anomalous triple gauge couplings for which stringent limits are derived.

Bibliography

[1] ATLAS Collaboration, *Electron reconstruction and identification efficiency measurements with the ATLAS detector using the 2011 LHC proton-proton collision data*, Eur. Phys. J. **C74** no. 7, (2014) 2941, arXiv:1404.2240 [hep-ex].

[2] ATLAS Collaboration, *Electron efficiency measurements with the ATLAS detector using the 2012 LHC proton-proton collision data*, ATLAS note: ATLAS-CONF-2014-032.

[3] ATLAS Collaboration, *Electron efficiency measurements with the ATLAS detector using the 2015 LHC proton-proton collision data*, ATLAS note: ATLAS-CONF-2016-024.

[4] ATLAS Collaboration, *Measurement of the W^+W^- production cross section in proton-proton collisions at $\sqrt{s} = 8$ TeV with the ATLAS detector* , ATLAS note: ATLAS-CONF-2014-033.

[5] ATLAS Collaboration, *Measurement of total and differential W^+W^- production cross sections in proton-proton collisions at $\sqrt{s} = 8$ TeV with the ATLAS detector and limits on anomalous triple-gauge-boson couplings*, JHEP **09** (2016) 029, arXiv:1603.01702 [hep-ex].

[6] ATLAS Collaboration, *Measurement of W^+W^- production in association with one jet in proton–proton collisions at $\sqrt{s} = 8$ TeV with the ATLAS detector*, Phys. Lett. **B763** (2016) 114, arXiv:1608.03086 [hep-ex].

[7] S. Glashow, *Partial Symmetries of Weak Interactions*, Nucl. Phys. **22** (1961) 579.

[8] S. Weinberg, *A Model of Leptons*, Phys. Rev. Lett. **19** (1967) 1264.

[9] A. Salam and J. C. Ward, *Electromagnetic and weak interactions*, Phys. Lett. **13** (1964) 168.

[10] H. Fritzsch, M. Gell-Mann, and H. Leutwyler, *Advantages of the Color Octet Gluon Picture*, Phys. Lett. **B47** (1973) 365–368.

[11] D. J. Gross and F. Wilczek, *Ultraviolet Behavior of Nonabelian Gauge Theories*, Phys. Rev. Lett. **30** (1973) 1343–1346.

[12] H. D. Politzer, *Reliable Perturbative Results for Strong Interactions?*, Phys. Rev. Lett. **30** (1973) 1346–1349.

[13] P. W. Higgs, *Broken Symmetries and the Masses of Gauge Bosons*, Phys. Rev. Lett. **13** (1964) 508.

[14] F. Englert and R. Brout, *Broken Symmetry and the Mass of Gauge Vector Mesons*, Phys. Rev. Lett. **13** (1964) 321–323.

[15] G. Guralnik, C. Hagen, and T. Kibble, *Global Conservation Laws and Massless Particles*, Phys. Rev. Lett. **13** (1964) 585.

[16] UA1 Collaboration, *Experimental Observation of Isolated Large Transverse Energy Electrons with Associated Missing Energy at* $\sqrt{s}$ *=540 GeV*, Phys. Lett. **B122** (1983) 103.

[17] UA1 Collaboration, *Experimental Observation of Lepton Pairs of Invariant Mass around* 95 GeV/c^2 *at the CERN SPS Collider*, Phys. Lett. **B126** (1983) 398.

[18] UA2 Collaboration, *Observation of Single Isolated Electrons of High Transverse Momentum in Events with Missing Transverse Energy at the CERN* $\bar{p}p$ *Collider*, Phys. Lett. **B122** (1983) 476.

[19] UA2 Collaboration, *Evidence for* $Z^0 \to e^+e^-$ *at the CERN* $\bar{p}p$ *Collider*, Phys. Lett. **B129** (1983) 130.

[20] ATLAS Collaboration, *Observation of a new particle in the search for the Standard Model Higgs boson with the ATLAS detector at the LHC*, Phys. Lett. **B716** (2012) 1–29, arXiv:1207.7214 [hep-ex].

[21] CMS Collaboration, *Observation of a new boson at a mass of 125 GeV with the CMS experiment at the LHC*, Phys. Lett. **B716** (2012) 30–61, arXiv:1207.7235 [hep-ex].

[22] F. Halzen and A. D. Martin, *Quarks and Leptons: An Introductory Course in Modern Particle Physics*. Wiley, 1984.

[23] M. E. Peskin and D. V. Schroeder, *An Introduction to Quantum Field Theory*. Westview Press, 1995.

[24] R. Ellis, W. Stirling, and B. Webber, *QCD and collider physics*, vol. 8. 1996.

[25] Particle Data Group, K. A. Olive *et al.*, *Review of Particle Physics*, Chin. Phys. **C38** (2014) 090001.

[26] M. Mulders and G. Zanderighi, eds., *Proceedings of the 2014 European School of High-Energy Physics*, ESHEP. CERN, Geneva, 2016.

[27] J. Benecke, T. T. Chou, C.-N. Yang, and E. Yen, *Hypothesis of Limiting Fragmentation in High-Energy Collisions*, Phys. Rev. **188** (1969) 2159–2169.

[28] A. D. Martin, W. J. Stirling, R. S. Thorne, and G. Watt, *Parton distributions for the LHC*, Eur. Phys. J. **C63** (2009) 189, arXiv:0901.0002 [hep-ph].

[29] Y. L. Dokshitzer, *Calculation of the Structure Functions for Deep Inelastic Scattering and* e^+ e^- *Annihilation by Perturbation Theory in Quantum Chromodynamics*, Sov. Phys. JETP **46** (1977) 641.

[30] V. Gribov and L. Lipatov, *Deep inelastic ep scattering in perturbation theory*, Sov. J. Nucl. Phys. **15** (1972) 438.

[31] G. Altarelli and G. Parisi, *Asymptotic Freedom in Parton Language*, Nucl. Phys. **B126** (1977) 298.

[32] W. Stirling, *Private communication*.

[33] A. Buckley *et al.*, *General-purpose event generators for LHC physics*, Phys. Rept. **504** (2011) 145–233, arXiv:1101.2599 [hep-ph].

[34] ATLAS Collaboration, *The ATLAS Simulation Infrastructure*, Eur. Phys. J. **C70** (2010) 823–874, arXiv:1005.4568 [physics.ins-det].

[35] B. Andersson, G. Gustafson, G. Ingelman, and T. Sjöstrand, *Parton Fragmentation and String Dynamics*, Phys. Rept. **97** (1983) 31.

[36] *LEP Design Report: Vol.2. The LEP Main Ring*.

[37] L. Evans and P. Bryant, *LHC Machine*, JINST **3** (2008) S08001.

[38] O. Brüning *et al.*, *LHC design report. Vol. I-III*, CERN-2004-003-V-1, CERN-2004-003-V-2, CERN-2004-003-V-3.

[39] ATLAS, *Luminosity determination in pp collisions at $\sqrt{s} = 8$ TeV using the ATLAS detector at the LHC*, arXiv:1608.03953 [hep-ex].

[40] S. van der Meer, *Calibration of the effective beam height in the ISR*, CERN note: CERN-ISR-PO-68-31.

[41] ATLAS Collaboration, *Improved luminosity determination in pp collisions at $\sqrt{s} = 7$ TeV using the ATLAS detector at the LHC*, Eur. Phys. J. **C73** (2013) 2518, arXiv:1302.4393 [hep-ex].

[42] https://twiki.cern.ch/twiki/bin/view/AtlasPublic/LuminosityPublicResults.

[43] ATLAS Collaboration, *The ATLAS Experiment at the CERN Large Hadron Collider*, JINST **3** (2008) S08003.

[44] G. Aad *et al.*, *ATLAS pixel detector electronics and sensors*, JINST **3** (2008) P07007.

[45] A. Ahmad *et al.*, *The Silicon microstrip sensors of the ATLAS semiconductor tracker*, Nucl. Instrum. Meth. **A578** (2007) 98–118.

[46] E. Abat *et al.*, *The ATLAS Transition Radiation Tracker (TRT) proportional drift tube: Design and performance*, JINST **3** (2008) P02013.

[47] ATLAS Collaboration, *Electron and photon energy calibration with the ATLAS detector using LHC Run 1 data*, Eur. Phys. J. **C74** no. 10, (2014) 3071, arXiv:1407.5063 [hep-ex].

[48] ATLAS Collaboration, *Two Dimensional Views of the Run-1 ATLAS Inner Detector Produced by the Use of Hadronic Interaction Vertices* , https://atlas.web.cern.ch/Atlas/GROUPS/PHYSICS/PLOTS/IDTR-2016-001/.

[49] T. Koffas and K. Tackmann, *ATLAS Tracker Material using Photon Conversions*, https://atlas.web.cern.ch/Atlas/GROUPS/PHYSICS/EGAMMA/PublicPlots/20110216/ATL-COM-PHYS-2011-120/.

[50] ATLAS Collaboration, *A study of the material in the ATLAS inner detector using secondary hadronic interactions*, JINST **7** (2012) P01013, arXiv:1110.6191 [hep-ex].

[51] B. Aubert *et al.*, *Construction, assembly and tests of the ATLAS electromagnetic barrel calorimeter*, Nucl. Instrum. Meth. **A558** (2006) 388–418.

[52] ATLAS Collaboration, *Performance of the ATLAS Trigger System in 2010*, Eur. Phys. J. **C72** (2012) 1849, arXiv:1110.1530 [hep-ex].

[53] ATLAS Collaboration, *Performance of the ATLAS Inner Detector Track and Vertex Reconstruction in the High Pile-Up LHC Environment*, ATLAS note: ATLAS-CONF-2012-042.

[54] R. Frühwirth, *Application of Kalman filtering to track and vertex fitting*, Nucl. Instrum. Meth. **A262** (1987) 444–450.

[55] ATLAS Collaboration, *Improved electron reconstruction in ATLAS using the Gaussian Sum Filter-based model for bremsstrahlung* , ATLAS note: ATLAS-CONF-2012-047.

[56] ATLAS Collaboration, *Electron performance measurements with the ATLAS detector using the 2010 LHC proton-proton collision data*, Eur. Phys. J. **C72** (2012) 1909, arXiv:1110.3174 [hep-ex].

[57] ATLAS Collaboration, *Expected electron performance in the ATLAS experiment*, ATLAS note: ATL-PHYS-PUB-2011-006.

[58] ATLAS Collaboration, *Performance of the ATLAS Electron and Photon Trigger in p-p Collisions at $\sqrt{s} = 7$ TeV in 2011* , ATLAS note: ATLAS-CONF-2014-048.

[59] ATLAS Collaboration, *Electron and photon trigger performance measurements using 2012 ATLAS data*, ATL-COM-DAQ-2014-058.

[60] ATLAS Collaboration, *Measurement of the muon reconstruction performance of the ATLAS detector using 2011 and 2012 LHC proton–proton collision data*, Eur. Phys. J. **C74** (2014) 3130, arXiv:1407.3935 [hep-ex].

[61] ATLAS Collaboration, *Muon reconstruction efficiency and momentum resolution of the ATLAS experiment in proton-proton collisions at $\sqrt{s} = 7$ TeV in 2010*, Eur. Phys. J. **C74** (2014) 3034, arXiv:1404.4562 [hep-ex].

[62] ATLAS Collaboration, *Expected Performance of the ATLAS Experiment - Detector, Trigger and Physics*, arXiv:0901.0512 [hep-ex].

[63] ATLAS Collaboration, *Performance of the ATLAS muon trigger in pp collisions at* $\sqrt{s}$ = 8 *TeV*, Eur. Phys. J. **C75** (2015) 120, arXiv:1408.3179 [hep-ex].

[64] W. Lampl, S. Laplace, D. Lelas, P. Loch, H. Ma, S. Menke, S. Rajagopalan, D. Rousseau, S. Snyder, and G. Unal, *Calorimeter clustering algorithms: Description and performance*.

[65] M. Cacciari and G. P. Salam, *Pileup subtraction using jet areas*, Phys. Lett. **B659** (2008) 119–126, arXiv:0707.1378 [hep-ph].

[66] M. Cacciari, G. P. Salam, and G. Soyez, *The Anti-k(t) jet clustering algorithm*, JHEP **04** (2008) 063, arXiv:0802.1189 [hep-ph].

[67] ATLAS Collaboration, *Jet energy measurement and its systematic uncertainty in proton-proton collisions at* $\sqrt{s}$ = 7 *TeV with the ATLAS detector*, Eur. Phys. J. **C75** (2015) 17, arXiv:1406.0076 [hep-ex].

[68] ATLAS Collaboration, *Data-driven determination of the energy scale and resolution of jets reconstructed in the ATLAS calorimeters using dijet and multijet events at* $\sqrt{s}$ = 8 *TeV*, ATLAS note: ATLAS-CONF-2015-017.

[69] ATLAS Collaboration, *Determination of the jet energy scale and resolution at ATLAS using* Z/γ*-jet events in data at* $\sqrt{s}$ = 8 *TeV*, ATLAS note: ATLAS-CONF-2015-057.

[70] ATLAS Collaboration, *Monte Carlo Calibration and Combination of In-situ Measurements of Jet Energy Scale, Jet Energy Resolution and Jet Mass in ATLAS*, ATLAS note: ATLAS-CONF-2015-037.

[71] ATLAS Collaboration, *Characterisation and mitigation of beam-induced backgrounds observed in the ATLAS detector during the 2011 proton-proton run*, JINST **8** (2013) P07004, arXiv:1303.0223 [hep-ex].

[72] ATLAS Collaboration, *Tagging and suppression of pileup jets with the ATLAS detector* , ATLAS note: ATLAS-CONF-2014-018.

[73] ATLAS Collaboration, *Calibration of the performance of* b*-tagging for* c *and light-flavour jets in the 2012 ATLAS data* , ATLAS note: ATLAS-CONF-2014-046.

[74] ATLAS Collaboration, *Performance of* b*-Jet Identification in the ATLAS Experiment*, JINST **11** no. 04, (2016) P04008, arXiv:1512.01094 [hep-ex].

[75] ATLAS Collaboration, *Calibration of* b*-tagging using dileptonic top pair events in a combinatorial likelihood approach with the ATLAS experiment* , ATLAS note: ATLAS-CONF-2014-004.

[76] ATLAS Collaboration, *Performance of Missing Transverse Momentum Reconstruction in Proton-Proton Collisions at 7 TeV with ATLAS*, Eur. Phys. J. **C72** (2012) 1844, arXiv:1108.5602 [hep-ex].

[77] ATLAS Collaboration, *Pile-up Suppression in Missing Transverse Momentum Reconstruction in the ATLAS Experiment in Proton-Proton Collisions at* $\sqrt{s}$ = 8 *TeV*, ATLAS note: ATLAS-CONF-2014-019.

[78] ATLAS Collaboration, *Performance of Missing Transverse Momentum Reconstruction in ATLAS studied in Proton-Proton Collisions recorded in 2012 at* $\sqrt{s} = 8$ *TeV*, ATLAS note: ATLAS-CONF-2013-082.

[79] P. Nason, *A New method for combining NLO QCD with shower Monte Carlo algorithms*, JHEP **0411** (2004) 040, arXiv:hep-ph/0409146 [hep-ph].

[80] S. Frixione, P. Nason, and C. Oleari, *Matching NLO QCD computations with Parton Shower simulations: the POWHEG method*, JHEP **0711** (2007) 070, arXiv:0709.2092 [hep-ph].

[81] S. Alioli, P. Nason, C. Oleari, and E. Re, *A general framework for implementing NLO calculations in shower Monte Carlo programs: the POWHEG BOX*, JHEP **1006** (2010) 043, arXiv:1002.2581 [hep-ph].

[82] S. Alioli, P. Nason, C. Oleari, and E. Re, *NLO vector-boson production matched with shower in POWHEG*, JHEP **07** (2008) 060, arXiv:0805.4802 [hep-ph].

[83] T. Sjöstrand, S. Mrenna, and P. Skands, *A Brief Introduction to PYTHIA 8.1*, Comput. Phys. Commun. **178** (2008) 852–867, arXiv:0710.3820 [hep-ph].

[84] ATLAS Collaboration, *The ATLAS Simulation Infrastructure*, Eur. Phys. J. **C70** (2010) 823–874, arXiv:1005.4568 [physics.ins-det].

[85] S. Agostinelli *et al.*, *GEANT4: A Simulation toolkit*, Nucl. Instrum. Meth. **A506** (2003) 250–303.

[86] P. Golonka and Z. Was, *PHOTOS Monte Carlo: A Precision tool for QED corrections in Z and W decays*, Eur. Phys. J. **C45** (2006) 97, arXiv:hep-ph/0506026.

[87] P. Sommer, *A Measurement of the Electron Identification Efficiency using* $W \to e\nu$ *Decays in the ATLAS Experiment*. Diploma thesis, Albert-Ludwigs-Universität Freiburg, 2012.

[88] ATLAS Collaboration, *Measurement of the photon identification efficiencies with the ATLAS detector using LHC Run-1 data*, arXiv:1606.01813 [hep-ex].

[89] H1 Collaboration, *Measurement of the Inclusive* ep *Scattering Cross Section at Low* Q^2 *and* x *at HERA*, Eur. Phys. J. **C63** (2009) 625–678, arXiv:0904.0929 [hep-ex].

[90] R. W. Brown and K. O. Mikaelian, W^+W^- *and* Z^0Z^0 *pair production in* e^+e^-*,* pp*, and* $\overline{p}p$ *colliding beams*, Phys. Rev. D **19** (1979) 922–934.

[91] M. J. G. Veltman, *Second Threshold in Weak Interactions*, Acta Phys. Polon. **B8** (1977) 475.

[92] J. Ohnemus, *Hadronic ZZ,* W^-W^+*, and* $W^\pm Z$ *production with QCD corrections and leptonic decays*, Phys. Rev. **D50** (1994) 1931–1945, arXiv:hep-ph/9403331 [hep-ph].

[93] L. J. Dixon, Z. Kunszt, and A. Signer, *Vector boson pair production in hadronic collisions at order* α_s *: Lepton correlations and anomalous couplings*, Phys. Rev. **D60** (1999) 114037, arXiv:hep-ph/9907305 [hep-ph].

[94] S. Dittmaier, S. Kallweit, and P. Uwer, *NLO QCD corrections to pp/ppbar –> WW+jet+X including leptonic W-boson decays*, Nucl. Phys. **B826** (2010) 18–70, arXiv:0908.4124 [hep-ph].

[95] J. M. Campbell, D. J. Miller, and T. Robens, *Next-to-Leading Order Predictions for WW+Jet Production*, Phys. Rev. **D92** no. 1, (2015) 014033, arXiv:1506.04801 [hep-ph].

[96] F. F. Cordero, P. Hofmann, and H. Ita, *W^+W^- + 3 Jet Production at the Large Hadron Collider in NLO QCD*, arXiv:1512.07591 [hep-ph].

[97] E. W. N. Glover and J. J. van der Bij, *Vector Boson Pair Production Via Gluon Fusion*, Phys. Lett. **B219** (1989) 488.

[98] T. Binoth, M. Ciccolini, N. Kauer, and M. Kramer, *Gluon-induced WW background to Higgs boson searches at the LHC*, JHEP **03** (2005) 065, arXiv:hep-ph/0503094 [hep-ph].

[99] J. M. Campbell, R. K. Ellis, and C. Williams, *Vector boson pair production at the LHC*, JHEP **07** (2011) 018, arXiv:1105.0020 [hep-ph].

[100] T. Gehrmann, M. Grazzini, S. Kallweit, P. Maierhöfer, A. von Manteuffel, S. Pozzorini, D. Rathlev, and L. Tancredi, *W^+W^- Production at Hadron Colliders in Next to Next to Leading Order QCD*, Phys. Rev. Lett. **113** no. 21, (2014) 212001, arXiv:1408.5243 [hep-ph].

[101] M. Grazzini, S. Kallweit, S. Pozzorini, D. Rathlev, and M. Wiesemann, *W^+W^- production at the LHC: fiducial cross sections and distributions in NNLO QCD*, arXiv:1605.02716 [hep-ph].

[102] F. Caola, K. Melnikov, R. Röntsch, and L. Tancredi, *QCD corrections to W^+W^- production through gluon fusion*, Physics Letters B **754** (2016) 275 – 280.

[103] LHC Higgs Cross Section Working Group, *Handbook of LHC Higgs Cross Sections: 3. Higgs Properties*, arXiv:1307.1347 [hep-ph].

[104] C. Anastasiou, C. Duhr, F. Dulat, F. Herzog, and B. Mistlberger, *Higgs Boson Gluon-Fusion Production in QCD at Three Loops*, Phys. Rev. Lett. **114** (2015) 212001, arXiv:1503.06056 [hep-ph].

[105] A. Bierweiler et al., *Electroweak corrections to W-boson pair production at the LHC*, JHEP **11** (2012) 093, arXiv:1208.3147 [hep-ph].

[106] A. Bierweiler, T. Kasprzik, and J. H. Kühn, *Vector-boson pair production at the LHC to $O(\alpha^3)$ accuracy*, JHEP **12** (2013) 071, arXiv:1305.5402 [hep-ph].

[107] M. Billoni, S. Dittmaier, B. Jäger, and C. Speckner, *Next-to-leading order electroweak corrections to $pp \to W^+W^- \to 4$ leptons at the LHC in double-pole approximation*, JHEP **12** (2013) 043, arXiv:1310.1564 [hep-ph].

[108] B. Biedermann, M. Billoni, A. Denner, S. Dittmaier, L. Hofer, B. Jäger, and L. Salfelder, *Next-to-leading-order electroweak corrections to $pp \to W^+W^- \to 4$ leptons at the LHC*, JHEP **06** (2016) 065, arXiv:1605.03419 [hep-ph].

[109] T. Binoth et al., *Gluon-induced W-boson pair production at the LHC*, JHEP **12** (2006) 046, arXiv:hep-ph/0611170.

[110] LHC Higgs Cross Section Working Group, *Handbook of LHC Higgs Cross Sections: 2. Differential Distributions*, arXiv:1201.3084 [hep-ph].

[111] P. Meade, H. Ramani, and M. Zeng, *Transverse momentum resummation effects in W^+W^- measurements*, Phys. Rev. **D90** no. 11, (2014) 114006, arXiv:1407.4481 [hep-ph].

[112] P. Jaiswal and T. Okui, *Explanation of the WW excess at the LHC by jet-veto resummation*, Phys. Rev. **D90** no. 7, (2014) 073009, arXiv:1407.4537 [hep-ph].

[113] P. Jaiswal, P. Meade, and H. Ramani, *Precision diboson measurements and the interplay of p_T and jet-veto resummations*, Phys. Rev. **D93** no. 9, (2016) 093007, arXiv:1509.07118 [hep-ph].

[114] M. Grazzini, S. Kallweit, D. Rathlev, and M. Wiesemann, *Transverse-momentum resummation for vector-boson pair production at NNLL+NNLO*, JHEP **08** (2015) 154, arXiv:1507.02565 [hep-ph].

[115] P. F. Monni and G. Zanderighi, *On the excess in the inclusive $W^+W^- \to l^+l^-\nu\bar{\nu}$ cross section*, JHEP **05** (2015) 013, arXiv:1410.4745 [hep-ph].

[116] M. S. Neubauer, *Diboson production at colliders*, Ann. Rev. Nucl. Part. Sci. **61** (2011) 223–250.

[117] G. Gounaris *et al.*, *Triple gauge boson couplings* in *AGS / RHIC Users Annual Meeting Upton, New York, June 15-16, 1995*. 1996. arXiv:hep-ph/9601233 [hep-ph].

[118] H. Aihara *et al.*, *Anomalous gauge boson interactions*, arXiv:hep-ph/9503425.

[119] ALEPH Collaboration, *ALEPH: A detector for electron-positron annnihilations at LEP*, Nucl. Instrum. Meth. **A294** (1990) 121–178, [Erratum: Nucl. Instrum. Meth.A303,393(1991)].

[120] DELPHI Collaboration, *The DELPHI detector at LEP*, Nucl. Instrum. Meth. **A303** (1991) 233–276.

[121] L3 Collaboration, *The Construction of the L3 Experiment*, Nucl. Instrum. Meth. **A289** (1990) 35–102.

[122] OPAL Collaboration, *The OPAL detector at LEP*, Nucl. Instrum. Meth. **A305** (1991) 275–319.

[123] DELPHI, OPAL, LEP Electroweak, ALEPH, L3, *Electroweak Measurements in Electron-Positron Collisions at W-Boson-Pair Energies at LEP*, Phys. Rept. **532** (2013) 119–244, arXiv:1302.3415 [hep-ex].

[124] CDF Collaboration, *The CDF-II detector: Technical design report*.

[125] D0 Collaboration, *The Upgraded D0 detector*, Nucl. Instrum. Meth. **A565** (2006) 463–537, arXiv:physics/0507191 [physics.ins-det].

[126] *Design report Tevatron 1 Project*.

[127] D0 Collaboration, *Measurement of the WW Production Cross Section with Dilepton Final States in $p\overline{p}$ Collisions at $\sqrt{s}$ = 1.96 TeV and Limits on Anomalous Trilinear Gauge Couplings*, Phys. Rev. Lett. **103** (2009) 191801.

[128] CDF Collaboration, *Measurement of the W^+W^- Production Cross Section and Search for Anomalous $WW\gamma$ and WWZ Couplings in $p\overline{p}$ Collisions at $\sqrt{s}$ = 1.96 TeV*, Phys. Rev. Lett. **104** (2010) 201801.

[129] J. M. Campbell and R. K. Ellis, *An Update on vector boson pair production at hadron colliders*, Phys. Rev. **D60** (1999) 113006, arXiv:hep-ph/9905386 [hep-ph].

[130] D0 Collaboration, *Search for Higgs boson production in oppositely charged dilepton and missing energy final states in* 9.7 fb^{-1} *of $p\overline{p}$ collisions at $\sqrt{s}$=1.96 TeV*, Phys. Rev. D **88** (2013) 052006.

[131] CDF Collaboration, *Measurement of the Production and Differential Cross Sections of W^+W^- Bosons in Association with Jets in $p\bar{p}$ Collisions at $\sqrt{s}$ = 1.96 TeV*, Phys. Rev. **D91** no. 11, (2015) 111101, arXiv:1505.00801 [hep-ex], [Addendum: Phys. Rev.D92,no.3,039901(2015)].

[132] D0, *Limits on anomalous trilinear gauge boson couplings from WW, WZ and $W\gamma$ production in $p\bar{p}$ collisions at $\sqrt{s}$ = 1.96 TeV*, Phys. Lett. **B718** (2012) 451–459, arXiv:1208.5458 [hep-ex].

[133] ATLAS Collaboration, *Measurement of W^+W^- production in pp collisions at $\sqrt{s}$=7 TeV with the ATLAS detector and limits on anomalous WWZ and $WW\gamma$ couplings*, Phys. Rev. **D87** no. 11, (2013) 112001, arXiv:1210.2979 [hep-ex], [Erratum: Phys. Rev.D88,no.7,079906(2013)].

[134] CMS Collaboration, *Measurement of the W^+W^- Cross section in pp Collisions at $\sqrt{s}$ = 7 TeV and Limits on Anomalous $WW\gamma$ and WWZ couplings*, Eur. Phys. J. **C73** no. 10, (2013) 2610, arXiv:1306.1126 [hep-ex].

[135] CMS Collaboration, *Measurement of W^+W^- and ZZ production cross sections in pp collisions at $\sqrt{s}$ = 8 TeV*, Phys. Lett. **B721** (2013) 190–211, arXiv:1301.4698 [hep-ex].

[136] CMS Collaboration, *Measurement of the* $\mathrm{W^+W^-}$ *cross section in pp collisions at $\sqrt{s}$ = 8 TeV and limits on anomalous gauge couplings*, Eur. Phys. J. **C76** no. 7, (2016) 401, arXiv:1507.03268 [hep-ex].

[137] D0 Collaboration, *Precision measurement of the ratio* $\mathrm{B}(t \to Wb)/\mathrm{B}(t \to Wq)$ *and Extraction of* V_{tb}, Phys. Rev. Lett. **107** (2011) 121802, arXiv:1106.5436 [hep-ex].

[138] G. Corcella *et al.*, *HERWIG 6.5: an event generator for hadron emission reactions with interfering gluons (including supersymmetric processes)*, JHEP **01** (2001) 010, arXiv:hep-ph/0011363.

[139] J. M. Butterworth, J. R. Forshaw, and M. H. Seymour, *Multiparton interactions in photoproduction at HERA*, Z. Phys. C **72** (1996) 637–646, arXiv:hep-ph/9601371.

[140] H.-L. Lai *et al.*, *New parton distributions for collider physics*, Phys. Rev. **D82** (2010) 074024, arXiv:1007.2241 [hep-ph].

[141] S. Frixione and B. R. Webber, *Matching NLO QCD computations and parton shower simulations*, JHEP **06** (2002) 029, arXiv:hep-ph/0204244.

[142] B. P. Kersevan and E. Richter-Was, *The Monte Carlo event generator AcerMC versions 2.0 to 3.8 with interfaces to PYTHIA 6.4, HERWIG 6.5 and ARIADNE 4.1*, Comput. Phys. Commun. **184** (2013) 919–985, arXiv:hep-ph/0405247.

[143] ATLAS Collaboration, *ATLAS tunes of PYTHIA 6 and Pythia 8 for MC11*, ATL-PHYS-PUB-2011-009, 2011.

[144] J. Pumplin *et al.*, *New generation of parton distributions with uncertainties from global QCD analysis*, JHEP **07** (2002) 012, arXiv:hep-ph/0201195.

[145] M. L. Mangano, M. Moretti, F. Piccinini, R. Pittau, and A. D. Polosa, *ALPGEN, a generator for hard multiparton processes in hadronic collisions*, JHEP **07** (2003) 001, arXiv:hep-ph/0206293.

[146] T. Gleisberg et al., *Event generation with SHERPA 1.1*, JHEP **02** (2009) 007, arXiv:0811.4622 [hep-ph].

[147] M. Czakon and A. Mitov, *Top++: A Program for the Calculation of the Top-Pair Cross-Section at Hadron Colliders*, Comput. Phys. Commun. **185** (2014) 2930, arXiv:1112.5675 [hep-ph].

[148] N. Kidonakis, *Two-loop soft anomalous dimensions for single top quark associated production with a* W^- *or* H^-, Phys. Rev. D **82** (2010) 054018, arXiv:1005.4451 [hep-ph].

[149] N. Kidonakis, *Next-to-next-to-leading-order collinear and soft gluon corrections for* t*-channel single top quark production*, Phys. Rev. D **83** (2011) 091503, arXiv:1103.2792 [hep-ph].

[150] N. Kidonakis, *NNLL resummation for* s*-channel single top quark production*, Phys. Rev. D **81** (2010) 054028, arXiv:1001.5034 [hep-ph].

[151] S. Catani and M. Grazzini, *An NNLO subtraction formalism in hadron collisions and its application to Higgs boson production at the LHC*, Phys. Rev. Lett. **98** (2007) 222002, arXiv:hep-ph/0703012.

[152] M. Beckingham, M. Duehrssen, E. Schmidt, M. Shapiro, M. Venturi, J. Virzi, I. Vivarelli, M. Werner, S. Yamamoto, and T. Yamanaka, *The simulation principle and performance of the ATLAS fast calorimeter simulation FastCaloSim* Tech. Rep. ATL-PHYS-PUB-2010-013, CERN, Geneva, 2010. https://cds.cern.ch/record/1300517.

[153] ATLAS Collaboration, *Observation and measurement of Higgs boson decays to WW^* with the ATLAS detector*, Phys. Rev. **D92** no. 1, (2015) 012006, arXiv:1412.2641 [hep-ex].

[154] ATLAS Collaboration, *Evidence for Electroweak Production of $W^{\pm}W^{\pm}jj$ in pp Collisions at $\sqrt{s} = 8$ TeV with the ATLAS Detector*, Phys. Rev. Lett. **113** no. 14, (2014) 141803, arXiv:1405.6241 [hep-ex].

[155] B. Mellado, X. Ruan, and Z. Zhang, *Extraction of Top Backgrounds in the Higgs Boson Search with the $H \to WW^{\star} \to \ell\ell + E_T^{miss}$ Decay with a Full-Jet Veto at the LHC*, Phys. Rev. **D84** (2011) 096005, arXiv:1101.1383 [hep-ph].

[156] ATLAS Collaboration, *Measurements of $W\gamma$ and $Z\gamma$ production in pp collisions at $\sqrt{s} = 7$ TeV with the ATLAS detector at the LHC*, Phys. Rev. **D87** no. 11, (2013) 112003, arXiv:1302.1283 [hep-ex].

[157] M. Grazzini, S. Kallweit, and D. Rathlev, *$W\gamma$ and $Z\gamma$ production at the LHC in NNLO QCD*, JHEP **07** (2015) 085, arXiv:1504.01330 [hep-ph].

[158] ATLAS Collaboration, *Measurements of $W^{\pm}Z$ production cross sections in pp collisions at $\sqrt{s} = 8$ TeV with the ATLAS detector and limits on anomalous gauge boson self-couplings*, Phys. Rev. **D93** no. 9, (2016) 092004, arXiv:1603.02151 [hep-ex].

[159] M. Grazzini, S. Kallweit, D. Rathlev, and M. Wiesemann, *$W^{\pm}Z$ production at hadron colliders in NNLO QCD*, arXiv:1604.08576 [hep-ph].

[160] F. Cascioli, T. Gehrmann, M. Grazzini, S. Kallweit, P. Maierhöfer, A. von Manteuffel, S. Pozzorini, D. Rathlev, L. Tancredi, and E. Weihs, *ZZ production at hadron colliders in NNLO QCD*, Phys. Lett. **B735** (2014) 311–313, arXiv:1405.2219 [hep-ph].

[161] M. Grazzini, S. Kallweit, and D. Rathlev, *ZZ production at the LHC: fiducial cross sections and distributions in NNLO QCD*, Phys. Lett. **B750** (2015) 407–410, arXiv:1507.06257 [hep-ph].

[162] D0 Collaboration, *Measurement of the $t\bar{t}$ production cross section in $p\overline{p}$ collisions at $\sqrt{s} =$ 1.96 TeV using secondary vertex b tagging*, Phys. Rev. D **74** (2006) 112004.

[163] ATLAS Collaboration, *Measurement of the top quark-pair production cross section with ATLAS in pp collisions at $\sqrt{s} = 7$ TeV*, Eur. Phys. J. **C71** (2011) 1577, arXiv:1012.1792 [hep-ex].

[164] C.-H. Kom and W. Stirling, *Charge asymmetry in W + jets production at the LHC*, The European Physical Journal C **69** no. 1-2, (2010) 67–73.

[165] ATLAS Collaboration, *Measurement of the inclusive $W^{\pm}$ and Z/γ cross sections in the electron and muon decay channels in pp collisions at $\sqrt{s} = 7$ TeV with the ATLAS detector*, Phys. Rev. **D85** (2012) 072004, arXiv:1109.5141 [hep-ex].

[166] R. D. Ball *et al.*, *A first unbiased global NLO determination of parton distributions and their uncertainties*, Nucl. Phys. **B838** (2010) 136, arXiv:1002.4407 [hep-ph].

[167] M. Botje, J. Butterworth, A. Cooper-Sarkar, A. de Roeck, J. Feltesse, *et al.*, *The PDF4LHC Working Group Interim Recommendations*, arXiv:1101.0538 [hep-ph].

[168] I. W. Stewart and F. J. Tackmann, *Theory Uncertainties for Higgs and Other Searches Using Jet Bins*, Phys. Rev. **D85** (2012) 034011, arXiv:1107.2117 [hep-ph].

[169] T. Gehrmann, M. Grazzini, S. Kallweit, P. Maierhöfer, A. von Manteuffel, S. Pozzorini, D. Rathlev, and L. Tancredi, *Private communication*.

[170] J. R. Andersen *et al.*, *Les Houches 2013: Physics at TeV Colliders: Standard Model Working Group Report*, arXiv:1405.1067 [hep-ph].

[171] S. Gieseke, T. Kasprzik, and J. H. Kühn, *Vector-boson pair production and electroweak corrections in HERWIG++*, Eur. Phys. J. **C74** no. 8, (2014) 2988, arXiv:1401.3964 [hep-ph].

[172] K. Rolbiecki and K. Sakurai, *Light stops emerging in WW cross section measurements?*, JHEP **09** (2013) 004, arXiv:1303.5696 [hep-ph].

[173] J. S. Kim, K. Rolbiecki, K. Sakurai, and J. Tattersall, *'Stop' that ambulance! New physics at the LHC?*, JHEP **12** (2014) 010, arXiv:1406.0858 [hep-ph].

[174] D. Curtin, P. Meade, and P.-J. Tien, *Natural SUSY in Plain Sight*, Phys. Rev. **D90** no. 11, (2014) 115012, arXiv:1406.0848 [hep-ph].

[175] K. Rolbiecki and J. Tattersall, *Refining light stop exclusion limits with W^+W^- cross sections*, Phys. Lett. **B750** (2015) 247–251, arXiv:1505.05523 [hep-ph].

[176] T. Adye, *Unfolding algorithms and tests using RooUnfold* in *Proceedings of the PHYSTAT 2011 Workshop, CERN, Geneva, Switzerland, January 2011, CERN-2011-006, pp 313-318*, pp. 313–318. 2011. arXiv:1105.1160 [physics.data-an].

[177] G. D'Agostini, *Improved iterative Bayesian unfolding*, arXiv:1010.0632 [physics.data-an].

[178] LHC Higgs Cross Section Working Group, *CERN Report 4: Part I Standard Model Predictions*.

[179] J. Alwall, R. Frederix, S. Frixione, V. Hirschi, F. Maltoni, O. Mattelaer, H. S. Shao, T. Stelzer, P. Torrielli, and M. Zaro, *The automated computation of tree-level and next-to-leading order differential cross sections, and their matching to parton shower simulations*, JHEP **07** (2014) 079, arXiv:1405.0301 [hep-ph].

[180] M. Bahr *et al.*, *Herwig++ Physics and Manual*, Eur. Phys. J. C **58** (2008) 639–707, arXiv:0803.0883 [hep-ph].

Acknowledgements

I want to take the completion of my Ph.D. as an opportunity to thank the many people in Freiburg and elsewhere that have helped and supported me throughout the years, and that sharpened my research interests and my knowledge in physics.

I want to thank Prof. Karl Jakobs for accepting me as a PhD student and giving me the liberty to develop and explore my research interests. He found time to provide valuable advice whenever necessary and despite his busy schedule. Thanks also for the possibility to spend such a long period at CERN and for many trips to workshops and conferences.

I am particularly grateful to my supervisor Kristin Lohwasser who taught me all about data analysis and politics in ATLAS. She supported me in all my endevours, pulled the strings in the back and always looked out for me. I thank her for all she has done for me and for her friendship over the past six years.

I very much profited from the experience of Christian Weiser and Valerio Dao. Thanks for the long discussions, for your insights and for teaching me quite a few things. Thanks to the members of the Freiburg group who made the presence in the office enjoyable, never forgot about me during my time at CERN and helped out whenever I ran into problems. This holds especially for my office mates, Francesca, Felix, Daniel, Giulia, and my fellow PhD students Hannah and Nils.

The intense work on the WW analysis was exciting and the atmoshpere in the team remained positive despite many setbacks. It was a pleasure to work with Dimitra and Karen and I thank especially Yusheng, for being a patient teacher, keeping calm even at stressful times and for joining and supporting me in my passion project, the 1-jet bin.

Finally, I thank my mother and sister for their moral support during the past years, as well as my relatives in Amoltertalgasse. Thanks to my father, for passing on his fascination for mathematics and the phenomena of nature.